MAGNETISM

Investigation of interlayer coupling in $[Fe/Cr]_n$ magnetic multilayer structures by the ferromagnetic resonance method (Review)

N. M. Kreines*

P. L. Kapitza Institute of Physics Problems, ul. Kosygina 2, 117334 Moscow, Russia
(Submitted December 28, 2001)
Fiz. Nizk. Temp. **28**, 807–821 (August–September 2002)

The properties and nature of the interlayer coupling and the possible types of magnetic ordering in magnetic superlattices and sandwiches remain topical questions in the physics of magnetic phenomena. The existing models describing the interaction between ferromagnetic layers via the nonferromagnetic spacer layer and the predicted temperature dependence of the coupling constants in those models are briefly reviewed. The effectiveness of the ferromagnetic resonance method for investigating the interlayer coupling is discussed. A review of recent experimental studies of the interlayer coupling in superlattices and sandwiches of the Fe/Cr system by this method over a wide range of temperatures is presented (including original papers by the author and co-workers). The experimental data are analyzed on the basis of the existing theories. The regions of applicability of these model for describing the properties of such systems. © *2002 American Institute of Physics.* [DOI: 10.1063/1.1511701]

1. INTRODUCTION

Metallic magnetic multilayer systems, or superlattices, which are periodic structures consisting of alternating thin layers of a ferromagnetic metal (Fe, Co, Ni, ...) and a nonferromagnetic metal (Ag, Au, Cr, Cu, Mn, ...), form a special class of materials with unusual physical properties. The discovery of the giant magnetoresistance effect in the Fe/Cr system[1,2] has led to a sharp growth in interest in the whole set of these objects and has stimulated intensive research on the magnetic, magnetoresistive, and other properties inherent to such structures. There have been many theoretical and experimental studies devoted to the interaction between neighboring ferromagnetic layers in a superlattice. The results of these studies have been written up in a number of review articles (see, e.g., Refs. 3–9). It has been shown experimentally that, depending on the thickness of the nonferromagnetic spacer in the multilayer or three-layer (sandwich) structure, a ferromagnetic, antiferromagnetic, or noncollinear ordering of the magnetic moments of the neighboring ferromagnetic layers can be realized. The interaction energy describing these magnetic structures is generally represented as a sum of two contributions, bilinear and biquadratic in the magnetizations of the neighboring layers. The competition of these two contributions can, generally speaking, lead to an arbitrary angle between the magnetizations of the neighboring ferromagnetic layers in zero magnetic field. The necessity of taking into account the second term in the expression for the interaction energy arose in connection with the experimentally observed 90-degree magnetic ordering in Fe/Cr/Fe (Ref. 10) and Co/Cu/Co (Ref. 11) samples. Subsequently the biquadratic exchange has been detected experimentally in many superlattices, but the mechanism giving rise to it has not been conclusively established. The large value obtained for the biquadratic in comparison with the bilinear exchange in a number of experiments raises doubts about whether the term quadratic in the magnetizations is being taken into account correctly in the expression for the energy. There is also a large discrepancy between the experimentally measured value of the bilinear exchange and the results of calculations from first principles. Not enough attention has been paid to the study of the temperature dependences of the two exchange constants. It would appear that a comparison of these with the theoretical predictions would permit reaching more definite conclusions as to the mechanism giving rise to the biquadratic exchange and to answer a number of other important questions. All of these problems are stimulating further experimental and theoretical research on multilayer magnetic metallic structures.

Extremely diverse experimental techniques are used to study the properties of superlattices, e.g., measurement of the magnetization curves with the use of Kerr, vibrational, and SQUID magnetometry, measurement of the magnetoresistance, determination of the magnetic structure by the neutron diffraction method, determination of the magnetic excitation spectra by the method of inelastic light scattering, and investigation of the quality of the interfaces by the method of Mössbauer spectroscopy.[8] Recently the quality of three-layer sandwich structures and the magnetic interactions in them have been investigated by modern methods of scanning tunneling microscopy, magnetic force microscopy, and scanning electron microscopy with polarization analysis (see also Refs. 5 and 12).

Among this large set of experimental methods of studying magnetic superlattices, an extremely simple and rather effective method is to investigate the ferromagnetic resonance (FMR) spectrum. This method has been used repeatedly by different groups (see the reviews cited as Refs. 3 and

13 and also Refs. 14–22) both for determining the uniaxial and in-plane magnetic anisotropy and for determining the coupling between neighboring ferromagnetic layers.

In this article we attempt to show the possibilities of the FMR method for studying the interlayer exchange in superlattices. Since there is a vast amount of published experimental material on this topic, we shall restrict discussion mainly to the data for the Fe/Cr system. This restriction (or choice) is also motivated by the circumstance that the author and co-workers have studied superlattices of this system.[17–22] Those results will be presented in greater detail.

2. MODELS OF THE INTERLAYER EXCHANGE INTERACTION

Let us briefly discuss the main theoretical models describing the interlayer coupling in multilayer magnetic structures.

As was mentioned in the Introduction, the energy of interaction between two ferromagnetic layers across a nonferromagnetic spacer is customarily written as a sum of two contributions:

$$E = -J_1 \cos\theta - J_2 \cos^2\theta, \tag{1}$$

where θ is the angle between the magnetic moments of the neighboring ferromagnetic layers, and J_1 and J_2 are phenomenological constants. The first term describes the bilinear exchange interaction of a Heisenberg nature. Depending on the value of the constants J_1, this term leads to collinear parallel or antiparallel ordering of the neighboring magnetic moments. The second term, which characterizes the biquadratic exchange, gives a preferential 90-degree ordering for negative values of the constant J_2.

2.1. Bilinear interaction

There are a number of theoretical models describing the nature of the bilinear exchange interaction. One of the first used the Ruderman–Kittel–Kasuya–Yosida (RKKY) theory, which had been developed previously for describing the interaction between magnetic impurities in a nonmagnetic matrix. In the case of superlattices this theory is used to treat the interaction between the magnetic moments of the layers and the spins of the conduction electrons of the spacer layer. It predicts the presence of an oscillatory dependence of this interaction on the thickness of the spacer and determines the values of the possible oscillation periods, but it encounters difficulties in estimating the value of the interaction itself. In another theoretical approach the interlayer coupling is determined by the dependence on the spin direction of the amplitude of electron reflection at the interface between the spacer and ferromagnetic layers. In both approaches the value of the period is determined by the extremal size of the Fermi surface (the critical spanning vector) of the spacer material in the direction normal to the surface of the sample. It is known that for the Fe/Cr/Fe system when the chromium is paramagnetic, two oscillation periods are observed: short, $\Lambda_S \sim 3$ Å (~ 2.11 chromium monolayers), and long, $\Lambda_L \sim 18$ Å (~ 12 chromium monolayers). Here J_1 can be written in the form (see Ref. 5 for more details)

$$J_1 = (1/nt)A_S \sin(2\pi nt/\Lambda_S + \Phi_S) + (1/n^2t^2)A_L \sin(2\pi nt/\Lambda_L + \Phi_L). \tag{2}$$

Here A_S, A_L and Φ_S, Φ_L, which are respectively the amplitudes and phases of the short- and long-period oscillations, are determined by the geometric features of the Fermi surface of the spacer material and the probabilities of reflection of electrons from the interfaces. The dependence of the amplitude of the short- and long-wavelength oscillations on the thickness t of the spacer layer is shown by the respective multiplicative factors in formula (2).

To acquire more familiarity with the details of the above and other models of the bilinear exchange, the reader is referred to two relatively recent review articles.[6,7] We note only that the many experimental results obtained at room temperature are described fairly well in the framework of the existing approaches.

The majority of the models[6,7] also predict an extremely simple form for the temperature dependence of J_1:

$$J_1(T) = J_1(0)\frac{T/T_0}{\sinh(T/T_0)}, \tag{3}$$

where $J_1(0)$ and T_0 are constants that depend on the parameters of the corresponding part of the Fermi surface. According to estimates, formula (3) implies a weak temperature dependence of the bilinear exchange.

The approach developed in Ref. 23 takes into account the influence of thermal spin fluctuations in the ferromagnetic films on the temperature dependence of the effective exchange interaction in the superlattices. As a result, the exchange between the ferromagnetic layers can be written as a product of functions $f_{SW}(T)$ and $f_e(T)$, where $f_e(T)$ is described by formula (3), in accordance with the RKKY theory, and $f_{SW}(T)$ is a renormalizing factor that arises due to the presence of thermal spin fluctuations at the interface and is proportional to $T^{3/2}$.

A comparatively small number of detailed experimental studies of the temperature dependence of $J_1(T)$ for different systems do not yet permit reaching unambiguous conclusions as to the regions of applicability of the existing theories.

2.2. Biquadratic interaction

Contrary to the bilinear interaction, the nature of which is rather reliably described using theories based on the concept of collectivized (itinerant) electrons,[6,7] the nature of the biquadratic interaction has not been established with certainty. The RKKY theory predicts the presence of a biquadratic term J_2 in the expression for the magnetic energy of an ideal superlattice (intrinsic mechanism).[7] According to calculations, its value $|J_2|$ is substantially less than $|J_1|$. Therefore, it should only be manifested at those spacer thicknesses for which $|J_1|$ is close to zero. The values of the biquadratic exchange constants obtained experimentally for practically any thicknesses of the spacer layer are in the majority of cases of the same order as the bilinear exchange constant. To eliminate this contradiction a number of theoretical models have been proposed, which take into account the presence of various kinds of defects existing in real samples (extrinsic mechanisms) and can give sufficiently large values of the biquadratic exchange constant. A detailed review of this topic is given in Ref. 4. Let us briefly list the "extrinsic" mechanisms that have been considered in the literature.

The *fluctuation mechanism* proposed by Slonczewski,[24] has its origins in the presence of a terrace or step at the interface between layers, causing fluctuations of the thickness of the nonferromagnetic spacer layer. The fluctuations ΔJ_1 of the bilinear exchange that arise in this case give rise to a biquadratic term J_2 in the expression for the magnetic energy. In the simplest case the relation between these quantities is expressed by the formula

$$J_2 = -\frac{4(\Delta J_1)^2 L}{\pi^3 A}\coth\left(\frac{\pi D}{L}\right), \tag{4}$$

where A is the exchange stiffness of the ferromagnetic layers of thickness D, and L is the width of a terrace one monolayer high. If $\Delta J_1 \sim 1/t$, then a dependence $J_2 \propto 1/t^2$ is obtained.

Another mechanism, also proposed by Slonczewski,[25] attributes the appearance of the biquadratic exchange to the presence of a *magnetic impurity ("loose spin")* inserted in the nonferromagnetic spacer layer of the sandwich. This mechanism leads to an exponential temperature dependence for the exchange constant: $I_2 \propto \exp(-\alpha T)$.

We should also mention the *magnetic dipole mechanism*[4] of formation of biquadratic exchange. It originates from the dipole fields arising at nonuniform interfaces in layered structures. It was found that the dipole fields arising at nonuniformities fall off with distance much more slowly than in the case of ideally smooth surfaces and, accordingly, can give rise to biquadratic exchange.

Alternative models for the mechanism of biquadratic exchange for magnetic structures with spacer layers of chromium and manganese are also considered. The authors of Ref. 26, in considering the $[\mathrm{Fe/Cr}]_n$ system, indicate that it is necessary for a peculiar sort of domain structure to form in such a superlattice in the case when sufficiently large atomically smooth parts of the iron–chromium interface exist.

To explain the noncollinear magnetic structure in the case of chromium or manganese spacer layers, Slonczewski[27] proposed a "*proximity magnetism*" model which assumes a different form of the interaction energy of neighboring iron layers in the structure as compared to the biquadratic exchange:

$$E = C_+(\theta) + C_-(\theta - \pi)^2. \tag{5}$$

Here θ is the angle between the magnetizations of the neighboring ferromagnetic layers, and C_+ and C_- are phenomenological constants. Such a form of the energy arises as a result of the presence of magnetic stiffness of the spacer and a strong exchange interaction across the boundary with the neighboring ferromagnetic layers.

The fact that the experimental data are discussed in the literature in the framework of the different models described above attests to the lack of a unified approach to the explanation of the nature of the biquadratic exchange in different systems.

3. ANALYTICAL CALCULATION OF THE STATIC MAGNETIZATION AND FERROMAGNETIC RESONANCE SPECTRUM OF A SUPERLATTICE

We present the results of an analytical calculation of the magnetization curves and FMR spectrum for superlattices in the biquadratic exchange model with the fourth-order anisotropy taken into account, in the case when the external magnetic field H lies in the plane of the film. In general form this calculation was done by the authors of Ref. 20 in application to the system $[\mathrm{Fe/Cr}]_n$, the elements of which have cubic symmetry. As in the other similar calculations, it was assumed that the magnetization of each ferromagnetic layer is uniform over the volume of the layer and equal to M_S regardless of the value of the external field, and the magnetic moment of each such layer precesses as a whole. The initial expression for the magnetic part of the energy of a multilayer structure per unit are of the film is written in Ref. 20 in the form

$$\begin{aligned} E = &-d\sum_{j=1}^{n}(\mathbf{H}\cdot\mathbf{M}_j) - \frac{J_1}{M_S^2}\sum_{j=1}^{n-1}(\mathbf{M}_j\cdot\mathbf{M}_{j+1}) \\ &- \frac{J_2}{M_S^4}\sum_{j=1}^{n-1}(\mathbf{M}_j\cdot\mathbf{M}_{j+1})^2 + d\frac{N_{zz}}{2}\sum_{j=1}^{n}(\mathbf{M}_j\cdot\mathbf{z})^2 \\ &- d\frac{K_u}{M_S^2}\sum_{j=1}^{n}(\mathbf{M}_j\cdot\mathbf{z})^2 - d\frac{H_a}{4M_S^3}\sum_{j=1}^{n}[(\mathbf{M}_j\cdot\mathbf{x})^4 \\ &+ (\mathbf{M}_j\cdot\mathbf{y})^4 + (\mathbf{M}_j\cdot\mathbf{z})^4], \end{aligned} \tag{6}$$

where J_1 and J_2 are the bilinear and biquadratic exchange constants, M_j is the magnetization of the jth layer of ferromagnetic metal, d is the layer thickness, N_{zz} is the demagnetizing factor, K_u describes the uniaxial anisotropy, H_a is the effective fourth-order anisotropy field, with easy axes **x**, **y**, and **z**, the axis **z** coinciding with the normal to the surface, and n is the number of ferromagnetic layers in the structure. Below for convenience we introduce an effective coefficient of surface anisotropy

$$k_{\mathrm{eff}} = N_{zz} - 2K_u/M_S^2. \tag{7}$$

We consider the limit of an infinite superlattice ($n \to \infty$), since only under that condition can the analytical calculation be carried through to the end. The calculation is done for the two most symmetric cases, when the external magnetic field is applied along the easy or hard axis of anisotropy in the film plane. Here it turns out that in a rather wide range of magnetic fields the condition of minimum energy leads to two-sublattice ordering of the ferromagnetic moments of the layers, with the sublattice magnetizations arranged symmetrically with respect to the external field. In this case one can obtain analytical expressions for the magnetization curves:

for $H_C^{E,H} < H < H_S^{E,H}$

$$H = \left(-\frac{4J_1 - 8J_2}{dM_S^2} \pm \frac{H_a}{M_S}\right)M + \left(-\frac{16J_2}{dM_S^4} \mp 2\frac{H_a}{M_S^3}\right)M^3, \tag{8}$$

for $H > H_S^{E,H}$

$$M = M_S. \tag{9}$$

Here the upper and lower signs and the superscripts E and H correspond to magnetic field directions along the easy and hard axes of anisotropy, respectively. The $M(H)$ curve determined by the implicit equation (8) describes a state with a nonzero angle between the sublattice magnetizations. Solution (9) pertains to a state of saturation, when the magneti-

zations of all the layers are oriented along the magnetic field. The value of the field at which saturation occurs is written in the form $H_S^{E,H}=-(4J_1+8J_2)/dM_S\mp H_a$. The magnetic field regions in which the solutions (8) and (9) correspond to a minimum of the system energy are discussed in detail in Ref. 20.

For calculating the oscillation spectrum of the system under consideration we used the Landau–Lifshitz equation without a dissipative term:

$$\gamma^{-1}(\partial M_j/\partial t)=\mathbf{M}_j\times(\partial E/\partial\mathbf{M}_j)d^{-1}, \tag{10}$$

where γ is the gyromagnetic ratio. For solving Eq. (10) the magnetization $\mathbf{M}_j$ is written as the sum of the static magnetization and a small correction in the form a wave propagating along the normal to the film plane:

$$\mathbf{M}_j=\mathbf{M}_j^{(0)}+\mathbf{m}_j\exp\{-i(\omega t-jq)\}. \tag{11}$$

The quantity q is the product of the wave vector and the superlattice period. It can be regarded as the phase difference in the precession of the magnetizations of neighboring ferromagnetic layers; $q=0$ corresponds to an acoustic mode, and $q=\pi$ to an optical mode.

After substituting (11) into (10) and linearizing the resulting equations with respect to m_j, we can use the condition of nontriviality of the solution to find the oscillation frequencies as functions of q and of the magnetic field H: for $H_C^{E,H}<H<H_S^{E,H}$

$$\frac{\omega_q^2}{\gamma^2}=\left[(A+BM^2)\cos^2\frac{q}{2}+K_{\text{eff}}+\frac{3H_1}{4M_S}\pm\frac{H_a}{M_S^3}(M_S^2-M^2)\right]$$
$$\times\left[(A+BM^2)M^2\cos^2\frac{q}{2}+(A+3BM^3)(M_S^2-M^2)\right.$$
$$\left.\times\sin^2\frac{q}{2}\pm\frac{H_a}{M_S^3}(M_S^2-M^2)(M_S^2-6M^2)\right]; \tag{12}$$

for $H>H_S^{E,H}$

$$\frac{\omega_q^2}{\gamma^2}=\left[H-H_S^{E,H}\sin^2\frac{q}{2}+K_{\text{eff}}M_S+\frac{3H_a}{4}\pm H_a\left(\cos^2\frac{q}{2}-\frac{3}{4}\right)\right]$$
$$\times\left(H-H_S^{E,H}\sin^2\frac{q}{2}+H_a\cos^2\frac{q}{2}\right), \tag{13}$$

where we have introduced the notation

$$A=-\frac{4J_1-8J_2}{dM_S^2},\quad B=-\frac{16J_2}{dM_S^4}. \tag{14}$$

For $H_a=0$ formulas (8), (9) and (12), (13) go over to the corresponding expressions from Ref. 18, and for $H=0$ they go over to the results of Ref. 28. We again stress that the formulas obtained are valid in the case of two-sublattice ordering of the magnetic moments, with a symmetric arrangement of the sublattice magnetizations with respect to the magnetic field, i.e., at large fields H_C (see Ref. 20).

4. EXPERIMENTAL RESULTS

4.1. Types of samples and methodological notes

The term ''multilayer magnetic structure'' or ''superlattice'' applies to samples of two types.

First, the so-called ''sandwich'' structures, consist of two layers of a ferromagnetic metal separated by a nonferromagnetic metal. The main advantages of working with sandwiches include, as a rule, higher sample quality and comparatively simple interpretation of the experimental data. On the other hand, in such samples the value of the magnetic anisotropy in the plane of the sandwich (film), as a rule, is comparable to the interlayer coupling effects. As a result, either a collinear or a 90-degree ordering of the magnetic moments of the ferromagnetic metal layers is realized in them. In some cases this can complicate the experimental determination of the interlayer exchange constants. In addition, the small total thickness of the ferromagnetic layers in the samples requires highly sensitive instrumentation in order to obtain reliable experimental results.

The second type of sample is a ''superlattice,'' i.e., a periodic structure consisting of a large number (in practice up to several tens) of identical layers of a ferromagnetic metal, separated by a nonferromagnetic spacer. Since each of the ferromagnetic layers interacts simultaneously with two neighbors, in such a structure the effects of the multilayer exchange are expressed much more strongly and are considerably larger than the anisotropy in the film plane. For example, the magnetic field required to ''collapse'' the magnetic moments of all the layers into a collinear structure in an $[\text{Fe/Cr}]_n$ superlattice can exceed 10 kOe[19,20,29] at a value of the fourth-order anisotropy field in the iron of around 500 Oe. In this situation, even in the absence of an external magnetic field, the direction of the magnetization vector in each of the ferromagnetic layers cannot coincide with the axis of easy magnetization — the ''easy'' axis of the magnetic anisotropy. Its direction is determined, first, by the minimum of the interlayer interaction energy. As a result, a so-called ''canted'' or noncollinear magnetic structure is observed, wherein the magnetic moments form two sublattices with a mutual ordering angle different from 0, 90°, and 180° (Refs. 20, 30, and 31). The large number of layers, including the ferromagnetic metal layers, in a superlattice eases the requirements on the sensitivity of the instrumentation used. However, this same circumstance complicates considerably the interpretation of the experimental results, both from magnetization and resonance measurements. In addition, the quality of multilayer samples is obviously somewhat lower than that of sandwiches on account of the large number of layers and interfaces.

The FMR spectra have been studied for both sandwiches and superlattices. Essentially all the experiments have been done under conditions where the external magnetic field is applied in the film plane. From what we have said (see Sec. 3) it is clear that the most reliable way of determining the interlayer coupling from FMR experiments is to register not only the uniform resonance mode but all nonuniform modes, including optical. The uniform resonance mode is excited by an rf field applied perpendicular to the external magnetic field. The excitation of nonuniform modes is done under conditions of parallel pumping, i.e., in an experimental geometry such that the rf magnetic field is parallel to the static field. Thus, to obtain the total FMR spectrum of a superlattice requires both methods of exciting resonance. However, the intensity of the absorption lines in the nonuniform modes is

low, since those modes can be excited only owing to the finite number of layers of ferromagnetic metal in the structure or a small nonuniformity in their thickness (see Refs. 13 and 32 for details). Therefore, it is often impossible to register all of the possible modes experimentally. In the case of nonidentical thicknesses of the ferromagnetic layers the intensity of the absorption line in the nonuniform modes increases, and they become easier to observe, but the theoretical interpretation of the spectrum of such a system becomes more difficult.

In the experimental study of the interlayer coupling by the FMR technique either a wide range of microwave frequencies and magnetic fields is used in order to excite all of the modes of the resonance spectrum of the superlattice (see, e.g., Refs. 13 and 18–22) or the uniform and nonuniform modes are excited at a single frequency and the anisotropy of their resonance fields in the plane of the sample is studied (see, e.g., Ref. 16). The experimental data obtained are processed in accordance with the corresponding theoretical model.

4.2. FMR in three-layer (sandwich) samples

A large fraction of the experimental studies of the FMR spectrum have been done on three-layer samples. In the early studies (on the observation of the biquadratic contribution to the energy of a superlattice) the processing of the measured spectra was done without taking the the biquadratic exchange into account. A rather complete review of the data obtained in this way is presented in Refs. 8 and 13.

Below we discuss the results of more recent studies that were not included in the reviews mentioned above and in which the experimental data were processed using the biquadratic exchange model.

A series of studies of the interlayer coupling in Fe/Cr/Fe sandwiches with different thicknesses of the chromium spacer (5–25 Å) in the temperature range 2–300 K was carried out by Brazilian scientists.[14–16] The samples used in those studies were grown both by molecular epitaxy and magnetron sputtering. The ferromagnetic resonance was excited at a frequency of 9.4 GHz, and the acoustic and optical modes were recorded. For both modes the resonant value of the magnetic field was studied as a function of its direction in the plane of the sandwich. The results of the measurements were discussed in the framework of the biquadratic exchange model. To determine the exchange constants at room temperature the authors used additional data obtained in a study of the magnetization curves and the inelastic (Brillouin) light-scattering spectra. Analysis of the whole set of results obtained at $T=300$ K led the authors to conclude that the model used describes the experimental data quite well. For the series of Fe/Cr/Fe samples investigated in those studies, with thicknesses t_{Cr} of the chromium spacer layer corresponding to the first antiferromagnetic maximum in the bilinear exchange, the value of the biquadratic energy constant J_2 decreases monotonically with increasing t_{Cr} and varies over the limits $0.058-0.019$ erg/cm^2 and $16>|J_1/J_2|>10$.

The temperature dependence of the interlayer coupling in the samples discussed above was investigated in Refs. 15 and 16 using only the FMR method. In Ref. 15 the $J_1(T)$ and $J_2(T)$ curves are presented for two samples with spacer

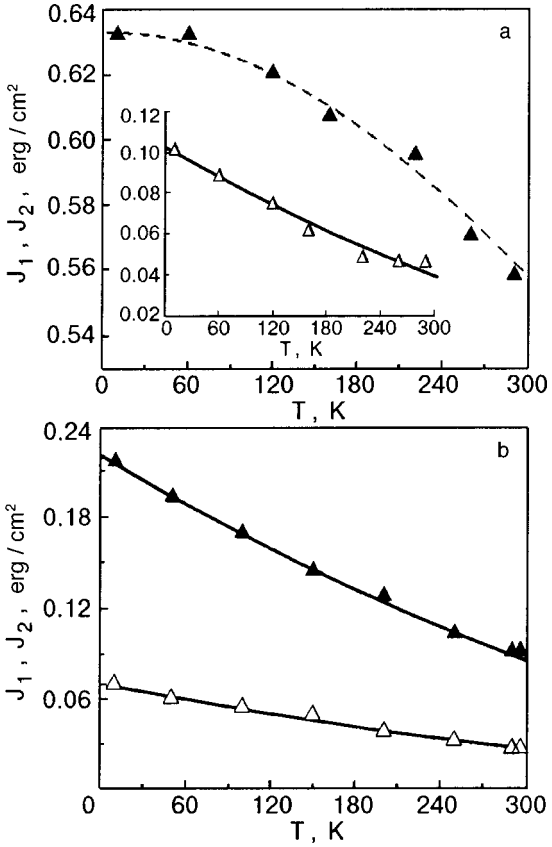

FIG. 1. Temperature dependence of the bilinear J_1 (▲) and biquadratic J_2 (△) exchange coupling for Fe(40 Å)/Cr(11 Å)/Fe(40 Å) (a) and Fe(40 Å)/Cr(15 Å)/Fe(40 Å) (b). The curves are the result of a calculation (see text).[15]

thicknesses of 11 and 15 Å (Fig. 1). The behavior of the biquadratic exchange constants is the same for both samples and conforms well to a quadratic temperature dependence: $J_2(T)=J_2(0)(1-T/T_0)^2$, where $T_0=790$ K and $J_2(0)$ is the value of the exchange constant for $T=0$ K. The temperature dependence of the bilinear exchange constant $J_1(T)$ for the two samples cannot be described by a single law. For the sample with $t_{Cr}=15$ Å $J_1(T)$ conforms well to the same dependence as $J_2(T)$, with the same value of the characteristic temperature T_0. However, the results obtained for the second sample are better described by a dependence derived from the RKKY theory:[6,7] $J_1(T)=0.633(T/340)/\sinh(T/340)$. In a more recent paper[16] in which the FMR method was used to study the temperature dependence of the interlayer coupling for three samples with $t_{Cr}=11$, 13, and 15 Å, the experimental data obtained are discussed in the framework of the renormalization theory proposed in Ref. 23 (see Sec. 2.1). A comparison of the temperature dependence of the exchange parameter $H_{ex}(T)/H_{ex}(10\text{ K})$ (Fig. 2) determined from the FMR experiments as the difference of the frequencies of the acoustic and exchange modes with the predictions of the theory mentioned above led the authors of Ref. 16 to conclude that the main contribution to this dependence is from spin fluctuations in the ferromagnetic films. Thus it follows from Refs. 15 and 16 that at the present time the temperature behavior of the interlayer coupling in sandwiches remains an open question.

Let us mention one more result from an unconventional

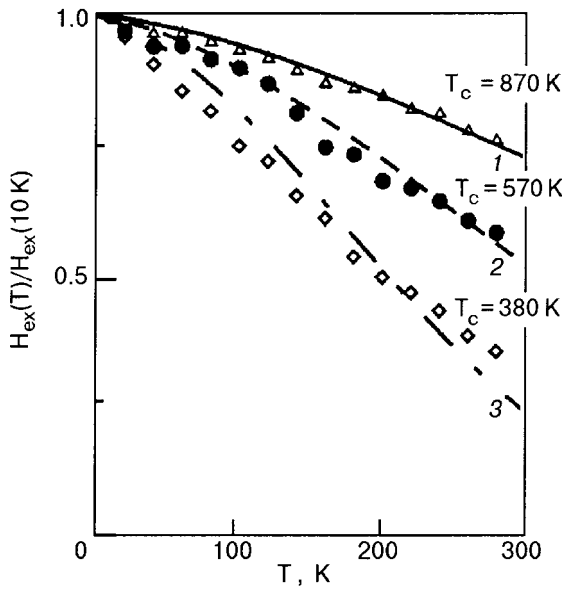

FIG. 2. Temperature dependence of the normalized effective exchange parameter H_{ex} for Fe(40 Å)/Cr(t_{Cr})/Fe(40 Å) samples with different thicknesses t_{Cr}, Å: 11 (*1*), 13 (*2*), and 15 (*3*). The symbols are experimental data, the curves are the results of a calculation. T_C is the characteristic temperature below which the spin-wave approach is valid.[16]

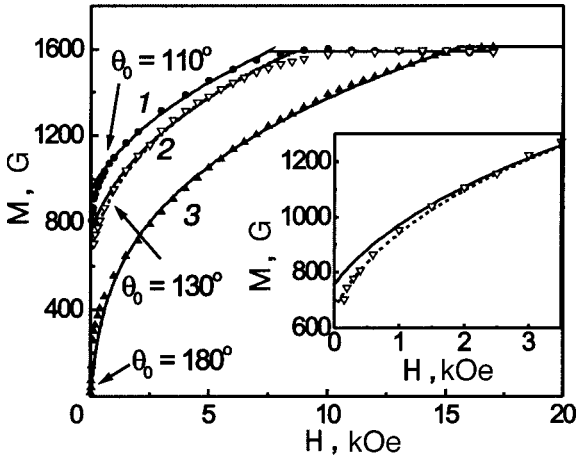

FIG. 3. Magnetic field dependence of the magnetization for three samples: [Fe(33 Å)/Cr(10 Å)]$_{16}$ (*1*), [Fe(48 Å)/Cr(7.6 Å)]$_{16}$ (*2*), and [Fe(20 Å)/Cr(10 Å)]$_{20}$ (*3*). The symbols are the experimental director. The solid curves were calculated using formulas (8) and (9), and the dashed curves by a numerical calculation. Inset: The low-field part of $M(H)$ for the sample [Fe(48 Å)/Cr(7.6 Å)]$_{16}$ on an expanded scale.[20]

FMR study of the interlayer coupling in a sandwich. In Ref. 33 the influence of optical irradiation at wavelength $\lambda = 0.5145$ μm on the interlayer coupling was observed in an Fe/Si/Fe three-layer system. The change of the resonant field under the influence of the irradiation was studied for different thicknesses of the silicon spacer in the temperature range from 77 to $\approx$300 K. The observed change of the magnetic state of the sample under irradiation was attributed by the authors to changes in the semiconductor spacer: a change in the concentration of charge carriers, which convey the interaction between the magnetic layers, and a change in the structure of the electron density of states function. It was noted in Ref. 33 that at low temperatures the photoinduced contribution to the coupling is always antiferromagnetic.

4.3. FMR in superlattices

The most comprehensive FMR investigation of the interlayer coupling in [Fe/Cr]$_n$ superlattices, to the best of the author's knowledge, was done by him and his co-workers in a series of studies.[17–22] In this Section we shall discuss the results in detail.

The [Fe/Cr]$_n$ superlattices studied in Refs. 17–22 were grown by molecular-beam epitaxy on the Katun' S apparatus at the Institute of Metal Physics (IMP), Urals Branch of the Russian Academy of Sciences. The [001] crystallographic axis of the iron and chromium films coincided with the normal to the plane of the sample. The samples used were characterized by the following parameters: the number of pairs of layers, n, varied from 8 to 24, the thickness of the chromium spacer varied from sample to sample in the range 7.7 $-$14 Å, and the thickness of the iron layers in different samples varied from 20 to 48 Å.

The FMR spectra were studied over a rather wide range of frequencies (9.5–37 GHz) in the temperature interval 2–400 K both with longitudinal and transverse excitation of the resonance. The external magnetic field was always applied in the plane of the sample along the hard [110] and easy [100] crystallographic axes of the anisotropy of the iron.

4.3.1. Measurements of the FMR spectra at room temperature

Let us first discuss the experimental results obtained at room temperature. In Refs. 17–20 the magnetization curves for all the samples were measured together with the FMR spectra. It was deemed important to compare the values of the exchange constants obtained independently by means of these two experimental techniques.

Analysis of the magnetization curves $M(H)$ measured at the IMP for all of the superlattices studied shows that in the absence of an external field the magnetic moments of the iron layers lie in the film plane. In a field applied parallel to this plane the form of the magnetization curves indicates the presence of an appreciable biquadratic exchange. For some of the samples even in zero field there was a large magnetic moment M_0, which indicates the existence of noncollinear magnetic ordering in them. The corresponding angle θ_0 between the magnetizations of neighboring iron layers is equal to 2 arccos(M_0/M_S), where M_S is the saturation magnetization. In the other samples the magnetization curves had a nonlinear approach to saturation. As an example, Fig. 3 shows the magnetic-field dependence of the magnetization for three different samples.

In all the samples the FMR study revealed the presence of several nonuniform modes in addition to the uniform acoustic mode of the FMR. Figure 4 shows a series of experimental curves of the derivative of the absorption lines obtained at different frequencies for one of the samples ([Fe(21 Å))/Cr(10 Å)]$_{12}$) in the case of longitudinal excitation of the resonance. The intense absorption line corresponds to the acoustic resonance mode, and the weaker and broader lines to excitation of nonuniform oscillations of the magnetization. The frequencies of the experimentally ob-

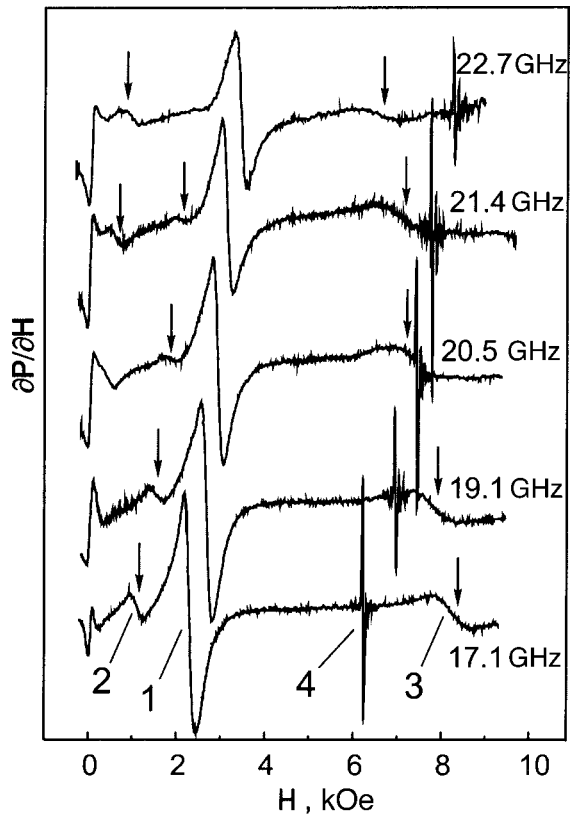

FIG. 4. Derivative of the microwave power absorption versus the magnetic field H for different frequencies of excitation under longitudinal pumping for the samples $[\mathrm{Fe}(21\ \text{Å})/\mathrm{Cr}(10\ \text{Å})]_{12}$ (Ref. 20).

served FMR modes for one of the superlattices are shown in Fig. 5 (points) as functions of the external magnetic field, applied both along the easy and hard axes of anisotropy of the sample.

For the purpose of determining the interlayer exchange from the experimental data, the FMR spectra for the samples were calculated according to formulas (12) and (13). The values of the constants J_1, J_2, and M_S used in constructing the $\omega_q(H)$ curves were obtained as the result of a fitting of the experimental magnetization curves in a field parallel to the film plane by formulas (8) and (9). The values of H_a and K_{eff} were chosen so as to best describe the acoustic branch of the resonance measured along the easy and hard axes of magnetization. The results of the calculation are shown by the solid curves in Fig. 5. The curves are given for modes of oscillation corresponding to values of q from 0 to π with a step of $\pi/(n-1)$, where n is the number of iron layers in the superlattice. It is immediately apparent that the number of experimentally observed resonance branches is considerably smaller than the number of iron layers in the structure. This is because all of the modes except the acoustic and optical modes can be excited only owing to the finite number of iron layers in the structure or a small nonuniformity of their thickness. This suggests that the observed modes correspond to the excitation of standing spin waves with wave vectors perpendicular to the film plane. Thus the proposed theory demonstrates qualitative agreement with experiment. However, it does not always permit a good quantitative description of the experimental spectra, since it does not take into account the influence of the finite value of the number of iron layers in real samples.

To take into account the real experimental situation, a numerical calculation of the spectrum of eigenmodes was carried out for a magnetic superlattice with a finite number of magnetic layers (see Ref. 20 for details). Here the magnetic part of the energy of the system, as in the analytical calculations, was written in the form (6), but the summation was done over the finite number of layers contained in the real samples. Such an approach leads to the result that a structure with a finite number of layers has a more complex magnetic ordering in a magnetic field than does the two-sublattice model structure considered in Sec. 3. The magnetic moments of the outer layers are more strongly canted than the others, and a distribution of angles between neighboring ferromagnetic layers is established over the whole superlattice, the values of the angle depending on the number of the layer. The numerical calculation of the FMR spectra made it possible to improve the agreement of the theoretical curves with the experimental results for all of the samples studied. For example, Fig. 6 shows the results for the

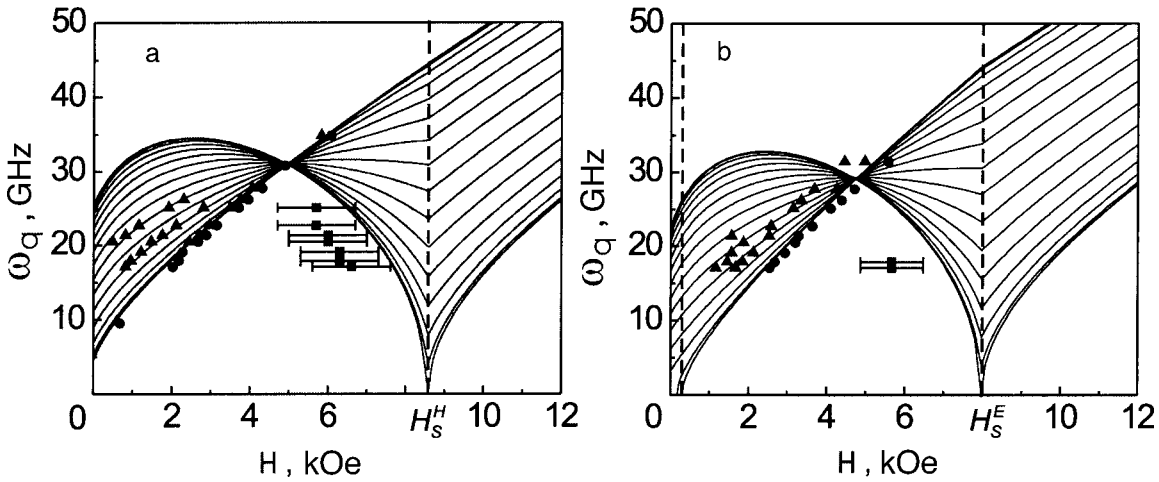

FIG. 5. FMR spectra along the hard (a) and easy (b) axes of magnetization for an $[\mathrm{Fe}(48\ \text{Å})/\mathrm{Cr}(7.6\ \text{Å})]_{16}$ sample. The symbols are the experimental data; the lines were calculated according to formulas (12) and (13) for the following parameter values: $J_1=-0.58$ erg/cm^2; $J_2=-0.50$ erg/cm^2, $M_S=1590$ G, $K_{\text{eff}}=12$, $H_a=300$ Oe.[20] (●) Acoustic modes of resonance.

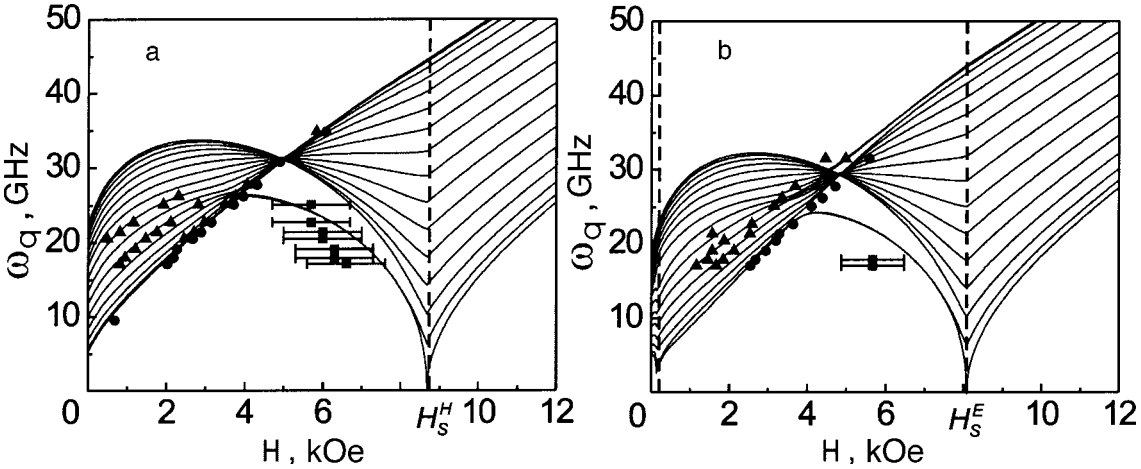

FIG. 6. FMR spectra in a field directed along the hard (a) and easy (b) axes of magnetization, for an $[Fe(48\ Å)/Cr(7.6\ Å)]_{16}$ sample. The symbols are the experimental data; the lines the result of a numerical calculation with the following parameter values: $J_1=-0.67$ erg/cm^2, $J_2=-0.47$ erg/cm^2, $M_S=1590$ G, $K_{\text{eff}}=12$, $H_a=300$ Oe.[20] (●)—Acoustic modes of resonance.

$[Fe(48\ Å)/Cr(7.6\ Å)]_{16}$ sample discussed earlier (see Fig. 5).

As a result, it turned out that the difference in the values of the exchange constants J_1 and J_2 extracted from the magnetization curves and independently from the FMR spectra for the same sample (see Fig. 7) is not more than 10–20%. Thus it has been shown that the interlayer coupling in superlattices can be quite reliably determined from FMR experiments.

Let us briefly discuss a feature of the absolute values of the interlayer coupling obtained from the FMR experiments for superlattices and sandwiches at room temperature. The bilinear exchange constants of nonferromagnetic spacers of the same thickness are practically the same for the two cases. The biquadratic exchange constants, on the other hand, can differ considerably, as they are apparently determined, both for sandwiches and superlattices, by the substrate material and the sample growth method and conditions. These questions have been discussed in detail in the literature.[4,5,8]

As an example, the data taken from Refs. 3, 15, and 20 are shown in Table I.

4.3.2. Measurements of the FMR spectra at intermediate temperatures

To elucidate the nature of the biquadratic exchange, it seemed useful to investigate the temperature dependence of the interlayer coupling constants in superlattices experimen-

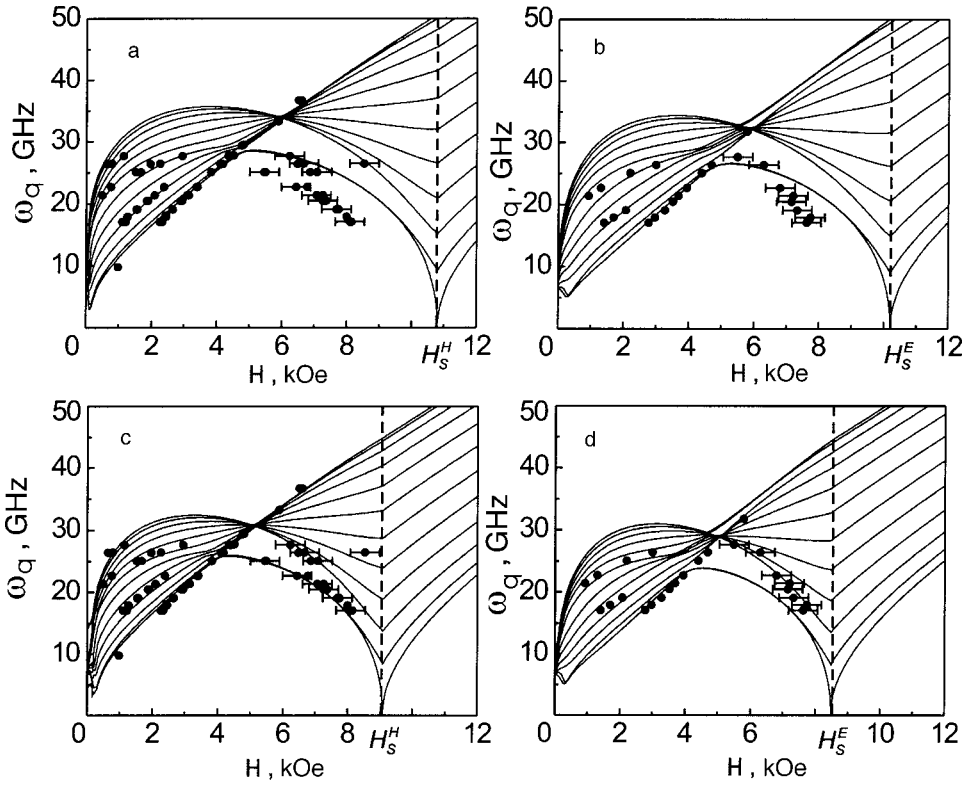

FIG. 7. FMR spectra in a field directed along the hard (a,c) and easy (b,d) axes of magnetization, for an $[Fe(21\ Å)/Cr(10\ Å)]_{12}$ sample. The points are experimental; the curves are the results of a numerical calculation. For graphs "a" and "b" the parameters were extracted from the magnetization curve: $J_1=-0.42$ erg/cm^2, $J_2=-0.24$ erg/cm^2, $M_S=1620$ G, $K_{\text{eff}}=11$, $H_a=300$ Oe; for graphs "c" and "d" the parameters were chosen so as to give the best fir to the experimental spectrum: $J_1=-0.38$ erg/cm^2, $J_2=-0.19$ erg/cm^2, $M_S=1620$ G, $K_{\text{eff}}=11$, $H_a=300$ Oe.[20]

TABLE I. Bilinear and biquadratic exchange constants.

Sample	$\lvert J_1\rvert$, erg / cm^2	$\lvert J_2\rvert$, erg / cm^2	$\lvert J_2/J_1\rvert$	Ref.
Fe(40 Å)/Cr(9.5 Å)/Fe(40 Å)/MgO	0.577	0.058	0.1	15
Fe(40 Å)/Cr(11 Å)/Fe(40 Å)/MgO	0.558	0.045	0.08	15
$[$Fe(33.2 Å)/Cr(7.7 Å)$]_{16}$/MgO	0.22	0.39	1.77	18
$[$Fe(21 Å)/Cr(10 Å)$]_{12}$/MgO	0.38	0.19	0.5	20
Fe*/Cr(7.5 Å)/Fe(29 Å)/Au	0.78	0.44	0.56	3
Fe*/Cr(10.1 Å)/Fe(29 Å)/Au	0.70	0.22	0.31	3

Note: Fe* is an iron whisker.

tally and to compare the data obtained with the predictions of the theory (see Sec. 2.2). With this goal the author and co-workers[21,22] investigated the FMR spectra of two samples in the frequency range 17–37 GHz in the temperature range 2–400 K. The experiments were done with both transverse and longitudinal excitation of the resonance, and the external magnetic field was applied in the film plane. For illustration of the rather strong influence of temperature on the interlayer coupling, Fig. 8 presents the FMR spectra taken at 78 and 293 K (Fig. 8) for one of the samples ($[$Fe(30 Å)/Cr(10 Å)$]_{10}$/MgO). It is seen that the influence of temperature is reflected most strongly in the behavior of the optical branch.

The processing of the experimental spectra obtained at different temperatures by numerical calculation in the biquadratic exchange model permitted the authors to obtain the temperature dependence of J_1 and J_2 and of the saturation field H_S. The results of this processing are presented in Figs. 9 and 10. It should be stressed that the values of all the calculated constants increase with decreasing temperature. The experimental results on the temperature dependence of the bilinear energy J_1 for both of the samples studied were approximated by formula (3), which derives from the RKKY theory[6,7] (solid curves in Fig. 9). Although these formulas, at first glance, give a fair description of our experimental results, it must be said that the same data are described rather well by a dependence of the form $J_1(T) \propto T^{3/2}$, which derives from the renormalization theory.[23] Unfortunately, it must be acknowledged that the large error of determination of the constants makes it impossible to discern any preference for one model or the other.

For analysis of the temperature dependence of the biquadratic exchange constant J_2 we used the two models proposed by Slonczewski: fluctuation and ''loose spin.'' It is seen from Fig. 9 that the observed dependence differs substantially from the exponential form predicted by the ''loose spin'' theory but is approximated rather well by the expression $J_2(T)=J_2(0)(1-T/T_2)^2$ (the solid curves in Fig. 9), which follows from the fluctuation model under certain conditions (see Ref. 15). For this reason the authors of Ref. 22 stated a preference for the fluctuation mechanism for the origin of biquadratic exchange. However, these same data for $J_2(T)$ are fairly well described, within the experimental error, by a linear temperature dependence $J_2=a(1-T/b)$ (the dashed lines in Fig. 9). A dependence of the latter form was obtained by this same group of authors in a study of the interlayer coupling in an Fe/Cr/Fe sample with a wedge-shaped chromium spacer in the temperature interval 77–480 K by the method of Kerr magnetometry (unpublished data). A linear temperature dependence of the biquadratic exchange constant has not yet been discussed in the literature.

A numerical comparison of the temperature behavior of the exchange parameter obtained for sandwiches in Ref. 16 (see Fig. 2) with the temperature dependence of the normalized saturation field for superlattices from Ref. 22 (see Fig. 10) was not made, but it is seen that the data of these studies are not inconsistent with each other.

Unfortunately, it must be said that the accuracy of determination of the exchange constants in the biquadratic exchange model from FMR experiments, just as from the magnetization curves taken on a Kerr magnetometer, is not very high. Because of this circumstance the form of the tempera-

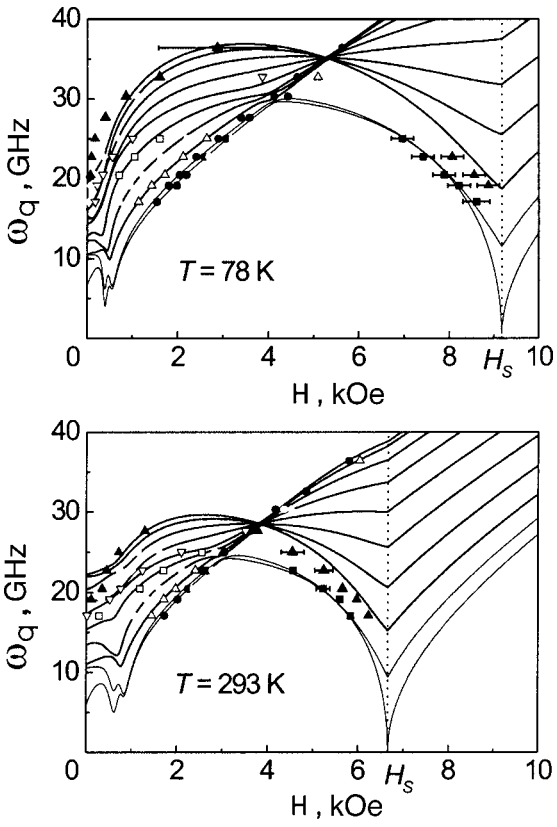

FIG. 8. FMR spectra for an $[$Fe(30 Å)/Cr(10 Å)$]_{10}$/MgO sample for two different temperatures in a magnetic field applied along the hard axis of anisotropy of iron in the film plane. The symbols are the experimental data points, and the curves are the result of a numerical calculation.[22]

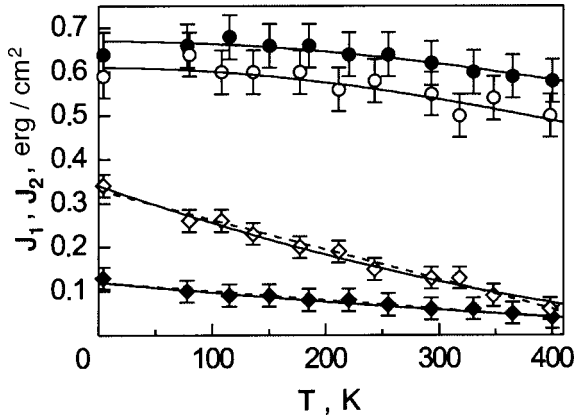

FIG. 9. Temperature dependence of the coupling constants J_1 (circles) and J_2 (rhombi) for two samples. The symbols are data calculated from the spectral spectrum: ○, ◇—for an $[Fe(30\ Å)/Cr(10\ Å)]_{10}/MgO$ sample, ●, ◆—for an $[Fe(20\ Å)/Cr(11\ Å)]_8/Al_2O_3$ sample. The curves are described in the text.[22]

ture dependence of the exchange constants cannot as yet be reliably determined. However, as a preliminary conclusion with allowance for the data obtained by the method of Kerr magnetometry it can be posited that the fluctuation and ''loose spin'' models of Slonczewski do not describe the experimentally obtained temperature dependence of the biquadratic exchange constant in the Fe/Cr/Fe system.

5. CONCLUSION

The study of multilayer Fe/Cr systems by the FMR method shows that the magnetic structure of this system is described rather well by the biquadratic exchange model. This result agrees with the conclusions drawn on the basis of measurements made by other experimental methods. It should be noted, however, that the large value of the constant $|J_2|$, which reaches, and for a number of samples even surpasses, the value of $|J_1|$, may raise doubts about the correctness of the model used.

Attempts to describe the experimental data for $[Fe/Cr]_n$ superlattices with the use of the Slonczewski magnetic proximity model have shown that it is unsuitable for this system. The shape of the FMR spectrum obtained in that model is fundamentally different from that observed experimentally (see Fig. 4 in Ref. 34). The calculated field dependence of the magnetization also disagrees with the measured dependence (see Fig. 7 in Ref. 20). We note, however, that, according to Refs. 12 and 34, this model gives a good description of the properties of magnetic superlattices with a manganese spacer.

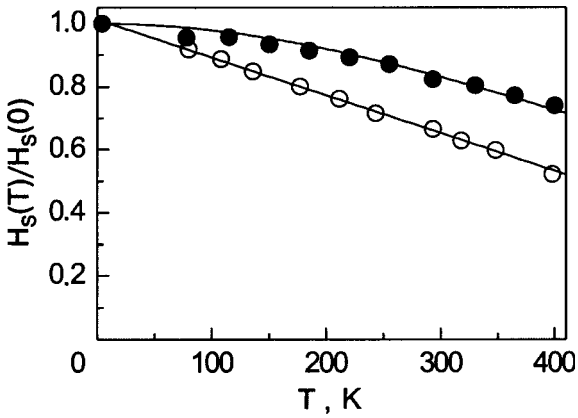

FIG. 10. Temperature dependence of the normalized saturation field $H_S(T)/H_S(0)$ for multilayer structures of $[Fe(30\ Å)/Cr(10\ Å)]_{10}/MgO$ (○) and $[Fe(20\ Å)/Cr(11\ Å)]_8/Al_2O_3$ (●). The curves are described in the text.[22]

Unfortunately, the authors of Ref. 26, who linked the magnetic order in an $[Fe/Cr]_n$ superlattice to a specific domain structure, did not give concrete formulas for comparison with experiment.

Thus at the present time the experimentally observed properties of $[Fe/Cr]_n$ superlattices are best described by the biquadratic exchange model.

The temperature dependence of the interlayer exchange interaction in these objects remains an open question.

We take this occasion to remark that in the early 1970s Viktor Valentinovich Eremenko and his very capable group lent invaluable assistance in organizing magnetooptical research on antiferromagnets at the Institute of Physics Problems. This assistance later led to a fruitful collaboration that was carried on for many years. We regret very much that this collaboration has been interrupted. We wish Prof. Eremenko continuing success in his work and hope to reestablish scientific contacts with him.

The author is grateful to A. B. Drovosekov and D. I. Kholin for helpful comments and to E. K. Zhdanova for technical assistance in preparing the manuscript.

This study was supported in part by the Russian Foundation for Basic Research (Projects Nos. 01-02-16716 and 00-15-96-574).

*E-mail: kreines@kapitza.ras.ru

[1] M. N. Baibich, J. M. Broto, A. Fert, F. Nguyen van Dau, F. Petroff, P. Etienne, G. Creuzet, A. Friederich, and J. Chaselas, Phys. Rev. Lett. **61**, 2472 (1988).
[2] G. Binasch, P. Grünberg, F. Saurebach, and W. Zinn, Phys. Rev. B **39**, 4828 (1989).
[3] B. Heinrich and J. Cochran, Adv. Phys. **42**, 523 (1993).
[4] S. O. Demokritov, J. Phys. D **31**, 925 (1998).
[5] D. T. Pierce, J. Unguris, R. J. Celotta, and M. D. Stiles, J. Magn. Magn. Mater. **200**, 290 (1999).
[6] M. D. Stiles, J. Magn. Magn. Mater. **200**, 332 (1999) and references therein.
[7] P. Bruno, Phys. Rev. B **52**, 411 (1995); J. Phys.: Condens. Matter **11**, 9403 (1999).
[8] B. Heinrich and J. A. C. Bland (Eds.), *Ultrathin Magnetic Structures*, Springer-Verlag, Berlin-Heidelberg (1994).
[9] B. Heinrich, Can. J. Phys. **78**, 161 (2000).
[10] M. Ruhrig, R. Schafer, A. Hubert, R. Mosler, J. A. Wolf, S. Demokritov, and P. Grünberg, Phys. Status Solidi A **125**, 635 (1991).
[11] B. Heinrich, J. F. Cochran, M. Kowalewski, J. Kirscher, Z. Celinski, A. S. Arrott, and K. Myrtle, Phys. Rev. B **44**, 9348 (1991).
[12] D. T. Pierce, A. D. Davies, J. A. Stroscio, D. A. Tulchinsky, J. Unguris, and R. J. Celotta, J. Magn. Magn. Mater. **222**, 13 (2000).
[13] P. E. Wigen and Z. Zang, Braz. J. Phys. **22**, 267 (1992).
[14] S. M. Rezende, C. Chesman, M. A. Lucena, A. Azevedo, and F. M. de Aguiar, J. Appl. Phys. **84**, 958 (1998) and references therein.
[15] A. Azevedo, C. Chesman, and M. Lucena, F. M. de Aguiar, S. M. Rezende, and S. S. P. Parkin, J. Magn. Magn. Mater. **177–181**, 1177 (1998).
[16] C. Chesman, N. S. Almeida, A. Azevedo, F. M. de Aguiar, and S. M. Rezende, J. Magn. Magn. Mater. **226–230**, 1770 (2001).
[17] N. M. Kreines, A. N. Kolmogorov, and V. F. Meshcheriakov, J. Magn. Magn. Mater. **177–181**, 1189 (1998).

[18] A. B. Drovosekov, N. M. Kreĭnes, D. I. Kholin, V. F. Meshcheryakov, M. A. Milyaev, L. N. Romashev, and V. V. Ustinov, JETP Lett. **67**, 727 (1998).
[19] A. B. Drovosekov, D. I. Kholin, A. N. Kolmogorov, N. M. Kreines, V. F. Mescheriakov, M. A. Milyaev, L. N. Romashev, and V. V. Ustinov, J. Magn. Magn. Mater. **198–199**, 455 (1999).
[20] A. B. Drovosekov, O. V. Zhotikova, N. M. Kreines, V. F. Meshcheryakov, M. A. Milyaev, L. N. Romashev, V. V. Ustinov, and D. I. Kholin, Zh. Éksp. Teor. Fiz. **116**, 1817 (1999) [JETP **89**, 986 (1999)].
[21] A. B. Drovosekov, D. I. Kholin, N. M. Kreines, O. V. Zhotikova, and S. O. Demokritov, J. Magn. Magn. Mater. **226–230**, 1779 (2001).
[22] A. B. Drovosekov, D. I. Kholin, N. M. Kreines, O. V. Zhotikova, S. O. Demokritov, and V. V. Ustinov, Fiz. Met. Metalloved. **91–93,** suppl. (2001), to be published.
[23] N. S. Almeida, D. L. Mills, and M. Teitelman, Phys. Rev. Lett. **75**, 733 (1995).
[24] J. C. Slonczewski, Phys. Rev. Lett. **67**, 3172 (1991).
[25] J. C. Slonczewski, J. Appl. Phys. **73**, 5957 (1993).
[26] V. D. Levchenko, A. I. Morozov, A. S. Sigov, and Yu. S. Sigov, Zh. Éksp. Teor. Fiz. **114**, 1817 (1998) [JETP **87**, 985 (1998)].
[27] J. C. Slonczewski, J. Magn. Magn. Mater. **150**, 13 (1995).
[28] Z. Zhang, L. Zhou, and P. E. Wigen, Phys. Rev. B **59**, 6094 (1994).
[29] N. G. Bebenin and V. V. Ustinov, Fiz. Met. Metalloved. **84**, vyp 2, 29 (1996).
[30] V. V. Ustinov, L. N. Romashev, V. I. Minin, A. V. Semerikov, and A. R. Del', Fiz. Met. Metalloved. **80(2)**, 71 (1995).
[31] A. Schreyer, J. F. Ankner, Th. Zeidler, M. Sch'afer, H. Zabel, P. Grünberg, and C. F. Majkrzak, Phys. Rev. B **52**, 16066 (1995).
[32] V. V. Ustinov, N. G. Bebenin, L. N. Romashev, V. I. Vinin, M. A. Milyaev, A. R. Del, and A. V. Semerikov, Phys. Rev. B **54**, 15958 (1996).
[33] G. S. Patrin, N. V. Volkov, and V. P. Kononov, JETP Lett. **68**, 307 (1998).
[34] M. Chirita, G. Robins, R. L. Stamps, R. Sooryakumar, M. E. Filipkowski, C. J. Guttierez, and G. A. Prinz, Phys. Rev. B **58**, 869 (1998).

Translated by Steve Torstveit

Purely antiferromagnetic spin waves (antimagnons) in tetragonal magnets and ways of exciting them

E. A. Turov* and I. F. Mirsaev

Institute of Metal Physics, Urals Branch of the Russian Academy of Sciences, ul. S. Kovalevskoĭ 18, 620219 Ekaterinburg, Russia

(Submitted November 2, 2001)
Fiz. Nizk. Temp. **28**, 822–833 (August–September 2002)

Purely antiferromagnetic oscillations (antimagnons) in tetragonal magnets with the crystal-chemical structure of the trirutiles (Fe_2TeO_6, etc.) are investigated theoretically. These oscillations were considered by Ukrainian physicists back in 1988, but not for tetragonal crystals and only in the case of an antiferromagnetic (AF) structure. In the present study, besides the AF phases the ferromagnetic phase in the same system of four magnetic sublattices is also considered. Ways of exciting the antimagnons, which are a fourth form of spin waves (in addition to the ferromagnons, quasiferromagnons, and quasiantiferromagnons), are also discussed. Independently of the means of excitation (electric or magnetic field, hypersound), antimagnons are defined as spin waves for which the total local ferromagnetic vector $\mathbf{M}(\mathbf{r})$ does not take part in the oscillations, but only the AF vector (or vectors) $\mathbf{L}(\mathbf{r})$. The eigenfrequencies and the corresponding susceptibilities are calculated. The presentation of this material is prefaced by a review of the status of the problem on the whole. It is noted that in the majority of cases the effects under consideration arise as a dynamic manifestation of the magnetoelectric and antiferroelectric interactions, even in magnets for which the static magnetoelectric effect is absent. © *2002 American Institute of Physics.*
[DOI: 10.1063/1.1511702]

INTRODUCTION

In 1988 Ukrainian physicists (including V. V. Eremenko) opened up a new chapter in the spin dynamics of magnets[1–5] by predicting the existence of so-called electroactive spin waves, excited not by a magnetic field $\mathbf{H}(t)$ but by an rf electric field $\mathbf{E}(t)$, and of the corresponding antiferroelectric resonance (AFER). The most surprising thing was that these fundamental articles went practically unnoticed (or underappreciated) by even the Ukrainian and Russian magnetologists as well as by the rest of the world (judging from the literature known to us, at least). The authors of the present article must confess to being among them. This explains (but does not excuse!) the ''rediscovery'' of this new type of magnons, in which only the antiferromagnetic (AF) vector (or vectors) **L** takes part in the oscillations while the total local magnetization **M** remains in a state of equilibrium, by one of the authors (E.T.) at the end of the year 2000.[6] The latter property means that such magnons can be excited only by a field $\mathbf{E}(t)$ (they are *electroactive*) owing to the magnetoelectric (ME) and antiferroelectric (AFE) interactions (corresponding to terms of the type

$$MLE \quad \text{and} \quad LLE \tag{1}$$

in the thermodynamic potential).

The fact that the authors were unpardonably ignorant of Refs. 1–5 did, however, play a certain positive role. They looked at the problem from a somewhat different angle and with a different methodological approach, using the macroscopic Landau–Lifshitz and Onsager equations (instead of the quantum equations in Refs. 1–5). In this way, of course, they examined some new aspects of the problem (had the author of Ref. 6 known about the detailed studies of Refs. 1–5, he would not have decided to study this topic).

In Ekaterinburg it all began with attempts by the authors of Refs. 7 and 8 (see also Ref. 9, a new book by a group of authors) to classify the types of spin waves according to the degree to which the **M** and **L** vectors participate in them and, accordingly, by the means of their excitation, using an extremely simple algorithm for separating the oscillatory variables with respect to independent modes (spin-wave representations). Three types of spin waves (magnons) were known: ferromagnons (only two components of the vector **M** oscillate); quasiferromagnons (besides these two components of **M**, the components of the vector(s) **L** also oscillate); and, finally, quasiantiferromagnons (in addition to the oscillations of **L**, one component of **M** also oscillates). It was natural to ask, why can't there exist oscillations of only the vector(s) **L** without the participation of **M**? It turns out that such oscillations can exist, and this follows from the aforementioned analysis of the spin-wave representations.[7–9] Here it is important that the magnetic atoms occupy definite positions at manyfold points (in any case, not onefold).

The author of Ref. 6 called such purely antiferromagnetic spin oscillations *antimagnons* (the term ''antiferromagnons'' suggested itself, but that is sometimes used as a general reference to all magnons in antiferromagnets).

Finally, it would be desirable to demonstrate what we have said on the simplest magnet with a twofold position of the atoms[6] and then to progress to more complex, four-sublattice cases.[10,11] A progression from simple to complex was followed in Ref. 12, which was intended as a sort of supplement to the book[9] to amend its unfortunate oversight

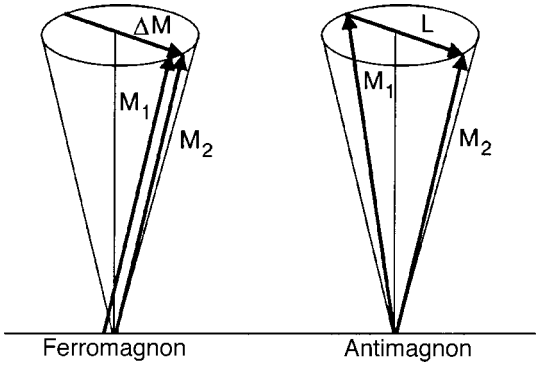

FIG. 1. Diagrams of two possible types of precession for a two-sublattice ferromagnet with magnetic atoms in a twofold noncentrosymmetric position.

'of Refs. 1–5 and give the authors of those papers their due.

What was new in the studies done at the Institute of Metal Physics as compared with Refs. 1–5 (not forgetting, of course, that our work was much later)?

1. Antimagnons exist not only in antiferromagnets (the only objects considered in Refs. 1–5 and 11) but also in ferro- and ferrimagnets.[6,13] The simplest and most obvious case is the two-sublattice ferromagnet with magnetic atoms in twofold noncentrosymmetric position in which the doubling occurs precisely on account of the center of symmetry $\bar{1}$ (space inversion). Figure 1 shows schematically the two possible types of oscillations (precession) for such a two-sublattice ferromagnet with a ground state with $\mathbf{M}_1\uparrow\uparrow\mathbf{M}_2$: type A (ferromagnon) is a precession of the total magnetization

$$\mathbf{M}=\mathbf{M}_1+\mathbf{M}_2, \tag{2}$$

and type B (antimagnon) is a precession of an antiferromagnetic vector that arises upon excitation,

$$\mathbf{L}=\mathbf{M}_1-\mathbf{M}_2. \tag{3}$$

For waves with wave vector $\mathbf{k}\neq 0$ the phase of the precession varies from point to point. Then the dispersion relation is quadratic in both cases—for ferromagnons and antimagnons.[10,12] The energy gap for ferromagnons is relativistic (on account of the magnetic anisotropy and external static magnetic field $\mathbf{H}_0$), while for antimagnons it is of an exchange nature. This agrees with what was found in Refs. 1–5 for antimagnons in four-sublattice antiferromagnets. In an antiferromagnetic two-sublattice ground state with $\mathbf{M}_1\uparrow\downarrow\mathbf{M}_2$ there are no antimagnons! At first glance the situation is paradoxical: purely AF oscillations (antimagnons) exist in a purely ferromagnetic (FM) phase. The obvious physical cause of this is seen in Fig. 1: the excitation of $\mathbf{L}$ entails an overcoming of the exchange interaction to break the parallel alignment of $\mathbf{M}_1$ and $\mathbf{M}_2$.

2. According to Refs. 1–5, antimagnons can also exist in an AF phase, provided that the magnetic structure is four-sublattice or higher (see also Refs. 11 and 12). Such AF structures are essentially the subject of those papers. For antimagnons to be excited ($\Delta\mathbf{L}\neq 0$), it is necessary that there exist invariants of the form (1), in which one of the magnetic vectors ($\mathbf{M}$ or $\mathbf{L}$) is centrosymmetric (CS) while the other is centroantisymmetric (CAS) ($\bar{1}\mathbf{L}=-\mathbf{L}$); $\mathbf{M}$ is always CS ($\bar{1}\mathbf{M}=\mathbf{M}$).

This pertains to electroactive antimagnons, which can be excited only by a field $\mathbf{E}(t)$. However, the first invariant in (1) also affords the possibility of exciting antimagnons by a magnetic field $\mathbf{H}(t)$ for $\mathbf{E}=\mathbf{E}_0=\text{const}$ if $\mathbf{M}\rightarrow\mathbf{H}(t)$. In this case $\mathbf{H}(t)$ excites $\mathbf{L}(t)$.[12,13] What shall we now call such oscillations of $\mathbf{L}(t)$: electro- or magnetoacitve? It is important to note that for both $\mathbf{E}=\mathbf{E}(t)$ and $\mathbf{H}=\mathbf{H}(t)$ (but in the latter case for $\mathbf{E}=\text{const}$) only oscillations of $\mathbf{L}(t)$ are excited, and in both cases this is due to the ME interaction. In addition, as was shown in Ref. 12, in certain cases there can exist purely AF oscillations, excited not by an electric or magnetic field but only by hypersound (and, of course, heat). Characteristically, in such cases, contrary to the general rule stated in Refs. 1–5, in such cases the position of the magnetic atoms can even be centrosymmetric. Therefore we considered it advisable to keep the name ''antimagnons'' as being more general, grouping together all magnons sharing a single trait, viz., those in which oscillations of $\mathbf{M}$ are absent, regardless of the means of their excitation. Thus antimagnons—electroactive, magnetoactive, and acoustoactive—make up a fourth type of spin waves complementary to ferromagnons, quasiferromagnons, and quasiantiferromagnons.

3. The use of the Onsager equations permitted the authors of Refs. 6 and 10–13 to treat antimagnons having an admixture of longitudinal oscillations and also purely longitudinal antimagnons (longitudinal with respect to the main basis vector: $\mathbf{M}$ or one of the $\mathbf{L}$'s).

4. The authors of Refs. 6 and 10–13 introduced new susceptibilities $\hat{\beta}(\omega)$ and $\hat{\delta}(\omega)$, specifying a linear relation of the form

$$\mathbf{L}=\hat{\beta}\mathbf{E} \quad \text{and} \quad \mathbf{L}=\hat{\delta}(\omega,\mathbf{E}_0)\mathbf{H}. \tag{4}$$

After calculating these with allowance for dissipation, one can also find easily the thermal losses due to excitation of antimagnons.

5. Antimagnons in ferrimagnets with three and four magnetic sublattices have also been considered.[12,13] In the latter case this was the ferrimagnetic compound Mn_2Sb.

6. Coupled antimagnon–electromagnetic waves have been investigated for the simplest case of a two-sublattice ferromagnet.[12] The possibility of these was mentioned back in Ref. 2. It was shown in Ref. 12 that this coupling can lead to a resonant (at the AFER frequency) Faraday effect for light.

7. Almost all of the effects mentioned above are dynamic manifestations of the ME (or AFE) interaction. They occur most often in magnets which lack a static ME effect (which can in general be forbidden by symmetry, as in hematite, for example). Although all of these effects have been discussed for frequencies in the exchange region (near the antimagnon resonance frequency), it turns out that these interactions can also be manifested in low-frequency phenomena; for example, according to Ref. 12, in the excitation of NMR by an electric field $\mathbf{E}(t)$, where $\mathbf{E}(t)$ and $\mathbf{L}(t)$ are connected by a quasiequilibrium relation. In particular, this pertains to hematite, orthoferrites, and other magnets with a CS exchange magnetic structure (EMS), provided that the position of the magnetic atoms is itself not CS.

TABLE I. Transformation rules for the vectors M and L_ξ ($\xi=a,b,c$) under the action of symmetry elements of the groups $Pnmm$ and $P4_2/mnm$. Also indicated are the magnetic point groups of the phases, specified by the rows Γ_i.

Γ_i	**M, L, E**	$\bar{1}\ 2_{1x}\ 2_z$	4_{2z}	Magnetic group
Γ_1	M_x, L_{ay}	+1+1−1	M_y, L_{ax}	$\bar{1}\,2_x\,2'_z$
Γ_2	M_y, L_{ax}	+1−1−1	$-M_x, -L_{ay}$	$\bar{1}\,2'_x\,2'_z$
Γ_3	M_z	+1−1+1	M_z	$\bar{1}\,2'_x\,4_z$
Γ_4	L_{bx}, L_{cy}, E_y	−1−1−1	$L_{by}, L_{cx}, -E_x$	$\bar{1}'\,2'_x\,2'_z$
Γ_5	L_{by}, L_{cx}, E_x	−1+1−1	$-L_{bx}, -L_{cy}, E_y$	$\bar{1}'\,2_x\,2'_z$
Γ_6	L_{az}	+1+1+1	$-L_{az}$	$\bar{1}\,2_x\,4'_z$
Γ_7	L_{bz}	−1+1+1	L_{bz}	$\bar{1}'\,2_x\,4_z$
Γ_8	L_{cz}, E_z	−1−1+1	$-L_{cz}, E_z$	$\bar{1}'\,2'_x\,4'_z$

8. It has been shown that (low-frequency!) antimagnons can exist in multilayer superstructures with a certain symmetry.[12]

9. The magnets considered in Refs. 1–5, with an AF EMS, belonged to the rhombic, rhombohedral, and hexagonal systems. Tetragonal crystals were not considered. Such crystals will be the subject of this article. We are talking not only about four-sublattice magnets with AF CAS structures, which are characteristic of the trirutiles (compounds of the Fe_2TeO_6 type) with easy-axis (EA) and easy-plane (EP) states, but also, for elucidating the physical picture of the phenomena and for future reference, the CS ferromagnetic and antiferromagnetic EMSs in a crystal with the same crystal-chemical structure. In addition, the use of the spin-wave representations in Refs. 8 and 9 and its development in application to uniaxial magnets (with allowance for the magnetic symmetry as well) will make it possible to bridge over from the rhombic and tetragonal crystals to the rhombohedral and hexagonal crystals[12] discussed in Refs. 1–5.

1. CRYSTALLINE AND POSSIBLE MAGNETIC STRUCTURES, THERMODYNAMIC POTENTIAL

Let us consider a tetragonal crystal with symmetry $P4_2/mnm$ (D_{4h}^{14}), in which the magnetic atoms occupy a fourfold position $4e$ (see Fig. 2.14 in Ref. 9). To the four magnetic sublattices with magnetizations $\mathbf{M}_\nu$ ($\nu=1,2,3,4$) there correspond 4 basis vectors (one ferromagnetic and three antiferromagnetic):

$$\begin{aligned}
&\mathbf{M}=\mathbf{M}_1+\mathbf{M}_2+\mathbf{M}_3+\mathbf{M}_4,\\
&\mathbf{L}_a=\mathbf{M}_1+\mathbf{M}_2-\mathbf{M}_3-\mathbf{M}_4,\\
&\mathbf{L}_b=\mathbf{M}_1-\mathbf{M}_2+\mathbf{M}_3-\mathbf{M}_4,\\
&\mathbf{L}_c=\mathbf{M}_1-\mathbf{M}_2-\mathbf{M}_3+\mathbf{M}_4.
\end{aligned} \tag{5}$$

The first two of these are CS, and the rest are CAS. Taking the elements $\bar{1}$, 2_{1x}, and 4_{2z} as generators of the group, we can write the permutation codes of the position $4e$ as[12]

$$\bar{1}\begin{pmatrix}1-2\\3-4\end{pmatrix}2_{1x}\begin{pmatrix}1-4\\2-3\end{pmatrix}4_{2z}\begin{pmatrix}1-3\\2-4\end{pmatrix}. \tag{6}$$

The dashes connect the labels of the atoms which are interchanged by the corresponding symmetry element. From (5) and (6) one can see not only the CS or CAS character of the basis vectors but also whether or not these vectors change sign in the permutations brought about by the other symmetry elements (2_{1x} and 4_{2z}).

Without giving a table of permutation transformations of the vectors (5), we write out directly the table of transformations of the components of these vectors, taking into account not only the permutation but also rotations (and reflections) produced by the elements of (6). This is in fact the table of irreducible representations of the space group D_{4h}^{14}.

We note that column III in Table I gives the rules for transformations under the action of elements $\bar{1}$, 2_{1x}, and 2_z, which are generators of the rhombic group $Pnmm$, which is a subgroup of the tetragonal group $P4_2/mnm$ ("+1" and "−1" indicate whether or not the function changes sign). Column IV gives additional rules for transformations under the action of the element 4_{2z}, which complements the group $Pnmm$ to $P4_2/mnm$. In addition, the last column gives the magnetic point groups with respect to which the functions in column II, which determine the corresponding phases for the group $Pnmm$, are invariant. We recall that $g'=g1'$ (where g is an element of the point group and $1'$ is the operation of time inversion).

Table I allows us to write an invariant expression for the thermodynamic potential density Φ. For brevity we limit consideration to the bilinear approximation with respect to the vectors (5) (although, generally speaking, this is not always sufficient[12]), adding only the ME and AFE interactions and sometimes also the Zeeman energy in a static field.

Thus,

$$\Phi=\Phi_{\rm mag}+\Phi_{\rm ME}+\Phi_{\rm AFE}. \tag{7}$$

Here

$$\begin{aligned}
\Phi_{\rm mag}=&\frac{1}{2}A_M\mathbf{M}^2+\frac{1}{2}\sum_\xi A_\xi\mathbf{L}_\xi^2+\frac{1}{2}K_M(M_x^2+M_y^2)\\
&+\frac{1}{2}\sum_\xi K_\xi(L_{\xi x}^2+L_{\xi y}^3)+r(L_{bx}L_{cy}+L_{by}L_{cx})\\
&+p(M_xL_{ay}+M_yL_{ax})-\mathbf{M}\cdot\mathbf{H}
\end{aligned} \tag{8}$$

is the magnetic energy, where A_M and A_ξ ($\xi=a,b,c$) are the exchange constants, and the remaining terms are relativistic. Further,

$$4M_0\Phi_{\rm ME}=-s_1(M_xE_x+M_yE_y)L_{bz}-s_2(M_xL_{bx}+M_yL_{by})E_z-s_3M_z(E_xL_{bx}+E_yL_{by})-s_4M_zE_zL_{bz}-d_1(M_xE_y+M_yE_x)L_{cz}-d_2(M_xL_{cy}+M_yL_{cx})E_z-d_3M_z(E_xL_{cy}+E_yL_{cx}) \quad (9)$$

gives the magnetoelectric interaction, and

$$4M_0\Phi_{\rm AFE}=-f_1L_{az}(E_xL_{by}+E_yL_{bx})-f_2L_{az}(E_xL_{cx}+E_yL_{cy})-f_3(L_{ax}E_y+L_{ay}E_x)L_{bz}-f_4(L_{ax}E_x+L_{ay}E_y)L_{cz}-f_5L_{az}L_{cz}E_z \quad (10)$$

the antiferromagnetic interaction. We note that for concrete magnetic structures only individual terms of the general expressions (9) and (10) remain; M_0 is the modulus of the sublattice magnetization vector.

We note immediately that in $\Phi_{\rm mag}$ (8) we will be mainly confined to the exchange approximation, keeping only the terms with A_M and A_ξ and the Zeeman term. (For now we are mostly concerned with the fundamental side of things).

From the equal-modulus model, $\mathbf{M}_\nu^2=M_0^2$, which corresponds to the condition

$$\mathbf{M}^2+\sum_\xi \mathbf{L}_\xi^2=(4M_0)^2,$$

we find

$$\mathbf{M}\cdot\mathbf{L}_a+\mathbf{L}_b\cdot\mathbf{L}_c=0,$$
$$\mathbf{M}\cdot\mathbf{L}_b+\mathbf{L}_a\cdot\mathbf{L}_c=0, \quad (11)$$
$$\mathbf{M}\cdot\mathbf{L}_c+\mathbf{L}_a\cdot\mathbf{L}_b=0,$$

and also the Landau–Lifshitz (LL) equations

$$\dot{\mathbf{M}}=\gamma\left(\mathbf{M}\times\frac{\partial\Phi}{\partial\mathbf{M}}+\mathbf{L}_a\times\frac{\partial\Phi}{\partial\mathbf{L}_a}+\mathbf{L}_b\times\frac{\partial\Phi}{\partial\mathbf{L}_b}+\mathbf{L}_c\times\frac{\partial\Phi}{\partial\mathbf{L}_c}\right),$$
$$\dot{\mathbf{L}}_a=\gamma\left(\mathbf{M}\times\frac{\partial\Phi}{\partial\mathbf{L}_a}+\mathbf{L}_a\times\frac{\partial\Phi}{\partial\mathbf{M}}+\mathbf{L}_b\times\frac{\partial\Phi}{\partial\mathbf{L}_c}+\mathbf{L}_c\times\frac{\partial\Phi}{\partial\mathbf{L}_b}\right),$$
$$\dot{\mathbf{L}}_b=\gamma\left(\mathbf{M}\times\frac{\partial\Phi}{\partial\mathbf{L}_b}+\mathbf{L}_a\times\frac{\partial\Phi}{\partial\mathbf{L}_c}+\mathbf{L}_b\times\frac{\partial\Phi}{\partial\mathbf{M}}+\mathbf{L}_c\times\frac{\partial\Phi}{\partial\mathbf{L}_a}\right),$$
$$\dot{\mathbf{L}}_c=\gamma\left(\mathbf{M}\times\frac{\partial\Phi}{\partial\mathbf{L}_c}+\mathbf{L}_a\times\frac{\partial\Phi}{\partial\mathbf{L}_b}+\mathbf{L}_b\times\frac{\partial\Phi}{\partial\mathbf{L}_a}+\mathbf{L}_c\times\frac{\partial\Phi}{\partial\mathbf{M}}\right), \quad (12)$$

where γ is the absolute value of the gyromagnetic ratio.

An important consequence of Eqs. (12) (it is also contained in conditions (11), which are integrals of the motion for these equations) is that if in the ground state only one of the basis vectors (5) is nonzero, then other vectors can only undergo oscillations that are perpendicular to it; there are no longitudinal oscillations. It can be shown that for transverse oscillations essentially the same results are obtained from the linear kinetics of the Onsager equations.[12,13]

2. PHASES AND SPIN-WAVE REPRESENTATIONS (MODES OF OSCILLATION)

From the standpoint of the aforementioned rhombic group, every row in the table corresponds to a certain magnetic structure (phase) in which only the components listed in that row are nonzero in the ground state. With the addition of the 4_{2z} axis, these phases can, of course, be combined into one phase which includes those components which are associated with this axis. For example, the phases Γ_1 and Γ_2 can comprise a single phase $\Gamma_{12}(M_x,L_{ay},M_y,L_{ax})$. However, they can also exist by themselves, depending on the concrete form of the magnetic anisotropy energy and the magnitude and direction of the magnetic field. From now on we shall consider only those phases which are characteristic for rhombic symmetry. The presence of a 4_{2z} axis will only come into play in leading to a definite relation between the constants of the thermodynamic potential and equality of the eigenfrequencies of the magnons for the two phases associated with this axis.

Turning now to the oscillatory modes and their eigenfrequencies, we note that here we have used the concept of spin-wave representations,[9,14,15] which makes it possible to divide the oscillatory variables into independent groups even before the equations of motion are written. The corresponding algorithm for this was formulated in Refs. 8 and 9 only for rhombic crystals. It is surprisingly simple: to the same spin-wave representation of a phase Γ_n, associate variables from the two rows Γ_m and $\Gamma_{m'}$ of the table for which the products of the numbers $(+1$ or $-1)$ give the numbers of the row Γ_n; schematically $\Gamma_m\Gamma_{m'}=\Gamma_n$. Here $m=m'$ is a possible case.

Let us consider for example the phase $\Gamma_6(L_{az}^0)$, which will be discussed below. For it, each of the Γ_{mm} is a spin-wave representation. In particular, these will be $\Gamma_{44}(\Delta L_{bx},\Delta L_{cy})$ and $\Gamma_{55}(\Delta L_{by},\Delta L_{cx})$ (the superscript 0 denotes the ground state, and the symbol Δ denotes the variational variables). What effect does the 4_{2z} axis have when one goes to the case of a tetragonal crystal by adding this axis? At first glance it would appear to mix the modes corresponding to the representations Γ_{44} and Γ_{55}, giving a single mode with the representations ΔL_{bx}, ΔL_{cy}, ΔL_{by}, and ΔL_{cx}. However, that is not the case: the modes $\Gamma_{44}(\Delta L_{bx},\Delta L_{cy})$ and $\Gamma_{55}(\Delta L_{by},\Delta L_{cx})$ remain independent! The latter follows merely from the circumstance that the variables of rows Γ_4 and Γ_5 have different magnetic symmetry—$\bar{1}'2_x'2_z'$ and $\bar{1}'2_x2_z'$, respectively—as a result of which the equations of motion for the pairs $\Delta L_{bx},\Delta L_{cy}$ and $\Delta L_{by},\Delta L_{cx}$, are different. The requirement that these equations be invariant with respect to the magnetic group of the ground state, $\Gamma_6(L_{az}^0)$, including the $4_z'$ axis, reduces simply to the fact that these equations then go over to each other under this transformation.

Analysis of the spin-wave representations for the other phases will be done directly during the discussion of each. (We note that the question of obtaining spin-wave representations for tetragonal and other uniaxial crystals by means of a modification of the algorithm that is stated above for the rhombic case is set forth quite fully and clearly in Ref. 12).

Let us consider easy-axis and then easy-plane structures (phases).

3. EASY-AXIS STRUCTURES

3.1. The $\Gamma_6(L_{az}^0)$ phase (magnetic group $\bar{1}2_x4'_z$)

This CS AF phase with $\mathbf{L}_a^0 \| \mathbf{Z}$, according to Table I, has the following spin-wave representations (modes): the antimagnon modes

$$\Gamma_{44}(L_{bx}, L_{cy}), \quad \Gamma_{55}(L_{by}, L_{cx}) \tag{13}$$

and the quasi-AF modes $\Gamma_{11}(M_x, L_{ay})$, $\Gamma_{22}(M_y, L_{ax})$.

Let us consider only the first two (the second two are not excited by an electric field).

This phase is realized only for $A_a<0$ and $A_b, A_c>0$ ($\mathbf{M}=0$). Using the first of equations (11) to eliminate the term containing $\mathbf{L}_a^2$, we obtain from (8) (in the exchange approximation) and (10) the quadratic form Φ_2 in the spin-wave variables (13):

$$\Phi_2 = \frac{1}{2}[\tilde{A}_b(L_{bx}^2 + L_{by}^2) + \tilde{A}_c(L_{cx}^2 + L_{cy}^2)] - f_1(L_{bx}E_y + L_{by}E_x) - f_2(L_{cy}E_y + L_{cx}E_x). \tag{14}$$

Here $\tilde{A}_b = A_b - A_a$ and $\tilde{A}_c = A_c - A_a$, and we have taken into account that $L_{az}^0 = 4M_0$. As a result, the LL equations (12) reduce to two independent systems:

$$\begin{aligned} \dot{L}_{bx} &= -\omega_0(\tilde{A}_c L_{cy} - f_2 E_y), \\ \dot{L}_{cy} &= \omega_0(\tilde{A}_b L_{bx} - f_1 E_y) \end{aligned} \tag{15}$$

and

$$\begin{aligned} \dot{L}_{by} &= \omega_0(\tilde{A}_c L_{cx} - f_2 E_x), \\ \dot{L}_{cx} &= -\omega_0(\tilde{A}_b L_{by} - f_1 E_x), \end{aligned} \tag{16}$$

where $\omega_0 = 4\gamma M_0$. In a field $\mathbf{E}(t) \propto \exp(-i\omega t)$ their solution gives

$$\begin{aligned} L_{bx} &= \frac{\omega_0(f_1\tilde{A}_c\omega_0 - i\omega f_2)}{\omega_L^2 - \omega^2} E_y, \\ L_{cy} &= \frac{\omega_0(f_2\tilde{A}_b\omega_0 + i\omega f_1)}{\omega_L^2 - \omega^2} E_y, \end{aligned} \tag{17}$$

$$\begin{aligned} L_{by} &= \frac{\omega_0(f_1\tilde{A}_c\omega_0 + i\omega f_2)}{\omega_L^2 - \omega^2} E_x, \\ L_{cx} &= \frac{\omega_0(f_2\tilde{A}_b\omega_0 - i\omega f_1)}{\omega_L^2 - \omega^2} E_x. \end{aligned} \tag{18}$$

Here ω_L is the frequency of the antimagnons (the AFER frequency in the terminology of Refs. 1–5), which is given by the expression

$$\omega_L^2 = \omega_0^2 \tilde{A}_b \tilde{A}_c. \tag{19}$$

It is of an exchange nature, as in the case of the other crystal systems considered in those papers. Taking into account the relativistic terms in (8) gives only small corrections, without altering the essence.

We call attention to the fact that Eqs. (15) and (16) and their solutions (17) and (18) are invariant with respect to the magnetic group $\bar{1}2_x4'_z$ of the phase under study, $\Gamma_6(L_{az}^0)$. Here the primed axis $4'_z$ takes (15) into (16) and (17) into (18). (In the second case it should be remembered that the time inversion operation $1'$ changes the sign of ω.) The frequency turns out to be the same for both modes (13). This is also a consequence of the presence of the symmetry axis 4_{2z} in the space group D_{4h}^{14}. Incidentally, formulas (18) are obtained from (17) by switching $x \leftrightarrow y$ and letting $\omega \to -\omega$.

At first glance the results (17) and (18) seem somewhat surprising: the tensor of the linear relation between $\mathbf{E}$ and $\mathbf{L}$ (which was called the antimagnon–electric susceptibility tensor $\hat{\beta}$ in Ref. 6) is complex-valued. This does not mean, however, that absorption occurs (without having dissipation taken into account!). Simply, the absorption is determined by another tensor—the effective electric susceptibility. Indeed, the AFE interaction (10) can be written in the form

$$\Phi_{\mathrm{AFE}} = -P_x E_x - P_y E_y. \tag{20}$$

Here $P_x = f_1 L_{by} + f_2 L_{cx}$ and $P_y = f_1 L_{bx} + f_2 L_{cy}$ are components of the effective polarization vector. Substituting L_{bx}, L_{by}, L_{cx}, and L_{cy} from (17) and (18), we obtain

$$P_x = \kappa E_x \quad \text{and} \quad P_y = \kappa E_y, \tag{21}$$

where

$$\kappa = \frac{\omega_0^2(f_1^2\tilde{A}_c + f_2^2\tilde{A}_b)}{\omega_L^2 - \omega^2}$$

is a real function of ω.

If dissipation is taken into account (for example, according to Bloch, which reduces to the simple replacement $\omega \to \omega + i\Gamma$ in this expression), we then obtain $\kappa = \kappa' + i\kappa''$ (we shall not write out the obvious formulas for the real and imaginary parts of κ). Also, we can find the thermal losses due to the excitation of antimagnons:

$$Q = -\overline{(P_x\dot{E}_x + P_y\dot{E}_y)}$$

(the overbar denotes averaging over a time $t \gg 2\pi/\omega$). The result is again obvious:

$$Q = \frac{1}{2}\omega\kappa''(|E_x|^2 + |E_y|^2). \tag{22}$$

3.2. The $\Gamma_7(L_{bz}^0)$ phase (magnetic group $\bar{1}'2_x4_z$)

This AF phase with a CAS main basis vector $\mathbf{L}_b^0 \| \mathbf{Z}$ ($L_{bz}^0 = 4M_0$), according to Table I, has two transverse quasi-AF representations:

$$\Gamma_{15}(M_x, L_{ay}, L_{by}, L_{cx}) \tag{23}$$

and

$$\Gamma_{24}(M_y, L_{ax}, L_{bx}, L_{cy}), \tag{24}$$

which remain independent even after the 4_{2z} axis is taken into account. In addition, generally speaking, the longitudinal modes $\Gamma_{38}(M_z, L_{cz})$ and $\Gamma_{67}(L_{az}, L_{bz})$ can also exist, but we shall not consider them here.

Although there are no transverse antimagnons in this phase, and the modes in Eqs. (23) and (24) are quasi-AF, we shall nevertheless give approximate results for them. First, because $\Gamma_7(L_{bz}^0)$ is the structure of an actual CAS antiferro-

magnet, Fe_2TeO_6 (see Sec. 7.2 of Ref. 9), with $T_N = 219$ K. Second, Eqs. (23) and (24) are quasi-AF modes with a comparatively low frequency

$$\omega_{\rm AF} = \gamma\sqrt{2H_E H_A} \tag{25}$$

(semiexchange, semirelativistic), excited by an electric field $\mathbf{E}(t)$ owing to the ME interaction (the first term in (9)).

In this case one should set $A_b<0$, $A_M>0$, $A_a>0$, $A_c>0$, and $K_b>0$ in Eq. (8). When Eq. (11) is taken into account, the quadratic form Φ_2 becomes

$$\begin{aligned}\Phi_2 = \frac{1}{2}[&\tilde{A}_M(M_x^2+M_y^2)+\tilde{A}_a(L_{ax}^2+L_{ay}^2)+\tilde{A}_c(L_{cx}^2+L_{cy}^2)\\ &+K_b(L_{bx}^2+L_{by}^2)]+p(M_xL_{ay}+M_yL_{ax})\\ &+r(L_{bx}L_{cy}+L_{by}L_{cx})-s_1(M_xE_x+M_yE_y)\\ &-f_3(L_{ax}E_y+L_{ay}E_x),\end{aligned} \tag{26}$$

where $\tilde{A}_M = A_M - A_b + K_M$, $\tilde{A}_a = A_a - A_b + K_a$, and $\tilde{A}_c = A_c - A_b + K_c$. It is natural that the relativistic interactions be taken into account here, since we are seeking the quasi-AF oscillations and their frequencies.

Thus we first consider the mode in Eq. (23). The solution of equations (12) shows that the corresponding susceptibilities to the field $\mathbf{E}(t)$ have two poles—one at a quasi-AF frequency of the form (25), or, more precisely,

$$\omega_{\rm AF}^2 = \omega_0^2\tilde{A}_M K_b, \tag{27}$$

and the other at an exchange frequency of the form $\omega_E = \gamma H_E$. Here

$$\omega_{\rm AF}^2 \gg \omega_E^2 \cong \omega_0^2\tilde{A}_a\tilde{A}_c. \tag{28}$$

Near the frequencies $\omega_{\rm AF}$ the principal effective components are M_x and L_{by} (it is for them that the corresponding eigenfrequency of the oscillations equals zero if the exchange approximation is used). This means that for this mode the other two components L_{ay} and L_{cx} of the set (23), which have a pole at the exchange frequency (27), follow along behind the first in a quasiequilibrium manner. Consequently, the pair L_{ay}, L_{cx} can be expressed in terms of M_x, L_{by} from the equations $\partial\Phi_2/\partial L_{ay} = \partial\Phi_2/\partial L_{cx} = 0$. As a result, we find

$$L_{ay} = -\frac{p}{\tilde{A}_a}M_x \quad \text{and} \quad L_{cx} = -\frac{r}{\tilde{A}_c}L_{by}, \tag{29}$$

and, after substituting these values into (26), we obtain Φ_2 in terms of the variables M_x and L_{by} only. The final solution of the LL equations (12) for them can be written in the form

$$M_x = \alpha_{xx}E_x, \quad L_{by} = \beta_{yx}E_x, \tag{30}$$

where

$$\alpha_{xx} \cong \frac{s_1^*\omega_0^2K_b^*}{\omega_{\rm AF}^2-\omega^2}, \quad \beta_{yx} \cong i\alpha_{xx}\frac{\omega}{\omega_0 K_b^*}$$

are components of the magnetoelectric and antiferroelectric susceptibility tensors. The asterisks on s_1^* and K_b^* denote their renormalization due to the "loading" by L_{ay} and L_{cx} from (29):

$$s_1^* = s_1 - \frac{f_3 p}{\tilde{A}_a}, \quad K_b^* = K_b - \frac{r^2}{\tilde{A}_c}.$$

In an analogous way, small relativistic corrections for both K_b and $\tilde{A}_M$ appear in formula (27) for the frequency of the quasi-AF resonance. The susceptibilities for the other two components, L_{ay} and L_{cx}, can of course also have a pole at the frequency $\omega_{\rm AF}$, but their value, according to (29), is less than that of M_x and L_{by} by a factor of the order of pM_0/H_E (or rM_0/H_E).

The corresponding calculation for the variables M_y, L_{ax}, L_{bx}, L_{cy} of the mode Γ_{24} in (24) give an analogous result: it is necessary only to switch $x \leftrightarrow y$ and $\omega \to -\omega$ in formulas (30). Here the total heat Q with allowance for dissipation is again determined by a formula of the form (22), but in which now $\kappa = s_1^*\alpha_{xx}$ ($\alpha_{yy} = \alpha_{xx}$).

3.3. The $\Gamma_8(L_{cz}^0)$ phase (magnetic group $\bar{1}'2_x'4_z'$)

In this phase there are two spin-wave representations for the transverse (to $\mathbf{L}_c^0$) modes of oscillation: $\Gamma_{14}(M_x, L_{ay}, L_{bx}, L_{cy})$ and $\Gamma_{25}(M_y, L_{ax}, L_{by}, L_{cx})$.

For Γ_{14} one should use formulas (27)–(30) with the substitutions $s_1 \to d_1$, $E_x \to E_y$, and switch the indices $b \leftrightarrow c$. Here, of course, one has

$$\omega_{\rm AF}^2 \cong \omega_0^2\tilde{A}_M K_c,$$

where $A_M = A_M - A_c + K_M$.

The corresponding modes for Γ_{25} are obtained from Γ_{14} by interchanging $x \leftrightarrow y$ and letting $\omega \to -\omega$.

3.4. The $\Gamma_3(M_z^0)$ phase (magnetic group $\bar{1}2_x'4_z$)

In this purely FM phase with $\mathbf{M}_0 \| \mathbf{Z}$ Table I gives for the transverse oscillations the spin wave representations: $\Gamma_{12}(M_x, M_y, L_{ax}, L_{ay})$—quasi-FM modes, and $\Gamma_{45}(L_{bx}, L_{by}, L_{cx}, L_{cy})$—antimagnon modes. The first ones are not excited by an electric field (the are no corresponding ME invariants), and we shall therefore consider only the second ones.

Keeping in mind that in the given case $A_M<0$ and $A_b, A_c>0$ ($\mathbf{L}_a = 0$, since this vector appears neither in the ground state nor among the oscillatory variables), in the exchange approximation we obtain from (8) and (9)

$$\begin{aligned}\Phi_2 = \frac{1}{2}\sum_\xi \tilde{A}_\xi(L_{\xi x}^2+L_{\xi y}^2) - s_3(L_{bx}E_x+L_{by}E_y)\\ -d_3(L_{cx}E_y+L_{cy}E_x)-M_zH_z.\end{aligned} \tag{31}$$

In the sum, ξ takes on two values, b and c, and $\tilde{A}_\xi = A_\xi - A_M$. Here the external static field $\mathbf{H} \| \mathbf{M}_0 \| \mathbf{Z}$, and in the other cases we shall (when possible) direct the field $\mathbf{H}$ so that it does not alter the symmetry of the ground state. The field term in (31) gives a contribution to the quadratic form, because it follows from the equal-modulus conditions (11) that

$$M_z \cong M_z^0 - \frac{1}{2M_z^0}(L_{bx}^2+L_{by}^2+L_{cx}^2+L_{cy}^2), \tag{32}$$

where $M_z^0 = 4M_0$.

Taking (31) and (32) into account and solving the LL equation, we find

$$L_{\xi x}=\beta^{\xi}_{xx}E_x+\beta^{\xi}_{xy}E_y,$$
$$L_{\xi y}=\beta^{\xi}_{yx}E_x+\beta^{\xi}_{yy}E_y \quad (\xi=b,c), \tag{33}$$

where

$$\beta^b_{xx}=\beta^b_{yy}=\frac{\omega_0^2\tilde{A}_b s_3}{\omega_b^2-\omega^2},\quad \beta^b_{xy}=-\beta^b_{yx}=-\frac{i\omega\omega_0 s_3}{\omega_b^2-\omega^2},$$
$$\beta^c_{xx}=-\beta^c_{yy}=-\frac{i\omega\omega_0 d_3}{\omega_c^2-\omega^2},\quad \beta^c_{xy}=\beta^c_{yx}=\frac{\omega_0^2\tilde{A}_c d_3}{\omega_c^2-\omega^2}. \tag{34}$$

Here

$$\omega_\xi=\omega_0\tilde{A}_\xi+\gamma H_z \tag{35}$$

is the antimagnon (AMG) resonance frequency, and $\xi=b,c$.

Typically in the approximation under consideration (i.e., the exchange approximation) there exist two independent AMG modes with different frequencies—the vectors $\mathbf{L}_b$ and $\mathbf{L}_c$ oscillate independently. However, when the relativistic terms (in this case, the terms containing r in Eq. (8)) are taken into account, these oscillations are coupled. Then, of course, the magnetic anisotropy must be taken into account in Eq. (8). As a result, both $\mathbf{L}_b$ and $\mathbf{L}_c$ and also the exchange frequencies ω_b and ω_c acquire relativistic corrections. Here the corrections from the coupling interaction are determined by a quantity quadratic in the small parameter $r/\tilde{A}_\xi$. (The magnetic anisotropy leads only to a slight renormalization of the constants $\tilde{A}_\xi$: $\tilde{A}_\xi\to\tilde{A}_\xi+K_\xi$.)

We now note that the FM phase $\Gamma_3(M_z^0)$, generally speaking, is not realized in trirutiles, which are the subject of discussion here. However, it can be obtained from an AF phase (e.g., from the phase $\Gamma_7(L_{bz}^0)$ realized in Fe_2TeO_6; see Sec. 7.2 of Ref. 9) if a field H_z strong enough to bring about a phase transition of the spin-flip (collapse) type is applied. In this case $A_b<0$ and $A_M>0$, and formula (35) for ω_b should be rewritten as

$$\omega_b=\gamma[H_z-4M_0(A_M-A_b)]. \tag{36}$$

From this it is seen that this mode is stable only in fields

$$H_z\geqslant H_{\text{flip}}=4M_0(A_M-A_b).$$

This situation is interesting in that it permits one to obtain an arbitrarily low AMG frequency as the field H_z approaches H_{flip} from above. For this it is necessary, of course, to have fields H_z of the order of the exchange fields.

4. EASY-PLANE CASE

If the main basis vector $\mathbf{L}^0\equiv\mathbf{L}_\perp^0$ (or, generally speaking, $\mathbf{M}_\perp^0$) lies in the basal plane XY, then one is dealing with a magnet of the easy-plane type.

4.1. The centrosymmetric phases $\Gamma_1(M_x^0,L_{ay}^0)$ and $\Gamma_2(M_y^0,L_{ax}^0)$

According to Table I, in the rhombic case it is possible in particular to have phases $\Gamma_1(M_x^0,L_{ay}^0)$ and $\Gamma_2(M_y^0,L_{ax}^0)$ which are slightly noncollinear structures: an AF with $L_\perp^0\approx 4M_0$ and an admixture of weak ferromagnetism $\mathbf{M}_\perp^0 \ll L_\perp^0$, or a FM with $M_\perp^0\approx 4M_0$ and an admixture of weak antiferromagnetism $L_\perp^0\ll M_\perp^0$ (Fig. 6.21 of Ref. 9). When the 4_{2z} axis is taken into account, these two phases become identical (in energy) and can be combined into one mixed phase $\Gamma_1+\Gamma_2$ with magnetic group $\overline{1}2_z'$ (consisting of elements common to the phases Γ_1 and Γ_2). Incidentally, the noncollinearity is due to the relativistic term with the coefficient p in (8).

The CS phases indicated can have both quasi-FM and quasi-AF modes and also AMG modes, but we shall not consider them in the present article.

4.2. Centroantisymmetric phases $\Gamma_4(L_{bx}^0,L_{cy}^0)$ and $\Gamma_5(L_{by}^0,L_{cx}^0)$

The easy-plane trirutiles of interest to us, such as Cr_2TeO_6 ($T_N=105$ K), Cr_2WO_6 ($T_N=69$ K), and V_2WO_6 ($T_N=370$ K), are CAS structures with vectors $\mathbf{L}_b^0$ and $\mathbf{L}_c^0$ in the ground state. They correspond to the AF phases $\Gamma_4(L_{bx}^0,L_{cy}^0)$ and $\Gamma_5(L_{by}^0,L_{cx}^0)$. In a tetragonal crystal these phases are energetically equal, so that they can be combined into a single phase $\Gamma_4+\Gamma_5$ with the magnetic group $\overline{1}'2_z'$.

Unfortunately, no experimental information on the orientation of $\mathbf{L}_b^0$ and $\mathbf{L}_c^0$ in the basal plane has been reported (see the discussion in Sec. 7.2 of Ref. 9). This combined phase $\Gamma_4+\Gamma_5$ corresponds to a spin-wave representation of the quasi-AF type:

$$\Delta L_{bx},\Delta L_{cy},\Delta L_{by},\Delta L_{cx},L_{az},M_z. \tag{37}$$

However, investigation of the thermodynamic potential Φ (8) for the indicated tetragonal phase $\Gamma_4+\Gamma_5$, in which, generally speaking, a biquadratic anisotropic term of the type $L_{bx}^2L_{by}^2$, etc. should be added, shows (at least for the equal-modulus model) that the minimum of Φ corresponds to the same phases $\Gamma_4(L_{bx}^0,L_{cy}^0)$ or $\Gamma_5(L_{by}^0,L_{cx}^0)$ as in the rhombic case, and also the diagonal phases with $\mathbf{L}_b^0\|[110]$, $\mathbf{L}_c^0=0$ or $\mathbf{L}_c^0\|[110]$, $\mathbf{L}_b^0=0$. For the first two, Table I gives 4 modes each:

— in the phase $\Gamma_4(L_{bx}^0,L_{cy}^0)$ these will be the AMG mode $\Gamma_{46}(\Delta L_{bx},\Delta L_{cy},L_{az})$ and the quasi-AF modes $\Gamma_{35}(M_z,L_{by},L_{cx})$, $\Gamma_{18}(M_x,L_{ay},L_{cz})$, and $\Gamma_{27}(M_y,L_{ax},L_{bz})$;

— in the phase $\Gamma_5(L_{by}^0,L_{cx}^0)$ they will be the analogous modes $\Gamma_{56}(\Delta L_{by},\Delta L_{cx},L_{az})$, $\Gamma_{34}(M_z,L_{bx},L_{cy})$, $\Gamma_{17}(M_x,L_{ay},L_{bz})$, and $\Gamma_{28}(M_y,L_{ax},L_{cz})$. What we have said can be verified from the requirement that the equations of motion be invariant with respect to the magnetic groups $\overline{1}'2_x'2_z'$ and $\overline{1}'2_x2_z'$ for Γ_4 and Γ_5, respectively. We consider only the AMG modes.

We note that the phases $\Gamma_4(L_{bx}^0,L_{cy}^0)$ and $\Gamma_5(L_{by}^0,L_{cx}^0)$ and also the modes corresponding to them in terms of symmetry are equivalent: they are obtained from the others by means of the 4_{2z} axis. Therefore it is sufficient to do the calculations only for one of the phases; let this be the $\Gamma_5(L_{by}^0,L_{cx}^0)$ phase with the AMG mode $\Gamma_{56}(\Delta L_{by},\Delta L_{cx},L_{az})$.

Here there can be two cases: the main basis vector is $\mathbf{L}_b^0$ (a) or $\mathbf{L}_c^0$ (b). Case (a) corresponds to Cr_2TeO_6, and case (b) to Cr_2WO_6 and V_2WO_6 (see Table 7.1 in Ref. 9).

Let $\mathbf{L}_b^0 \| \mathbf{Y}$ ($L_{by}^0 \approx 4M_0$). Then from the requirement that Φ_{mag} (8) be minimum we find that for the ground state under consideration (with allowance for the conditions $A_b<0$, $A_a>0$, and $A_c>0$)

$$\frac{L_{cx}^0}{L_{by}^0} \cong -\frac{r}{A_c - A_b} \ll 1. \tag{38}$$

In this case the LL equations (12) reduce to the system

$$\begin{aligned} \dot{L}_{cx} &= \gamma L_{by}^0 [\tilde{A}_a L_{az} - f_1 E_x], \\ \dot{L}_{az} &= -\gamma L_{by}^0 \tilde{A}_c \Delta L_{cx}, \end{aligned} \tag{39}$$

where $\tilde{A}_a = A_a - A_b$, $\tilde{A}_c = A_c - A_b$. It follows from the noncollinearity of the ground state (the admixture of the vector L_{cx}^0) and conditions (11) that here the oscillatory component parallel to $\mathbf{L}_b^0$ is also nonzero:

$$\Delta L_{by} = -\frac{L_{cx}^0}{L_{by}^0} \Delta L_{cx}. \tag{40}$$

However, because of the relativistic smallness of the ratio (38), it is small.

The corresponding equations for the phase $\Gamma_4(L_{bx}^0, L_{cy}^0)$ are obtained from equations (39) by operating on the latter with 4_{2z}, which has the effect shown in Table I. Note that we are talking about the operation of the crystal-chemical space group, which takes one phase into another.

Ultimately the result is as follows:

$$\begin{aligned} &\text{for } \mathbf{L}_b^0 \| \mathbf{Y}: && \text{for } \mathbf{L}_b^0 \| \mathbf{X}: \\ &\Delta L_{cx} = \frac{i\omega\omega_0 f_1}{\omega_{Lb}^2 - \omega^2} E_x, && \Delta L_{cy} = -\frac{i\omega\omega_0 f_1}{\omega_{Lb}^2 - \omega^2} E_y, \\ &L_{az} = \frac{\omega_0^2 \tilde{A}_c f_1}{\omega_{Lb}^2 - \omega^2} E_x, && L_{az} = \frac{\omega_0^2 \tilde{A}_c f_1}{\omega_{Lb}^2 - \omega^2} E_y; \end{aligned} \tag{41}$$

$$\begin{aligned} &\text{for } \mathbf{L}_c^0 \| \mathbf{Y} && \text{for } \mathbf{L}_c^0 \| \mathbf{X} \\ &\Delta L_{bx} = \frac{i\omega\omega_0 f_2}{\omega_{Lc}^2 - \omega^2} E_y, && \Delta L_{by} = -\frac{i\omega\omega_0 f_2}{\omega_{Lc}^2 - \omega^2} E_x, \\ &L_{az} = \frac{\omega_0^2 \tilde{A}_b f_2}{\omega_{Lc}^2 - \omega^2} E_y, && L_{az} = \frac{\omega_0^2 \tilde{A}_b f_2}{\omega_{Lc}^2 - \omega^2} E_x. \end{aligned} \tag{42}$$

Here the upper pairs of formulas (41) correspond to the case when the main basis vector is $\mathbf{L}_b^0$ for both phases: $\mathbf{L}_b^0 \| \mathbf{Y}$ (left) and $\mathbf{L}_b^0 \| \mathbf{X}$ (right). Also given are the formulas for the case when $\mathbf{L}_c^0$ is the main basis vector for both phases ($\mathbf{L}_c^0 \| \mathbf{Y}$ and $\mathbf{L}_c^0 \| \mathbf{X}$). For these two cases, respectively, the AMG resonance frequency is given by the expressions

$$\omega_{Lb}^2 = \omega_0^2 \tilde{A}_a \tilde{A}_c, \tag{43}$$

where $\tilde{A}_a = A_a - A_b$, $\tilde{A}_c = A_c - A_b$, $\omega_0 = \gamma L_b^0$,

and

$$\omega_{Lc}^2 = \omega_0^2 \tilde{A}_a \tilde{A}_b, \tag{44}$$

where now $\tilde{A}_a = A_a - A_c$, $\tilde{A}_b = A_b - A_c$, and $\omega_0 = \gamma L_c^0$. For the second case there is also a relativistic longitudinal (with respect to $\mathbf{L}_c^0$) component, analogous to (40). For example, for $\mathbf{L}_c^0 \| \mathbf{X}$ it is equal to

$$\Delta L_{cx} = -\frac{L_{by}^0}{L_{cx}^0} \Delta L_{by}.$$

We shall not give the results pertaining to the mixed phase $\Gamma_4 + \Gamma_5$, even for the most interesting case, when $\mathbf{L}_b^0$ or $\mathbf{L}_c^0$ is directed along a diagonal of the basal square, [110]. This case is interesting because, first, it is possible that this phase, and not the phase considered above, is realized in the easy-plane trirutiles mentioned. (As we have said, experiment does not permit making an unambiguous choice.) In addition, this orientation state is characterized by being collinear. In that case, at least in the equal-modulus model, we have only two possibilities (see Sec. 7.2 of Ref. 9):

$$\mathbf{L}_b^0 \| [110], \ \mathbf{L}_c^0 = 0 \ \text{ or } \ \mathbf{L}_c^0 \| [110], \ \mathbf{L}_b^0 = 0.$$

In formulas (41) and (42) (and in (34), by the way) the dissipation and then the thermal losses Q should have been taken into account. However, this can be done, if desired, by the interested reader (e.g., on the pattern of Sec. 4.1).

CONCLUSION

Let us discuss some specific results of this study which pertain mainly to trirutiles.

For the easy-axis AF structure $\Gamma_7(L_{bz}^0)$, which is characteristic for Fe_2TeO_6, perhaps the most interesting result is the existence of a low-frequency (quasi-AF) mode with frequency (27) and susceptibility (30), excited by an electric field $\mathbf{E}(t)$.

For detection of the low-frequency antimagnons the FM phase $\Gamma_3(M_z^0)$, obtained artificially as a result of a phase transition of the spin-flip type in a sufficiently strong magnetic field H_z, is also of interest. After the spin flip in fields $H_z > H_{\text{flip}}$ the antimagnon frequency (36) can be made arbitrarily low. The susceptibility to a field $\mathbf{E}(t)$ is given by formulas (33) and (34).

In the case of an easy-plane state (Sec. 4.2) we considered the CAS phases $\Gamma_4(L_{bx}^0, L_{cy}^0)$ and $\Gamma_5(L_{by}^0, L_{cx}^0)$. Their AMG frequencies for the modes $\Gamma_{46}(\Delta L_{bx}, \Delta L_{cy}, L_{az})$ and $\Gamma_{56}(\Delta L_{by}, \Delta L_{cx}, L_{az})$ is found in the exchange region. If the main basis vector is $\mathbf{L}_b^0$ (as for Cr_2TeO_6), then the AMG frequency is given by formula (43) for $\mathbf{L}_b^0 \| \mathbf{Y}$ and $\mathbf{L}_b^0 \| \mathbf{X}$. When the main basis vector is $\mathbf{L}_c^0$ (as for Cr_2WO_6 and V_2WO_6), then it corresponds to the frequency (44).

In trirutiles, which comprise an extremely large class of AF compounds, it is mainly the static ME effect that has been studied up till now. Of course, it would be very desirable to observe the AFER in them as a dynamic manifestation of the aforementioned ME and AFE interactions, which were discussed in detail in Sec. 4.

In this last remark the authors have in fact turned to the question of further studies in the region of dynamic phenomena associated with the **E** field in magnets. One naturally wonders whether there exist some phenomena of the indicated ME and AFE nature in the low-frequency region. It turns out that such phenomena do exist, and not only those which were mentioned above (low-frequency electroactive magnons). There is an effect in which the NMR is excited by an electric field at a frequency $\omega \approx \omega_n \ll \omega_L$. This effect was demonstrated for extremely simple examples in Ref. 12. It would be desirable to do such a study for a series of specific

magnets. This would include the trirutiles discussed in the present article, the ground state of which is CAS, and even the CS magnets such as hematite and the orthoferrites, in which the excitation of NMR is possible because the field $\mathbf{E}(t)$ excites oscillations of the CAS vectors $\mathbf{L}$ (which do not exist in the ground state).

Turning to Secs. 3.2 and 3.3, in which we discussed the possibility of resonance in an electric field $\mathbf{E}(t)$ at the quasi-AF mode with a frequency of the form (25), we should call attention to an interesting paper[16] reporting the experimental discovery of such a resonance in the tetragonal AF Nd_2CuO_4. However, that compound has an exchange-noncollinear magnetic structure (of the ''rectangular cross'' type), which we have not considered here.

In Ref. 12 some 15 problems were stated and touted for further study, not only in connection with antimagnons but also with other manifestations of the ME and AFE interactions. In particular, the present paper gives the solution to one of these problems. Perhaps we should mention just a few of the more important problems from the list given in Ref. 12: first, surface AMG waves and ways of exciting them (here we can also include the surface NMR); second, coupled AMG electromagnetic waves and AMG elastic waves. On the experimental side, we would like to point out that the experimental detection of the effects considered in Refs. 1–5 and in the present study is of fundamental importance.

Finally, we should say a few words about the intensity of the AMG resonance (of the values of the corresponding susceptibilities) in comparison, e.g., with the ordinary AFMR. At the same frequency their relative value is determined by the static magnetizations caused by the electric field, $M_E = \alpha E$ (the ME effect with susceptibility α) and by the magnetic field $M_H = \chi_0 H$ (χ_0 is the AF susceptibility). Their ratio

$$\frac{M_E}{M_H} = \frac{\alpha}{\chi_0}\frac{E(t)}{H(t)}$$

serves to some degree as a characteristic of the relative intensity of the AMG resonance and AFMR. Since at the antinodes of the electromagnetic wave $E(t)$ and $H(t)$ are identical, and α and χ_0 can also be of the same order of magnitude (e.g., $\alpha \sim \chi_0 \sim 10^{-3}$; see Ref. 9), the intensities of these resonances can be comparable in value.

This study was supported by the Russian Foundation for Basic Research (Project No. 99-02-16268).

*E-mail: turov@imp.uran.ru

[1] D. A. Yablonskii and V. N. Krivoruchko, Fiz. Nizk. Temp. **14**, 656 (1988) [Sov. J. Low Temp. Phys. **14**, 363 (1988)].
[2] V. N. Krivoruchko and D. A. Yablonskiĭ, Zh. Éksp. Teor. Fiz. **94**, 268 (1988) [*sic*].
[3] D. A. Yablonskiĭ and V. N. Krivoruchko, Fiz. Tverd. Tela (Leningrad) **30**, 2069 (1988) [Sov. Phys. Solid State **30**, 1785 (1988)].
[4] V. V. Eremenko, V. N. Krivoruchko, N. M. Lavrinenko, and D. A. Yablonskiĭ, Fiz. Tverd. Tela (Leningrad) **30**, 3605 (1988) [Sov. Phys. Solid State **30**, 2070 (1988)].
[5] D. A. Yablonskiĭ and V. N. Krivoruchko, in *Problems of Physical Kinetiks and Solid State Physics* [in Russian], Naukova Dumka, Kiev (1990).
[6] E. A. Turov, JETP Lett. **73**, 87 (2001).
[7] E. A. Turov and A. V. Kolchanov, in *Magnetism of Transition Metals and Alloys* [in Russian], Izd. UrO RAN, Ekaterinburg (2000).
[8] E. A. Turov, A. V. Kolchanov, V. V. Men'shenin, I. F. Mirsaev, and V. V. Nikolaev, Usp. Fiz. Nauk **168**, 1303 (1998).
[9] E. A. Turov, A. V. Kolchanov, V. V. Men'shenin, I. F. Mirsaev, and V. V. Nikolaev, *Symmetry and the Physical Properties of Antiferromagnets* [in Russian], Fizmatlit, Moscow (2001).
[10] E. A. Turov and A. V. Kolchanov, in *Proceedings of the International Syposium on Magnetism EAST MAG-2001* [in Russian], Ekaterinburg (2001).
[11] A. V. Kolchanov and E. A. Turov, in *Proceedings of the International Syposium on Magnetism EAST MAG-2001* [in Russian], Ekaterinburg (2001).
[12] E. A. Turov, *Spin Dynamics of Magnets with Magnetoelectric and Antiferroelectric Interactions. Antimagnons. NMR in an Electric Field* [in Russian], IFM UrO RAN, Ekaterinburg (2001).
[13] I. F. Mirsaev and E. A. Turov, Zh. Éksp. Teor. Fiz. **121**, 419 (2002) [JETP Lett. **94**, 356 (2002)].
[14] Yu. A. Izyumov, N. A. Chernoplekov, *Neutron Spectroscopy, Ser. Neutrons and Solids*, edited by R. P. Ozerov [in Russian], Énergoatomizdat, Moscow (1983), Vol. 3, p. 101.
[15] V. G. Bar'yakhtar, I. M. Vitebskiĭ, and D. A. Yablonskiĭ, Zh. Éksp. Teor. Fiz. **76**, 1381 (1979) [Sov. Phys. JETP **49**, 703 (1979)].
[16] A. S. Smirnov, S. N. Barilo, and D. I. Zhigunov, Zh. Éksp. Teor. Fiz. **100**, 1690 (1991) [Sov. Phys. JETP **73**, 934 (1991)].

Translated by Steve Torstveit

On the conditions for the existence of 1D magnetic solitons with frequency characteristics falling in the continuous spectrum

A. M. Kosevich* and V. I. Grishaev

B. Verkin Institute for Low Temperature Physics and Engineering, National Academy of Sciences of Ukraine, pr. Lenina 47, 61103 Kharkov, Ukraine

(Submitted February 13, 2002; revised February 27, 2002)
Fiz. Nizk. Temp. **28**, 834–839 (August–September 2002)

Solutions of a modified (with higher-order dispersion taken into account) sine-Gordon equation in the form of a double soliton (4π kink) and a pair of spatially separated bound kinks are investigated. An analytical condition for the absence of radiation from the soliton at large distances is formulated. The previous finding of the existence of a discrete set of nonradiative composite solitons is confirmed. The physical meaning of this result is that at certain distances between kinks the radiation generated by one of the kinks completely quenches the field of the other kink outside the soliton as a result of ordinary interference of waves in antiphase. © *2002 American Institute of Physics.* [DOI: 10.1063/1.1511703]

1. One of the basic equations describing the nonlinear dynamics of one-dimensional (1D) systems is the sine-Gordon (sG) equation. It is used for analysis of nonlinear excitations in quasi-1D ferromagnets, antiferromagnets,[1] and chains of Josephson junctions.[2] We will be interested in the soliton solutions of a slightly modified sG equation containing higher-order dispersion:

$$\frac{\partial^2 u}{\partial t^2}=\frac{\partial^2 u}{\partial x^2}+\beta\frac{\partial^4 u}{\partial x^4}-\sin u, \quad \beta>0. \tag{1}$$

Equation (1) is curious in that, unlike the usual sG equation, where among the nonlinear elementary excitations is a set of moving 2π kinks, it has an exact solution in the form of a 4π kink moving with a completely determined velocity

$$V_0=\pm\sqrt{1-\sqrt{\frac{4}{3}\beta}}. \tag{2}$$

This solution was first obtained in Ref. 3 and agrees with the numerical results of Refs. 4 and 5. However, in Ref. 5, besides a soliton moving with velocity (2), a spectrum of similar solitons with a definite discrete set of velocities was obtained numerically. In Ref. 6 an analytical method of perturbation theory was developed that made it possible to show that the solitons of Eq. (1) can be treated as bound states of a pair of 2π kinks of the sG equation.

The dynamical solitons of Eq. (1) are unusual in that, while being spatially localized excitations of a 1D system, they have frequency characteristics that fall in the continuous spectrum of elementary excitations of the linearized equation. It is ordinarily assumed that a localized excitation cannot exist in such a situation, since its presence in a nonlinear medium will give rise to the radiation of small (harmonic) oscillations of the system. However, it has been shown[7] that localized excitations are strictly forbidden only when the linearized equation is of second order with respect to the spatial derivatives (a wave equation or Schrödinger equation). The situation is altered if the linearized equation contains higher-order spatial derivatives (in other words, if higher-order dispersion is taken into account). In Ref. 7 the physical conditions for the existence of localized nonlinear excitations with frequencies falling in the continuous spectrum were formulated, and the connection between these conditions and the form of the linearized equation was pointed out. It is easy to understand qualitatively why such conditions arise.

We consider for simplicity an equation of the nonlinear Schrödinger type:

$$-i\frac{\partial\Psi}{\partial t}=\frac{\partial^2\Psi}{\partial x^2}+g\frac{\partial^4\Psi}{\partial x^4}+F(|\Psi|^2)\Psi, \tag{3}$$

where $g=-|g|<0$, and $F(u)$ is a nonlinear function for which $F(0)=0$. The linearized equation has eigen solutions of the form

$$\Psi(x,t)=\exp(ikx-i\omega t), \tag{4}$$

which correspond to a dispersion relation

$$\omega=k^2+|g|k^4, \tag{5}$$

all the frequencies of which are positive ($\omega>0$).

Let us assume that Eq. (3) has a soliton solution $\Psi_s=f_s(x)e^{-i\omega t}$, where $f_s(x)=0$ for $x\to\pm\infty$. At what frequencies is this possible?

The fall-off of the amplitude of $f_s(x)$ at infinity means that at large enough distances it will be described by the linearized equation, and its form will correspond to eigensolutions with dispersion relation (5). If $g=0$, then it follows from (5) that to a fixed frequency ω there corresponds a pair of values $k=\pm\sqrt{\omega}$. Consequently, for $\omega>0$, waves (4) of nonzero amplitude will exist at infinity (a perturbation localized at finite x and having frequency ω will inevitably generate radiation at that frequency). However, for $\omega<0$ we have $k=\pm i\sqrt{|\omega|}$, and therefore at infinity the solution will behave as $f_s(x)=e^{-\sqrt{|\omega|}|x|}$. This means that dynamical solitons localized in space can exist only if their frequencies are outside the continuous spectrum of the dispersion relation $\omega=k^2$. Analogous conditions for the existence of dynamical magnetic solitons of the Landau–Lifshitz equation are discussed in Ref. 8.

If $g\neq 0$, then the situation is fundamentally altered. Now to a fixed positive frequency ω there correspond two pairs of values: a pair of real k,

$$k^2=\frac{1}{2|g|}(\sqrt{1+4|g|\omega}-1) \tag{6}$$

and a pair of purely imaginary $k=i\kappa$,

$$\kappa^2=\frac{1}{2|g|}(\sqrt{1+4|g|\omega}+1). \tag{7}$$

This means that at large distances from the center of the soliton (where the equation is linear) there can simultaneously exist both a solution that is decaying with increasing coordinate [corresponding to the parameter (7)] and also a solution propagating as a wave with wave vector (6). While the first corresponds to a localized (solitonic) part of the perturbation, the second is caused by the radiation of the dynamical soliton. Generally speaking, the radiation exists in the presence of any dynamical localized perturbation in such a system. However, it was shown in Ref. 7 that radiation is absent for such $k=k(\omega)$ when the spatial Fourier component of the last term in (3), due to the soliton solution, goes to zero:

$$\int e^{ikx}F(|f_s(x)|^2)f_s(x)dx=0. \tag{8}$$

It is clear that there can only be a discrete set of frequencies (and wave numbers) for which condition (8) can hold. It turns out that the possibility of such a situation finds its explanation in the study of the properties of the linearized system and its wave solutions. In particular, in the case of a composite soliton solution analogous to a bound state of two moving simple solitons (in our case kinks), a curious observation was made.[9,10] For such a soliton radiation is absent if the distance between its two constituents is equal to an odd number of half waves of the radiation field of the linearized equation. The meaning of this condition is physically simple: linear waves radiated by each member of the pair under such a condition quench one another outside the boundaries of the soliton as a result of interference.

As an example, let us confirm the statements and conjectures made above with an analysis of the existence conditions of nonradiative solitons of Eq. (1).

2. Working on the basis of the results of Ref. 3, we seek a soliton solution of Eq. (1) for $\beta>0$ in radiationless form:

$$u_s(x-Vt)=2u_s^0(x-Vt). \tag{9}$$

Here $u_s^0(x)$ is a kink solution of the ordinary sG equation (obtained by setting $\beta=0$ in Eq. (1)):

$$u_s^0(x)=4\ \operatorname{arctg}\exp(-x/l), \tag{10}$$

where the soliton velocity V satisfies the condition $V<1$.

To understand the physical meaning of the problems that arise in such a choice of solution, we have drawn a graph of the dispersion relation (see Fig. 1) of the linearized equation (1), viz., of the relation

$$\omega^2=1+k^2+\beta k^4, \tag{11}$$

and we write (9) in the form a packet of linear waves (''phonons''):

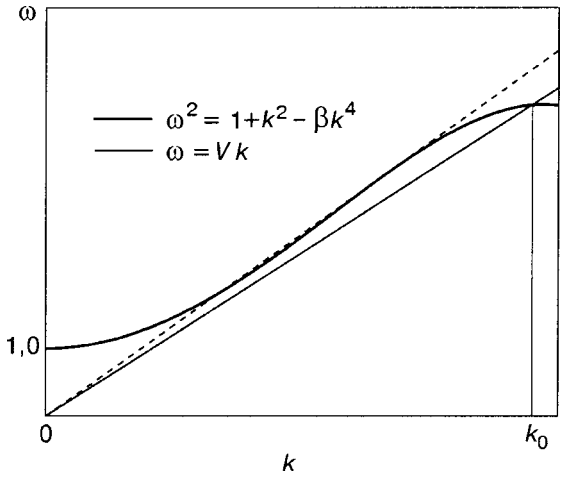

FIG. 1. Graph of the dispersion relation of the linearized equation (1).

$$u_s(x-Vt)=\sum_k C(k)e^{ik(x-Vt)}, \tag{12}$$

where $C(k)$ are Fourier components of the of the function under study.

We see that this packet is formed by ''phonons'' with a dispersion relation

$$\omega=kV, \tag{13}$$

a graph of which crosses that of dispersion relation (11) at a point with wave number k_0.

The presence of this crossing means that the interaction of the soliton with the spectrum of harmonic oscillations described by the linearized equation (1) causes the radiation of waves with wave number k_0, i.e., the Cherenkov radiation of real phonons will occur. Consequently, the steady motion of soliton (9) with a constant velocity V turns out to be impossible for $V<1$.

However, it is stated in Ref. 7 that there are values of the parameters V and l of solution (9) such that radiation is absent. Let us find these parameters from the condition that there be no radiation of linear waves. We shall use the following relations:

1) For $x\gg 1$ we have $u_s^0(x)=4\exp(-x/l)\ll 1$, and therefore the relation between the parameters V and l can be found from the linearized equation (1):

$$(1-V^2)l^2+l^4-\beta=0. \tag{14}$$

2) We rewrite equation (1) in the form of a linear equation with a right-hand side equal to $\sin u$ and we substitute $u=u_s(x-Vt)$ into the right-hand side:

$$\frac{\partial^2 u}{\partial x^2}+\beta\frac{\partial^4 u}{\partial x^4}-\frac{\partial^2 u}{\partial t^2}=\sin u_s(x-Vt)=\sin 2u_0^s(x-Vt). \tag{15}$$

We treat the function on the right-hand side of Eq. (15) as a localized force $f_s(x-Vt)$, which is a source of the field $u(x)$ of the linear equation:

$$f_s(x)=\frac{\sinh x(1-\sinh^2 x)}{\cosh^4 x}. \tag{16}$$

At large distances ($x \gg Vt$) the localized part of the soliton solution vanishes, and the field $u(x)$ can be nonzero only on account of the radiation given by the expression

$$u(x,t)=\int G(x-x')f_s(x'-Vt)dx', \tag{17}$$

where $G(x)$ is the Green's function of the equation

$$\frac{\partial^2 u}{\partial x^2}+\beta\frac{\partial^4 u}{\partial x^4}-\frac{\partial^2 u}{\partial t^2}=0. \tag{18}$$

The wave (nondecaying with distance) part of the Green's function of equation (18) has the obvious form

$$G_\omega(x)=A(\omega)e^{ikx}, \tag{19}$$

where k is related to the frequency by the dispersion relation

$$\omega^2=k^2-\beta k^4. \tag{20}$$

Substituting (19) into (17), we obtain

$$u(x,t)=2A(\omega)e^{ik(x-Vt)}\int_{-\infty}^{\infty}e^{ik\xi}f_s^0(\xi)d\xi. \tag{21}$$

We see that the role of the frequency, as expected, is played by $\omega=kV$, and therefore the wave number k appearing in (19) is related to the velocity by an equation derived from (20):

$$V^2=1-\beta k^2. \tag{22}$$

Thus the radiation field is absent if

$$Q(k)\equiv\int_{-\infty}^{\infty}e^{ik\xi}\sin u_s(\xi)d\xi=0, \tag{23}$$

where the integrand in the Fourier component is given by formula (16).

The integral (23) can be evaluated in explicit form:

$$Q(k)=\frac{\pi(k^2l^2-2)}{2\cosh\left(\dfrac{kl\pi}{2}\right)}. \tag{24}$$

From requirement (21) it follows directly that

$$k^2l^2=2. \tag{25}$$

Equations (14), (22), and (25) enable us to find the basic parameters V and l of the soliton. In particular, it turns out that the soliton velocity V is exactly equal to the value given by Eq. (2), which was obtained in Ref. 3.

Thus we have shown that the physical condition for the absence of radiation by a soliton with certain frequency characteristics that fall in the continuous spectrum of the harmonic oscillations is indeed the condition that the corresponding Fourier component of the driving force $f_s(x,t)$ be equal to zero.

3. Besides solitons (9) in the form of a double kink of the sG equation, the nonlinear equation (1) has a discrete series of solitons of a more complex structure, viz., solitons consisting of two spatially separated bound kinks.[6,7] Let us elucidate the conditions under which a soliton excitation of this type does not cause radiation.

Following Ref. 6, we write the desired solution of equation (1) in the form

$$u_s(x-Vt)=u_s^0(x-\Delta-Vt)+u_s^0(x+\Delta-Vt), \tag{26}$$

where 2Δ is the distance between the centroids of the two kinks, which at the frequencies of interest to us is assumed to be independent of time.

Repeating the arguments of the previous paragraph, we arrive at the same conditions (14), (22), and (23), but the latter corresponds to the Fourier component of the function

$$f_s(x)=f_s^0(x-\Delta)+f_s^0(x+\Delta), \tag{27}$$

where the soliton velocity V satisfies the condition $V<1$. Finding the Fourier component of interest with allowance for the symmetry of expression (26) reduces to the evaluation of the following integral:

$$Q(k)=\int[\sin u_s^0(x+\Delta)\cos u_s^0(x-\Delta)+\sin u_s^0(x-\Delta)\cos u_s^0(x+\Delta)]\sin kx\,dx. \tag{28}$$

It is easy to see that

$$\sin u_s(x)=-\frac{2\sinh x}{\cosh^2 x};\quad \cos u_s(x)=1-\frac{2}{\cosh^2 x}, \tag{29}$$

and $Q(k)$ is equal to the sum of two integrals:

$$Q(k)=I_1(\Delta)+I_2(\Delta), \tag{30}$$

where

$$I_1(\Delta)=4\int\frac{\sinh\dfrac{\xi+\Delta}{l}}{\cosh^2\dfrac{(\xi+\Delta)}{l}}\sin k\xi d\xi=-\frac{4\pi l^2\cos k\Delta}{\cosh\dfrac{kl\pi}{2}}; \tag{31}$$

$$I_2(\Delta)=-4\int\frac{\sinh\dfrac{\xi-\Delta}{l}+\sin\dfrac{\xi+\Delta}{l}}{\left[\cosh^2\dfrac{\xi-\Delta}{l}\cosh^2\dfrac{\xi+\Delta}{l}\right]^2}\sin k\xi d\xi$$

$$=-16\cosh\frac{\Delta}{l}\int\frac{\sinh\dfrac{\xi}{l}\sin k\xi d\xi}{\left[\cosh\dfrac{2\xi}{l}+\cosh\dfrac{2\Delta}{l}\right]^2}$$

$$=\frac{4\pi l\cosh\dfrac{\Delta}{l}}{\cosh\dfrac{kl\pi}{2}\sinh^2\dfrac{\Delta}{l}}\left[\frac{\cosh\dfrac{\Delta}{l}\sin k\Delta}{\sinh\dfrac{\Delta}{l}}-kl\cos k\Delta\right]. \tag{32}$$

Substituting (31) and (32) into (30), we obtain an expression for the Fourier component which we seek:

$$Q(k)=\frac{2\pi l\cosh^2\dfrac{\Delta}{l}}{\cosh\dfrac{kl\pi}{2}\sinh^3\dfrac{\Delta}{l}}\left[2\sin k\Delta-kl\sinh\frac{2\Delta}{l}\cos k\Delta\right]. \tag{33}$$

The requirement that $Q(k)=0$ reduces to the relation

$$kl\cdot\sinh\frac{2\Delta}{l}=2\tan(k\Delta), \tag{34}$$

which, together with (14) and (22), allows us to find all the soliton parameters: velocity V, the distance 2Δ between its constituent kinks, the effective width l of the soliton, and the value of the wave number k ensuring a radiationless regime of soliton dynamics at a specified value of the nonlinearity parameter β. It is clear that three relations are insufficient for determination of these four parameters. However, by eliminating two of them, we can establish a relation between the remaining two. Let us discuss the relation between the parameters k and Δ. Substituting (22) into (14), we obtain an equation that gives the dependence of l on k:

$$l^{-2}=\frac{1}{2\beta}(\sqrt{\beta^4k^8+4\beta}-\beta^2k^4). \tag{35}$$

Relations (34) and (35) can be used to establish a relation between Δ and k. However, one can do a qualitative analysis of this relation by proceeding directly from Eq. (34), rewriting it in a somewhat different form:

$$q\sinh\frac{2k\Delta}{q}=2\tan(k\Delta),\quad q=kl. \tag{36}$$

It is clear that for $\Delta\to 0$ this goes over to relation (25) obtained earlier.

The graphical solution of this equation for $\Delta\neq 0$ reduces to finding the points of intersection of the graphs of the left- and right-hand sides of (36). Assuming that in the parameter region of interest one can set $q\sim 1$, we see that the graph of the left-hand side of (36), which increases monotonically with increasing argument $k\Delta$, intersects the graph of the functions $\tan(k\Delta)$ at an infinite number of points, the height of which increases rapidly with increasing argument. These are the points at which

$$k\Delta\approx\frac{\pi}{2}(2n+1),\quad n=0,1,2,\ldots. \tag{37}$$

As an illustration, Fig. 2 shows the graphs of the left- and right-hand sides of (36) for three values of q corresponding to several different values of β. It is clearly seen in the figure that the points of intersection of the graphs approach the straight lines (37).

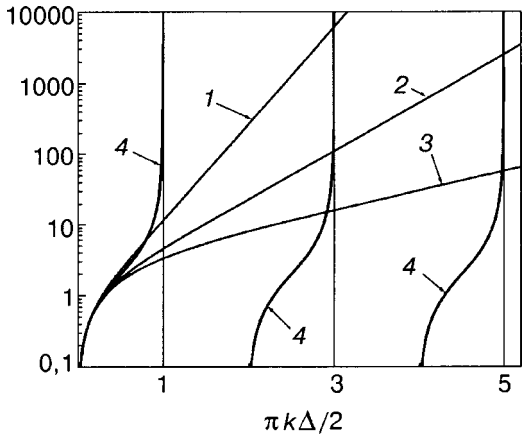

FIG. 2. Intersection of the graphs of the function $q\sinh\pi k\Delta/q$ [$q=0.5$ (*1*), $q=1$ (*2*), $q=3$ (*3*)] with the graphs of the function $2\tan(\pi k\Delta/2)$ (*4*).

For a machine calculation of the unknown quantity $k\Delta$ we substitute (35) into (34) and obtain the explicit dependence of k on Δ in the form

$$k\left[\frac{1}{2\beta}(\sqrt{\beta^4k^8+4\beta}-\beta^2k^4)\right]^{-1/2}\times\sinh\left\{2\Delta\left[\frac{1}{2\beta}(\sqrt{\beta^4k^8+4\beta}-\beta^2k^4)\right]^{1/2}\right\}=2\tan k\Delta. \tag{38}$$

By specifying various fixed values of q, one can find the corresponding solutions of equation (38).

A numerical calculation shows that for the first roots of equation (36) the difference of the exact values from the estimate (37) reduces to the following values:

	$q=0.5$	$q=1$	$q=3$
$n=0$	$\frac{\pi}{2}-k\Delta=0.01592$	0.3169	1.57
$n=1$	$\frac{3\pi}{2}-k\Delta=10^{-6}$	$3.2\cdot10^{-4}$	0.0602
$n=2$	$\frac{5\pi}{2}-k\Delta=5.8\cdot10^{-7}$	$<10^{-5}$	0.00713
$n=3$	$\frac{7\pi}{2}-k\Delta<1\cdot10^{-10}$	$<10^{-8}$	$8.7\cdot10^{-4}$

Consequently, starting with $n=2$, condition (37) can be replaced by the equality

$$k\Delta=\frac{\pi}{2}(2n+1), \tag{39}$$

which has a very curious physical meaning and simple interpretation. An individual moving kink can in principle generate radiation whose wave number k is determined by the soliton velocity V. The kinks are separated by a distance 2Δ, and therefore condition (39) means that the waves radiated by the first and second kinks are in antiphase. Consequently, the radiation from one of the kinks completely quenches the field of the other kink outside the soliton as a result of ordinary interference of waves in antiphase. This result can be regarded as an illustration of the possibility of existence of a composite nonradiative soliton, which was stated in Ref. 10. To some degree a solution of the type (27) is in fact a solution of Eq. (1), which was discussed in Ref. 6.

The authors are grateful to M. M. Bogdan for a discussion and helpful advice. This study was supported in part by INTAS Grant No. 167 (for 1999).

The authors are honored to coordinate our paper with the jubilee of Acad. Viktor Eremenko, who has made an outstanding contribution to the study of the dynamics of magnetically ordered media.

*E-mail: kosevich@ilt.kharkov.ua

[1] H. J. Mikeska and M. Steiner, Adv. Phys. **90**, 191 (1991).
[2] K. Nakajima, Y. Onodera, T. Nakamura, and R. Sato, J. Appl. Phys. **45**, 4095 (1974).
[3] M. M. Bogdan and A. M. Kosevich, in *Nonlinear Coherent Structures in Physics and Biology*, Vol. 329 of NATO ASI Ser. Phys., Plenum Press, New York (1994), p. 373.
[4] M. Peyrard and M. D. Kruskal, Physica D **14**, 88 (1984).
[5] G. L. Alfimov, V. M. Eleonskii, N. E. Kulagin, and N. N. Mitskevich, Chaos **3**, 405 (1993).
[6] M. M. Bogdan, A. M. Kosevich, and G. A. Maugin, Wave Motion **34**, 1 (2001).
[7] A. M. Kosevich, Fiz. Nizk. Temp. **26**, 620 (2000) [Low Temp. Phys. **26**, 453 (2000)].
[8] A. M. Kosevich, B. A. Ivanov, A. S. Kovalev, *Nonlinear Magnetization Waves. Dynamical and Topological Solitons* [in Russian], Naukova Dumka, Kiev (1983); A. M. Kosevich, and B. A. Ivanov, and A. S. Kovalev, Sov. Sci. Rev. A, Phys. **6**, 161 (1985).
[9] B. A. Malomed, Phys. Rev. E **47**, 2874 (1993).
[10] A. V. Buryak and N. N. Akhmediev, Phys. Rev. E **52**, 3572 (1995); A. V. Buryak, *ibid.* **52**, 1156 (1995).

Translated by Steve Torstveit

Magnetic properties of copper metaborate CuB_2O_4

G. A. Petrakovskiĭ, A. I. Pankrats,* M. A. Popov, A. D. Balaev, D. A. Velikanov, A. M. Vorotynov, and K. A. Sablina

L. V. Kirenskiĭ Institute of Physics, Siberian Branch of the Russian Academy of Sciences, Akademgorodok, 660036 Krasnoyarsk, Russia

B. Roessli, J. Schefer, A. Amato, and U. Staub

Laboratory for Neutron Scattering, ETH Zurich & Paul Scherrer Institute, CH-6232 Villigen PSI, Switzerland

M. Boehm

Laboratory for Neutron Scattering, ETH Zurich & Paul Scherrer Institute, CH-6232 Villigen PSI, Switzerland; Institut Laue-Langevin, 38042 Grenoble, Cedex 9, France

B. Ouladdiaf

Institut Laue-Langevin, 38042 Grenoble, Cedex 9, France
(Submitted February 4, 2002)
Fiz. Nizk. Temp. **28**, 840–849 (August–September 2002)

The results of experimental research on the magnetic and resonance properties, heat capacity, muon spin relaxation, and neutron scattering of single-crystal copper metaborate CuB_2O_4 are reviewed. The results of a symmetry analysis and of modeling by the method of the phenomenological thermodynamic potential are presented. The magnetic structure of the crystal in various temperature intervals of the magnetic ordering region is discussed. © *2002 American Institute of Physics.* [DOI: 10.1063/1.1511704]

INTRODUCTION

The discovery of high-temperature superconductivity has stimulated a heightened interest in research on the magnetic properties of copper oxide compounds that, though not superconducting, have fragments of crystal structure identical to those of high-T_c superconductors (HTSCs). A peculiarity of the divalent copper ion is that it forms a greater diversity of magnetic structures than any other chemical element. As an example of the wide range of magnetic properties of copper oxide compounds we can cite the oxocuprates which we investigated previously, among which one encounters a three-dimensional antiferromagnet with a four-spin exchange interaction (Bi_2CuO_4),[1] a spin-Peierls chain magnet ($CuGeO_3$),[2,3] a two-dimensional antiferromagnet with a broken ladder structure ($LiCu_2O_2$),[4] and a spin glass ($CuGa_2O_4$).[5] Research has begun on the triclinic magnet $Cu_5Bi_2B_4O_{14}$, which has a ferro- or ferrimagnetic structure.[6]

We have recently grown single crystals of copper metaborate CuB_2O_4. The first studies of the physical properties of this compound show that in the temperature region below 20 K it has a complex state diagram, in certain regions of which the compound has a modulated (incommensurate) magnetic structure. In the majority of cases such structures arise as a result of a competition of exchange excitations.[7] In these cases the crystal structure does not impose any restrictions on the possibility of realization of such magnetic structures. Dzyaloshinskiĭ first pointed out the possibility for modulated structures to arise on account of relativistic interactions.[8] The physical cause of the onset of incommensurate structures in these cases is an antisymmetric Dzyaloshinskiĭ–Moriya exchange interaction. Formally such magnetic structures can be described by including in the thermodynamic potential a Lifshitz invariant[7] containing linearly the first derivatives of the two-component order parameter with respect to the coordinates. It should be noted that in this case an important restriction is placed on the symmetry of the crystal: the Lifshitz invariant can be included in the thermodynamic potential only for crystals lacking a center of inversion.

The incommensurate structure arising in copper metaborate belongs to this less-common type of modulated structure due to relativistic interactions. It is therefore of great interest to do comprehensive studies of such structures on high-quality single crystals.

In this paper we present the results of experimental studies of the magnetic and certain other physical properties of copper metaborate CuB_2O_4 and discuss the magnetic structure of the crystal in different temperature intervals of the magnetic ordering region.

EXPERIMENTAL DATA

The technology for growing large, high-quality single crystals of copper metaborate is set forth in Ref. 9. X-ray and neutron diffraction studies[10] at room temperature have shown that CuB_2O_4 is a tetragonal crystal, space group $I\bar{4}2d$, with lattice parameters $a=11.528$ Å and $c=5.607$ Å. The unit cell contains 12 formula units (Fig. 1). The copper ions Cu^{2+} occupy two nonequivalent positions: Cu(b)—the $4b$ position, point symmetry $S_4(0,0,1/2)$, and Cu(d)—the $8d$ position, point symmetry $C_2(0.0815,1/4,1/8)$. The Cu(b) ion is

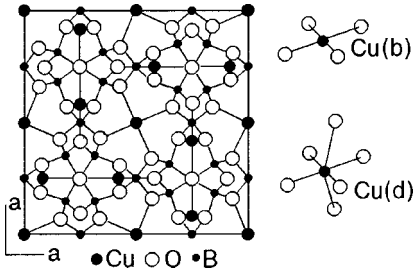

FIG. 1. Crystal structure of copper metaborate.

located at the center of a square formed by four oxygen ions; the Cu(d) ion is surrounded by six oxygen ions localized at the vertices of a distorted octahedron. A special high-resolution neutron diffraction study[10] showed that the crystal does not undergo any structure phase transitions down to a temperature of 1.5 K.

Magnetic measurements made on the crystals showed that the magnetic susceptibility has sharp features at the temperatures $T_I = 10$ K and $T_N = 20$ K. The results of a magnetic susceptibility measurement[11] on a SQUID magnetometer for orientations of the magnetic field along and perpendicular to the tetragonal axis of the crystal are shown in Fig. 2. One notices the sharp anisotropy of the susceptibility. For a magnetic field applied in the basal plane of the crystal a jump in the susceptibility is observed at a temperature of 20 K, and the susceptibility grows rapidly as the temperature is decreased further. At the temperature T_I the susceptibility decreases abruptly by approximately an order of magnitude and then increases monotonically on further decrease of the temperature to 4.2 K. For a magnetic field applied along the tetragonal axis of the crystal the temperature dependence of the susceptibility is smooth throughout the whole temperature range. The paramagnetic Curie temperature and the effective magnetic moment of the copper ion, determined from the high-temperature part of the magnetic susceptibility, have the values $\theta = -9.5$ K and $\mu_{\text{eff}} = 1.77\mu_B$, respectively.

The field dependence of the magnetization measured on a vibrating magnetometer[12] with a magnetic field up to 60 kOe oriented along the tetragonal axis of the crystal is smooth throughout the investigated temperature interval. At the same time, for a field orientation in the tetragonal plane

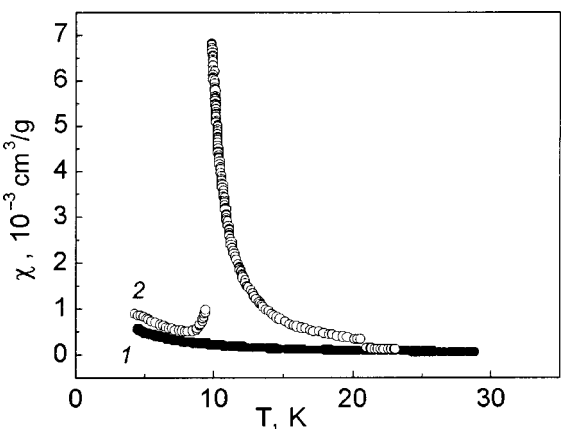

FIG. 2. Temperature dependence of the magnetic susceptibility of a copper metaborate single crystal. The magnetic field was parallel to the tetragonal axis of the crystal (*1*) and to the basal plane of the crystal (*2*).

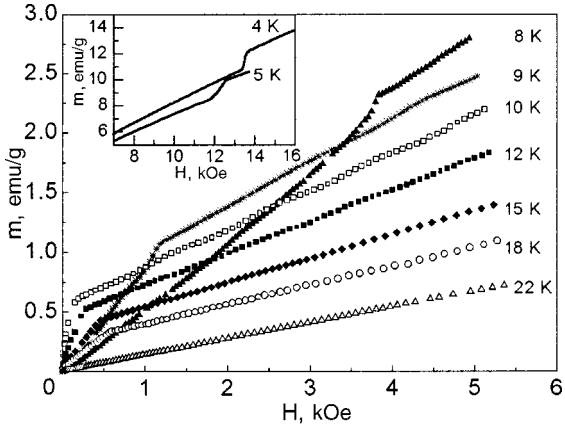

FIG. 3. Field dependence of the magnetization for $\mathbf{H} \perp \mathbf{c}$.

there are kinks on the magnetization curves (Fig. 3). In the temperature region 10–18 K the magnetization curves attest to the existence of a spontaneous magnetic moment in the basal plane of the crystal. The value of the spontaneous moment is $m_0 = 0.56$ emu/g at $T = 10$ K. When the temperature is lowered below T_I the spontaneous magnetization vanishes, and a feature appears on the magnetization curves at higher magnetic fields. The linear approximation of the high-field linear parts of the field dependence of the magnetization in the temperature interval 4.2–10 K shows that above these fields a spontaneous magnetic moment again appears in the crystal.

The anomalies of the magnetic susceptibility described above are accompanied by features of the temperature dependence of the heat capacity (Fig. 4).[11] The temperature dependence of the heat capacity exhibits two anomalies at temperatures coinciding with the anomalies of the magnetic susceptibility. In addition, at a temperature below 4 K the heat capacity has a feature in the form a broad maximum.

The data of muon spin relaxation (μSR) measurements in Ref. 11 also confirm the presence of magnetic transformations at temperatures of 20 and 10 K. Later measurements[13] down to temperatures ~ 0.1 K reveal an additional magnetic transformation at a temperature below 2 K (Fig. 5). It can be

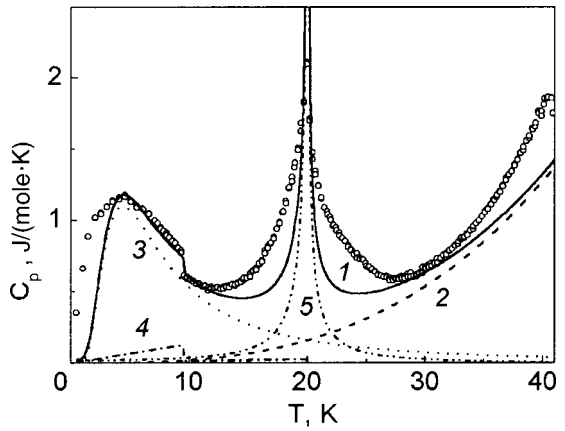

FIG. 4. Temperature dependence of the heat capacity of a single crystal of copper metaborate: the unfilled circles are experimental,[11] and the curves are: *1*—the result of the modeling, *2*—the Debye contribution, *3*—an anomaly of the Schottky type, *4*—the Landau contribution, *5*—the Ginzburg estimate.

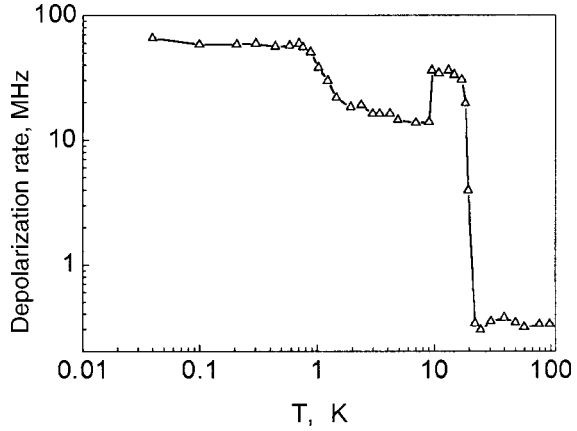

FIG. 5. Temperature dependence of the muon spin relaxation in copper metaborate.

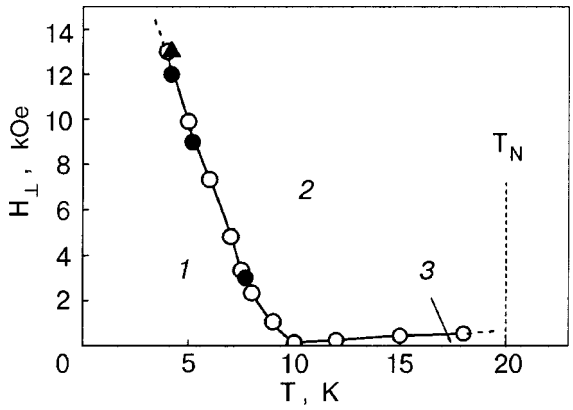

FIG. 7. $H_{\perp}-T$ phase diagram of the states of copper metaborate: magnetic (○) and resonance (●) measurements; the data of Ref. 15 (▲).

assumed that this temperature also corresponds to a reorganization of the spin system of copper metaborate.

Magnetic resonance in CuB_2O_4 has been investigated in a wide range of frequencies, magnetic fields, and temperatures.[14] Figure 6 shows the frequency–field curves of the magnetic resonance in CuB_2O_4 measured at $T=4.2$ K for two orientations of the magnetic field: $\mathbf{H}\|\mathbf{c}$ and $\mathbf{H}\perp\mathbf{c}$. For $\mathbf{H}\|\mathbf{c}$ the dependence is smooth and almost linear. For the orientation $\mathbf{H}\perp\mathbf{c}$, however, a jump of the frequency is observed at $H_{c\perp}=12$ kOe as the field is increased (see inset "a"). This jump is due to a phase transition from the low-temperature state 1 to a state 2 with a field-induced spontaneous magnetic moment at $H=H_{c\perp}$. Inset "b" shows the temperature dependence of the resonance field measured at different frequencies for $\mathbf{H}\perp\mathbf{c}$. For measurements at frequencies of 10.6 and 28.65 GHz in the low-temperature region one observes sharp changes of the resonance field that are also consistent with a phase transition. The temperatures at which these changes occur decreases with increasing frequency. For the measurement at frequency 56.59 GHz no anomalies of the resonance field exist down to 4.2 K.

Figure 7 shows the $H_{\perp}-T$ phase diagram obtained from the data of the resonance and magnetic measurements. The dashed line corresponds to a transition from the paramagnetic state to the magnetically ordered state 2. It is clear from the phase diagram that the absence of low-temperature anomalies of the resonance parameters at frequency 56.59 GHz is due to the fact that at $T=4.2$ K the CuB_2O_4 crystal is already found in state 2, since the resonance field corresponding to this frequency, $H\approx 18$ kOe, is higher than the critical value $H_{c\perp}=12$ kOe. In addition, analysis of the resonance and magnetic data have shown[14] that at the transition from state 2 to state 1 the magnetic moments of the copper ions remain in the basal plane, but the spontaneous magnetic moment vanishes. In this study we have made the assumption that a helicoidal (modulated) magnetic structure is realized in the low-temperature state 1 of CuB_2O_4. A helicoidal magnetic structure in the low-temperature state of CuB_2O_4 is evidenced by the absence of angular dependence of the resonance parameters in the basal plane in fields below $H_{c\perp}$ and the presence of angular dependence in fields above $H_{c\perp}$ (Fig. 8). For a simple helix in the absence of external magnetic field the local antiferromagnetic vectors are distributed uniformly over all directions in the basal plane. An external magnetic field deforms the helix, transforming it into a fan structure in which the antiferromagnet vectors are distributed within a sector with angular size α. If the value of α is comparable to the period of the tetragonal angular dependence, $\pi/2$, then averaging over all the local positions will

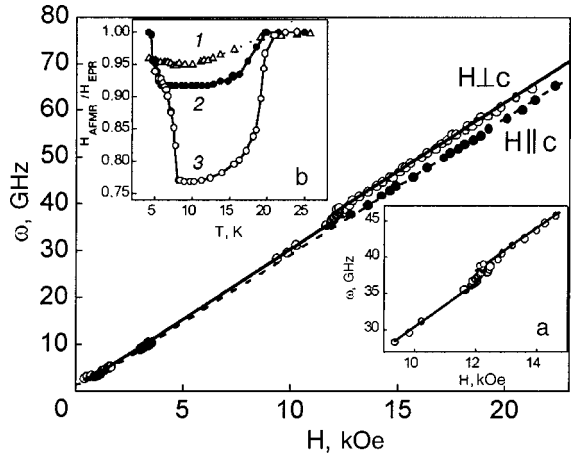

FIG. 6. Frequency–field curves of the magnetic resonance at $T=4.2$ K for $\mathbf{H}\|\mathbf{c}$ and $\mathbf{H}\perp\mathbf{c}$. Inset "a" shows a fragment of the frequency–field curve for $\mathbf{H}\perp\mathbf{c}$. Inset "b" shows the temperature dependence of the resonance field for frequencies ω [GHz]: 56.59 (*1*), 28.65 (*2*), 10.6 (*3*).

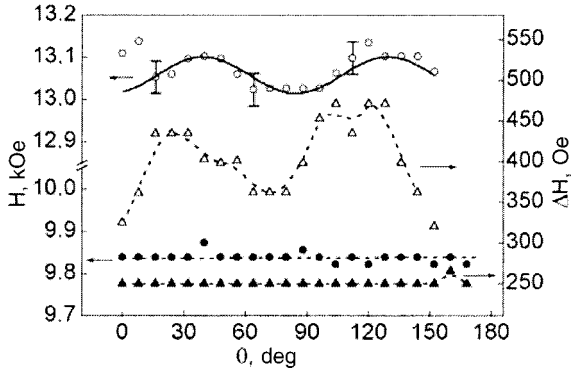

FIG. 8. Angular dependence of the resonance field and of the linewidth in the tetragonal plane at $T=4.2$ K and frequencies [GHz]: 41.51 (○,△); 29.008 (●,▲).

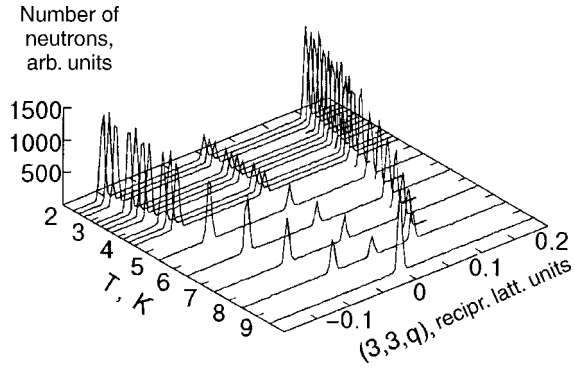

FIG. 9. Temperature dependence of the position of the magnetic satellites $(3,3,0+q)$ and $(3,3,0-q)$.

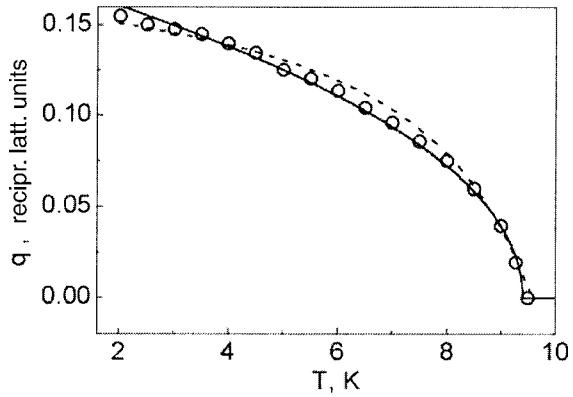

FIG. 10. Temperature dependence of the wave vector q of the incommensurate structure. The solid curve was constructed from the power law (1), and the dashed curve is the result of modeling by the method of the phenomenological thermodynamic potential.

lead to the absence of angular dependence of the resonance parameters in the basal plane.

To investigate the magnetic structure of copper metaborate CuB_2O_4 in various regions of the phase diagram, neutron diffraction studies were done on a single crystal grown with the boron isotope ^{11}B to reduce the neutron absorption.[10,13,15]

The intensities of some of the Bragg peaks, especially those of the forbidden reflections (110) or (002), increase with decreasing temperature in the region 10–20 K, indicating that an antiferromagnetic structure is realized in CuB_2O_4 in this temperature interval. In reciprocal lattice space such a structure is described by a propagation vector $\mathbf{q}=0$, so that the magnetic and crystal-chemical cells coincide. In this state the magnetic moments of the Cu(b) and Cu(d) ions are ordered differently: at $T=12$ K the magnetic moments of the ions equal about $1\mu_B$ per atom for Cu(b) and about $0.25\mu_B$ for Cu(d). A detailed description of the magnetic structure of CuB_2O_4 in state 2 will be given below.

In the temperature region below T_I magnetic satellites appear near the magnetic peaks on the neutronogram of CuB_2O_4; these satellites are located at symmetric positions with respect to the reciprocal lattice points of the commensurate phase (Fig. 9). Here the magnetic structure of copper metaborate becomes incommensurate along the tetragonal axis of the crystal and is described by a spin-density wave with phase modulation.[10] The period of the spin modulation increases continuously from $q\approx 0$ near 10 K to $q=(0,0,0.15)$ at a temperature of 1.8 K (Fig. 10). At this temperature the modulation of the spin structure is characterized by a period $c/0.15\approx 40$ Å. The temperature dependence of the magnitude of the wave vector of the incommensurate phase of the spin structure obeys a power law:

$$q(T)=A(T_I-T)^{0.5}. \tag{1}$$

Relation (1) gives a good description of the temperature dependence of the wave vector of the incommensurate phase throughout the investigated temperature range (the solid curve in Fig. 10).

In a fitting of the magnetic structure at $T=2$ K the best agreement is obtained for a simple helix with a magnetic moment $0.7\mu_B$ for Cu(d).

A strong diffuse scattering superimposed on the Bragg peaks for neutron scattering vector Q_0 along the crystallographic direction [001]. The intensity of the diffuse scattering increases as the temperature is increased from 1.8 K and reaches a maximum value near the temperature T_I (Ref. 10). The diffuse scattering is observed even at the lowest temperature reached in the experiment. This behavior differs markedly from the usual behavior of the spin subsystem of three-dimensional magnets with localized spins, for which critical fluctuations are limited to a small temperature region near the phase transition.

In addition to the first-order magnetic satellites corresponding to the wave vector **q** of the helix, higher-order satellites, the position of which corresponds to a wave vector 3**q**, appear on the magnetic neutronogram near the temperature T_I of the phase transition from the incommensurate to the commensurate structure (Fig. 11).[10]

The strong diffuse scattering of neutrons and the appearance of higher harmonics of the magnetic satellites near the temperature T_I attest to the fact that the modulated structure is a lattice of magnetic solitons. Unlike a simple helix, such a magnetic structure can be represented in the form a helix with a nonconstant spatial rate of change of the phase of the modulation. If one moves along the **z** axis along the helix, there will be regions of slow variation of the phase, which can be attributed to domains, and regions of rapid variation—domain walls. This character of the modulation of the magnetic structure is due to magnetic anisotropy in the tetragonal plane of the crystal.

The neutron results presented above were obtained in the absence of an applied magnetic field. However, on the curves

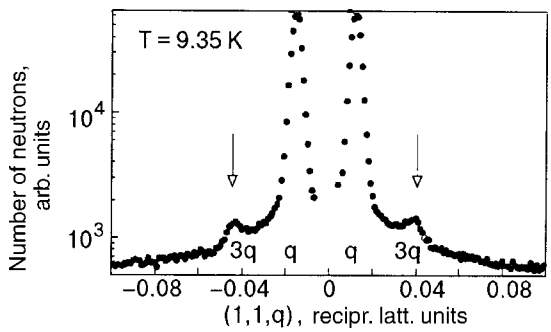

FIG. 11. Principal magnetic satellites $(1,1,q)$ and $(1,1,-q)$ and their higher harmonics at $T=9.35$ K.

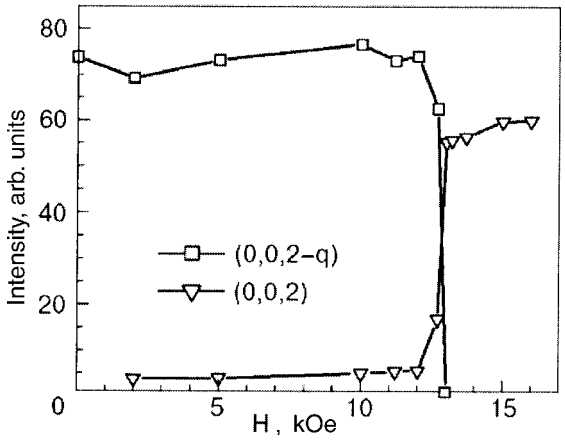

FIG. 12. Field dependence of the intensity of the reflections (0,0,2) and $(0,0,2-q)$ in copper metaborate at $T=4.2$ K.

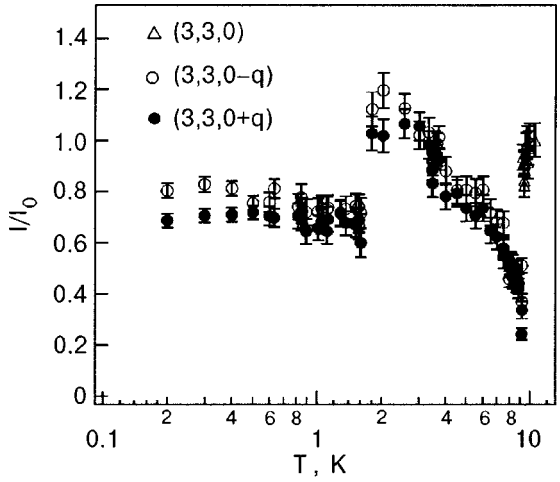

FIG. 13. Temperature dependence of the intensity of the magnetic reflections in copper metaborate.

of the field dependence of the magnetization measured in a temperature interval 10–20 K in a magnetic field applied in the tetragonal plane of the crystal (Fig. 3), one observes a kink, the critical field of which increases with increasing temperature. Thus in this temperature interval in low fields there exists a transition from state 2 to a state 3 (see Fig. 7) in which there is no spontaneous magnetic moment. We assume that in this state the magnetic structure will also be modulated, but the modulation vector is considerably smaller than the resolving power of neutronography, so that it is impossible to distinguish between states 2 and 3 by neutron scattering.

Neutron-scattering studies[15] done at $T=4.2$ K in the presence of a magnetic field of up to 15 kOe applied in the tetragonal plane confirmed that a transition from an incommensurate to a commensurate phase occurs at a field of around 13 kOe. It is seen in Fig. 12 that in the transition region there is a certain interval of fields in which on the neutronogram the central peak (0,0,2), characteristic for the high-field commensurate phase, coexists with a magnetic satellite $(0,0,2-q)$, which belongs to the incommensurate state. Thus the transition in field from the incommensurate phase 1 to the commensurate phase 2, in contrast to the analogous transition in temperature in the absence of magnetic field, is a first-order transition. This conclusion is confirmed by the field dependence of the wave vector of the helix, which decreases in a jump to zero when the magnetic field reaches the critical value 13 kOe. It should also be noted that in the presence of a magnetic field of 10 kOe the higher harmonics of the magnetic satellites are observed throughout the temperature region in which the incommensurate state exists and not only near the phase transition temperature, as in the experiment with no magnetic field.

Neutron diffraction studies of the magnetic structure of CuB_2O_4 have also been done in the low-temperature region,[13] where anomalies of the μSR and heat capacity are observed. It was found that the magnetic satellites are observed down to temperatures of ~ 0.2 K, i.e., the magnetic structure remains incommensurate, and no anomalies of the temperature dependence of the wave vector of the structure are observed in this region. However, the temperature dependence of the intensity of the magnetic satellites $(3,3,0-q)$ and $(3,3,0+q)$ at a temperature of 1.8 K exhibits a downward jump of approximately 40% (Fig. 13). This indicates that the magnetic structure at 1.8 K undergoes a transformation, the nature of which is not yet understood.

DISCUSSION OF THE RESULTS

The set of experimental data presented above indicates that rearrangements of the spin system of copper metaborate occur at temperatures of 20, 10, and 2 K. While the data are insufficient for analysis of the last of these phase transitions, we can draw the following conclusions about the first two.

In the commensurate phase 2 the magnetic structure is that of a weak ferromagnet. The propagation vector $\mathbf{q}=0$ corresponds to a coincidence of the magnetic and crystal-chemical cells. The point group of the crystal is $\bar{4}2m$, which contains eight symmetry elements:[16] 1, $\bar{4}_3^1$, 4_3^2, $\bar{4}_3^3$, 4_1^2, 4_2^2, m_4, and m_5. At $\mathbf{q}=0$ this group has five irreducible representations. Four of them, Γ_1, Γ_2, Γ_3, and Γ_4, are one-dimensional, and one of them, denoted Γ_5, is two-dimensional. The decomposition of the representation for copper metaborate gives $\Gamma_{4b}=\Gamma_1+\Gamma_2+2\Gamma_5$, and $\Gamma_{8d}=\Gamma_1+2\Gamma_2+2\Gamma_3+\Gamma_4+3\Gamma_5$. The magnetic modes $S_{b1z}+S_{b2z}$ and $S_{b1z}-S_{b2z}$, which correspond, respectively, to the representations Γ_2 and Γ_1 of the $4b$ position, permit one to describe the ferromagnetic or antiferromagnetic ordering along the tetragonal axis **c**. The modes associated with the representation Γ_5, viz., $(S_{b1x}+S_{b2x},-S_{b1y}-S_{b2y})$ and $(S_{b1y}-S_{b2y},S_{b1x}-S_{b2x})$, describe a noncollinear magnetic structure in the tetragonal plane. For the $8d$ positions the magnetic modes are:

Γ_1: $S_{d1x}+S_{d2y}-S_{d3x}-S_{d4y}$;

Γ_2: $S_{d1y}-S_{d2x}-S_{d3y}+S_{d4x}$ and

$S_{d1z}+S_{d2z}+S_{d3z}+S_{d4z}$;

Γ_3: $S_{d1y}+S_{d2x}-S_{d3y}-S_{d4x}$ and

$S_{d1z}-S_{d2z}+S_{d3z}-S_{d4z}$;

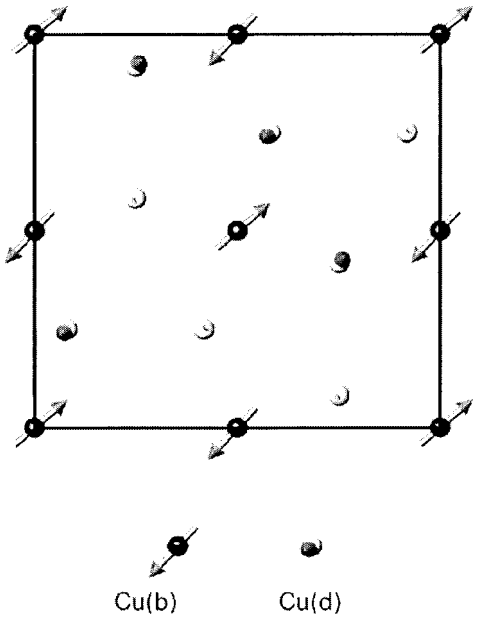

FIG. 14. Antiferromagnetic structure of copper metaborate in the commensurate state: Cu(b) and Cu(d) are represented by the dark and light symbols, respectively.

$$\Gamma_4: \quad S_{d1x}-S_{d2x}-S_{d3y}+S_{d4y};$$

$$\Gamma_5: \quad (S_{d1x}+S_{d3x}, -S_{d2y}-S_{d4y}),$$

$$(S_{d2x}+S_{d4x}, -S_{d1y}-S_{d3y}) \text{ and}$$

$$(S_{d2z}-S_{d4z}, S_{d1z}-S_{d3z}).$$

Analysis of the neutron diffraction pattern,[10] including 25 purely magnetic peaks, showed that the spins of both Cu(b) and Cu(d) of copper metaborate form a noncollinear magnetic structure (Fig. 14). In the spin subsystem of Cu(b) the antiferromagnetic vector in the tetragonal plane is dominant, and the vectors orthogonal to it—the ferromagnetic vector in the tetragonal plane and the antiferromagnetic vector along the **c** axis—are relatively small. In the spin subsystem of Cu(d) the antiferromagnetic vector along the **c** axis is dominant, and the orthogonal antiferromagnetic vector in the tetragonal plane is relatively small. The ferromagnetic vector in the plane is not detected within the experimental error limits. The magnetic moment of Cu(d) in the commensurate phase is much smaller than the magnetic moment of Cu(b). All of the vectors listed can be matched up with magnetic modes obtained from a symmetry analysis. It should be noted once again that, in spite of the fact that the magnetic structure presented is based on analysis of the neutron diffraction data obtained in the temperature range 10–20 K in the absence of an applied magnetic field, it corresponds to the state 2 induced by a small magnetic field on the phase diagram of Fig. 7. This conclusion is confirmed by the data of Ref. 13, in which a refinement of the magnetic structure was done at $T=12$ K in a magnetic field of 400 Oe applied in the tetragonal plane. In accordance with the phase diagram, this field is sufficient to induce a transition of the crystal to state 2 at a temperature of 12 K.

In the incommensurate phase 1 at $T<10$ K the magnetic structure is ordered in the form of a helix. For theoretical analysis of the magnetic properties of copper metaborate by the method of the phenomenological thermodynamic potential it is important that there is no center of inversion $\bar{1}$ among its symmetry elements. It enters only in combination with a 90° rotation about the **c** axis: $\bar{4}_3^1$ and $\bar{4}_3^3$. Therefore, it is permissible for the thermodynamic potential to contain an invariant of the Lifshitz type bilinear in the two-component order parameter and its spatial derivative.

In Ref. 17 such properties of a crystal as the temperature dependence of the wave vector of the modulation of the magnetic structure and heat capacity were analyzed in the framework of a phenomenological approach. The thermodynamic potential was written in the form of a functional of two two-component order parameters, (η_{A1}, η_{A2}) and (η_{B1}, η_{B2}):

$$\Phi = \int \left\{ \frac{\alpha_A}{2}\eta_A^2 + \frac{\beta_A}{4}\eta_A^4 + \frac{\gamma_A}{4}\eta_A^4\cos(4\varphi_A) \right.$$
$$+ \frac{\delta_A}{2}[(\nabla\eta_A)^2 + \eta_A^2(\nabla\varphi_A)^2] - \sigma_A\eta_A^2\varphi_A' + \frac{\alpha_B}{2}\eta_B^2$$
$$+ \frac{\beta_B}{4}\eta_B^4 + \frac{\gamma_B}{4}\eta_B^4\cos(4\varphi_B) + \frac{\delta_B}{2}[(\nabla\eta_B)^2$$
$$\left. + \eta_B^2(\nabla\varphi_B)^2] - \sigma_B\eta_B^2\varphi_B' + \kappa\eta_A\eta_B\cos(\varphi_A-\varphi_B) \right\} dV, \tag{2}$$

where

$$\alpha_A = \alpha_{A0}(T-T_A), \quad \alpha_B = \alpha_{B0}(T-T_B),$$

$$\eta_A^2 = \eta_{A1}^2 + \eta_{A2}^2, \quad \varphi_A = \arctan(\eta_{A2}/\eta_{A1}),$$

$$\eta_B^2 = \eta_{B1}^2 + \eta_{B2}^2, \quad \varphi_B = \arctan(\eta_{B2}/\eta_{B1}),$$

$\alpha_{A0}>0$, $\alpha_{B0}>0$, $\beta_A>0$, $\beta_B>0$, $\delta_A>0$, $\delta_B>0$, ∇ is the del operator, and $f' \equiv df/dz$. Both parameters transform according to the representation Γ_5, and they differ by a linear combination of magnetic modes transforming according to this representation. The parameter η_A is associated with the transition at 20 K and, according to the magnetic and neutron-diffraction data given above, consists primarily of the modes $(S_{b1x}+S_{b2x}, -S_{b1y}-S_{b2y})$ and $(S_{b1y}-S_{b2y}, S_{b1x}-S_{b2x})$. The description of the helical magnetic structure below 10 K is achieved by including in the thermodynamic potential a Lifshitz invariant constructed from the two-component parameter η_B. The presence in (2) of other order parameters is not decisive for the description of the evolution of the states in copper metaborate as the temperature is lowered from the paramagnetic phase above 20 K to the incommensurate phase below 10 K.

The analysis is done in the approximation of a constant modulus of the order parameter, which is suitable for the case when the Lifshitz invariants and the invariants of the anisotropy and the interaction between subsystems are relatively small in comparison with the remaining invariants.

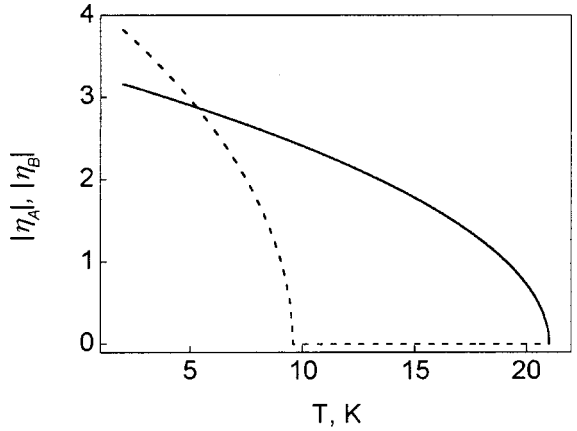

FIG. 15. Modeled temperature dependence of the moduli of the order parameters: $|\eta_A|$ (solid curve) and $|\eta_B|$ (dashed curve).

The resulting relations can be used to model the temperature dependence of η_A, η_B and the wave number $q=2\pi/\lambda$ (the dashed curve in Fig. 10), and, with the aid of the standard relation $C_p=-T\partial^2\Phi/\partial T^2$, the temperature dependence of the specific heat $c_p=C_p/V$ of the crystal for the following parameters of the thermodynamic potential:

$$\alpha_A=1.6(T-20),\quad \beta_A=2.7,\quad \gamma_A=0,$$

$$\delta_A=0.16,\quad \sigma_A=0,\quad \kappa=0.01,$$

$$\alpha_B=4(T-9.6),\quad \beta_B=2,\quad \gamma_B=0.01,$$

$$\delta_B=0.16,\quad \sigma_B=0.1.$$

The values of the parameters are given in kelvins. As we see from Fig. 15, in the temperature region 10–20 K the order parameter η_B is small compared to η_A and it increases rapidly with decreasing temperature below 10 K. The analogous growth of the wave vector $q\equiv 2\pi/\lambda$ in Fig. 10 agrees with the experimentally observed behavior (Figs. 9 and 10) but differs qualitatively in that q is nonzero already at temperatures below 20 K: in the temperature region where the invariants of the anisotropy are small compared with the Lifshitz invariants, it it equal to

$$q\approx\sigma/\delta,\quad \text{where}\quad \delta=\delta_A\eta_A^2+\delta_B\eta_B^2,\quad \sigma=\sigma_A\eta_A^2+\sigma_B\eta_B^2,$$

and for $\sigma_A=0$ it varies basically in the same way as η_B.

In calculating the heat capacity we took into account not only the jump (described by Landau theory) at the transition and the Ginzburg estimate for the contribution of thermal fluctuations of the order parameter but also the contributions of acoustic phonons and anomalies of the Schottky type. At a temperature of 20 K the fluctuation contribution inherent to a second-order phase transition, with a maximum at the transition point is dominant. The experimental curves of the temperature dependence of the heat capacity of a CuB_2O_4 single crystal (Fig. 4) have a step-like feature at 9.6 K. It is due to the rapid growth of the order parameter in the second spin subsystem, which is nonzero already at temperatures below 20 K because of the bilinear interaction with the first subsystem. The field induced by this interaction suppresses the thermal fluctuations in the second subsystem. For this reason the latter were not taken into account in the calculation. We note that the step at 9.6 K is observed against the background of a broad maximum that increases with decreasing temperature; this maximum can be attributed to a Schottky-type anomaly not described in the phenomenological approach. The deviation of the experimental from the calculated dependence of the heat capacity as the temperature is lowered below 3.5 K is due to the approach to the transition near 2 K.

Thus a comprehensive set of experimental and theoretical studies has shown that in the temperature region 10–20 K the CuB_2O_4 crystal has a long-period modulated magnetic structure with a small propagation vector along the tetragonal axis of the crystal. Under the influence of a weak (less than 1 kOe) magnetic field applied in the tetragonal plane, a transition occurs to a commensurate noncollinear magnetic structure that is formed by two subsystems of copper ions and is characterized by the presence of a spontaneous magnetic moment. Below 10 K the magnetic structure of this compound is an incommensurate soliton lattice with a propagation vector directed along the tetragonal axis of the crystal.

This study was supported by the Russian Foundation for Basic Research, Grant 01-02-17270.

*E-mail: pank@iph.krasn.ru

[1] G. Petrakovskii, K. Sablina, A. Pankrats, A. Vorotinov, A. Furrer, B. Roessli, and P. Fischer, J. Magn. Magn. Mater. **140–144**, 1991 (1995).
[2] G. A. Petrakovskiĭ, K. A. Sablina, A. M. Vorotynov, A. I. Kruglik, A. G. Klimenko, A. D. Balaev, and S. S. Aplesnin, Zh. Éksp. Teor. Fiz. **98**, 1382 (1990) [Sov. Phys. JETP **71**, 772 (1990)].
[3] G. A. Petrakovskiĭ, Izv. Vyssh. Uchebn. Zaved. Fiz., No. 1, 91 (1998).
[4] A. M. Vorotynov, A. I. Pankrats, G. A. Petrakovskiĭ, K. A. Sablina, V. Pashkovich, and G. Shimchak, Zh. Éksp. Teor. Fiz. **113**, 1866 (1998) [JETP **86**, 1020 (1998)].
[5] G. A Petrakovskii, K. S. Aleksandrov, L. N. Bezmaternikh, S. S. Aplesnin, B. Roessli, F. Semadeni, A. Amato, C. Baines, J. Bartolome, and M. Evangelisti, Phys. Rev. B **63**, 184425 (2001).
[6] G. A. Petrakovskiĭ, K. A. Sablina, A. I. Pankrats, D. A. Velikanov, A. D. Balaev, O. A. Bayukov, V. I. Tugarinov, A. M. Vorotynov, A. D. Vasil'ev, G. V. Romanenko, and Yu. G. Shvedenkov, Fiz. Tverd. Tela (St. Petersburg) **44**, 1280 (2002) [Phys. Solid State **44**, 1339 (2002)].
[7] Yu. A. Izyumov, *Neutron Diffraction on Long-Period Structures* [in Russian], Énergoatomizdat, Moscow (1987).
[8] I. E. Dzyaloshinskiĭ, Zh. Éksp. Teor. Fiz. **47**, 992 (1964) [Sov. Phys. JETP **20**, 665 (1965)].
[9] G. A. Petrakovskiĭ, K. A. Sablina, D. A. Velikanov, A. M. Vorotynov, N. V. Volkov, and A. F. Bovina, Kristallografiya **45**, 926 (2000) [Crystallogr. Rep. **45**, 853 (2000)].
[10] B. Roessli, J. Shefer, G. Petrakovskii, B. Ouladdiaf, M. Boehm, U. Staub, A. Vorotinov, and L. Bezmaternikh, Phys. Rev. Lett. **86**, 1885 (2001).
[11] G. Petrakovskii, D. Velikanov, A. Vorotinov, A. Balaev, K. Sablina, A. Amato, B. Roessli, J. Schefer, and U. Staub, J. Magn. Magn. Mater. **205**, 105 (1999).
[12] G. A. Petrakovskiĭ, A. D. Balaev, and A. M. Vorotynov, Fiz. Tverd. Tela (St. Petersburg) **42**, 313 (2000) [Phys. Solid State **42**, 321 (2000)].
[13] M. Boehm, B. Roessli, J. Shefer, B. Ouladdiaf, A. Amato, C. Baines, U. Staub, and G. Petrakovskii, Physica B (2002) (in press).
[14] A. I. Pankrats, G. A. Petrakovskiĭ, and N. V. Volkov, Fiz. Tverd. Tela (St. Petersburg) **42**, 93 (2000) [Phys. Solid State **42**, 96 (2000)].
[15] J. Shefer, M. Boehm, B. Roessli, G. Petrakovskii, B. Ouladdiaf, and U. Staub, Appl. Phys. A: Solids Surf. (2002) (in press).
[16] O. V. Kovalev, *Irreducible and Induced Representations and Corepresentations of Fedorov Groups* [in Russian], Nauka, Moscow (1986).
[17] G. A. Petrakovskii, M. A. Popov, B. Roessli, and B. Ouladdiaf, Zh. Éksp. Teor. Fiz. **120**, 926 (2001) [JETP **93**, 809 (2001)]

Translated by Steve Torstveit

Phase transformations of the decomposition type in systems with orbital degeneracy

M. A. Ivanov

Institute of Metal Physics, National Academy of Sciences of Ukraine, pr. Vernadskogo 36, 03680 Kiev-142, Ukraine

N. K. Tkachev

Institute of High-Temperature Electrochemistry, Urals Branch of the Russian Academy of Sciences, ul. S. Kovalevkoĭ 20, 620219 Ekanterinburg, Russia

A. Ya. Fishman*

Institute of Metallurgy, Urals Branch of the Russian Academy of Sciences, ul. Amundsena 101, 620016 Ekaterinburg, Russia

(Submitted November 1, 2001; revised January 2, 2002)
Fiz. Nizk. Temp. **28**, 850–859 (August–September 2002)

The immiscibility phase diagrams of systems exhibiting the cooperative Jahn–Teller effect are investigated. It is found that the Jahn–Teller mechanism of interaction between ions is capable of describing the main topologically different types of immiscibility phase diagrams in quasibinary systems. [DOI: 10.1063/1.1511705]

1. INTRODUCTION

It is known from the theory of phase equilibria that phase transforms of the first or second order (structural, magnetic, spin-reorientation, and other types) in multicomponent systems are accompanied by the appearance of two-phase regions on the temperature–concentration phase diagram (see, e.g., Ref. 1). For example, upon any substitutions in a system with a first-order structural phase transition, a coexistence region of phases with high and lowered symmetries is immediately formed.[2] The phase diagrams of mixed condensed systems with limited solubility of the components are characterized by great topological diversity. The problem of their microscopic description and the identification of the mechanisms responsible for the characteristic features of the diagrams remains topical to this day. In this connection, crystalline systems containing Jahn–Teller (JT) centers are ideal objects for modeling the various phase transformations in systems with cooperative interactions. The JT mechanism of interparticle interaction is responsible for phase transformations to the JT glass phase,[3,4] structural transitions with ferro- and antiferrodistortive ordering,[5] and transitions of the spin-reorientation type.[6,7] It can also be considered established that stabilization effects due to the splitting of degenerate states of ions in the field of the surrounding charges will lead to separation (decomposition) of mixed condensed systems (see, e.g., Refs. 8–10).

The problem addressed in the present study is to describe the topologically distinct immiscibility phase diagrams. Here the same model should be usable for analysis of several phase transformations at once: structural, spin-reorientation, and decomposition.

An extremely simple model for describing a region of limited solubility in JT systems was used in Refs. 9, 11, and 12. There, in a calculation of the free energy of the JT subsystem, the three lowest vibronic levels corresponding to minima of the adiabatic potential of ions with an E term in the ground state were taken into account. Tunnel splitting effects were assumed to be negligible against the background of the splittings of these levels by the cooperative JT interaction. The parameters of this model are the constants of the linear and harmonic interaction of the degenerate center with the JT deformations. The temperature of the structural phase transition, the tetragonal JT deformation in the low-temperature phase, and the values of the jumps of the order parameter and enthalpy at the structural phase transition were expressed in terms of those parameters. However, this model has proven to be less than fully adequate for describing another kind of system in which the character of the phase transformations can change when the JT ions are replaced by orbitally nondegenerate ions or by JT ions of a different species.

It is therefore of interest to clarify whether it is possible to describe topologically different immiscibility phase diagrams in the framework of a rather simple model that takes into account only the JT interaction in the system. For treating the JT subsystem we use the model proposed by Kanamori,[5] in which the harmonic interactions are treated as relatively weak compared to the JT interactions proper. In such a model one can describe both first-and second-order structural phase transitions. In that case, in systems with JT ordering of the ferrodistortive type it is the anharmonic interactions that determine the value of the jump-like changes of the order parameter at a first-order phase transition. With a suitable choice of JT constants for the initial compound it should be possible to describe all of the investigated immiscibility phase diagram even without adjustable fitting parameters. The effectiveness of this approach has been confirmed in our analysis[13] of experimental data for the crystals $Mn_{3-x}Al_xO_4$ and $Mn_{3-x}Cr_xO_4$.

In the present paper we focus our attention on an analysis of the conditions for the appearance of topologically different immiscibility phase diagrams in crystalline systems containing $3d$ ions and having degenerate or quasi-

degenerate ground states. We consider quasibinary systems in which the JT ion are replaced by orbitally nondegenerate ions or by other JT ions. It is shown that a simple microscopic model that takes into account the various JT interactions in the system turns out to be sufficient for describing several types of phase transformations at once: structural, spin-reorientation, and decomposition. It is found that the JT mechanism of interparticle interaction permits description of the great diversity of immiscibility phase diagrams, at least in systems of the quasibinary type, and many of the results obtained here can be used for qualitative analysis of the experimental phase diagrams with phase separation, not only for substances with JT ions but also for other mixed condensed systems.

2. MODEL OF STRUCTURAL PHASE TRANSITIONS BROUGHT ABOUT BY THE COOPERATIVE JAHN–TELLER EFFECT

The simplest model description of structural phase transformations in a cooperative JT system was proposed by Kanamori.[5] According to Ref. 5, the Hamiltonian of the JT subsystem of a cubic crystal with a structural phase transformation of the ferro type can be written in the form

$$H=\sum_s (\lambda\langle\sigma_s^z\rangle+Ve+p\Omega Ke^2)\sigma_s^z, \tag{1}$$

for an E term $\sigma_s^z\begin{pmatrix}-1 & 0\\ 0 & 1\end{pmatrix}$,

for a T term $\sigma_s^z=\begin{pmatrix}-1 & 0 & 0\\ 0 & 1/2 & 0\\ 0 & 0 & 1/2\end{pmatrix}$,

where λ is the molecular field parameter, σ_s^z is the orbital (pseudospin) operator defined in the space of ground state functions at site s (a doublet for an E term or a triplet for a T term); V is the interaction constant of the JT ions with the uniform strain $e\equiv e_{JT}=e_{zz}-(e_{xx}+e_{yy})/2$; p is the anharmonic interaction parameter, Ω is the volume of the crystal per orbitally degenerate ion; K is the "bare" elastic modulus describing the elastic energy of the crystal for a strain $e\equiv e_{JT}$ in the absence of the JT subsystem; the summation is over all degenerate ions with indices s. The molecular field parameter λ in (1) is determined by all types of intercenter interactions that depend on the orbital state of the ions except for the interaction via the uniform JT deformation [the second term in (1)]. Singling out that term can be justified only in the case of JT ferroelastics, where for given concentrations of JT ions it is known beforehand that a ferrodistortive phase forms in the process of ordering at low temperatures. In diluted JT systems with competing interactions the use of Hamiltonian (1) inevitably leads to physically incorrect results (see Ref. 3).

The free energy of the system per JT ion in the absence of effects of substitution of the JT ions is described by the following expression:

$$F_{JT}=F_0-k_BT\ln\left(\sum_i \exp\left\{-\frac{E_i}{k_BT}\right\}\right), \tag{2}$$

$$F_0=\frac{1}{2}K\Omega e^2+p_1K\Omega e^3,$$

where k_B is Boltzmann's constant, T is the absolute temperature, E_i is the energy of splitting of the degenerate levels by the cooperative interaction, F_0 is the elastic energy of the crystal due to the strain $e\equiv e_{JT}$, and p_1 is the parameter of the anharmonic interaction with the strains in the crystal in the absence of orbital degeneracy.

For the sake of brevity, unless otherwise stipulated, we shall from now on consider the case of a ground orbital doublet. Then

$$F_{JT}=\frac{1}{2}K\Omega e^2+p_1K\Omega e^3 - k_BT\ln\left(2\cosh\frac{\lambda\langle\sigma^z\rangle+Ve+p\Omega Ke^2}{k_BT}\right). \tag{3}$$

The minimum of the free energy (3) is reached at the equilibrium value of the uniform strain $e_{\rm eq}$, which is determined by the equation

$$z=\frac{1+2pz}{1+3p_1z}\tanh\frac{z+\nu z(1+3p_1z)(1+2pz)^{-1}+pz^2}{t},$$

$$\nu=\lambda K\Omega/V^2. \tag{4}$$

Here we have introduced the relative strain $z=e_{\rm eq}/e_0$ ($e_0=V/(K\Omega)$ is the strain at $T\to 0$ K) and the dimensionless temperature $t=k_BT/Ve_0=K\Omega k_BT/V^2$.

In the absence of anharmonicity (for $p=p_1=0$) this model for JT ions with a twofold degenerate ground state describes a second-order structural phase transition. For $p\neq 0$ the phase transition occurs by a first-order transformation, and the jumps in entropy ΔS, enthalpy ΔH, and tetragonal JT deformation Δe turn out to be larger for larger absolute values of the anharmonicity parameter. Figure 1 shows how the temperature and entropy of the structural transition and the order parameter z depend on the value of the anharmonic interaction.

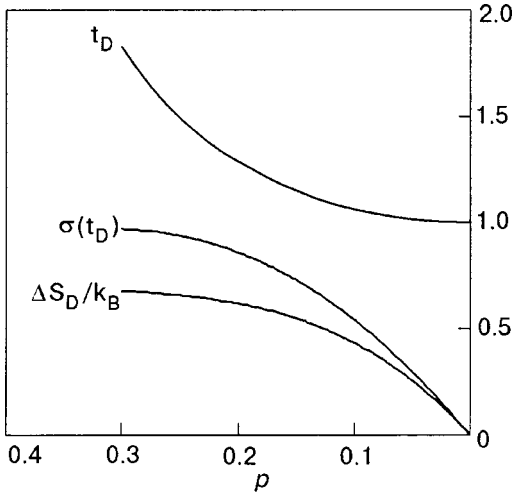

FIG. 1. Dependence of the transition temperature t_D, transition entropy $\Delta S_D/k_B$, and jump of the order parameter $\sigma(t_D)=z(t_D)/[1+2pz(t_D)]$ on the value of the anharmonicity parameter p.

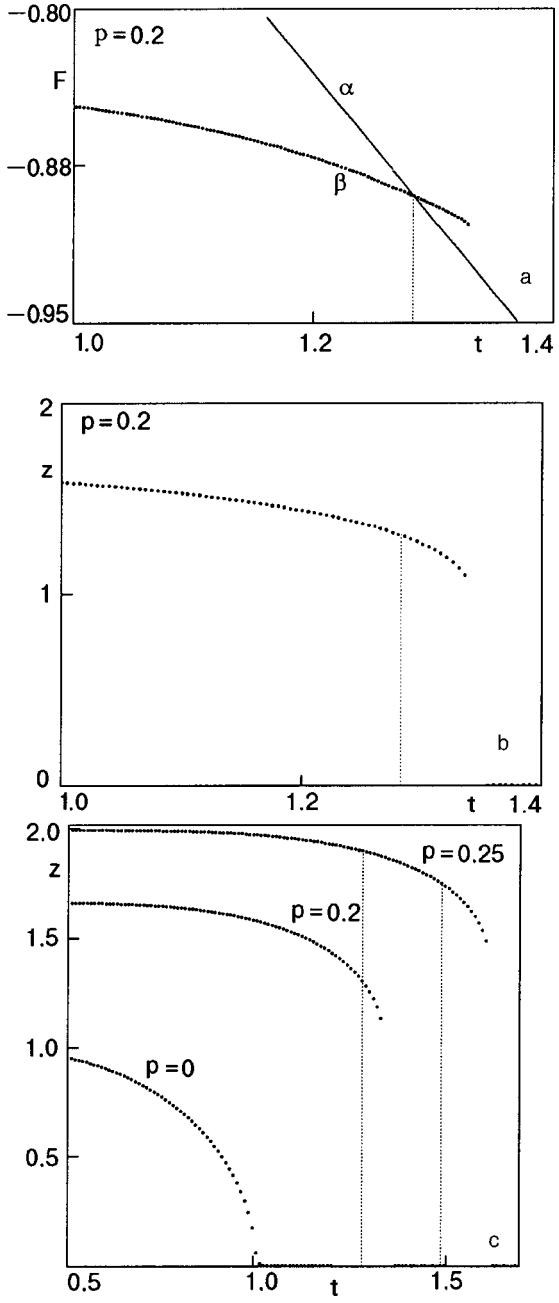

FIG. 2. Temperature dependence of the free density (a) (α is the cubic and β the tetragonal phase) and of the tetragonal JT deformation (b, c).

A characteristic feature of the model of a cooperative JT effect of the ferro type (see Fig. 2) is the presence of a rather large existence region of the metastable ''superheated'' tetragonal state with $z \neq 0$ in the temperature region above the temperature T_D of the structural transition.

In systems with threefold degenerate JT ions an effect of the ferro type occurs as a first-order phase transformation independently of whether one-center anharmonic interactions proportional to the parameters p and p_1 are present in the system.[5]

3. QUASIBINARY SYSTEMS WITH SUBSTITUTION OF JT IONS BY ORBITALLY NONDEGENERATE IONS

The generalization of the Kanamori model to the case of quasibinary systems $A_{X_{JT}}B_{1-X_{JT}}$ (X_{JT} is the concentration of JT ions in the solution) does not present any difficulties. In this approximation one can treat multicomponent solid solutions in which substitution occurs only in the sublattice of the JT ions.

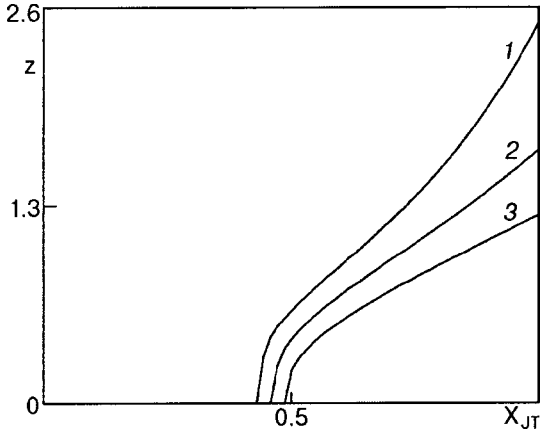

FIG. 3. Concentration dependence of the JT deformation at a fixed temperature $t=0.5$ and different values of $p=0.3$ (*1*), 0.2 (*2*), and 0.1 (*3*).

The contribution of the splitting effect of degenerate centers to the free energy F of the solid solution should obviously be proportional to their concentration X_{JT} in the quasibinary system. Here the free energy F includes the configurational contribution, which can be approximated as an ideal solution. As a result, when the JT ions are replaced by orbitally nondegenerate ions we have

$$F = Ve_0 f, \quad f = f_{JT} + f_{id}, \tag{5}$$

$$f_{JT} = \frac{z^2}{2} - X_{JT} t \ln\left(2\cosh\frac{z+pz^2}{t}\right)$$

$$z = X_{JT}(1+2pz)\tanh\frac{z+pz^2}{t}$$

$$f_{id} = -t[X_{JT}\ln X_{JT} + (1-X_{JT})\ln(1-X_{JT})], \tag{6}$$

where $X_{JT} = N_A/N$, with N being the total number of cations in the sublattice under consideration ($N = N_A + N_B$), N_A and N_B are the numbers of Jahn–Teller ions (A) and substituent ions (B), respectively. For simplicity and to reduce the number of parameters of the theory, the quantities ν and p_1 in (5) are assumed equal to zero.

In analyzing the free energy F and its various derivatives, we first solved Eq. (4), which describes the composition dependence and temperature dependence of the tetragonal JT deformation $e_{eq} = ze_0 = zV/(K\Omega)$. The concentration dependence of the equilibrium JT deformation and of the free energy of solution calculated with the use of expressions (5) and (6) for a quasibinary system with a random distribution of mixed ions is shown in Figs. 3 and 4. The free energy curves clearly display the regions of ''concavity'' which are characteristic of systems that undergo phase separation, and the width of these regions increases with decreasing temperature.

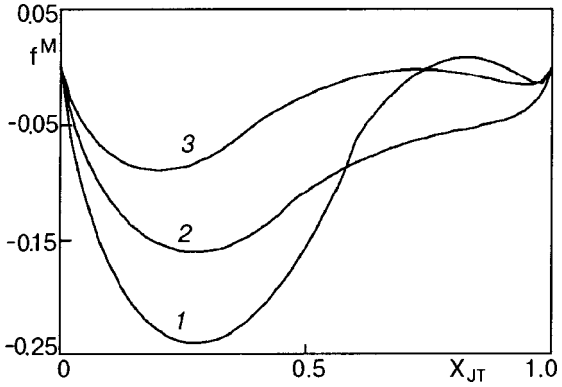

FIG. 4. Concentration dependence of the free energy of mixing $f^M = f(X_{JT}) - X_{JT}^{f(1)} - (1-X_{JT})^{f(0)}$ for $p=0.1$ and temperatures $t=0.4$ (*1*), 0.5 (*2*), and 0.75 (*3*).

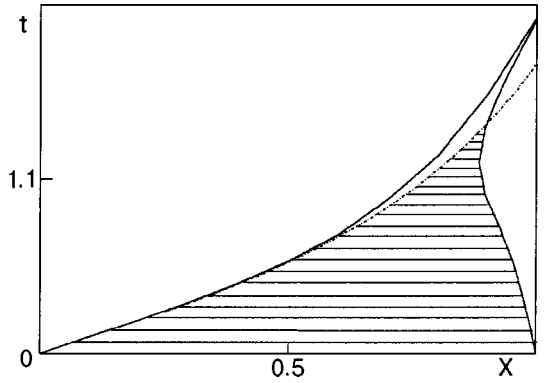

FIG. 5. Boundaries of the region of absolute (spinodal) instability of the system for a value of the anharmonicity parameter $p=0.3$. The solid curves show the upper boundary of the existence region of the metastable tetragonal phase and the branch of the spinodal curve corresponding to Eq. (8). The dotted curve shows the concentration dependence of the temperature of the structural phase transition. The shaded area is the region of absolute instability of the solid solution.

Region of absolute instability of a solid solution

Expressions (5) and (6) can be used to calculate the chemical potentials μ_A and μ_B of the components and the exchange chemical potential μ_{ex} of a quasibinary solid solution:[14]

$$\mu_{ex} = \frac{\partial F}{\partial X_{JT}} \equiv \mu_A - \mu_B, \tag{7}$$

$$\frac{\mu_{ex}}{k_B T} = -\ln\left(2\cosh\frac{z+pz^2}{t}\right) + \ln\left(\frac{X_{JT}}{1-X_{JT}}\right),$$

$$\mu_A = F + (1-X_{JT})\mu_{ex}$$

$$\frac{\mu_A}{k_B T} = \frac{z^2}{2t} - \ln\left(2\cosh\frac{z+pz^2}{t}\right) + \ln X_{JT}.$$

The spinodal (absolute) instability of the solid solution is determined by the equation[2]

$$\frac{\partial^2 F}{\partial X_{JT}^2} = \frac{\partial \mu_{ex}}{\partial X_{JT}} = 0, \ \rightarrow \tag{8}$$

$$t - (1+2pz)[X_{JT}(1+2pz)^2 - z^2] = 0.$$

It is clear that the spinodal curve should lie completely in the low-symmetry tetragonal phase. Then the formal solution of equation (8) can belong to both the regions of the equilibrium and metastable ''superheated'' tetragonal states. The latter solution for $X_{JT} \rightarrow 1$ tends toward the upper boundary of the existence region of the ''superheated'' low-symmetry phase of the pure compound. As a result, for $X_{JT} \rightarrow 1$ there occurs a crossing of the tetra branch of the spinodal with the curve of the concentration dependence of the temperature of the structural phase transitions of the solid solution. The typical shape of the region of absolute (spinodal) instability of a solution is shown in Fig. 5. It is seen that, unlike systems with a second-order structural phase transition, the apex of the region of spinodal instability of the solution does not coincide with a critical point of lines of phase decomposition.

Configuration of the two-phase region

The binodals, the boundaries of the phase coexistence region, are determined by the standard system of equations—equality of the chemical potentials of the components, $\mu_A(t, X_{JT}, z)$ and $\mu_B(t, X_{JT}, z)$, in the low- and high-symmetry crystalline states. To these two equations we must add Eq. (4) for the tetragonal deformation z of the lattice at $T < T_D$, so that the total system of equations for calculating the two branches of the binodal, $X_\alpha(t)$ and $X_\beta(t)$, take the form

$$\begin{cases} \mu_A(t, X_\alpha, 0) = \mu_A(t, X_\beta, z_\beta), \\ \mu_B(t, X_\alpha, 0) = \mu_B(t, X_\beta, z_\beta), \\ z_\beta = X_\beta(1+2pz_\beta)\tanh[(z_\beta + pz_\beta^2)/t]. \end{cases} \tag{9}$$

The binodals calculated for systems with different values of the parameter p are shown in Fig. 6. In the case of a second-order structural phase transition ($p=0$) the phase-separation region is dome-shaped, with a tricritical point (1/3,1/3) on the $t - X_{JT}$ phase diagram. Above the temperature $t=1/3$ a complete mixing of the components occurs. For $p \neq 0$ the

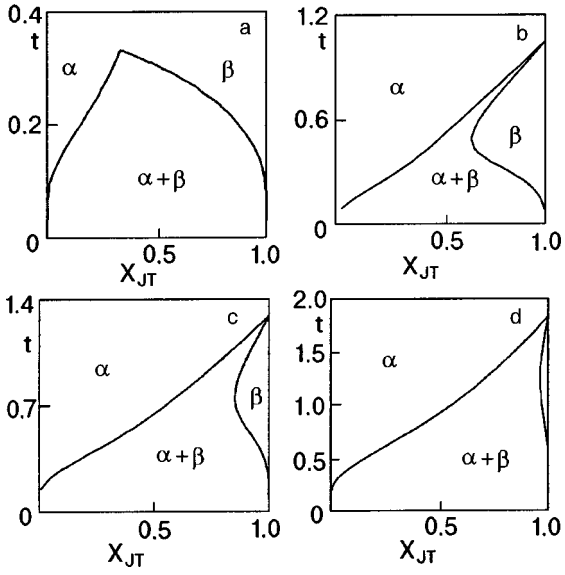

FIG. 6. Phase diagrams for mixed JT systems. The calculated binodals correspond to different values of the anharmonicity parameter p: 0 (a), 0.1 (b), 0.2 (c), 0.3 (d). The indices α and β refer to the cubic and tetragonal phases, respectively.

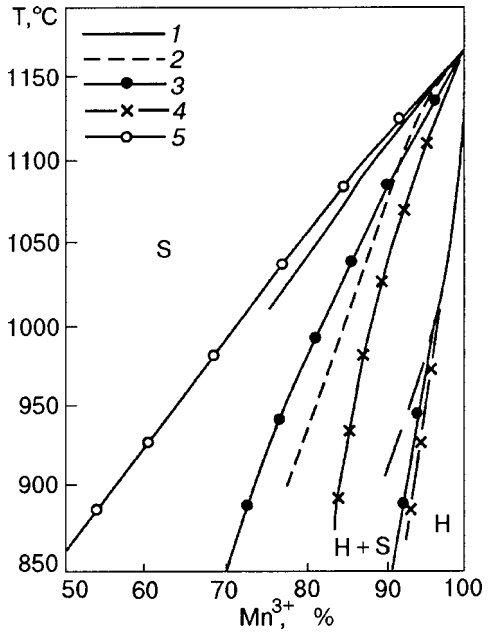

FIG. 7. Experimental phase diagrams as functions of the concentration of the JT ion Mn^{3+} in the octa positions of the solution $Mn_{3-x}A_xO_4$ (Ref. 15): Mn–Ti–O (*1*), Mn–Al(Cr)–O (*2*), Mn–Co–O (*3*), Mn–Ni–O (*4*), Mn–Mg–O (*5*). S is the spinel (cubic) phase, H is the Hausmannite phase with tetragonal Jahn–Teller deformation of the crystal lattice, and H+S is the two-phase region.

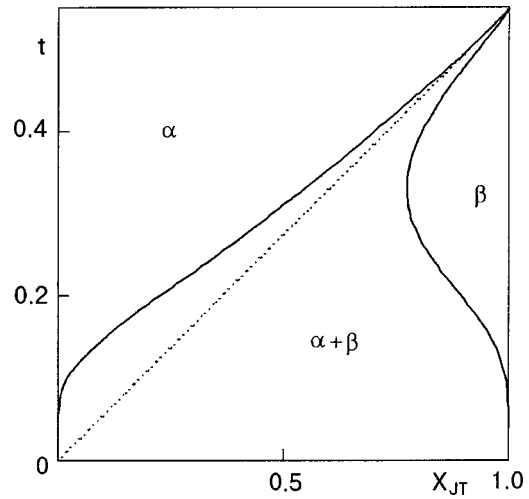

FIG. 8. Theoretical phase diagram for systems containing JT ions with a three-fold degenerate ground state. The dotted line is a line of phase transitions in a single-phase system with randomly distributed ions; α and β are the cubic and tetragonal phases, respectively.

diagram takes the typical form for systems with a first-order structural phase transition. It is seen that the two-phase coexistence region of the cubic and tetragonal phases widens with increasing $|p|$, while the region of homogeneity of the tetra phase narrows considerably. We also note the specific (retrograde) configuration of the boundary of the tetra phase.

The model considered here enables one to describe the corresponding fragments of the phase diagrams of multicomponent systems containing JT ions. Examples of such diagrams for oxides of the form $Mn_{3-x}A_xO_4$ with the spinel structure are presented in Fig. 7.[15]

The typical phase diagram of systems containing JT ions with a threefold degenerate ground state is shown in Fig. 8. We consider only the case $p_1=p=0$, when the region of the metastable tetragonal state is extremely narrow, and the entropy of the transition is a quantity of the order of $\Delta S \approx 0.23k_B$.

4. QUASIBINARY SYSTEMS WITH SUBSTITUTION OF ONE KIND OF JT IONS BY ANOTHER

Let us now analyze the behavior of mixed crystalline systems in which one type of JT ion is replaced by another, i.e., by JT ions with different parameters of the Hamiltonian (1). For simplicity we restrict discussion to a change of only one parameter for the new JT ions, viz., the anharmonicity parameter, which we denote by p_2. Then the limiting compositions of the JT systems with $X=0$ and $X=1$ differ at least in respect to the temperatures of the structural phase transformations. This is seen, in particular, from the Landau expansion for the free energy in the case of comparatively small values of the anharmonicity parameters:

$$t_D = t_D^0\{1+6[p_1 - pX - (1-X)p_2]^2\}, \tag{10}$$

where $t_D^0=1$ is the temperature of the second-order structural phase transition in a system with negligibly small anharmonicity parameters. The characteristic of the JT deformation at these compositions remains the same only when p and p_2 are of the same sign. If the signs of the parameters p and p_2 in the JT subsystem are different, then a configurational anisotropy arises, and, as a consequence, there can be a phase transition of the spin-reorientation type with the onset of a canted phase.[6]

The free energy and chemical potentials of the ions to be mixed in such systems with a chaotic distribution of atoms are described, in analogy with (7), by the expressions

$$\frac{\mu_A}{k_BT} = -\ln\left(\cosh\frac{z+pyz^2}{t}\right) + \ln X,$$

$$\frac{\mu_B}{k_BT} = -\ln\left(\cosh\frac{z+p_2yz^2}{t}\right) + \ln(1-X),$$

$$\frac{\mu_{ex}}{k_BT} = -\ln\left(\cosh\frac{z+pyz^2}{t} \Big/ \cosh\frac{z+p_2yz^2}{t}\right) + \ln\frac{X}{1-X},$$

$$F = X\mu_A + (1-X)\mu_B, \quad y=\cos 3\varphi,$$

$$\cot\varphi = \frac{2e_{zz}-e_{xx}-e_{yy}}{\sqrt{3}(e_{xx}-e_{yy})}, \tag{11}$$

where the quantity y determines the character of the resultant JT deformation of the crystal. The parameter y, unlike the examples considered earlier, can turn out to be unequal to ± 1. The corresponding equations for determining the equilibrium values of the order parameters z and y have the form

$$1+3p_1zy - X\frac{1+3pzy+2(pz)^2}{E(z,y)}\tanh\left(\frac{E(z,y)}{t}\right)$$

$$-(1-X)\frac{1+3p_2zy+2(p_2z)^2}{e(z,y)}\tanh\left(\frac{e(z,y)}{t}\right)=0,$$

$$p_1 - \frac{Xp}{E(z,y)}\tanh\left(\frac{E(z,y)}{t}\right) - \frac{(1-X)p_2}{e(z,y)}\tanh\left(\frac{e(z,y)}{t}\right)=0,$$

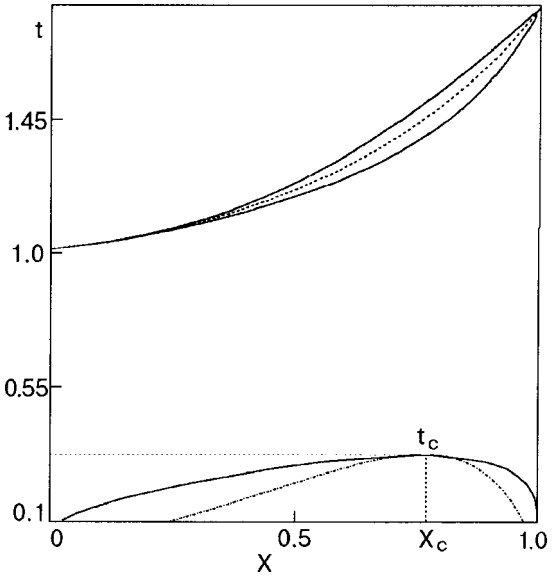

FIG. 9. Phase diagram of a quasibinary JT system in the absence of competing anisotropy ($p=0.3$, $p_2=0.5$, $p_1=0$). The dashed line in the upper part of the diagram is a line of structural phase transitions in a system with a random distribution of two types of JT ions. The dot-and-dash line in the lower part of the diagram shows the curve of absolute—spinodal—instability of the system.

$$E(z,y)=z\sqrt{1+2pyz+(pz)^2},$$

$$e(z,y)=z\sqrt{1+2p_2yz+(p_2z)^2}. \tag{12}$$

The boundaries of the phase states are determined by the standard equilibrium conditions—equality of the chemical potentials of the atoms in the coexisting phases.

Immiscibility in the absence of competing interactions

Of course, the simplest form of the immiscibility phase diagrams obtains in the case of identical types of deformations at the JT ions being mixed together. A typical phase diagram is shown in Fig. 9. We see that the two-phase region has a cigar-shaped form in the high-temperature region of the diagram and a dome-shaped form in the low-temperature region. Here the region of the low-temperature spinodal instability can be described to good approximation by the expression

$$t_s=4X(1-X)(p-p_2)^2[1-2(Xp+(1-X)p_2)]^{-3}. \tag{13}$$

The apex of the spinodal and dome of phase decomposition in the low-temperature region coincide (at the critical point t_c, X_c).

Another form of phase diagram, different from Fig. 9, obtains when the critical temperature of the limiting compositions with $X=0$ and $X=1$ are very different (by an order of magnitude or more). In that case, with decreasing transition temperature of one of the components of the ''cigar'' initially becomes wider and then it crosses with the rising dome. In the asymptotic limit $t_D(0)/t_D(1)\to 0$ this diagram corresponds to the case of the dilution of a JT system by nondegenerate ions (see Fig. 6).

Immiscibility in systems with competing interactions

A characteristic feature of mixed JT systems with competing anharmonic interactions is the formation of a so-called intermediate or canted phase.[6,7] It is of interest to elucidate how such states transform under conditions when phase decomposition can occur. Let us consider for simplicity a solution with two types of JT ions, differing only in the sign of the anharmonicity parameters: $p_2=-p$. In such a

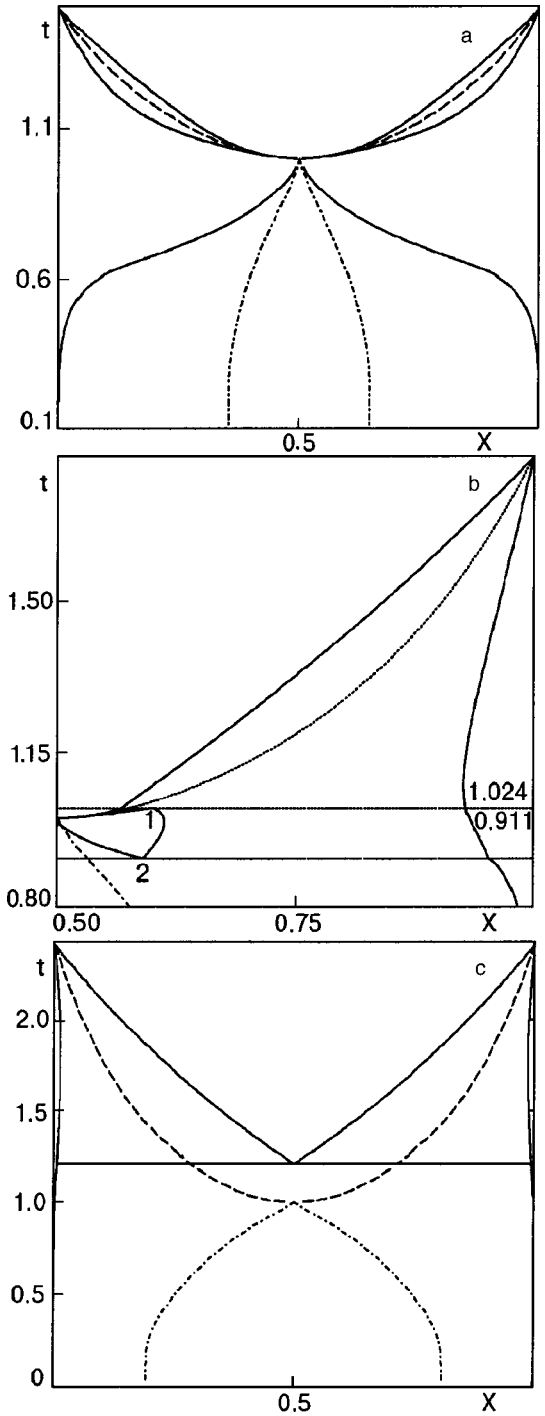

FIG. 10. Phase diagrams of a quasibinary JT system with competing anisotropy: $p=0.25$ (a), 0.3 (b), 0.35 (c). The solid curves are phase boundaries. The dashed curve in the upper part of the diagram shows a line of structural phase transitions in a system with a random distribution of two types of JT ions. The dot-and-dash line in the lower part of the diagram is the boundary of the canted phase. Numbers 1 and 2 denote points of three-phase equilibrium.

system with a random distribution of JT ions the line of first-order structural phase transformations has a parabolic shape, and the vertex of the parabola ($t_c=1, X_c=1/2$) is the critical point, where a second-order structural phase transition occurs. Here, at temperatures in the region below the critical temperature $t \leqslant t_c=1$, i.e., in the ferrodistortive phase, there occur (second-order) phase transitions of the spin-reorientation type from states with $y=-1$ (at $X<1/2$) or $y=1$ (for $X>1/2$) to an intermediate (in the respect to the type of distortion) phase with $|y| \neq 1$.

Typical phase diagrams for these systems are shown in Fig. 10. It is seen how the topology of the phase states and, in particular, the shape of the immiscibility regions are altered as the anharmonicity parameter p is varied. The single-phase regions of orbital ordering on the left-hand side of the diagrams correspond to values $y=-1$ and those on the right, to $y=1$. The cigar-shaped two-phase regions in the upper parts of the diagrams represent equilibria of the para–ferro type (cubic and tetragonal phases of a ferroelastic). In the lower part of the diagram the two-phase regions are associated mainly (''a'' and ''c'' completely, and ''b'' partially) with the equilibrium between ferrodistortive states with different types of tetragonal distortion, i.e., $y=-1$ and $y=1$.

It is interesting to note that the canted phase of a solid solution with a random distribution of JT ions always lies inside the region of the two-phase state of the system, where phases with angular parameters $y=1$ and $y=-1$ coexist. In other words, in the equilibrium state the decomposition of the solution is preferable to the formation of a canted phase. It is expected that in systems where, because of kinetic limitations the equilibrium state is not realized, the tendency toward decomposition should be manifested in the formation of complexes with a higher concentration of one or the other of the constituents of the mixture in the corresponding concentration intervals.

The segment of the phase diagram with $p=0.3$ (Fig. 10b) illustrates the specifics of the transition of the topology of the phase diagram from one type to another: from azeotropic to eutectic. It is seen that in a comparatively narrow temperature interval near $t_c=1$ there are new two-phase and three-phase equilibria of the ferro–ferro and para–ferro–ferro types in each half of the phase diagram ($X \geqslant 1/2$ and $X \leqslant 1/2$). Accordingly, additional points of three-phase equilibria are manifested both above and below $t_c=1$. These features of the phase diagrams can be understood from the concentration dependences of the exchange chemical potential and free energy of a solid solution with a random distribution of ions (Figs. 11 and 12).

Near the critical point ($X=1/2$, $t=1$) one can expand the thermodynamic potential in a series in the order parameters and find the character of the critical temperature dependence of the difference of the concentrations in the coexisting phases. Thus for the lines of equilibrium of the cubic $X_\beta(t)$ and tetragonal $X_\alpha(t)$ phases at temperatures $t>t_c=1$ we have the following temperature dependence of the concentration difference $\delta(t)=X_\alpha(t)-X_\beta(t)$ (the order parameter for the decomposition phase transitions):

$$\delta(t) \cong 3^{3/2} 2^{-1/2} p (t-1)^{3/2}. \tag{14}$$

Analogous temperature dependence of the concentration difference in the coexisting phases, $\sim(1-t)^{3/2}$, is also observed for the equilibrium of two low-temperature phases ($t<t_c$) with different signs of the tetragonal deformations. Thus the character of the critical behavior of the order parameter $\delta(t)$ near the point ($X=1/2$, $t=1$) differs substantially from the conventional linear temperature dependences of the order parameter for decomposition phase transitions near critical temperatures (temperatures of structural phase transformations of systems with $X=0$ and $X=1$).[2]

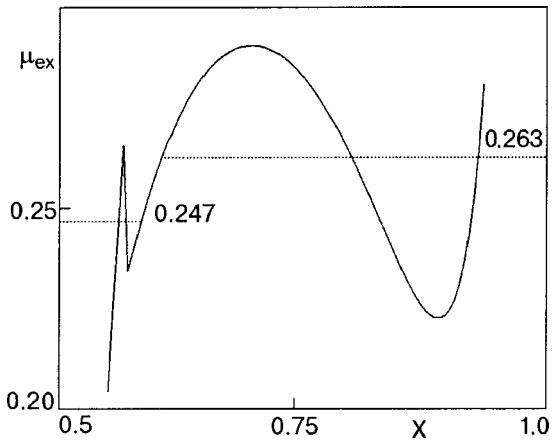

FIG. 11. Concentration dependence of the exchange potential at a temperature $t=1.0175$. The dotted line shows the Maxwell construction for the boundaries of the phase decomposition region.

5. CONCLUSION

The analysis in this paper has shown that the phenomenon of limited solubility is a characteristic property of degenerate systems, and the JT model of cooperative intercenter interactions enables one to describe a wide class of immiscibility phase diagrams. We have established that the topological features of the decomposition phase diagrams in JT and other similar crystalline systems are determined by anisotropic, anharmonic interactions. It is clear that the introduction of asymmetry in the framework of the model of JT systems with competing anisotropy permits description of all the basic types of immiscibility phase diagrams for qua-

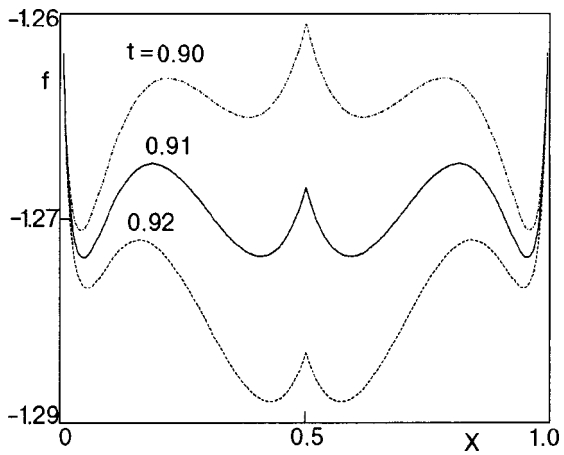

FIG. 12. Concentration dependence of the free energy of a solid solution at temperatures $t=0.9$, 0.91, and 0.92; $y=1$ for $X>1/2$ and $y=-1$ for $X<1/2$.

sibinary systems. We have also shown that the so-called canted phases in systems with competing anisotropy can correspond only to a metastable state of the solution, since its decomposition into phases with opposite types of dominant anisotropy is thermodynamically favorable. We have described the possible types of two- and three-phase states of the solution, involving para and ferro phases of differing concentration. Thus the model developed can become a basis for calculating the phase equilibria in complex systems containing $3d$ ions with different electronic structure, charge, and character of the distribution over nonequivalent positions.

The presence of degenerate or pseudodegenerate states can lead to limited-solubility effects even in systems with topological disorder. However, in them the mechanism responsible for the splitting of the degenerate $3d$ states is radially different from that considered previously for crystals with the cooperative effect. For example, in the case of solutions with different types of $3d$ ions in an anionic environment it is due to the random (and fluctuating in time) deviation of the configuration of the nearest-neighbor anion environment of the $3d$ ion from the high-symmetry configuration. As a result, the stabilization of the electronic states and the character of the phase diagram should be determined by the random fields and the concentration dependence of their dispersion. Nevertheless, for both types of solutions (crystalline with the cooperative JT effect and molten) the presence of degenerate states can stimulate phase decomposition.

The authors are grateful to K. Yu. Shunyaev and Yu. V. Golikov for interest in this study and helpful discussions.

This work was done with the financial support of the Russian Foundation for Basic Research (Project No. 00-03-32335).

*E-mail: fishman@r66.ru

[1] M. A. Krivoglaz, *Theory of X-Ray and Thermal Neutron Scattering by Real Crystals*, Plenum Press, New York (1969), Naukova Dumka, Kiev (1984); M. A. Krivoglaz and A. A. Smirnov, *The Theory of Order-Disorder in Alloys*, Macdonald, London (1964), Fizmatgiz, Moscow (1958).
[2] L. D. Landau and E. M. Lifshitz, *Statistical Physics*, 3rd ed., Pergamon Press, Oxford (1980), Nauka, Moscow (1976).
[3] M. A. Ivanov, V. Ya. Mitrofanov, and A. Ya. Fishman, Fiz. Tverd. Tela (Leningrad) **20**, 3023 (1978) [Sov. Phys. Solid State **20**, 1744 (1978)].
[4] F. Mehran and K. W. H. Stevens, Phys. Rev. B **27**, 2899 (1983).
[5] J. Kanamori, J. Appl. Phys. **31**, 14S (1960).
[6] M. Kataoka and J. Kanamori, J. Phys. Soc. Jpn. **32**, 113 (1972).
[7] K. I. Kugel' and D. I. Khomskiĭ, Usp. Fiz. Nauk **136**, 621 (1982) [Sov. Phys. Usp. **25**, 231 (1982)].
[8] S. Krupicka, *Physics of Ferrites and Related Magnetic Oxides* [Russian translation from Czech], Vol. 1, Mir, Moscow (1976).
[9] P. Holba, M. A. Khilla, and S. Krupicka, J. Phys. Chem. Solids **34**, 387 (1973).
[10] M. A. Ivanov, N. K. Tkachev, and A. Ya. Fishman, Fiz. Nizk. Temp. **25**, 616 (1999) [Low Temp. Phys. **25**, 459 (1999)].
[11] R. G. Zakharov, S. A. Petrova, N. K. Tkachev, A. Ya. Fishman, and K. Yu. Shunyaev, Zh. Fiz. Khim. **74**, 871 (2000).
[12] A. Ya. Fishman, M. A. Ivanov, and N. K. Tkachev, *NATO Science Series. Mathematics, Physics and Chemistry*, Vol. 39, Kluwer Academic Publishers, Dordrecht-Boston-London (2001), p. 183.
[13] M. A. Ivanov, V. L. Lisin, N. K. Tkachev, and K. Yu. Shunyaev, Zh. Fiz. Khim. **76**, 719 (2002).
[14] I. Prigogine and R. Defay, *Chemical Thermodynamics* Longmans, London (1962), Nauka, Novosibirsk (1966).
[15] V. F. Balakirev, V. P. Barkhatov, and Yu. V. Golikov S. G. Maĭzel', *Manganites: Equilibrium and Unstable States* [in Russian], Izd. UrO RAN, Ekaterinburg (2000).

Translated by Steve Torstveit

Possibility of formation and reversible rearrangement of equilibrium domain structure in antiferromagnets

E. V. Gomonay*

National Technical University of Ukraine "Kiev Polytechnical University," pr. Peremogi 37, 03056 Kiev, Ukraine

V. M. Loktev**

National Technical University of Ukraine "Kiev Polytechnical University," pr. Peremogi 37, 03056 Kiev, Ukraine; N. N. Bogolyubov Institute of Theoretical Physics, National Academy of Sciences of Ukraine, ul. Metrologicheskaya 14b, 03143 Kiev, Ukraine

(Submitted January 8, 2002)
Fiz. Nizk. Temp. **28**, 860–871 (August–September 2002)

It is shown that the magnetoelastic interaction can play a substantial role in the formation of the equilibrium domain structure in antiferromagnets having two or more equivalent easy directions of the axis of magnetic anisotropy. It is demonstrated with the use of the methods of nonlinear theory of elasticity in the framework of a phenomenological model that the surface of the crystal can and does serve as a source of fictitious ''elastic charges'' of incompatibility, which have consequences analogous to those of the magnetostatic charges that arise on the surface of ferromagnetic crystals and lead to the formation of domains. Here the surface of the crystal is treated as a special phase with its own magnetic, elastic, and magnetoelastic properties. The field of the ''elastic charges'' is long-ranged, and, accordingly, its contribution to the stray (''detwinning'') energy, which plays the main role in the formation of the equilibrium domain structure, is proportional to the volume of the sample rather than its surface area. The formation of the domain structure is nothing more than the restoration of the initial global symmetry of the crystal in those cases when the phase transformation that breaks this symmetry is described by an order parameter which is conjugate to the shear strain. The conditions for the absence of ''elastic charges'' inside the sample impose certain restrictions on the morphology of the magnetoelastic domain structure in antiferromagnets. It is shown how the character of the equilibrium state of the crystal is influenced by disclinations arising at places where three or more domains come together. [DOI: 10.1063/1.1511706]

1. INTRODUCTION

The problem of the origin and description of the domain structure in antiferromagnetic (AFM) crystals has a long history (starting with the work of Néel[1]) and has been discussed repeatedly in the literature (see, e.g., Refs. 2–5). This problem is intimately related to the problem of the origin of domain walls in materials in which the phase transitions are accompanied by the onset of spontaneous shear strains, the tensor of which has the same symmetry as the primary order parameter (the so-called ferroelastic or thermoelastic transitions). Ordinarily at such a transition the spontaneous strains appear simultaneously with the reorganization of the electronic structure of the material (as, e.g., in martensitic phase transformations) or with the onset of a vector/tensor order parameter of a magnetic, polarization, or other nature.

In the case when there are several crystallographically equivalent directions for the vector that is the primary order parameter, so that the strain tensor is also degenerate, the domain structure is in a state of thermodynamic equilibrium and changes reversibly under the influence of an external magnetic field and/or mechanical stresses. External fields can also bring the sample completely into a single-domain state, but the domain structure will nevertheless be restored after the field is removed.

The nature of the equilibrium domain structure in ferro- and ferrimagnets with opposite directions of the magnetization vectors in adjacent domains, has been studied for a long time and in detail (see, e.g., Ref. 6); its formation is attributed to the finite size of the sample and to demagnetizing effects due to the formation of fictitious magnetic charges on the surface of the sample (or at an interface of two media with different magnetic properties). However, for magnetic media that do not have an uncompensated magnetic moment (e.g., AFMs) or materials with vanishingly small spontaneous magnetizations (weak ferromagnets) the origin of the experimentally observed[7–10] equilibrium domain structure essentially remains an open question.

In Refs. 11 and 12 we proposed a possible mechanism for the formation of the equilibrium domain structure, based on surface effects: it was proposed that the change in the shape of the sample due to the onset and rearrangement of the domain structure leads to a lowering of the surface energy. Despite the extremely good qualitative and quantitative agreement with the experimental results from measurements of the magnetostriction of the easy-plane AFM $CoCl_2$ in an

external magnetic field,[7] the region of applicability of this model is limited to crystals of sufficiently small size or to samples with a well-developed surface (such as films), for which surface effects can play a substantial role.

In this paper we attempt to generalize the results obtained previously[11,12] and to show that the formation of a thermodynamically equilibrium domain structure in the course of a thermoelastic (ferroelastic) phase transition can be explained by the influence of a rather rigid (slightly deformable) surface of the crystal and, what is particularly important, that the corresponding contribution to the energy of the sample depends on its volume and not on the surface area, and for this reason the domain formation is independent of the size of the crystal.

It is a great honor for us to dedicate this article to the outstanding Ukrainian experimental physicist Prof. V. V. Eremenko, whose contributions to the physics of low temperatures, magnetic phenomena, and magnetooptics and, in particular, to the development of methods of visualizing the domain structure in magnetic media (see, e.g., Refs. 3, 13, and 14) are widely known and universally acknowledged.

2. MODEL

Consider a sample having a volume V and bounded by a surface of area S. We assume that at a temperature above the temperature of the magnetic phase transition the sample is unstressed and unstrained. Below the critical temperature the crystal lattice becomes unstable with respect to the onset of spontaneous strains induced by fluctuations of the primary order parameter (the magnetization, polarization, etc.). The spontaneous strains, as in the case of martensitic phase transformations and transitions to an AFM state, may also be due to nonlinear elastic effects. We emphasize that in both cases there are no demagnetizing effects.

In an unbounded sample the spatial distribution of the spontaneous strain tensor $\hat{u}(\mathbf{r})$, where $\mathbf{r}$ is the radius vector of a given point, is described by an equation obtained from the condition that the elastic (and magnetoelastic) energy $f_{\text{elas}}(\hat{u})$ of the crystal be minimum with respect to the variable $\hat{u}$:

$$\frac{\partial f_{\text{elas}}(\hat{u})}{\partial \hat{u}(\mathbf{r})} = 0. \tag{1}$$

Equation (1) is equivalent to the condition that there be no internal forces: $\operatorname{div}\hat{\sigma}(\mathbf{r}) = 0$, where $\hat{\sigma}$ is the stress tensor. Furthermore, in the analysis of the equilibrium elastic state in terms of the strain tensor it is necessary to consider an additional condition—the compatibility of the strains in the absence of internal defects.[1)] In the approximation of the linear theory of elasticity the condition of compatibility can formally be written as the condition that a certain tensor vanish (see, e.g., Ref. 15):

$$\eta(\mathbf{r}) \equiv -\operatorname{curl}(\operatorname{curl}\hat{u}(\mathbf{r}))^T = 0,$$
$$\eta_{il} = -e_{ijk}e_{lmp}\nabla_j\nabla_m u_{kp}, \tag{2}$$

where e_{ijk} is the Levi-Civita symbol, and the operation T corresponds to transposition. In a homogeneous unbounded crystal the elastic energy density $f_{\text{elas}}(\hat{u})$ is independent of the spatial derivatives of the strain tensor, and as a result the equilibrium strains are also uniform, and condition (2) is trivially satisfied.

The situation changes radically in the presence of a surface, which is specified in parametric form by the equation $\mathbf{r} = \mathbf{r}_S$. The surface of the crystal has special elastic, magnetic, and magnetoelastic properties different from those of the bulk, and it can be treated as a separate phase.[2)] By virtue of the inhomogeneity that arises in this way, the uniform strains given by Eq. (1) inevitably lead to additional stresses in the crystal. The contribution of the corresponding, purely surface energy to the total energy of the crystal is described by term of the type[16]

$$F_{\text{surf}} = \int dS\left[\alpha_S + \hat{\beta}_S\hat{u}_S(\mathbf{r}_S) + \frac{1}{2}\hat{u}_S(\mathbf{r}_S)\hat{\hat{c}}_S\hat{u}_S(\mathbf{r}_S)\right], \tag{3}$$

where α_S and $\hat{\beta}_S$ are coefficients of surface tension, $\hat{\hat{c}}_S$ is the tensor of the surface elastic constants, and $\hat{u}(\mathbf{r}_S)$ is the surface strain tensor. We note that the first two terms in expression (3) are responsible for the establishment of the equilibrium shape of the sample (corresponding to the minimum surface energy at a fixed volume), and the last term can be important in the analysis of phase transitions accompanied by the onset of spontaneous strains.

Below we shall assume that the properties of the surface of the sample are specified by the preparation process and that the surface itself is rather inert in the sense that it does not relax when external fields are applied and varied. In this model one can eliminate the influence of the surface tension (3), since we are actually assuming that the energy barrier determining the change of the equilibrium shape of the crystal in the presence of spontaneous strains is quite high in comparison with the change of the thermodynamic potential at the phase transition, and the corresponding relaxation time is rather long compared with the characteristic time for rearrangement of the crystal structure. This approximation is justified for transitions to an AFM state by virtue of the smallness of the magnetic energy and the derivatives of the spontaneous strains (the maximum value of the spontaneous strain at a magnetic phase transition is not more than $\approx 10^{-3}$), and also for a series of thermoelastic martensitic transformations occurring at rates close to the sound velocity.

Near the surface the spontaneous strains arising in the course of the thermoelastic phase transition can be written as a sum of three terms:

$$\hat{u}(\mathbf{r}) = \frac{1}{3}\hat{\mathbf{1}}\operatorname{Tr}\hat{u} + \hat{u}_{\text{shear}} + [(\mathbf{n}_S\hat{u})\otimes\mathbf{n}_S + \mathbf{n}_S\otimes(\hat{u}\mathbf{n}_S) - \mathbf{n}_S\otimes\mathbf{n}_S(\mathbf{n}_S\hat{u}\mathbf{n}_S)], \tag{4}$$

where $\hat{\mathbf{1}}$ is the unit matrix, $\mathbf{n}_S$ is the normal to the surface of the crystal at the given point, and the symbol $\otimes$ denotes the direct tensor product of vectors. The first term in (4) describes a relative change in volume which preserves the shape of the sample (isomorphous striction). The three terms in square brackets form the components of the strain tensor corresponding to displacements along the vector normal to the surface, $\mathbf{n}_S$, and the second term, which is made up in such a way that its trace is zero, corresponds to the shear (with respect to S) strains. The first term is important for

describing magnetic phase transitions (it can influence the positions of the transition point) but can be dropped in a treatment of thermoelastic phase transitions, since it is not associated with a change of symmetry of the crystal and, hence, cannot affect the processes of establishment and rearrangement of the domain structure of a magnetoelastic and/or purely elastic origin. For this same reason we can also neglect the last term in (4). Thus, in what follows we shall consider only the shear part of the strain tensor,[3] $\hat{u}_{\rm shear}$, and define the strained state relative to the state with isomorphous striction, which can be taken into account rather trivially.

For the simplest assumption, that of an absolutely rigid surface which does not deform at the phase transition, i.e., for $\hat{\hat{c}}_S=\infty$, the boundary conditions at the surface of the sample reduce to the conditions of the absence of stress,

$$\left\{\frac{\partial f_{\rm elas}(\hat{u})}{\partial \hat{u}}\right\}_{\mathbf{r}\in S}\mathbf{n}_S(\mathbf{r}_S)=0, \tag{5}$$

and the absence of strain,

$$\mathbf{n}_S(\mathbf{r}_S)\times\hat{u}(\mathbf{r}_S)\times\mathbf{n}_S(\mathbf{r}_S)=0,$$
$$e_{ijk}e_{lmp}u_{jm}(\mathbf{r}_S)n_S^k(\mathbf{r}_S)n_S^p(\mathbf{r}_S)=0, \tag{6}$$

which are easily obtained from the definition of the tangential component of the strain tensor. The vector $\mathbf{n}_S(\mathbf{r}_S)$ defines the normal to the surface of the sample at the given point.

Consequently, the problem of establishing the spatial distribution of strains in a sample of specified shape upon the transition through the critical point can be stated as follows: the equilibrium strain field $\hat{u}(\mathbf{r})$ must satisfy Eqs. (1) and (2) in the bulk of the sample ($r\in V\backslash S$) and Eqs. (5) and (6) on its surface ($\mathbf{r}=\mathbf{r}_S\in S$).

At a thermoelastic phase transition or a transition to an AFM state, spontaneous strains inevitably arise in the crystal, breaking its local symmetry. Here the appearance of uniform strains in a sample of arbitrary shape leads to a violation of condition (6), at least at some points of the surface. The only exception is for a sample of a special shape—a very thin disk or slab cut in such a way that the surface of the slab coincides with the plane of the uniform shear.[4]

3. STRAY ENERGY

To elucidate the character of the distribution of the nonuniform strains (e.g., magnetoelastic domains in an AFM) we use an analogy with the well-known problem of the formation of domains in a ferromagnet. We assume that the equilibrium (and, generally speaking, nonuniform) shear strain of the crystal, which satisfies condition (6), consists of two parts:

$$\hat{u}_{\rm shear}(\mathbf{r})=\hat{u}_{\rm ms}(\mathbf{r})+\hat{u}_{\rm ch}(\mathbf{r}). \tag{7}$$

The term $\hat{u}_{\rm ms}(\mathbf{r})$ corresponds to the spontaneous strain, which is due to the transition to a magnetically ordered state, and is determined from the condition of minimum free energy (1). The term $\hat{u}_{\rm ch}(\mathbf{r})$ gives additional strains created by ''elastic charges'' generated by the incompatibility at the surface of the crystal:

$$\hat{e}_{\rm elas}(\mathbf{r})=-\mathbf{n}_S\times\hat{u}_{\rm ms}(\mathbf{r}_S)\times\mathbf{n}_S\delta'[\mathbf{n}_S(\mathbf{r}-\mathbf{r}_S)], \tag{8}$$

where δ' is the derivative of the Dirac delta function with respect to its argument. The function $\hat{u}_{\rm ch}(\mathbf{r})$ is a solution of the equation (the details may be found in Teodosiu's book[15])

$$\mathrm{rot}(\mathrm{rot}\,\hat{u}_{\rm ch}(\mathbf{r}))^T=\hat{e}_{\rm elas}(\mathbf{r}). \tag{9}$$

The particular solution of Eq. (9) has the form

$$\hat{u}_{\rm ch}(\mathbf{r})=\frac{1}{4\pi}\int_V d\mathbf{r}_1\frac{\hat{e}_{\rm elas}(\mathbf{r}_1)-\hat{\mathbf{1}}\,\mathrm{Tr}\,\hat{e}_{\rm elas}(\mathbf{r}_1)}{|\mathbf{r}-\mathbf{r}_1|}$$
$$=\frac{1}{4\pi}\int_S dS\frac{(\mathbf{n},\mathbf{r}-\mathbf{r}_S)}{|\mathbf{r}-\mathbf{r}_S|^3}\hat{\mathbf{U}}(\mathbf{r}_S)=\frac{1}{4\pi}\int d\Omega_{\mathbf{r}}\hat{\mathbf{U}}(\mathbf{r}_S), \tag{10}$$

where $d\Omega_{\mathbf{r}}$ is the element of solid angle under which the surface point $\mathbf{r}_S$ is viewed from the given point $\mathbf{r}$ inside the crystal. The quantity

$$\hat{\mathbf{U}}(\mathbf{r}_S)\equiv\hat{u}_{\rm ms}(\mathbf{r})+\mathbf{n}_S\otimes\mathbf{n}_S\,\mathrm{Tr}\,\hat{u}_{\rm ms}(\mathbf{r})-\mathbf{n}_S\otimes(u'_{\rm ms}(\mathbf{r})\mathbf{n}_S)$$
$$-(\hat{u}_{\rm ms}(\mathbf{r})\mathbf{n}_S)\otimes\mathbf{n}_S$$

introduced in Eq. (10) can be interpreted as a ''charge'' density on the surface of the crystal which creates an additional stress field that leads to twinning [by analogy with ferromagnets, in which the magnetic charges create a stray (''demagnetizing'') field, these stresses may be called stray (''detwinning'') stresses]:

$$\hat{\sigma}(\mathbf{r})=\hat{\hat{c}}\hat{u}_{\rm ch}(\mathbf{r}), \tag{11}$$

where $\hat{\hat{c}}$ is the tensor of elastic constants. The distribution of the equilibrium strains in the presence of an undeformable surface can be found from the equation

$$\frac{\partial f_{\rm elas}(\mathbf{r})}{\partial\hat{u}(\mathbf{r})}=\hat{\hat{c}}\hat{u}_{\rm ch}(\mathbf{r}), \tag{12}$$

which is obtained by combining Eqs. (1) and (11). It is easy to see that Eq. (12) can also be obtained by variation of a free-energy functional with respect to strain tensor components under the condition of compatibility of the strains (2) in the bulk of the sample:[5]

$$\Phi=\int_V d\mathbf{r}f_{\rm elas}(\mathbf{r})-F_{\rm stray}, \tag{13}$$

where we have introduced the stray energy

$$F_{\rm stray}=\frac{1}{4\pi}\int_V d\mathbf{r}\int_S dS\frac{(\mathbf{n},\mathbf{r}-\mathbf{r}_S)}{|(\mathbf{r}-\mathbf{r}_S)|^3}\hat{u}(\mathbf{r})\hat{\hat{c}}\hat{\mathbf{U}}(\mathbf{r}_S), \tag{14}$$

which we did not consider in Refs. 11 and 12.

The approach developed above allows one to solve the complex problem of the equilibrium domain structure in a nonlinear medium in the presence of an external magnetic field in terms of the strain tensor, which, unlike the displacement vector, is an observable quantity and has a symmetry related to the symmetry of the primary order parameter of the phase transition.

Continuing the analogy with the problem of the domain structure of a ferromagnet, we call attention to certain features of the internal twinning fields in thermoelastic crystals. First of all, it follows from formulas (10) and (11) that the ''elastic charges'' due to the incompatibility of the strains on

the surface create additional strains $\hat{u}_{\rm ch}$ and the macroscopic stresses corresponding to them, the value of which will depend substantially on the shape of the sample. The stress field created by these charges, like the Coulomb field, is long-ranged, and therefore its contribution to the energy is proportional to the crystal volume V. Thus the domain-formation effect under consideration is not a surface effect and does not depend on the dimensions of the sample.

Contrary to the case of ferromagnets, for which the fictitious magnetic charges on the surface are scalar quantities, the ''elastic charges'' (including those in an AFM) have a tensor character [see, e.g., Eq. (8)], which substantially complicates the problem. However, when the sample is in the form of a thin slab, the twinning stresses inside the crystal are uniform, and the problem can be solved completely. This is the case that we shall consider below. The additional (magneto)elastic strain field (10) has another remarkable property: it is scale invariant. In other words, the distribution of the strains inside the sample depends only on the angle at which the part of the surface containing the ''elastic charges'' is viewed from a given point of the crystal. Consequently, any transformation that preserves the shape of the sample will not be reflected in the distribution of the additional strains.

From what we have said above, we can draw a rather general conclusion. In the case of phase transitions brought about by a change in temperature, the macroscopic symmetry of the crystal as a whole does not change. While on the microscopic level the transition takes place with a spontaneous breaking of symmetry, and the microscopic order parameter (e.g., the antiferromagnetic vector in an AFM) is symmetry-conjugate to the shear components of the strain tensor, the locally broken symmetry is restored on average through the formation of a domain structure of elastic origin.

4. EQUILIBRIUM DOMAIN STRUCTURE

As we see from expressions (13) and (14), below the temperature of the magnetic phase transition the shape of the sample is substantially influenced by the distribution of equilibrium strains. Let us consider this effect in more detail for the simple example of when the sample is in the form of a thin slab and the corresponding twinning stresses are uniform.

Let the orientation of the surface of the sample be specified by the vector normal $\mathbf{n}_S$, the coordinates of which are defined in relation to the crystalline axes in the high-symmetry (paramagnetic) phase. The transverse dimensions L in the plane of the slab will be assumed to be substantially larger than its thickness d. Then the main contribution to the stray energy (14) is from the magnetostriction averaged over the volume of the crystal:

$$\langle \hat{u}_{\rm ms} \rangle = \frac{1}{V} \int_V dV \hat{u}_{\rm ms}(\mathbf{r}). \tag{15}$$

Substituting (15) into (10) and (11), we obtain a simple expression for the stresses created by the ''charges'':

$$\hat{\sigma}_{\rm macro} = \hat{\hat{c}} \langle \hat{\mathbf{U}}(\mathbf{r}_S) \rangle. \tag{16}$$

in final form the stray energy is obtained from Eqs. (14) and (16)

$$f_{\rm stray} = L^2 d \{ \langle \hat{u}_{\rm ms} \rangle \hat{\hat{c}} \langle \hat{u}_{\rm ms} \rangle + \mathbf{n}_S \otimes \mathbf{n}_S {\rm Tr} \langle \hat{u}_{\rm ms} \rangle - \mathbf{n}_S \otimes (\langle \hat{u}_{\rm ms} \rangle \mathbf{n}_S) - (\langle \hat{u}_{\rm ms} \rangle \mathbf{n}_S) \otimes \mathbf{n}_S \}. \tag{17}$$

If we restrict discussion to shear strains only, i.e., $\hat{u}_{\rm ms} = \hat{u}_{\rm shear}$, as was done above [see Eqs. (4) and (7)], then the stray energy takes the form

$$F_{\rm stray} = L^2 d \langle \hat{u}_{\rm ms} \rangle \hat{\hat{c}} \langle \hat{u}_{\rm ms} \rangle \geqslant 0, \tag{18}$$

which explicitly implies the positive definiteness of this energy for shear strains of any type. As in the case of ferromagnets, in the absence of external field (for a sample whose shape in the paramagnetic phase does not lower the crystal symmetry) the stray energy $F_{\rm stray}$ can be minimized only by having the average shear strains vanish. We note that expression (18) agrees with formula (2) of our previous paper,[11] which was derived exclusively on the basis of phenomenological considerations.

The value of $F_{\rm stray}$ (18) depends in an obvious way on the shape of the sample, in this case on the orientation of the surface of the slab with respect to the crystallographic axes. In particular, if the normal $\mathbf{n}_S$ to the surface of the sample is directed along a principal axis C_n of the crystal ($n=3$, 4, or 6), then the macroscopic symmetry of the sample will coincide with the symmetry point group of the crystal and should not change at the phase transition. This means that for such a geometry all types of domains should be represented in equal measure.

The calculations done above show convincingly that the onset of uniform spontaneous shear strains in a sample of finite size should lead to a substantial increase in the energy of the crystal as a whole, and therefore is energetically unfavorable. There is a close analogy between the onset of long-range elastic fields in materials undergoing a phase transition with spontaneous strains and the dipole fields in ferromagnets (the analogy between the equations for the electromagnetic fields in matter and the equations of the theory of elasticity was noted by de Wit more than 40 years ago[17]). The case of a weak ferromagnet requires special treatment, since in such a material the domain structure can be formed on account of both the weak (of the order of the small magnetization) dipolar and the long-range magnetoelastic interactions. Investigation of the competing contributions is beyond the scope of this paper.

Another important question arising in the analysis of expression (17) is basically whether it is in fact energetically favorable for the domain (twin) structure to be established at a magneto- or thermoelastic phase transition. The point is that a nonuniform strain distribution inevitably involves an increase in the energy of the domain walls (even if the domain boundaries are coherent). To compare the energy advantage of ''detwinning'' (18) to the energy cost due to the domain-wall contribution, let us follow the procedure used in the case of ferromagnets (see, e.g., Ref. 18). We consider a regular domain structure consisting of alternating domains of two types, which are characterized by strain tensors $\hat{u}_1$ and $\hat{u}_2$. We assume that the period d_{DS} of the domain structure is much smaller than the thickness of the slab, $d_{DS} \ll d$, that the

domains are coherently joined, and there are no ''closing'' domains (i.e., near the surface the strain inside a domain is the same as in the bulk).

Standard manipulations based on expressions (13) and (14) show that the contribution from the ''elastic charges'' to the free energy is given by[6)]

$$F_{\rm ch}=L^2 d_{DS}\xi_1\xi_2(\hat{u}_1-\hat{u}_2)\hat{\hat{c}}(\hat{u}_1-\hat{u}_2)\cos\vartheta, \tag{19}$$

where ϑ is the angle between the plane of the surface of the slab and the boundary between domains, and $\xi_1=(1-\xi_2)$ is the volume fraction of domains of the first type.

The contribution of the domain walls to the total energy is given by the expression

$$F_{DW}=L^2\sigma_{DW}\frac{d}{d_{DS}}, \tag{20}$$

where σ_{DW} is the surface energy per unit area of one domain wall.

The total energy $F=F_{\rm ch}+F_{DW}$ is minimum with respect to the period of the domain structure when

$$d_{DS}^{\rm opt}=\frac{\sqrt{\sigma_{DW}d}}{\sqrt{\xi_1\xi_2(\hat{u}_1-\hat{u}_2)\hat{\hat{c}}(\hat{u}_1-\hat{u}_2)\cos\vartheta}}\propto\sqrt{\frac{\sigma_{DW}d}{f_{\rm elas}}}. \tag{21}$$

The quantity in the denominator of the first fraction in expression (21) is essentially the energy density of the ''elastic charges'' (cf. formula (19)), which, in turn, is proportional to the elastic energy density $f_{\rm elas}=\hat{u}\hat{\hat{c}}\hat{u}/2$.

The energy associated with the appearance of a domain structure with the optimum period (21) will be

$$F=2L^2\sqrt{\xi_1\xi_2(\hat{u}_1-\hat{u}_2)\hat{\hat{c}}(\hat{u}_1-\hat{u}_2)\cos\vartheta\sigma_{DW}d}$$
$$\propto L^2 d f_{\rm elas}\sqrt{\frac{a}{d}}. \tag{22}$$

Here we have adopted the following estimate for the surface energy of a domain wall: $\sigma_{DW}\propto f_{\rm elas}a$, where a is the thickness of the transition layer.

Thus the contribution due to nonuniform strains and the short-wavelength distribution of ''charges'' is proportional to the ratio $d_{DS}/d\propto\sqrt{a/d}\ll 1$ and is therefore much less than the stray energy (17), which for a uniform strain, as we have said, is proportional to the volume of the crystal and to the elastic energy of the spontaneous strains. This means that for sufficiently large samples the formation of the domain structure in magneto- and thermoelastic crystals lowers the energy of the crystal by an extremely significant amount.[7)]

5. DOMAIN STRUCTURE IN AN ANTIFERROMAGNET WITH ANISOTROPY OF THE EASY-PLANE TYPE

Let us now illustrate the role of the stray energy for the simple example of a two-sublattice AFM in the form of a thin slab whose surface is perpendicular to a principal axis of the crystal and coincides with the easy plane for the magnetic vectors (spins). Good examples of such a system are single crystals of $CoCl_2$ (symmetry group D_{3d}) or of the underdoped compound $YBa_2Cu_3O_{6+x}$ with $x\leqslant 0.3$ (symmetry group D_{4h}). For these crystals the stray energy (17) takes the form

$$F_{\rm stray}=L^2 d\left[\frac{1}{2}c_{11}(\langle u_{xx}\rangle^2+\langle u_{yy}\rangle^2)+c_{12}\langle u_{xx}\rangle\langle u_{yy}\rangle\right.$$
$$\left.+2c_{66}\langle u_{xy}\rangle^2\right], \tag{23}$$

where the Z axis is chosen along the principal symmetry axis C_n (and perpendicular to the plane of the slab). The free energy of the crystal in an external magnetic field **H** (the weak demagnetizing effect due to the small field-induced magnetic moment is neglected) can be written in general form as

$$F=L^2 d\sum_k \xi_k\left[E_{\rm an}+\frac{M_0}{2H_E}(\mathbf{H}\cdot\mathbf{l}_k)^2\right.$$
$$\left.+M_0^2\hat{u}_k\hat{\hat{\lambda}}_{me}\mathbf{l}_k\otimes\mathbf{l}_k+\frac{1}{2}\hat{u}_k\hat{\hat{c}}\hat{u}_k\right]+F_{\rm stray}. \tag{24}$$

Expression (24) contains the magnetic anisotropy energy density $E_{\rm an}$ and the magnetoelastic energy, determined by the fourth-rank tensor of coefficients $\hat{\hat{\lambda}}_{me}$, and we have introduced the following notation: M_0 is the saturation magnetization, $2H_E$ is the spin-flip field of exchange origin, $\mathbf{l}_k$ and $\hat{u}_k$ is the antiferromagnetic vector and the spontaneous magnetostriction tensor in the kth domain ($k=1,2,3$ for $CoCl_2$ and $k=1,2$ for $YBa_2Cu_3O_{6+x}$), ξ_k is the volume fraction of the kth domain, and the angle brackets denote averaging over the volume of the crystal: $\langle\hat{u}\rangle=\Sigma_k\xi_k\hat{u}_k$ (recall that $\Sigma_k\xi_k=1$).

Minimizing expression (24) with respect to the components of the AFM vector, the strain tensor, and the domain fraction ξ_k, we find that as a result of a redistribution of the domains, the effective magnetic field inside the sample is equal to zero up until the external field reaches a critical value equal to

$$|\mathbf{H}|=H_{MD}\equiv\lambda_{\rm eff}M_0\sqrt{\frac{H_E M_0}{c_{\rm eff}}}, \tag{25}$$

where $\lambda_{\rm eff}$ and $C_{\rm eff}$ are certain combinations of magnetoelastic and elastic constants which depend on the symmetry of the particular crystal. The quantity H_{MD} can be interpreted as the field at which the sample is brought to a single-domain state (the ''monodomainization field'');[11,12,20] this field is well measured in experiment (see, e.g., Refs. 9, 10, and 21).

In fields less than H_{MD} the shear strain

$$\langle u_{\rm shear}\rangle=\frac{\lambda_{\rm eff}M_0^2}{C_{\rm eff}}\left\{\frac{H}{H_{MD}}\right\}^2=u_0\left\{\frac{H}{H_{MD}}\right\}^2 \tag{26}$$

is a quadratic function of the magnitude of the external magnetic field, expressed in units of H_{MD}. (In Eq. (26) u_0 is the value of the spontaneous shear strain.)

Thus in the framework of the adopted model the low-field dependence of any macroscopic characteristic that is determined by the fraction of elastic domains should satisfy the law of corresponding states, i.e., for $H<H_{MD}$ it should have a universal character as a function of the reduced coordinate $H/H_{\rm MD}$. We have studied universality[8)] of this type for the example of the field dependence of the magnetostriction in the underdoped compound $YBa_2Cu_3O_{6.3}$ in Ref. 20.

We note that in our description it was implicitly assumed that the magnetic characteristics of the surface (e.g., the ori-

entation and value of the sublattice magnetizations) do not change when an external magnetic field is applied. A change of the properties of the surface in the course of the rearrangement of the domain structure under the influence of the field, and also the presence of defects pinning the domain walls, can lead to partial irreversibility and hysteresis in the dependence of the macroscopic characteristics of a crystal on the external magnetic field. A detailed analysis of this topic is beyond the scope of this paper.

6. MORPHOLOGY OF THE DOMAIN STRUCTURE

Finally, let us discuss the particulars of the microstructure of an AFM in the presence of domains of an elastic nature and what brings it about. Direct observations show[21–23] that the morphology and mutual positioning of the domains in many AFMs are very similar to the morphology of twins and twin variants in martensites. As a rule, the domains are plane-parallel slabs of approximately equal (or comparable) thickness, which adjoin one another along a boundary parallel to crystallographic planes of symmetry. When an external magnetic field is applied, the domain walls are displaced parallel to the initial plane while maintaining the plane-parallel structure of all the domains. In crystals having more than two easy AFM directions[22] one sometimes observes a herringbone or parquet structure in which there exist several systems of ''twins,'' corresponding to different pairs of magnetoelastic domains. These systems, in turn, are also found in a twin relationship, and the boundaries between them are in large measure planar, but their thickness is of the order of the thickness of the individual domains. (We stress that, unlike martensites, in which the domains can have a wedge-shaped or acicular form, and the martensitic phase can exist as a lenticular inclusion in an austenitic matrix, in an AFM only plane-parallel systems of domains have been observed.)

For interpretation of the observed morphology of the domain structure, let us turn to a model of ''elastic charges'' arising at internal interfaces. Generally speaking, the problem of the distribution of the magnetization (AFM vector) inside a domain wall with the magnetoelastic strains taken into account is quite complicated, since, in particular, it requires solving a system of partial differential equations for the three components of the displacement vector, which cannot be reduced to a single equation because of the isotropicity and long-ranged nature of the elastic forces. However, following the technique proposed in Ref. 24, we shall assume that the boundaries between domains are sufficiently narrow that in the analysis of the domain structure of the sample one does not have to worry about the details of the distribution of the AFM vector inside the domain wall. In this case for analysis of the optimum orientation of the domain wall (assuming that it is planar or, at least, a relatively smooth surface with a large radius of curvature) it is sufficient to use equations (7)–(10) in which the normal $\mathbf{n}_S$ should be understood to be the normal $\mathbf{n}_{12}$ to the boundary between domains 1 and 2, and in place of $\hat{u}_{\rm ms}$ in formula (9) we should take the difference of the spontaneous strains in the adjacent domains:

$$\hat{e}_{\rm elas} = -\mathbf{n}_{12}\times(\hat{u}_1-\hat{u}_2)\times\mathbf{n}_{12}\delta'[\mathbf{n}_{12}(\mathbf{r}-\mathbf{r}_{12})]. \tag{27}$$

As we see from Eq. (27), ''elastic charges'' do not arise ($\hat{e}_{\rm elas}(\mathbf{r})=0$) if the tangential (with respect to the boundary) components of the strain tensor in adjacent domains are equal; in that case the strains in adjacent domains are compatible and do not create additional long-range stresses.[9)] In the theory of elasticity, walls of this type are called Nye walls (see Ref. 25). They are reminiscent of the Bloch walls observed in a ferromagnet in the sense that the latter analogously do not contain magnetic charges creating a long-range fields. If the fields did not compensate each other, the incompatible strains at the wall would create uncompensated ''elastic charges'' which, according to formula (10), would give rise to a long-range strain field giving a nonnegative contribution (10) to the energy of the crystal and would thus increase the surface energy σ_{DW} of a domain wall. Continuing the analogy with magnetism, we could call such boundaries Néel walls. It is clear that from an energy standpoint the formation of walls of the Nye type is preferable, and since the conditions of compatibility hold only for certain symmetric directions of $\mathbf{n}_{12}$, these walls should be planar, as has been observed experimentally.[21–23]

Another example we might consider is the domain wall in the $CoCl_2$. As we have said above, in the paramagnetic phase the symmetry group of the crystal is D_{3d}, and the magnetic structure in the uniform state in fields much less than the exchange fields is uniquely described by the angle ϕ between the AFM vector and the twofold axis (the X axis) lying in the basal plane (it is assumed that the magnetic field $\mathbf{H}$ is perpendicular to the principal axis C_3 of the crystal).[11] The spontaneous strains, $\hat{u}_{\rm ms}(\mathbf{r})$, which are determined from the condition that the free energy (1) be minimum, have the following form:

$$u_{xx}^{\rm ms}-u_{yy}^{\rm ms}=-\Lambda_1\cos 2\phi,\quad 2u_{xy}^{\rm ms}=-\Lambda_1\sin 2\phi,$$

$$u_{xz}^{\rm ms}=\Lambda_2\sin 2\phi,\quad u_{yz}^{\rm ms}=\Lambda_2\cos 2\phi,$$

$$u_{xx}^{\rm ms}+u_{yy}^{\rm ms}=2M_0^2\frac{2c_{13}\lambda_{31}-c_{33}(\lambda_{11}+\lambda_{12})}{(c_{11}+c_{12})c_{33}-c_{13}^2},$$

$$u_{zz}^{\rm ms}=2M_0^2\frac{c_{13}(\lambda_{11}+\lambda_{12})-(c_{11}+c_{12})\lambda_{31}}{(c_{11}+c_{12})c_{33}-c_{13}^2},$$

$$\Lambda_1=4M_0^2\frac{c_{44}\lambda_{66}+2c_{14}\lambda_{41}}{c_{66}c_{44}-c_{14}^2},$$

$$\Lambda_2=2M_0^2\frac{c_{14}\lambda_{66}+2c_{66}\lambda_{41}}{c_{66}c_{44}-c_{14}^2}, \tag{28}$$

where the components of the fourth-rank tensor $\hat{\lambda}_{me}$ introduced in (24) are written in the Voigt indices, the first index being associated with the elastic variables and the second with the magnetic variables. As we see from expressions (28), only the shear components of the strain tensor depend on the orientation of the AFM vector, in accordance with what we have said above.

In the absence of magnetic field (external or effective internal) the equilibrium magnetic configuration corresponds to three different equivalent values of ϕ: 0 (domain of type 1) and $\pm 2\pi/3$ (domains of types 2 and 3), corresponding to

an orientation of the AFM vector along one of the three twofold axis. At the boundary separating domains 2 and 3 the components $u_{xy}^{\rm ms}$ and $u_{xz}^{\rm ms}$ have jumps:

$$\Delta u_{xy}^{\rm ms} \equiv u_{xy}^{(2)} - u_{xy}^{(3)} = \frac{\sqrt{3}}{2}\Lambda_1,$$

$$\Delta u_{xz}^{\rm ms} \equiv u_{xz}^{(2)} - u_{xz}^{(3)} = -\sqrt{3}\Lambda_2. \qquad (29)$$

Substitution of (29) into (27) shows that in the case when the plane of the domain wall is perpendicular to the twofold symmetry axis (the axis $\mathbf{n}_{23} \| X$), the elastic charge density at the boundary $\hat{e}_{\rm elas} = 0$, i.e., the domain wall is a Nye wall. For any other orientation of the plane of the domain wall the tensor $\hat{e}_{\rm elas} \neq 0$; for example, if $\mathbf{n}_{23} \| Y$, a ''charge'' component $(\hat{e}_{\rm elas})_{xz} = -\sqrt{3}\Lambda_2$ appears, and the wall will be of the Néel type.

Analysis of the spatial distribution of the domains requires special attention. It follows from all we have said above that if only two types of AFM domains, differing in the orientation of the AFM axes, can exist in the crystal, as, e.g., in $YBa_2Cu_3O_{6+x}$, then a sandwich consisting of domains 1 and 2 alternating periodically through a plane-parallel slab will create the minimum internal stresses, which are localized either inside the domain walls or near the surface of the sample in a layer of the order of the period of the domain structure. If three or more types of domains can exist, as in the AFMs $CoCl_2$, NiO, $KCoF_3$, etc., then the question of an alternative structure arises, e.g., one in which each domain is in the form of a triangular prism. In such a structure the domain walls as before do not create additional stresses, but, according to Refs. 24–26, in the region where three domains come together a disclination should arise, which in turn creates additional strain fields that decay logarithmically with distance, and they would inevitably increase the energy of the crystal as a whole.

Let us consider in more detail the formation of disclinations and the fields they create, taking as an example a rhombohedral AFM of the $CoCl_2$ type. The coherent junction of domains 2 and 3 along a plane with $\mathbf{n}_{23} \| X$ is possible only if in addition to the strain there is a small rotation, specified by a vector ω directed along a principal axis of the crystal:

$$\omega_z = e_{xyz}\Delta u_{xy} n_x^2 = -\frac{\sqrt{3}}{2}\Lambda_1, \qquad (30)$$

where Δu_{xy} is defined in (29). In the case when only two domains are adjoining and the boundary is infinite, a relative rotation of the crystalline axes will not cause additional stresses. However, when three domains join together, because of the rotation of each of them, a defect known as a disclination must arise in an unstrained crystal (with a wedge-shaped region of a shortage or excess density of material; see Fig. 1).

In an ideal lattice without discontinuities the absence of such a defect is compensated by the stresses necessary to bring the sides of the wedge together. We assume that domains 1, 2, and 3 border each other along planes perpendicular to the three twofold symmetry axes, and all three planes intersect along a line parallel to the Z axis. Since the domain walls are Nye walls, the junction is an edge disclination.[25,26]

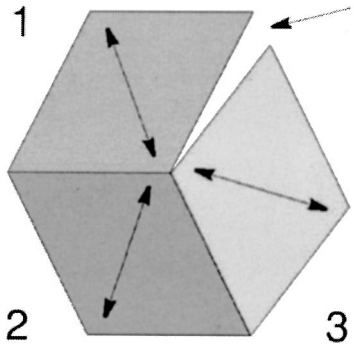

FIG. 1. Disclination at the junction point of three domains in a crystal of the $CoCl_2$ type. The two-headed arrows correspond to directions of the AFM vectors in each of the domains. The arrow indicates the wedge-shaped discontinuity due to the rotations of each of the domains at the transition to the magnetically ordered state.

The Frank vector Ω for this disclination is given as the sum of the vectors of rotation on each of the boundaries, taken with the opposite sign:

$$\Omega_z = \frac{3\sqrt{3}}{2}\Lambda_1. \qquad (31)$$

The sign of the vector Ω is determined by the sign of the magnetostriction constant. By convention[26] a negative value of Ω corresponds to a shortage of material (see Fig. 1). As we see from formula (31), the three-domain junction under discussion gives rise to disclinations of only one sign.

The general formula for the strain field of such an ''isolated disclination line'' was derived in Ref. 26. Substituting expression (31) into that formula, we obtain, in cylindrical coordinates ρ, Θ,

$$u_{xx}^{\rm disc} + u_{yy}^{\rm disc} = \frac{3\sqrt{3}\Lambda_1(c_{66}-2c_{12})}{4\pi(c_{66}-c_{12})}(\ln\rho + 2),$$

$$u_{xx}^{\rm disc} - u_{yy}^{\rm disc} = -\frac{3\sqrt{3}\Lambda_1 c_{66}}{8\pi(c_{66}-c_{12})}\cos 2\Theta,$$

$$2u_{xy}^{\rm disc} = -\frac{3\sqrt{3}\Lambda_1 c_{66}}{8\pi(c_{66}-c_{12})}\sin 2\Theta. \qquad (32)$$

A comparison of formulas (28) and (32) shows that the presence of the junction gives rise to additional strains having the same order of magnitude as the spontaneous magnetostrictive strains. The isomorphous part [the first expression in (32)] depends logarithmically on the distance ρ to the disclination. The shear component [the second expression in (32)] does not depend on the distance at all but does depend on the direction and, as a result of the magnetoelastic interactions, can alter the local magnetic anisotropy fields and lead to a substantially nonuniform distribution of AFM vectors around the disclination. The presence of the disclination subsystem can lead to partial compensation of the shear components, but it nevertheless entails the onset of unavoidable isomorphous strains, the energy contribution of which, on account of the long-ranged character, is proportional to the volume of the sample, and it is therefore energetically less favorable than the regular structure consisting of pairs of domains of different types. When an external field is applied, the unpinned disclinations, which are topological defects, should

tend to come out to the surface. (We note that for the example considered there can be no processes of annihilation of disclinations, since all of the disclinations are of the same sign.) If the disclinations are pinned by defects of another type (e.g., impurity atoms, vacancies, etc.), their position under the influence of the external field does not change, but on account of the displacement of the domain walls the distribution of additional strains (32) created by the disclinations can change. After removal of the external field the pinned disclinations can serve as nuclei for the formation of domains of a definite type and thus, just as the ''elastic charges'' on the surface of the crystal, they can bring about reversible behavior of the domain structure in an external magnetic field.

7. CONCLUSIONS

The model proposed in this paper for description of the formation of an equilibrium and reversible domain structure in AFMs and materials undergoing phase transitions accompanied by substantial spontaneous shear strains is based on the assumption that the surface of the crystal has special magnetic, elastic, and magnetoelastic properties different from those of the bulk, which may be due to both dimensional effects and to defects on the surface. The absolutely or highly rigid surface creates fictitious ''elastic charges'' of incompatibility. These charges serve as sources of long-range stress fields which are analogous to the demagnetizing fields in ferromagnets and lead to the formation of a domain structure. The energy contribution from these fields is proportional to the volume of the sample, since the value of the field increases in inverse proportion to the distance from the ''charge.'' Consequently, the domain structure that arises entails a substantial decrease in the total energy of the crystal. For macroscopic samples (the thickness of which exceeds the optimum period of the domain structure) the energy cost due to the contribution of the domain walls is substantially smaller than the advantage due to the formation of the nonuniform state, and this leads to thermodynamic stability of the domain structure. An external magnetic field leads to a reversible rearrangement of the domain structure, and in the low-field region the dependence of the macroscopic characteristics of the crystal on the ratio H/H_{MD} should be of a universal character (the law of corresponding states[20]). The characteristic field H_{MD} at which the sample will be brought to a single-domain state is determined by the magnetostriction constant, while its temperature dependence is governed by the structure of the stress field, the density of defects (including in the paramagnetic phase), and, possibly, the prehistory of the sample. In an ideal (defect-free) crystal the formation of a regular stripe structure consisting of alternating domains of two types is preferred. The formation of junctions of three or more domains causes a disclination to form, which creates long-range stress fields and thus increases the energy of the crystal. The details of the morphology of the domain walls, their motion in the process of bringing the sample to a single-domain state, and the formation of the domain structure at phase transitions would be useful and interesting to study by the visual magnetooptical methods developed and tested by V. V. Eremenko and his co-workers. This would confirm (or refute) the model developed here and would sharpen the conclusions as to the nature of the domain structure in AFMs.

We are grateful to V. G. Bar'yakhtar, M. A. Ivanov, and S. M. Ryabchenko for numerous fruitful discussions on the problems of the mechanism of domain structure formation in AFMs. E. V. G. acknowledges with gratitude the technical and financial support of A. A. Malyshenko.

This study was done as part of a project financed by the Ministry of Education of Ukraine (Registration No. 0100U002336) and was also supported in part by the Foundation for Basic Research of Ukraine, Project F7/514-2001.

*E-mail: malyshen@ukrpack.net
**E-mail: vloktev@bitp.kiev.ua

[1)] In essence this condition reduces to the following. The change of the elastic state of the crystal is described by a displacement vector that has three independent components. In experiments one does not directly measure the displacement of the points of the crystal but rather the relative displacement, i.e., the strain tensor. A symmetric strain tensor has six components, but obviously only three of them are independent. The conditions of compatibility serve as additional relations which reduce the number of independent components to three and reflect the absence of discontinuities and ''folds'' in the sample.

[2)] The difference of such characteristics as the ordering temperature in the bulk of the crystal and on the surface follows from the obvious difference of the coordination number of the atoms or dimensional effects. Differences can also be due to the fact that, as a rule, defects and impurities segregate from the bulk of the crystal onto its surface, substantially altering the chemical and physical properties of the latter.

[3)] We note that the isomorphous striction and shear strain form a basis of different irreducible representations of the symmetry group of the crystal in the paramagnetic phase (the isomorphous striction always transforms according to the identity representation, while the shear strain is associated with a lowering of the symmetry of the paramagnetic phase and cannot transform according to the identity representation). The separate treatment of the contributions of the isomorphous and shear strains essentially means that we are neglecting in the free energy of the crystal the small terms due to anharmonicity.

[4)] Such a situation arises, for example, in pure cobalt at the fcc–hcp structural phase transition. The phases are transformed to each other by a shearing of the close-packed planes, and so the interphase boundary is coherent (i.e., the compatibility of the strains of the fcc and hcp phases is not disrupted) even on the microscopic level. The conditions of compatibility between the strained volume and the surface also holds in a trivial manner when the normal to the surface of the sample is oriented along a direction of compression (dilatation) spontaneously arising at a phase transition. However, for a sample of finite size, incompatibility arises on the lateral surface of the crystal.

[5)] Equation (12) in divergence form can also be obtained by variation of the functional (13), (14) with respect to the three components of the displacement vector. In that case the compatibility conditions will obviously be satisfied automatically.

[6)] An analogous expression was obtained in Ref. 19 by proceeding from Saint-Venant's empirical principle.

[7)] If the thickness of the sample is of the order of the optimum period (21) of the domain structure or less, then a state with uniform strain is preferable from an energy standpoint.

[8)] The universal dependence of the magnetostriction on the field normalized to the spin-flip field ($H/2H_E$) which was observed in Ref. 9 pertains to the high-field part and to the single-domain state.

[9)] We note that an analysis with allowance for the structure of the domain wall in an AFM shows that ''elastic charges'' of opposite sign are localized inside the wall at distances of the order of the characteristic scale of the magnetic nonuniformity, but at large distances from the boundary the fields of these changes compensate each other.

[1] L. Néel, Proc. Intern. Conf. Theor. Physics, Kyoto and Tokyo Sci. Council Jrn, Tokyo (1954).
[2] M. M. Farztdinov, Usp. Fiz. Nauk **84**, 611 (1964) [Sov. Phys. Usp. **7**, 855 (1982)].
[3] V. V. Eremenko and N. F. Kharchenko, Sov. Sci. Rev., Sect. A **5**, 1 (1984).
[4] V. G. Bar'yakhtar, A. N. Bogdanov, and D. A. Yablonskii, Sov. Phys. Usp. **31**, 810 (1988).
[5] A. N. Bogdanov and I. E. Dragunov, Fiz. Nizk. Temp. **24**, 1136 (1998) [Low Temp. Phys. **24**, 852 (1998)].
[6] L. Néel, J. Phys. Radium **5(241)**, 265 (1944).
[7] V. M. Kalita, A. F. Lozenko, S. M. Ryabchenko, and P. A. Trotsenko, Ukr. Fiz. Zh. **43**, 1469 (1998).
[8] A. Janossy, F. Simon, T. Feher, A. Rockenbauer, L. Korecz, C. Chen, A. J. S. Chowdhury, and J. W. Hodby, Phys. Rev. B **59**, 1176 (1999).
[9] V. M. Kalita, A. F. Lozenko, and S. M. Ryabchenko, Fiz. Nizk. Temp. **26**, 671 (2000) [Low Temp. Phys. **26**, 489 (2000)].
[10] E. V. Amitin, A. G. Baĭkalov, A. G. Blinov, L. A. Boyarskiĭ, V. Ya. Dikovskiĭ, K. R. Zhdanov, M. Yu. Kameneva, L. P. Kozeeva, and A. P. Shelkovnikov, JETP Lett. **70**, 352 (1999).
[11] E. V. Gomonaj and V. M. Loktev, Fiz. Nizk. Temp. **25**, 699 (1999) [Low Temp. Phys. **25**, 520 (1999)].
[12] E. V. Gomonaj and V. M. Loktev, Acta Phys. Pol. A **97**, 459 (2000).
[13] V. V. Eremenko, *Introduction to the Optical Spectroscopy of Magnets* [in Russian], Naukova Dumka, Kiev (1971).
[14] V. V. Eremenko, N. F. Kharchenko, and L. I. Beliy, J. Appl. Phys. **50**, 7751 (1979).
[15] C. Teodosiu, *Elastic Models of Crystal Defects*, Springer-Verlag, Berlin (1982), Mir, Moscow (1985).
[16] V. I. Marchenko and A. Ya. Parshin, Zh. Éksp. Teor. Fiz. **79**, 257 (1980) [Sov. Phys. JETP **52**, 129 (1980)].
[17] R. de Wit, Solid State Phys. **10**, 249 (1960).
[18] Ch. Kittel, Rev. Mod. Phys. **21**, 541 (1949).
[19] A. L. Roytburd, J. Appl. Phys. **83**, 228 (1998).
[20] E. V. Gomonay and V. M. Loktev, Fiz. Nizk. Temp. **27**, 436 (2001) [Low Temp. Phys. **27**, 325 (2001)].
[21] M. Safa and B. K. Tanner, Philos. Mag. B **37**, 739 (1978).
[22] B. K. Tanner, Contemp. Phys. **20**, 187 (1987).
[23] J. Baruchel, M. Schlenker, and W. L. Roth, J. Appl. Phys. **48**, 5 (1977).
[24] M. Kleman and M. Schlenker, J. Appl. Phys. **43**, 7184 (1972).
[25] M. Kleman, J. Appl. Phys. **45**, 1377 (1974).
[26] R. de Wit, J. Phys. C **5**, 529 (1972).

Translated by Steve Torstveit

Role of paramagnetic ions in the formation of the low-temperature current through a molecular wire

É. G. Petrov*

N. N. Bogolyubov Institute of Theoretical Physics, National Academy of Sciences of Ukraine, ul. Metrologicheskaya 14b, 03143 Kiev, Ukraine

(Submitted February 4, 2002)
Fiz. Nizk. Temp. **28**, 872–884 (August–September 2002)

The mechanism of formation of the inelastic current through a molecular wire is considered under conditions of strong interaction between the electrons being transported and rapid vibrational and spin relaxation within each electron localization center in the wire. It is shown that paramagnetic ions with ''frozen'' orbital moments in the electron localization centers are capable not only of giving rise to a spin-polarized current but also of blocking the current itself. © *2002 American Institute of Physics.* [DOI: 10.1063/1.1511707]

1. INTRODUCTION

It is now clear that further miniaturization of the basic elements of electronics will involve the use of semiconductor[1] and molecular[2] nanostructures. The latter are exceptionally promising in connection with the possibility of synthesizing molecules with prespecified properties, opening up a way of constructing different types of compact molecular transport and conversion systems (molecular wires, switches, diodes, amplifiers, etc.[3–7]). A great leap in molecular electrons occurred in the second half of the 1990s, when it became possible to measure the current through an individual molecule found between microelectrodes (see, e.g., Refs. 8–10). In this case the molecule plays the role of a molecular wire with a markedly nonlinear current–voltage characteristic $I(V)$. Various theoretical model are now being developed to explain the nonlinearity of the current in short molecular wires and to elucidate the mechanisms of regulation of the current by an electric field.[8,11–14]

We note, however, that a magnetic field **h** can also play a large role in the regulation of the interelectrode current. For example, the study of the transport properties of granular magnetic solids[15] and antiferromagnetically coupled magnetic multilayers[16,17] has revealed the presence of a giant magnetoresistance due to reorientation of the spins by a magnetic field. Another important effect is due to the appearance of a large spin polarization of the electrons in the process of their tunneling either through a layer of a ferromagnetic insulator in metal–insulated–metal[18,19] and metal–insulator–vacuum[20] systems or through ferromagnetic semiconductor heterostructures.[21,22] The observation of a coherent spin current due to electrons and holes has made it possible to talk about the start of a new field of solid-state electronics—spintronics.[23,24] The spin polarization effect is theoretically predicted for metal–molecular-wire–metal systems in which the molecular wire contains structural groups with paramagnetic ions.[25–27] It has been shown[25,26] that if the orbital moment of paramagnetic ions in the ground state is ''frozen,'' then at low temperatures an elastic mechanism of formation of the interelectrode current leads to strict polarization of the electrons that have passed through the wire, and the current $I(h)$ reaches a saturation value as the magnetic field h is increased. If the formation of the current is due to an inelastic mechanism, then at low temperatures a complete blocking of the interelectrode current can occur.[27] In the papers cited the situation considered was one in which the states of the transported electron on the paramagnetic ions lay higher than the Fermi level of the electrodes, and these states played a virtual role, providing (together with the nonmagnetic centers of the wire) a superexchange coupling either directly between the electrodes[25,26] or between widely separated terminal groups of the molecular wire.[27]

The goal of the present study is to examine the mechanism of formation of inelastic interelectrode current through a molecular wire under conditions such that the motion of the electron along the wire occurs by hops between electron localization centers on paramagnetic ions. These ions can be constituents of the terminals or internal structural groups of the wire. Examples of such molecular wires are oligoporphyrin linear structures[6,28] and also molecular chains containing transition-metal complexes.[5,29,30]

2. KINETIC MODEL OF THE INTERELECTRODE CURRENT

The mechanism of formation of the interelectrode current through a molecular wire depends substantially on the relationship between the characteristic times of the dynamic and dissociative processes in the entire transport system.[11,13,26,27] In the case of weak dissipation a purely elastic mechanism of tunneling is realized, whereas strong intraterm relaxation in the molecular wire (i.e., relaxation between vibrational sublevels of electronic terms belonging to the structural groups of the wire) will lead to the formation of an inelastic interelectrode current I (see Fig. 1). The hopping mechanism considered here refers to the inelastic electron transport process, which is characterized by the rates of transition between each of the electrodes and the corresponding terminal group of the wire (the rates χ_L, χ_R and χ_{-L}, χ_{-R}) and also between the electron localization centers in the wire (rates κ_1 and κ_2, Fig. 1a; or $g_1, g_2, \ldots, g_{N-1}$ and $r_2, r_3, \ldots, r_N$, Fig. 1b). The rates are calculated by the formula

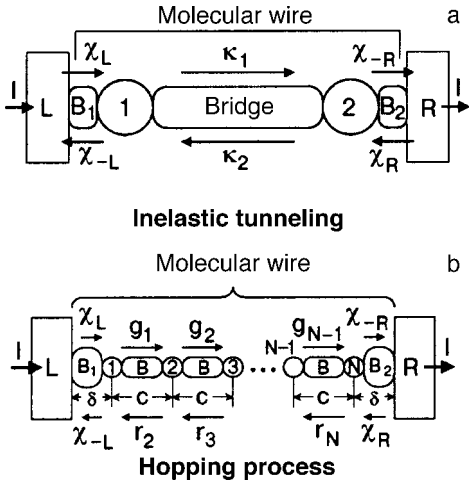

FIG. 1. Kinetic scheme of formation of an interelectrode current through a molecular wire containing N centers of localization of the transported electron. L and R are the left and right electrodes, separated from the terminal groups of the wire by structures B_1 and B_2. The electron localization centers $n=1,2,\ldots,N$ are connected together by bridge structures. In the case of two widely separated centers (a) the limiting stage is the long-distance tunneling of an electron through the bridge between centers, which occurs by a superexchange mechanism at rates κ_1 and κ_2, and not the hopping of the electron between the electrodes and the adjacent terminal groups of the wire (the forward $\chi_{L(R)}$ and backward $\chi_{-L(-R)}$ rates). In the case of a large number of centers (b) the distance c between electron localization centers can be small, and so the tunneling rates for forward g_N and backward r_N hops of the electron between centers can exceed the rates $\chi_{L(R)}$ and $\chi_{-L(-R)}$.

$$\kappa_{n\to m}=\frac{2\pi}{\hbar}\sum_{\{v\},\{v'\}}\sum_{\{M\},\{M'\}}|\langle m(\{M'\}\{v'\})|\hat{V}|n(\{M\}\{v\})\rangle|^2 W_n(\{M\}\{v\})\,\delta[E_n(\{M\}\{v\})-E_m(\{M'\}\{v'\})], \tag{1}$$

where $\langle m(\{M'\}\{v'\})|\hat{V}|n(\{M\}\{v\})\rangle$ is the transition matrix element between states $|n(\{M\}\{v\})\rangle$ and $|m(\{M'\}\{v'\})\rangle$, which correspond to finding an electron at centers n and m. The quantity

$$W_n(\{M\}\{v\})=\exp[-E_n(\{M\}\{v\})/k_BT]\times\left[\sum_{\{M\},\{v\}}\exp[-E_n(\{M\}\{v\})/k_BT]\right]^{-1} \tag{2}$$

(k_B and T are Boltzmann's constant and the temperature) is the statistical weight of the state $|n(\{M\}\{v\})\rangle$, which, like the corresponding energy $E_n(\{M\}\{v\})$, is characterized by a set of magnetic $\{M\}$ and vibrational $\{v\}$ quantum numbers. In the next Section we will give concrete expressions for the rates; here we will only note that the structure of formula (1) reflects the presence of fast relaxation in both the system of vibrational levels and in the system of magnetic sublevels. Therefore, the results obtained in this paper pertain to transport systems in which the vibrational and spin–lattice relaxation times are much shorter than the time for an electron to hop between localization centers.

Rapid relaxation means that the position of the electron at any center n is characterized by an integral occupation number of the center, $P_n(t)$. The kinetic equations are written for the $P_n(t)$ $(n=1,2,\ldots,N)$ and for the number of electrons $N_{L(R)}(t)=\Sigma_{\sigma=\pm1/2}N_{L(R)\sigma}(t)$ occupying the conduction band of each of the electrodes (σ is the projection of the electron spin, equal to $\pm1/2$). Since in the system under study the paramagnetic ions are assumed to be isolated from each other, the influence of the magnetic field can be manifested only at low temperature, when the electron hops occur by a tunneling mechanism in accordance with the scheme illustrated in Fig. 2. For molecular nanoelectronics the molecular chains of interest are short. In that case, however, the role of the Coulomb interaction between electrons being transported through the wire becomes important. We use a model in which the Coulomb repulsion is so strong that only single electrons can pass through the wire. Thus, if there is even one electron being transported in the wire, then an additional electron cannot enter the wire.[13] The interelectrode current can be found from the expression $I=e\dot{N}_L(t)=-e\dot{N}_R(t)$, where e is the charge of the electron and $\dot{N}_L(t)$ is the number of electrons that go from electrode L to the molecular wire ($\dot{N}_R(t)$ is the number of electrons that go from the wire to electrode R). In this model

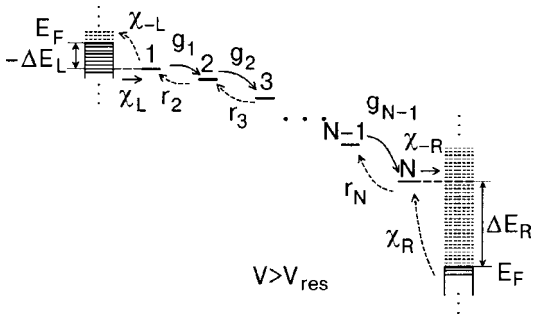

FIG. 2. Diagram of the tunneling hops of an electron in the formation of the interelectrode current under conditions of a large potential difference V between electrodes. The energy distance to the Fermi level of the right electrode, ΔE_R, is always positive and increases with increasing V, while that for the left electrode, ΔE_L decreases to zero and under conditions of the resonance transition ($V=V_{res}$) becomes negative. The energy levels in the conduction band which are occupied (unoccupied) by electrons are denoted by solid (dashed) horizontal lines. The electron energy levels in the molecular wire are represented by the single horizontal lines. At low temperature a one-way transport is achieved in which all of the reverse processes (denoted by dashed arrows) are suppressed.

$$\dot{N}_L(t)=\chi_L W_0(t)-\chi_{-L}P_1\prod_{j=2}^{N}P_j(t);$$

$$\dot{N}_R(t)=\chi_R W_0(t)-\chi_{-R}P_N\prod_{j=1}^{N-1}P_j(t),$$

where $W_0(t)=\Pi_{j=1}^{N}(1-P_j(t))$; χ_L and χ_R are the rates at which an electron goes from the electrodes to the nearest terminal centers of the wire, and χ_{-L} and χ_{-R} are the rates at which an electron goes from the terminal groups to the electrodes. To find the populations we use the following system of nonlinear equations:[13]

$$\dot{\mathbf{P}}(t)=-\hat{\mathbf{A}}\mathbf{B}(t)+\mathbf{R}(t), \tag{3}$$

where $\mathbf{B}(t)\equiv\mathbf{U}(t)W_0(t)$, $\mathbf{R}(t)\equiv\mathbf{C}W_0(t)$. The components of the vectors $\mathbf{P}(t)$ and $\mathbf{U}(t)$ are the populations $P_n(t)$ and

the auxiliary quantities $U_n(t) \equiv P_n(t)/(1-P_n(t))$, respectively. The components C_n of the vector **C** and the elements A_{nm} of the matrix $\hat{\mathbf{A}}$ are defined as

$$C_n = \chi_L \delta_{n,1} + \chi_R \delta_{n,N}; \tag{4}$$

$$A_{nm} = [(\chi_{-L} + g_1)\delta_{n,1} + (g_n + r_n)(1-\delta_{n,1})(1-\delta_{n,N}) + (\chi_{-R} + r_N)\delta_{n,N}]\delta_{n,m} - g_{n-1}(1-\delta_{n,1})\delta_{n,m+1} - r_{n+1}(1-\delta_{n,N})\delta_{n,m-1}. \tag{5}$$

In Eq. (5) g_n and r_n are the rates of the forward and backward hops of an electron between the nearest localization centers in the wire.

The nonlinearity of the system of equations (3) is due to the factor $W_0(t) = \Pi_{j=1}^{N}(1-P_j(t))$ that characterizes the statistical weight of the state of the molecular wire when there are no electrons being transported in the wire. Below we analyze the dependence of the current on the magnetic field under steady-state conditions, when $\dot{N}_L(t) = -\dot{N}_R(t) = \text{const}$ and the populations $P_n(t)$ are constants. The steady-state populations will be denoted by P_n. Setting $\dot{\mathbf{P}}(t) = 0$ in (3), we see that under steady-state conditions the quantity

$$J = \chi_L - \chi_{-L} U_1 = g_1 U_1 - r_2 U_2 = g_2 U_2 - r_3 U_3 = \ldots = \chi_{-R} U_N - \chi_R, \tag{6}$$

which plays the role of the flux of particles, is conserved. The interelectrode current is given by the formula

$$I = e W_0 J, \tag{7}$$

from which we see that the quantity

$$W_0 = \prod_{j=1}^{N} (1-P_j) = \prod_{j=1}^{N} (1+U_j)^{-1} \tag{8}$$

plays the role of the transmission (blocking) factor. An analytical expression for the flux is

$$J = \frac{1}{\mathrm{Det}(N)} \chi_L g_1 \ldots g_{N-1} \chi_{-R} - \chi_R r_N \ldots r_3 r_2 \chi_{-L}, \tag{9}$$

where $\mathrm{Det}(N)$ is the determinant of the matrix $\hat{\mathbf{A}}$. Using formulas (6) and (9), one can find the auxiliary quantities U_n (and, hence, P_n) in analytical form. For example, in the case of a molecular wire with two electron localization centers (Fig. 1a) we have

$$J = \frac{\chi_L \chi_{-R} \kappa_1 - \chi_{-L} \chi_R \kappa_2}{\chi_{-L}\chi_{-R} + \chi_{-L}\kappa_2 + \chi_{-R}\kappa_1}; \tag{10}$$

$$U_1 = \frac{\chi_L \chi_{-R} + (\chi_L + \chi_R)\kappa_2}{\chi_{-L}\chi_{-R} + \chi_{-L}\kappa_2 + \chi_{-R}\kappa_1};$$

$$U_2 = \frac{\chi_{-L} \chi_R + (\chi_L + \chi_R)\kappa_1}{\chi_{-L}\chi_{-R} + \chi_{-L}\kappa_2 + \chi_{-R}\kappa_1}. \tag{11}$$

Let us also give analytical expressions for a regular molecular wire, when

$$\alpha = g_1 = g_2 = \ldots = g_{N-1},$$

$$\beta = \gamma\alpha = r_2 = r_3 = \ldots = r_N. \tag{12}$$

Here the ratio of the backward and forward rates for the hopping of an electron between adjacent units of the wire,

$$\gamma = \exp(-eVc/lk_BT), \tag{13}$$

is expressed in terms of the potential drop over the length c of a hop. The overall potential drop over the entire length of the molecular wire, $l = 2\delta + (N-1)c$ (see Fig. 1b), is equal to V. Taking relations (12) and (13) into account, we obtain

$$J = \frac{\xi \chi_L \zeta_L [1 - \exp(-eV/k_BT)]}{\xi(1-\gamma^{N-1}) + \zeta_L(\xi + \gamma^{N-1})(1-\gamma)}; \tag{14}$$

$$U_n = \frac{\chi_L}{\chi_{-L}} \times \frac{\xi(1-\gamma^{N-n}) + \lambda\gamma^{N-n-1}[\xi(1-\gamma^{n-1}) + \zeta_L(1+\xi)(1-\gamma)]}{\xi(1-\gamma^{N-1}) + \zeta_L(\xi+\gamma^{N-1})(1-\gamma)}, \tag{15}$$

where we have introduced the rate ratios

$$\zeta_L \equiv \alpha/\chi_{-L}, \quad \xi \equiv \chi_L/\chi_R \tag{16}$$

and the parameter

$$\lambda = \exp(-2eV\delta/lk_BT). \tag{17}$$

The general formulas (6)–(9) and their particular analytical forms (10) and (11) (for a wire with two electron localization centers) and (14)–(16) (for a wire with N identical localization centers) are sufficient for a quantitative analysis ofthe function $I(h)$ for different particular cases. It is necessary only to specify the type of paramagnetic ions present in the electron localization centers $n = 1, 2, \ldots, N$ and then to determine the dependence of the electron hopping rates on the magnetic field h.

3. SPIN DEPENDENCE OF THE TRANSITION RATES

In real systems the electronic configuration of the paramagnetic ion and its electronic terms are formed by the combined effects of the internal exchange and spin–orbit interactions with allowance for the crystalline field acting on the electrons.[31,32] In this paper we restrict consideration to electron transport processes involving the participation of paramagnetic ions of the iron group with ''frozen'' orbital moments in the electronic ground state. In this case the spin–orbit interaction is small, and so the spin S of the ion and its projection M onto the direction of the applied magnetic field **h** are good quantum numbers. In addition, we assume that if the paramagnetic ion is found in the electronic ground state, the attachment of an additional electron will make the spin of the ion equal to $S' = S - 1/2$. This decrease of the spin applies to ions for which the number of electrons in the unfilled $3d$ shell is equal to or greater than the number of one-electron $3d$ states. For example, the ground state of the ions Mn^{2+} (Fe^{3+}) and Ni^{3+} have the electronic configurations $t_{2g}^3 e_g^2$ and $t_{2g}^6 e_g^2$, with the corresponding spins $S = 5/2$ and $S = 1$.[31,32] (The symbols t_{2g} and e_g denote the one-electron states in an octahedral crystalline field.) The capture of an additional electron transforms the initial electronic configurations into the configurations $t_{2g}^4 e_g^2$ and $t_{2g}^6 e_g^3$, with spins $S' = 2$ and $S' = 1/2$, respectively. As we shall show below, this decrease of the spin of the ion leads to some specific electron transport effects (see also Refs. 25–27).

We consider a tunneling hopping mechanism of electron transport along the molecular wire under conditions where the terminal groups 1 and N of the wire are separated from the electrons by special nonmagnetic structures B_1 and B_2, and the paramagnetic ions of the wire are coupled to one another via nonmagnetic bridge groups B. Here the hopping of an electron between localization centers on the wire and the exchange spin–spin coupling between the ions are brought about by a superexchange mechanism. The energy of this exchange and the spin dipole–dipole inter-ion coupling will be neglected in comparison with the energy of the Zeeman splitting and the energy of the single-ion spin anisotropy. Thus we are considering a model of identical noninteracting magnetic centers in which the spin states of each nth paramagnetic ion are specified either by the quantum numbers $S_n=S$, $M_n=-S,\ldots,+S$ (if the ion does not contain an additional electron) or $S_n'=S-1/2$, $M_{n'}=-(S-1/2),\ldots,(S-1/2)$ (if the ion has captured an electron being transported). Taking the spin–orbit coupling into account by the energy of the axial single-ion anisotropy $K(S_z^2)$ (Refs. 31 and 32) and denoting the energy of the ion in the absence of an additional electron by the symbol 0, we write the energy of the nth paramagnetic ion in the two cases, respectively, as

$$\varepsilon_n^0=E_{n\{v_n\}}^0+E_n^{0\mathrm{mag}}(M_n),$$

$$E_n^{0\mathrm{mag}}(M_n)=-\mu_B g h M_n+K^0 M_n^2, \tag{18}$$

$$\varepsilon_n=E_{n\{v_n'\}}+E_n^{\mathrm{mag}}(M_n'),$$

$$E_n^{\mathrm{mag}}(M_n')=-\mu_B g h M_n'+K(M_n')^2, \tag{19}$$

where $E_{n\{v_n\}}^0$ and $E_{n\{v_n'\}}$ are the vibrational energies of the terms of the nth center, and $E_n^{0\mathrm{mag}}(M_n)$ and $E_n^{\mathrm{mag}}(M_n')$ are the magnetic energies of the paramagnetic ion in this center with allowance for the axial single-ion anisotropy. For ions with a ''frozen'' orbital moment the anisotropy parameter K^0 is small (of the order of 10^{-2} cm^{-1}; Ref. 32). If the ion captures an additional electron, however, a partial ''thawing'' of the orbital moment occurs, and the single-ion anisotropy constant K increases by several orders of magnitude, reaching values of 0.1–1 cm^{-1} (Refs. 29 and 30). Therefore, in calculating the transition rates it is sufficient to take the single-ion anisotropy into account only for ions with an excess electron.

For calculating the transition matrix elements appearing in the general expression for the rate (1), we shall use the Condon approximation, according to which the electronic and vibrational states are separable, so that

$$\langle m(\{M'\}\{v'\})|\hat{V}|n(\{M\}\{v\})\rangle \approx\langle\{v_m'\}|\{v_m\}\rangle\langle\{v_n\}|\{v_n'\}\rangle\langle(S_m'M_m')\times(S_nM_n)|\hat{V}|(S_n'M_n')(S_mM_m)\rangle, \tag{20}$$

where $\langle\{v_m'\}|\{v_m\}\rangle$ is the overlap integral between the vibrational states of the mth center when that center contains an excess electron ($\{v_m'\}$) and when it does not ($\{v_m\}$). The dependence on the spin state of the centers is determined by the second, purely electronic, matrix element of expression (20). In Refs. 25 and 26 it is shown that in the case when the ion spin and its projection are good quantum numbers, the matrix element $\langle(S_m'M_m')(S_nM_n)|\hat{V}|(S_n'M_n')(S_mM_m)\rangle$ can be calculated using the method of $6j$ symbols.[33] Let S_{mn} and M_{mn} be the total spin and the total projection of two centers; then, following Ref. 26, we obtain

$$\langle(S_m'M_m')(S_nM_n)|\hat{V}|(S_n'M_n')(S_mM_m)\rangle = V_{mn}\Phi(S_m'M_m';S_nM_n|S_n'M_n';S_mM_m), \tag{21}$$

where V_{mn} is the reduced matrix element, which does not depend on the spin state of the pair of ions. The dependence on the spin state is concentrated in the spin factor

$$\Phi(S_m'M_m';S_nM_n|S_n'M_n';S_mM_m) = \sum_{S_{mn}M_{mn}} C^{S_{mn}M_{mn}}_{S_m'M_m'S_nM_n} C^{S_{mn}M_{mn}}_{S_mM_mS_n'M_n'} \delta_{M_{mn},M_m'+M_n} \times\delta_{M_{mn},M_n'+M_m}(-1)^{S_m+S_n+S_m'+S_n'} \times\sqrt{(2S_n'+1)(2S_m'+1)}\begin{Bmatrix} S_m & 1/2 & S_m' \\ S_n & S_{mn} & S_n' \end{Bmatrix}, \tag{22}$$

where $C^{JM}_{J_1M_1J_2M_2}$ and $\{\ldots\}$ are the Clebsch–Gordan and $6j$ symbols, respectively.[33]

The reduction of the transition matrix element (21) to a product of spatial and spin factors makes it possible to simplify expression (1) substantially. Here we note that since the energy of the paramagnetic ion is the sum of vibrational and magnetic energies [see expressions (18) and (19)], the overall statistical weight (2) can be represented as a product of the statistical weights for the vibrational states

$$W_n^{0\mathrm{vib}}(\{v_n\})=(Z_n^{0\mathrm{vib}})^{-1}\exp(-E_{n\{v_n\}}^0/k_BT),$$

$$(Z_n^{0\mathrm{vib}})^{-1}=\sum_{\{v_n\}}(-E_{n\{v_n\}}^0/k_BT); \tag{23}$$

$$W_n^{\mathrm{vib}}(E_{n\{v_n'\}})=(Z_n^{\mathrm{vib}})^{-1}\exp(-E_{n\{v_n'\}}/k_BT),$$

$$(Z_n^{\mathrm{vib}})^{-1}=\sum_{\{v_n'\}}(-E_{n\{v_n'\}}/k_BT) \tag{24}$$

and the statistical weights for the magnetic states

$$W_n^{0\mathrm{mag}}(E^{0\mathrm{mag}}(M_n))=(Z_n^{0\mathrm{mag}})^{-1}\times\exp[-E^{0\mathrm{mag}}(M_n)/k_BT],$$

$$(Z_n^{0\mathrm{mag}})^{-1}=\sum_{M_n=-S}^{S}\exp[-E^{0\mathrm{mag}}(M_n)/k_BT]; \tag{25}$$

$$W_n^{\mathrm{mag}}(E^{\mathrm{mag}}(M_n'))=(Z_n^{\mathrm{mag}})^{-1}\exp[-E^{\mathrm{mag}}(M_n')/k_BT],$$

$$(Z_n^{\mathrm{mag}})^{-1}=\sum_{M_n'=-S'}^{S'}\exp[-E^{0\mathrm{mag}}(M_n)/k_BT]. \tag{26}$$

In the absence of spin–spin interactions the magnetic energy of the ion is not more than a few reciprocal centimeters, even in high magnetic fields ($h\approx 5$ T), and therefore the magnetic energy in the δ function in expression (1) can be neglected in comparison with the vibrational energy of the term. As a

result, the transition rate $\kappa_{n\to m}(h)$ reduces to a product of two factors: $\kappa_{n\to m}(h)=Q_{n\to m}F_{nm}(h)$, where the first factor is independent of the magnetic field h.

In the investigated hopping model for the formation of the current through a regular molecular wire it is sufficient to elucidate the magnetic-field dependence of the transition rates α and $\chi_{L(R)}$ only. The transition rates β and $\chi_{-L(-R)}$ are related to the former by relations (13) and

$$\chi_{L(R)}=(Z^{\rm vib}_{1(N)}/Z^{0\rm vib}_{1(N)})\exp[-\Delta E_{L(R)}/k_BT]\chi_{-L(-R)}. \quad (27)$$

In Eq. (27) the quantities

$$\Delta E_L=\Delta E_0-eV\delta/l\equiv e(V_{\rm res}-V)\,\delta/l<0$$

and

$$\Delta E_R=\Delta E_0+eV\delta/l\equiv e(V_{\rm res}+V)\,\delta/l>0$$

are the energy gaps between the lowest energy levels of an electron localized on the left and right terminal centers of the wire, respectively, and the Fermi level of the corresponding electrode (see Fig. 2). Here $\Delta E_0=E_{1\{v_1'=0\}}-E^0_{1\{v_1=0\}}-E_F=E_{N\{v_N'=0\}}-E^0_{N\{v_N=0\}}-E_F$ is the energy gap in the absence of a potential difference V. Since we are considering tunneling transitions at low temperatures, it is assumed that the energy gaps $|\Delta E_L|$ and ΔE_R are much greater than the thermal energy k_BT. (Since for observation of magnetic effects the magnetic energy of an ion must not exceed the thermal energy, we have dropped the small magnetic energy from the definition of the gaps ΔE_L and ΔE_R.)

The rate χ_L is the sum of the partial rates $\chi_{L\mathbf{k}\sigma}$ of transition of an electron from electrode L to the left-hand terminal group 1 when the electron on the electrode has spin projection σ and wave vector $\mathbf{k}$. This means that in the matrix element (21) it is necessary to set $n=L\mathbf{k}$, $m=1$, $S_n'=1/2$, $M_n'=\sigma$, $S_m=S$, $M_m=M_1$, $S_m'=S-1/2$, $M_m'=M_1'$, $S_n=0$, $M_n=0$, and the summation in (22) is over the fixed value $S_{mn}=S-1/2$ with allowance for the fact that $M_{mn}=M_1+\sigma=M_1'$. As a result, we obtain

$$\chi_{Lk}\equiv\kappa_{L\mathbf{k}\to 1}=Q_{L\mathbf{k}}F_L(h), \quad (28)$$

where

$$Q_{L\mathbf{k}}=\frac{2\pi}{\hbar}\sum_{v_1,v_1'}|\langle\{v_1'\}|\{v_1\}\rangle|^2W^{0\rm vib}_1(\{v_1'\})\times n_F(E_{L\mathbf{k}}-eV\delta/1)[E_{L\mathbf{k}}+E^0_{1\{v_1\}}-E_{1\{v_1'\}}] \quad (29)$$

($n_F(E)=[\exp((E-E_F)/k_BT)]^{-1}$ is the Fermi distribution function), and

$$F_L(h)=\sum_\sigma \eta_\sigma,$$

$$\eta_\sigma=\sum_{M_1=-S}^{S}W^{0\rm mag}_1(E^{0\rm mag}(M_1))|c^{(S-1/2)M_1+\sigma}_{SM_1(1/2)\sigma}|^2. \quad (30)$$

In deriving (30) we have taken into account that $C^{JM}_{JM00}=1$. We note that the spin-independent factor (29) contains only one overlap integral of the vibrational functions, $\langle\{v_1'\}|\{v_1\}\rangle$, since the electron transition under consideration involves only one electron localization center. The structure of the spin-dependent factor (30) reflects the fact that the occupation of the kth state of the conduction band by an electron in the external magnetic fields under consideration is practically independent of the electron spin projection. This is due to the smallness of the magnetic energy μ_Bgh in comparison with the Fermi energy E_F (Ref. 26).

For finding the spin dependence of the rate α it is necessary to take into account that the overlap of the electronic wave functions of the magnetic ions n and $m=n+1$ is brought about via a nonmagnetic bridge B (Fig. 1), i.e., the hopping of an electron occurs by a superexchange mechanism.[11,26,27] This means that the electron passes in a virtual manner from the paramagnetic ion n to the nonmagnetic ligand l_1, from ligand l_1 to the next nonmagnetic ligand l_2, etc., until the passage of the electron from ligand l_r to the paramagnetic ion $m=n+1$ (the ligands are not shown in Fig. 1). To find the dependence of the corresponding electronic matrix element V_{mn} on the spin state of the paramagnetic ions, we note that for a small value of the matrix elements of the indicated transitions $V_{l_1n},V_{l_2l_1},V_{l_3l_2},\ldots,V_{ml_r}$ (in comparison with the energy difference ΔE_{l_j} for an electron on any ligand l_j and on the paramagnetic ion), the superexchange coupling leads to the expression

$$V_{mn}=V_{ml_r}V_{l_1n}\prod_{j=2}^{r}V_{l_jl_{j-1}}/\Delta E_{l_j}.$$

All of the matrix elements of the transition of an electron between ligands are spin-independent quantities. Only the matrix elements V_{ml_r} and V_{l_1n} depend on the spin state, and this dependence is easily found from formulas (21) and (22). Here the structure of the matrix element V_{ml_r} is identical to that of $\chi_{L\mathbf{k}}$ if $L\mathbf{k}$ is replaced by l_r and 1 is replaced by m. To find the matrix element V_{l_1n} it is necessary to set $m=l_1$ in Eqs. (21) and (22) and to take into account that $S_n'=S-1/2$, $M_n'=\sigma+M_n$, $S_m=S_{l_1}=0$, $M_m=M_{l_1}=0$, $S_m'=S_{l_1}'=1/2$, $M_m'=M_{l_1}'=\sigma$, $S_n=S$, $S_{mn}=S-1/2$, and $M_{mn}=M_n+\sigma=M_n'$. Thus we find (for $m=n+1$)

$$\alpha\equiv\kappa_{n\to m}=Q_{n\to m}F_S(h), \quad (31)$$

where

$$Q_{n\to m}=|V^0_{nm}|^2\frac{2\pi}{\hbar}\sum_{v_n,v_n'}\sum_{v_m,v_m'}|\langle\{v_n'\}\rangle\{v_n\}|^2\times|\langle\{v_m\}|\{v_m'\}\rangle|^2W^{0\rm vib}_n(\{v_n\})W^{\rm vib}_m(\{v_m'\})\times\delta[E_{n\{v_n'\}}+E^0_{m\{v_m\}}-E^0_{n\{v_n\}}-E_{m\{v_m'\}}]; \quad (32)$$

$$F_S(h)=\sum_\sigma\sum_{M_n'=-S'}^{S'}\sum_{M_m=-S}^{S}W^{\rm mag}_n\times(E^{\rm mag}(M_n'))W^{0\rm mag}_m(E^{0\rm mag}(M_m))\times|C^{(S-1/2)M_n'}_{SM_n(1/2)\sigma}C^{(S-1/2)M_m'}_{SM_m(1/2)\sigma}|^2\delta_{M'n,M_{n+\sigma}}\delta_{M'm,M_{m+\sigma}}. \quad (33)$$

4. DEPENDENCE OF THE CURRENT ON THE MAGNETIC FIELD

Let us illustrate the general theoretical results for some particular examples.

4.1. One paramagnetic ion in a molecular chain

Suppose the molecular wire contains one electron localization center with a paramagnetic ion having spin S. This means that only the rates χ_L, χ_{-L}, χ_R, and χ_{-R} are responsible for the formation of the interelectrode current (7).

The corresponding steady-state current I and steady-state population P_1 of the paramagnetic ion are determined by the expressions

$$J=\frac{\chi_L\chi_{-R}[1-\exp(-eV/k_BT)]}{\chi_{-L}+\chi_{-R}+\chi_L+\chi_R},$$

$$P_1=\frac{\chi_L+\chi_R}{\chi_{-L}+\chi_{-R}+\chi_L+\chi_R}. \tag{34}$$

According to relation (27) and the conditions $\Delta E_L<0$, $\Delta E_R>0$ (see Fig. 2), the inequalities $\chi_L \geqslant \chi_{-L}$, χ_R and $\chi_R \leqslant \chi_{-R}$ hold. Then the occupation of the paramagnetic ion by an electron being transported, $P_1 \approx \chi_L/(\chi_L+\chi_{-R})$, may be large or small. Let us examine the particular case when at low temperatures $\exp(-eV/k_BT)\approx 0$, and the limiting stage of the transport process is the departure of an electron from the paramagnetic ion to electrode R, so that $\chi_L \geqslant \chi_{-R}$. Then $P_1 \approx 1$, and the expression for the current is expressed as $I=e\chi_{-R}=e\Sigma_{\mathbf{k}\sigma}\chi_{-R\mathbf{k}\sigma}$. The partial hopping rate of an electron from the paramagnetic center to the right-hand electrode $\chi_{-R\mathbf{k}\sigma}$ is calculated the same way as the rate $\chi_{L\mathbf{k}\sigma}$. Therefore $\chi_{-R\mathbf{k}}=Q_{R\mathbf{k}}F_{-R}(h)$, where $Q_{-R\mathbf{k}}$ is given by formula (29) but with $W_1^{0\mathrm{vib}}(\{v_1'\})$ and $n_F(E_{L\mathbf{k}}-eV\delta/l)$ replaced by $W_1^{\mathrm{vib}}(\{v_1\})$ and $1-n_F(E_{R\mathbf{k}})$, respectively. The dependence on the spin state of the ion is carried by the factor $F_{-R}(h)=\Sigma_\sigma n_\sigma(h)$, where

$$\eta_\sigma(h)=\sum_{M_1'=(S-1/2)}^{S-1/2} W_1^{\mathrm{mag}} \times(E^{\mathrm{mag}}(M_1'))\left|C^{(S-1/2)M_1'}_{S(M_1'-1/2)(1/2)\sigma}\right|^2. \tag{35}$$

With the introduction of (35) the interelectrode current can be written as

$$I=\sum_\sigma I_\sigma, \quad I_\sigma=I_0\eta_\sigma(h), \tag{36}$$

where $I_0\equiv e\Sigma_{\mathbf{k}}Q_{-R\mathbf{k}}$ is a factor independent of the magnetic field. Figure 3 shows the characteristic steplike behavior of η_σ and, hence, of the low-temperature current I_σ as a function of magnetic field. We note that after passing through the molecular wire the current becomes spin polarized. The presence of the step (plateau) can be explained as follows. At low temperature only the lowest energy level of the paramagnetic ion is occupied. In the absence of single-ion anisotropy this level in a field $h\neq 0$ corresponds to an ion spin projection $M_1'=-(S-1/2)$. In the presence of anisotropy, however, under conditions such that $K>0$, there is a competition between the Zeeman energy $\mu_B g h M_1'$ and the anisotropy energy $K(M_1')^2$. Therefore the minimum values of the total magnetic energy (19) of the ion will depend on the value of the magnetic field h. These minimum values will correspond to negative values of the spin projection lying in the interval

$$-1/2 \geqslant M_1' \geqslant -(S-1/2). \tag{37}$$

A change of the minimum value occurs under the condition $E^{\mathrm{mag}}(M_1')=E^{\mathrm{mag}}(M_1'-1)$, which also determines the magnetic fields at which switching between adjacent plateaus occurs:

$$h_0(M_1')=K(1-2M_1')/\mu_B g. \tag{38}$$

The spin polarization is determined by the quantities $\eta_{+1/2}(h)$ and $\eta_{-1/2}(h)$. In magnetic fields exceeding the saturation field $h_{0s}=h_0(M_1'=-S+1/2)$, it follows from (35) that $\eta_{+1/2}(h)=2S/(2S+1)$ and $\eta_{-1/2}(h)=1/(2S+1)$. Therefore, in the current coming out of the molecular wire the number of electrons with spin projection $\sigma=+1/2$ is larger than the number of electrons with spin projection $\sigma=-1/2$ by a factor of $2S$. This means that, e.g., for $S=5/2$ (Mn^{2+} and Fe^{3+} ions) the fraction of electrons with $\sigma=+1/2$ is about 83%.

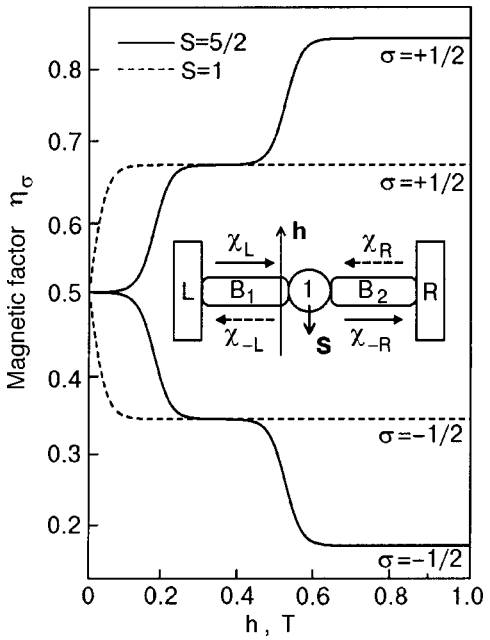

FIG. 3. Dependence of the low-temperature interelectrode current $I_\sigma=I_0\eta_\sigma(h)$ on the magnitude of the magnetic field h at one paramagnetic center under the conditions $\chi_L \geqslant \chi_{-L}$, χ_R and $\chi_R \leqslant \chi_{-R}$. The formation of the current is limited by the rate χ_{-R}. A strong polarization of the current coming out of the wire is observed. Here η_σ was calculated according to formula (35) for $K=0.8$ cm^{-1}.

4.2. Two localization centers for the transported electron in a molecular wire

In the presence of two electron localization centers (Fig. 1a) the flux of particles is determined by formula (10). Because centers 1 and 2 are far apart, the potential drop over the length c is quite large compared to the thermal energy k_BT. Therefore the rate κ_1 for the transition of an electron from center 1 to center 2 is much higher than the rate κ_2 of the reverse transition. As a result, when the inequality $\kappa_1 \geqslant \kappa_2$ is taken into account, expression (10) reduces to

$$J \approx \frac{\chi_L \kappa_1}{\chi_{-L} + \kappa_1}, \tag{39}$$

while

$$U_1 = \frac{\chi_L}{\kappa_1 + \chi_{-L}}, \quad U_2 = \frac{\chi_L}{\chi_{-R}} \frac{\kappa_1}{\kappa_1 + \chi_{-L}}. \tag{40}$$

At low temperatures the rate χ_{-L} is small compared to χ_L. It can also be small compared to the hopping rate κ_1. In that case the current (7), in accordance with formulas (8), (39), and (40), can be written in the form

$$I \approx e\chi_L \frac{1}{1+\chi_L/\kappa_1} \frac{1}{1+\chi_L/\chi_{-R}} \approx \begin{cases} \dfrac{e\kappa_1}{1+\chi_L/\chi_{-R}}, & (\chi_L \gg \kappa_1), \\ \dfrac{e\chi_L}{1+\chi_L/\chi_{-R}}, & (\kappa_1 \gg \chi_L). \end{cases} \tag{41}$$

The long-distance character of the superexchange hopping between centers 1 and 2 makes for a low rate κ_1, which can be much less than the rate χ_L. Therefore, in the case of a large distance between centers 1 and 2 one can expect the inequality $\chi_L \gg \kappa_1$ to hold. If the bridge B_1 is longer than the bridge B_2, one can also expect that $\chi_L \ll \chi_{-R}$, which leads to a simple expression for the current:

$$I = e\kappa_1 = I_0 \eta(h). \tag{42}$$

In expression (42) the magnetic-field-dependent factor $\eta(h)$ is determined by the spin state of centers 1 and 2. The analytical form of the component $I_0 = e\alpha_0$, which is independent of the magnetic field, is determined by the rate α_0, which is given by expression (32) for $n=1$ and $m=2$.

Current between nonmagnetic and paramagnetic centers

Suppose that of the two electron localization centers, only center 2 contains a paramagnetic ion. Then $\eta(h) = \Sigma_\sigma \eta_\sigma(h)$, where

$$\eta_\sigma(h) = W_1(\sigma) \sum_{M_1=-S}^{S} W_2^{0\,\mathrm{mag}} \times (E^{\mathrm{mag}}(M_2)) \left| C_{SM_1(1/2)\sigma}^{(S-1/2)M_1+\sigma} \right|^2. \tag{43}$$

Here the quantity

$$W_1(\sigma) = \exp(-\mu_B g h/k_B T) / \sum (-\mu_B g h/k_B T)$$

determines the weight of the spin state of the excess electron arriving at the nonmagnetic center 1 from electrode L. Using the distribution (25) and substituting the explicit form of the Clebsch–Gordan coefficients[33] into (43), we obtain

$$\eta_{\pm 1/2}(h) = W_1(\pm 1/2) \frac{S}{2S+1} (1 \pm B_S(\mu_B g h S/k_B T)), \tag{44}$$

where

$$B_S(x) = \frac{2S+1}{2S} \coth\left(\frac{2S+1}{2S} x\right) - \frac{1}{2S} \coth\left(\frac{x}{2S}\right)$$

is the Brillouin function. (In deriving the analytical form (44) we set $K^0 \approx 0$, since for ions with a ''frozen'' orbital moment the magnetic anisotropy energy, as we have said, is small.) It follows from formula (44) that in high magnetic fields, when $\exp(-\mu_B g h/k_B T) \ll 1$, a complete blocking of the interelectrode current occurs. The physical explanation of this is that at high magnetic fields and low temperatures the only states that remain occupied are those with the minimum spin projections both for the electron at the nonmagnetic center ($\sigma = -1/2$) and for the paramagnetic ion ($M_1 = -S$). Taking into account that in the transfer of an electron to center 2 the total spin projection $M_1' = M_1 + \sigma$ is conserved, we necessarily obtain $M_1' = -(S+1/2)$. However, for the type of paramagnetic ions considered here, the capture of an additional electron by the ion necessarily decreases the total spin of the ion, and therefore only the minimum total spin projection, equal to $M_1' = -(S-1/2)$, can be realized, and not $M_1' = -(S+1/2)$, i.e., in a high magnetic field the transport of an electron becomes spin forbidden. Mathematically this follows from the fact that $B_S(x) \to 0$ for $x \to 0$. Figure 4 illustrates the onset of current blocking as the magnetic field is increased.

If only center 1 contains a paramagnetic ion, then the magnetic component of the current $\eta_\sigma(h)$ is determined by expression (35) found above. The difference is that, even though the electrons entering center 2 are spin polarized in proportion to $\eta_{+1/2}(h)/\eta_{-1/2}(h)$, the rapid spin relaxation at center 2 eliminates this polarization, reducing it to the standard Boltzmann factor $W_2(+1/2)/W_2(-1/2)$.

Current between two paramagnetic centers

Suppose that both centers contain identical paramagnetic ions and that the magnetic fields $\mathbf{h}_1$ and $\mathbf{h}_2$ acting on the

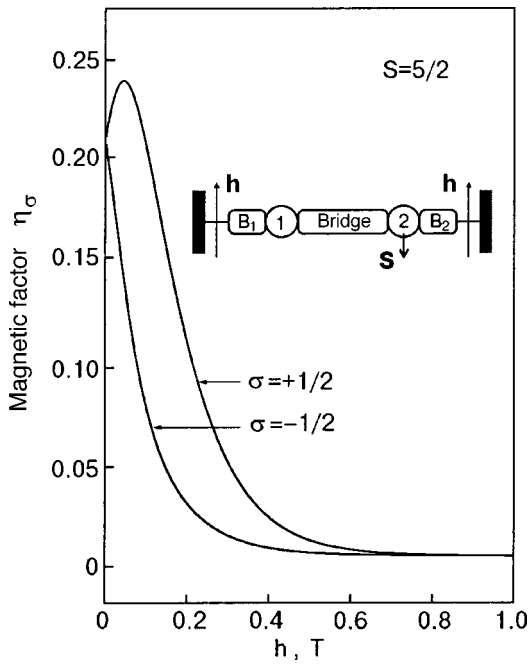

FIG. 4. Blocking of the current by a magnetic field under conditions when the molecular wire contains two electron localization centers, and the limiting stage of the current formation is the hopping of an electron from the nonmagnetic center 1 to the center 2 containing a paramagnetic ion. Here η_σ was calculated according to formula (43) for $K^0 = 0$.

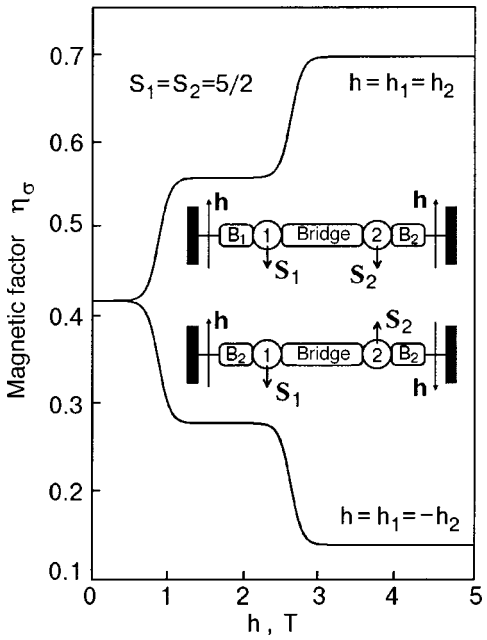

FIG. 5. Regulation of the current by a magnetic field under conditions when the molecular wire contains two centers with identical paramagnetic ions, and the limiting state of the current formation is the hopping of an electron from center 1 to center 2. Changing the direction of the magnetic field acting on the paramagnetic ion 2 will lead to a sharp drop of the value of the current. Here η_σ was calculated by formulas (45) and (46) for $K^0=0$, $K=0.8\ \mathrm{cm}^{-1}$.

paramagnetic ions can have the same or different directions. Then the factor that determines the magnetic-field dependence of the interelectrode current (42) looks like

$$\eta(h)=\sum_{M_1,M_1'}\sum_{M_2,M_2'} W_1^{\mathrm{mag}}(E^{\mathrm{mag}}(M_1')) \times W_2^{0\mathrm{mag}}(E^{\mathrm{mag}}(M_2))|F(M_1,M_2';M_1',M_2)|^2, \tag{45}$$

where

$$F(M_1,M_2';M_1',M_2)=\sum_\sigma C^{(S-1/2)M_2'}_{(1/2)\sigma SM_2} C^{(S-1/2)M_1'}_{(1/2)\sigma SM_1}\delta_{\sigma+M_1,M_1'}\delta_{\sigma+M_2,M_2'}. \tag{46}$$

Figure 5 shows the steplike behavior of the magnetic component of the current, which determines the interelectrode current, as a function of the field strength h; this behavior is due to the presence of single-ion anisotropy of the ion that captures an excess electron during electron transport through the molecular chain. Since, in the absence of an excess electron the single-ion anisotropy is weak ($K\gg K^0$), the plateau-switching field is determined by expressions (37) and (38). One notices in particular the sharp decrease of the current with increasing magnetic field when the local magnetic fields acting on the magnetic ions have different directions. Under conditions of saturation, when $h>h_0s=h_0(M_1'=-S+1/2)$, the analytical expressions for the magnetic factors have the form

$$\eta(h)=\frac{(2S)^2}{(2S+1)^2},\quad (\mathbf{h}_1\uparrow\uparrow\mathbf{h}_2)$$

$$\eta(h)=\frac{2S}{(2S+1)^2},\quad (\mathbf{h}_1\uparrow\downarrow\mathbf{h}_2), \tag{47}$$

and so the current decreases by a factor of $2S$ when the direction of the magnetic field is changed.

4.3. *N* paramagnetic electron localization centers

The general expressions (6)–(15) found above can be used to investigate various cases of the formation of an interelectrode current passing through a molecular chain. Let us consider the regime of one-way electron transport, when the current is formed by hops of an electron from left to right, i.e., when

$$\chi_{-L}=r_2=r_3=\ldots=r_N=\chi_R=0. \tag{48}$$

A similar situation is realized when $V>V_{\mathrm{res}}$. Under condition (48) the flux (9) is given by the simple expression $J\approx\chi_L$, while $U_n\cong\chi_a/g_n$ $(n=1,2,...,N-1)$ and $U_N\cong\chi_L/\chi_{-R}$. Then the current (7) takes the form

$$I=e\chi_L\frac{1}{1+\chi_L/\chi_{-R}}\prod_{n=1}^{N-1}\frac{1}{1+\chi_L/g_n}. \tag{49}$$

In contrast to a wire with two centers, where the bridge length between centers was assumed large, for a wire with $N>2$ the distances between electron localization centers can be less than the distances between the electrodes and the corresponding terminal groups. Then the inequality $\chi_L\ll g_n$ can hold, which means that the limiting stage of the interelectrode electron transport process is the hopping of the electron from electrode L to the terminal center 1 and from

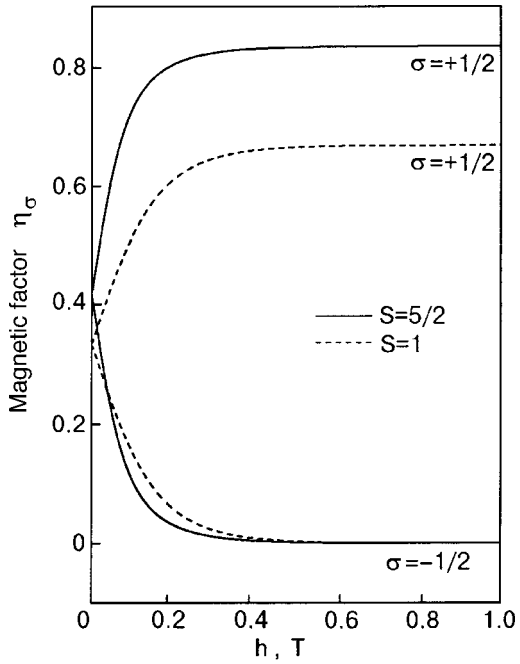

FIG. 6. Spin polarization of the current coming out of electrode R under conditions of a one-way transport of electrons through a molecular wire containing N centers. The limiting stage of the kinetic process is the hopping of an electron from electrode R to terminal group 1. Here η_σ was calculated according to formula (50) for $K^0=0$.

the terminal center N to electrode R. The corresponding expression (49) for the current reduces to $I \simeq eX_L X_{-R}/(\chi_L + \chi_{-R})$. Let the bridge B_2 be shorter than B_1, so that $\chi_L \ll \chi_{-R}$. Then the current $I \simeq e\chi_L = I_0 F_L(h)$, where $I_0 = e\Sigma_{\mathbf{k}} Q_{L\mathbf{k}}$, and the magnetic-field-independent quantity $Q_{L\mathbf{k}}$ is defined in (29). Since the magnetic factor $F_L(h)$ is specified by expression (30), the current can be represented in the form (36), where now

$$\eta_{\pm 1/2}(h) = \frac{S}{2S+1}[1 \pm B_S(\mu_B g h S/k_B T)]. \tag{50}$$

Figure 6 shows that at high magnetic fields only the electrons entering from electrode L and having spin projection $\sigma = +1/2$ can be captured by terminal group 1. Therefore, at low temperature the current coming from electrode L will immediately be sharply polarized.

If the formation of the interelectrode current is limited by the hopping of the electron between localization centers in the wire, then the $I(h)$ dependence will have a complicated character, which will be given in a separate paper. We note only that on different parts of the wire the spin polarization of the current can be substantially different.

CONCLUSION

In this paper we have examined one possible scheme for the regulation of the interelectrode current by a magnetic field in a microelectrode–molecular-wire–microelectrode nanostructure when the molecular wire contains paramagnetic ions with a ''frozen'' orbital moment. The regulation is due to the influence of statistical and dynamical factors. The statistical factor determines the predominance of the weight of the state with the minimum projection of the spin of the paramagnetic ion. The dynamical factor determines the quantum probability of capture of the electron being transported by the paramagnetic ion and of escape of the electron from the paramagnetic ion. The probability of capture and escape is determined by the spin conservation laws, and limitations thus arise on the realization of hopping in the nanostructure under study. The spin conservation laws lead to both the blocking of the current by a high magnetic field and the spin polarization of the current. In this paper we have considered the situation where there is no spin–spin interaction between paramagnetic ions. Therefore the indicated effects of the magnetic field can be manifested only at low temperature ($\simeq 1$ K). These same effects become possible at much higher temperatures if instead of individual paramagnetic ions one uses exchange-coupled clusters of several paramagnetic ions. Then the spin state of each ion will be formed in the rather high magnetic field produced by the other ions of the cluster. In that way one can expect to make progress in molecular spintronics.

This study was performed as part of the Russia–Ukraine Project on Nanophysics and Nanoelectronics and the program of the National Academy of Sciences of Ukraine ''Research on Fundamental Problems of the Structure and Properties of Matter on the Macroscopic and Microscopic Levels'' (Subject No. 0102U002329).

*E-mail: epetrov@bitp.kiev.ua

[1] D. Goldhaber-Gordon, M. Montemerlo, J. C. Love, G. J. Opiteck, and J. C. Ellenbogen, Proc. IEEE **85**, 521 (1997).
[2] M. Reed, Proc. IEEE **87**, 652 (1999).
[3] A. Aviram and M. Ratner, Chem. Phys. Lett. **29**, 277 (1974).
[4] F. L. Carter (Ed), *Molecular Electronics*, Marcel Dekker, New York (1982).
[5] M. C. Petty, M. R. Bryce, and D. Bloor (Eds.), *An Introduction to Molecular Electronics*, Oxford University Press, New York (1995).
[6] Molecular Electronics, M. Ratner and J. Jortner (Eds.), Blackwell Science, Oxford (1997).
[7] A. Aviram and M. Ratner (Eds.), *Molecular Electronics: Science and Technology*, New York Acad. Sci., New York (1998).
[8] S. Datta, W. Tian, S. Hong, R. Reifenberger, and C. P. Kubiak, Phys. Rev. Lett. **79**, 2530 (1997).
[9] J. Chen, M. A. Reed, A. M. Rawlett, and J. M. Tour, Science **286**, 550 (1999).
[10] F. Moresco, G. Meyer, and K.-H. Rieder, Phys. Rev. Lett. **86**, 672 (2001).
[11] V. Mujica, A. Nitzan, Y. Mao, W. Davis, M. Kemp, A. Roitberg, and M. A. Ratner, in *Electron Transfer: From Isolated Molecules to Biomolecules*, Part Two, edited by J. Jortner and M. Bixon; Adv. Chem. Phys. **107**, 403 (1999).
[12] J. Seminario, A. G. Zacarias, and J. M. Tour, J. Am. Chem. Soc. **122**, 3015 (2000).
[13] E. G. Petrov and P. Hänggi, Phys. Rev. Lett. **86**, 2862 (2001).
[14] Y. Xue, S. Datta, and M. A. Ratner, J. Chem. Phys. **115**, 4292 (2001).
[15] L. Xing, Y. C. Chang, M. B. Salamon, D. M. Frenkel, J. Shi, and J. P. Lu, Phys. Rev. B **48**, 6728 (1993).
[16] M. N. Baibich, J. M. Broto, A. Fert, F. Nguyen Van Dau, F. Petroff, P. Etienne, G. Creuzet, A. Friederich, and J. Chazelas, Phys. Rev. Lett. **61**, 2472 (1988).
[17] G. E. W. Bauer, Phys. Rev. Lett. **68**, 1676 (1992).
[18] P. M. Tedrow, J. E. Tkaczyk, and A. Kumar, Phys. Rev. Lett. **56**, 1746 (1986).
[19] M. J. De Weert and S. M. Girvin, Phys. Rev. B **37**, 3428 (1988).
[20] G. Baum, E. Kisker, A. H. Mahan, W. Raith, and B. Reihl, Appl. Phys. **14**, 149 (1977).
[21] R. Fiederling, M. Klein, W. Ossau, G. Schmidt, A. Waag, and L. W. Molenkamp, Nature (London) **402**, 787 (1999).
[22] Y. Ohno, D. K. Young, B. Beschoten, F. Matsukura, H. Ohno, and D. D. Awschalom, Nature (London) **402**, 790 (1999).
[23] J. M. Kikkawa and D. D. Awschalom, Nature (London) **397**, 139 (1999).
[24] I. Malajovich, J. J. Berry, N. Samarth, and D. D. Awschalom, Nature (London) **411**, 770 (2001).
[25] E. G. Petrov, I. S. Tolokh, and V. May, Phys. Rev. Lett. **79**, 4006 (1997).
[26] E. G. Petrov, I. S. Tolokh, and V. May, J. Chem. Phys. **108**, 4386 (1998).
[27] E. G. Petrov, I. S. Tolokh, and V. May, J. Chem. Phys. **109**, 9561 (1998).
[28] J. P. Collman, J. T. McDevitt, G. T. Yee, C. R. Leidner, L. G. McCullough, W. A. Little, and J. B. Torrance, Proc. Natl. Acad. Sci. U.S.A. **83**, 4581 (1986).
[29] R. L. Carlin, *Magnetochemistry*, Springer, Berlin (1986).
[30] O. Kahn, *Molecular Magnetism*, VCH, New York (1993).
[31] V. V. Eremenko, *Introduction to the Optical Spectroscopy of Magnets* [in Russian], Naukova Dumka, Kiev (1975).
[32] C. J. Ballhausen, *Introduction to Ligand Field Theory*, McGraw-Hill, New York (1962), Nauka, Moscow (1964).
[33] D. A. Varshalovich, and A. N. Moskalev, and V. K. Khersonskii, *Quantum Theory of Angular Momentum*, World Scientific, Singapore (1988), Nauka, Moscow (1976).

Translated by Steve Torstveit

Noncollinear magnetic structures in an Fe/Si/Fe film with a ferromagnetic interlayer exchange interaction

A. B. Chizhik[a] and S. L. Gnatchenko

B. Verkin Institute for Low Temperature Physics and Engineering, National Academy of Sciences of Ukraine, pr. Lenina 47, 61103 Kharkov, Ukraine

M. Baran, K. Fronc, R. Szymczak, and R. Zuberek

Institute of Physics, Polish Academy of Sciences, Al. Lotnikow 32/56, 02-668 Warsaw, Poland
(Submitted January 22, 2002)
Fiz. Nizk. Temp. **28**, 885–889 (August–September 2002)

Results are presented from magnetic and magnetooptical studies of the magnetic configurations in a three-layer film Fe(30 Å)/Si(14 Å)/Fe(30 Å) in which ferromagnetic and biquadratic exchange between iron layers is observed and which also possesses cubic and uniaxial anisotropy. These studies were done at temperatures of 300 and 10 K. It was found that in the absence of magnetic field a noncollinear magnetic structure, the form of which changes with temperature, is observed in this system. A calculation of the stable noncollinear configurations is done on the basis of a model in which it is assumed that both the exchange interaction constant and the cubic and uniaxial anisotropy constants in the iron layer change with temperature. The values of the angles characterizing the magnetization direction in the iron layers in the stable noncollinear configurations are determined on the basis of a comparative analysis of the experimental data and the results of the calculation. It is shown that both the angle between the magnetization directions in the two iron layers and the direction of the easy axis of the system as a whole change with temperature.
[DOI: 10.1063/1.1511708]

Noncollinear magnetic structures in the layered system Fe/Si has been studied rather intensively in recent years.[1–7] These studies are motivated by the diversity of both the stable configurations themselves and the phase transitions between them, which are observed in a magnetic field or on changes in temperature. It is known that this diversity stems from the presence of a bilinear and a biquadratic exchange interaction between the iron layers and by the competition between these exchanges and between the exchange and the magnetic anisotropy. Layered structures of this type in which antiferromagnetic and biquadratic exchange exist simultaneously are now quite widely studied. On the other hand, until now there have been practically no experimental studies of the magnetic structures arising in Fe/Si layered structures, which have ferromagnetic together with the biquadratic exchange. It is therefore of interest to consider the results of Ref. 8, in which a three-layer Fe(30 Å)/Si(14 Å)/Fe(30 Å) film was studied by the ferromagnetic resonance (FMR) method at temperatures of 300 and 4.2 K. Analysis of the angular dependence of the FMR presented in Ref. 8 revealed the presence of bilinear and biquadratic ferromagnetic exchanges in the system. It was also shown that cubic and uniaxial anisotropy are present in the iron layers, and the easy axes of the uniaxial anisotropy in the two layers have different directions. It was observed that the cubic and uniaxial anisotropy constants have different temperature dependences in the two iron layers on account of the difference of the coefficients of thermal expansion of the materials of the films (Fe, Si) and substrate (GaAs).

The goal of the present study was to carry out magnetic and magnetooptical investigations of the magnetic configurations in a three-layer Fe(30 Å)/Si(14 Å)/Fe(30 Å) film, in which ferromagnetic and biquadratic exchange exist together with cubic and uniaxial anisotropy.

We present the results of measurements on an Fe(30 Å)/Si(14 Å)/Fe(30 Å) film grown by magnetron sputtering on a single-crystal GaAs substrate cut parallel to the (001) plane. The experiments were done at temperatures of 300 and 10 K with the aid of a magnetooptical setup utilizing the longitudinal Kerr effect and an MPMS-5 Quantum Design SQUID magnetometer. In the magnetooptical experiments, light from a He–Ne laser reflected off the surface of the film, passed through an analyzer, and fell on a photomultiplier. The external magnetic field was applied simultaneously in the plane of incidence of the light and the film plane, (001). As a result of the experiments we obtained the field dependences of the rotation angle Φ of the plane of polarization of the light reflected from the sample for different directions of the magnetic field in the film plane. The value of the rotation angle Φ in this experimental geometry is proportional to the projection M^* of the magnetization of the system on the magnetic field direction. In the experiments on the SQUID magnetometer the magnetic field was again applied in the film plane. The magnetic measurements gave the field dependences of M^* for different directions of the magnetic field in the film plane. The magnetooptical and magnetic-field dependences were normalized to the value Φ_S of the rotation angle in the saturated state and by the saturation magnetization M_S, respectively.

Figure 1 shows examples of the field dependences Φ/Φ_S

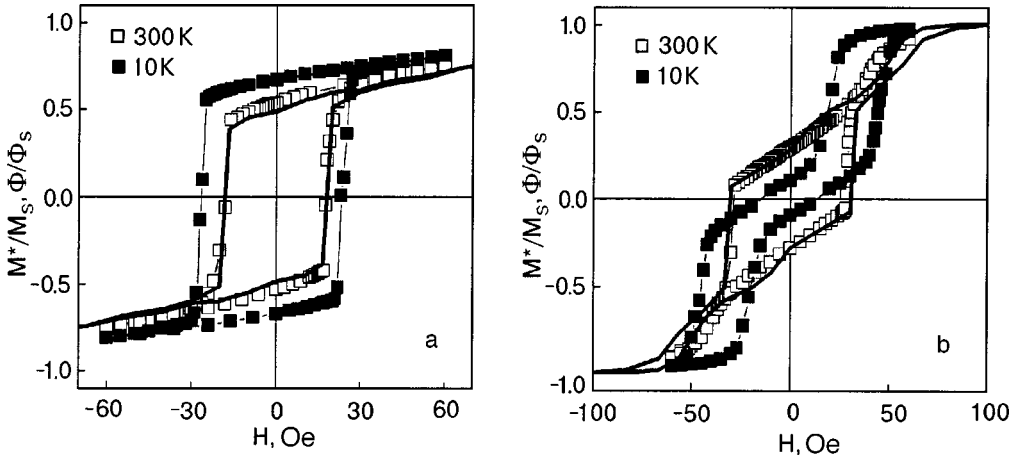

FIG. 1. Field curves of the projection of the magnetization on the magnetic field direction (points) and of the angle of rotation of the plane of polarization of reflected light (curves) for two magnetic field directions in the film plane: $\alpha=-45°$ (a) and 90° (b). The magnetooptical curves were measured at $T=300$ K.

and M^*/M_S for two directions of the magnetic field. The angle α is measured from the [100] direction. The problem addressed in the present study was to determine experimentally the magnetic configuration of the system in the absence of magnetic field. For this reason during the analysis of the experimental results, our attention was directed toward finding out how the normalized projection of the magnetization M_R^*/M_S and the normalized rotation angle Φ_R/Φ_S of the plane of polarization measured in zero magnetic field varied with the angle α at the two temperatures investigated.

Figure 2 shows the dependence of Φ_R/Φ_S on the angle α at 300 K and the dependence of M_R^*/M_S on that angle at 300 and 10 K. The experimental angular dependences are described rather well by the function $a\cos(\alpha-\beta)$ (the dotted curves in Fig. 2). Here $a=0.99$ and $\beta=26°$ at 300 K, and $a=0.99$ and $\beta=7°$ at 10 K. Analysis of the experimental results on the assumption that the magnetic moments inside the two iron layers are ordered ferromagnetically and that the magnetization in the first and second iron layers make angles of θ_1 and θ_2 with the [100] direction (see the inset in Fig. 2), we can draw the following conclusion. The fact that the experimental curves are described well by the function $a\cos(\alpha-\beta)$ attests to the fact that for each temperature the experimental points correspond to the projections of the magnetization of only one stable noncollinear configuration.

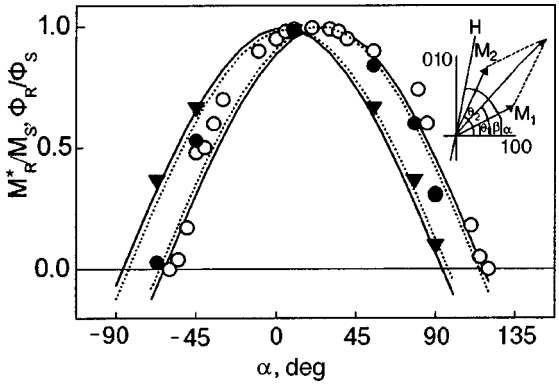

FIG. 2. Experimental angular dependence Φ_R/Φ_S at a temperature of 300 K (○) and of M_R^*/M_S at temperatures of 300 K (●) and 10 K (▼). The dashed curves show an approximation of the experimental results by the function $a\cos(\alpha-\beta)$. The solid curves show the calculated angular dependence of the projection of the magnetization of the stable state of the system on the magnetic field direction for 300 and 4.2 K.

In the general case in the system under study in the absence of magnetic field, depending on what direction the magnetic field is applied in during magnetization reversal, one of several stable (absolutely stable or metastable) angular configurations can be obtained.[4] In that case the angular dependence of the projection of the magnetization would not be described by a simple $\cos\alpha$ function, since in zero magnetic field after magnetization reversal in different directions, different angular configurations could be realized.

A stable angular configuration in the film under study is described by a pair of angles θ_1 and θ_2, which determine the directions of the magnetic moments in the two iron layers. Here $(\theta_1+\theta_2)/2=\beta=26°$ at 300 K, and $(\theta_1+\theta_2)/2=\beta=7°$ at 10 K. Thus we can conclude that the stable noncollinear structure rotates by an angle of 19° in the (001) plane as the temperature is lowered.

Our experimental results were analyzed in the framework of a theoretical model which, in accordance with the results of Ref. 8, incorporated the ferromagnetic and biquadratic exchange interaction between the two magnetic layers of iron and also the cubic and uniaxial anisotropy in the iron layers.

The expression for the energy of this system can be written in the form

$$E \quad I_1\cos(\theta_1-\theta_2) \quad I_2\cos^2(\theta_1-\theta_2)$$

$$K_{C1}d\cos^2\theta_1\sin^2\theta_1 \quad K_{C2}d\cos^2\theta_2\sin^2\theta_2$$

$$K_{U1}d\sin^2(\theta_1-\varphi_1) \quad K_{U_2}d\sin^2(\theta_2-\varphi_2), \tag{1}$$

where I_1 and I_2 are the bilinear (ferromagnetic) and biquadratic exchange interactions, K_{C1} and K_{C2} are the cubic anisotropy constants in the two iron layers, K_{U1} and K_{U2} are the uniaxial anisotropy constants in the two iron layers, d is the thickness of an iron layer, φ_1 and φ_2 are the angles specifying the direction of the easy axes of the uniaxial anisotropy in the iron layers (measured from the [100] direction). In the calculations we used the values of the constants which were obtained in Ref. 8 at temperatures of 300 and 4.2 K (see Table I).

TABLE I. Values of the constants used in the calculations CALL-OUTS: erg/cm^3 erg/cm^2 deg.

T, K	K_{C1}, erg / cm^3	K_{C2}, erg / cm^3	K_{U1}, erg / cm^3	K_{U2}, erg / cm^3	I_1, erg / cm^2	I_2, erg / cm^2	φ_1, deg	φ_2, deg
300	53000	12000	282000	110000	0.3	0.003	45	22
4.2	80000	107000	268000	304000	0.31	0.008	45	25

A numerical analysis of Eq. (1) showed that in this system there exist stable magnetic configurations which are described by the following set of angles specifying the directions of the magnetic moments in the two iron layers: $\theta_1 = 30°$ and $\theta_2 = 24°$ at 300 K (accordingly, $\beta_1 = (\theta_1 + \theta_2)/2 = 27°$, $\delta_1 = \theta_1 - \theta_2 = 6°$), and $\theta_1 = 10°$ and $\theta_2 = -2°$ at 4.2 K (accordingly, $\beta_2 = (\theta_1 + \theta_2)/2 = 4°$, $\delta_2 = \theta_1 - \theta_2 = 12°$). Thus the calculation showed that as the temperature is lowered, a rotation of the stable configuration in the (001) plane occurs, and the angle δ between the directions of the magnetic moments in the two iron layers increases. This may be due both to a stronger growth of the biquadratic exchange constant in comparison with the growth of the bilinear exchange constant as the temperature is lowered and to a difference in the temperature dependence of the cubic and uniaxial anisotropy constants in the two iron layers.

For comparing the calculated and experimental results we constructed the angular dependences of the projection of the total magnetization of the stable state of the system according to the formula $[\cos(\alpha - \beta_1) + \cos(\alpha - \beta_2)]/2$ for the two temperatures at which the calculation was done (the solid curves in Fig. 2). At low temperatures the experimental results obtained at 10 K were compared with the results of the calculation done for 4.2 K, since the constants needed in the calculations were obtained in Ref. 8 only at temperatures of 4.2 and 300 K. The rather good agreement of the experimental and calculated angular dependences attests to the fact that the form of the noncollinear configurations in the layered system under study is close to the form obtained as a result of the calculations. The experimentally observed features adequately reflect the concrete form of the stable angular configuration and also its calculated variation and rotation with temperature.

In closing, we should note that in this study we investigated stable configurations in a three-layer Fe/Si/Fe structure with ferromagnetic and biquadratic exchange. This was the first study of a layered structure in which ferromagnetic and biquadratic exchange coexist with a complex system of cubic and uniaxial anisotropies. The stable noncollinear configurations were calculated on the basis of a model in which it was assumed that both the exchange interaction constants and the cubic and uniaxial anisotropy constants in the iron layers vary with temperature. A comparison of the results of the calculation with experiment showed that in the absence of magnetic field this system has a noncollinear magnetic structure in which both the angle between the magnetization directions in the two iron layers and the direction of the easy axis of the system as a whole vary with temperature.

This article is dedicated to the 70th-year jubilee of Viktor Valentinovich Eremenko.

[a)]E-mail: chizhik@ilt.kharkov.ua

[1] E. E. Fullerton and S. D. Bader, Phys. Rev. B **53**, 5112 (1996).
[2] Y. Saito, K. Inomata, and K. Yusu, Jpn. J. Appl. Phys. **35**, L100 (1996).
[3] J. Kohlhepp, F. J. A. den Broeder, M. Valker, and A. van der Graaf, J. Magn. Magn. Mater. **165**, 431 (1997).
[4] A. B. Chizhik, K. Fronc, S. L. Gnatchenko, D. N. Merenkov, and R. Zuberek, J. Magn. Magn. Mater. **213**, 19 (2000).
[5] A. B. Chizhik, D. N. Merenkov, and S. L. Gnatchenko, Fiz. Nizk. Temp. **27**, 886 (2001) [Low Temp. Phys. **27**, 655 (2001)].
[6] G. J. Strijkers, J. T. Kohlhepp, H. J. M. Swagten, and W. J. M. de Jonge, Phys. Rev. Lett. **84**, 1812 (2000).
[7] R. R. Gareev, D. E. Burgler, M. Buchmeier, D. Oliggs, R. Schreiber, and P. Grunberg, Phys. Rev. Lett. **87**, 157 202prl);2001.
[8] R. Zuberek, M. Gutowski, K. Fronc, E. Mosiniewicz-Szablewska, W. Paszkowicz, E. Molins, A. Roig, and H. Szymczak, Mater. Sci. Forum **373**, 141 (2001).

Translated by Steve Torstveit

Manifestation of the Jahn–Teller effect in the EPR spectrum of the metalorganic complex $[Cu(en)2H_2O]SO_4$

A. G. Anders,* A. I. Kaplienko, O. V. Kravchina, and V. S. Bondarenko

B. Verkin Institute for Low Temperature Physics and Engineering, National Academy of Sciences of Ukraine, pr. Lenina 47, 61103 Kharkov, Ukraine

A. Feher,** M. Orendáč, A. Orendáčová, M. Kajňaková, and J. Černák

Department of Experimental Physics Faculty of Science, P. J. Šafárik University, Park Angelinum 9, 04154 Košice, Slovakia

(Submitted March 4, 2002)
Fiz. Nizk. Temp. **28**, 890–895 (August–September 2002)

The temperature dependence of the resonance spectrum of $[Cu(en)2H_2O]SO_4$ single crystals is investigated in the temperature range 2.3–60 K at a frequency of ~73 GHz. At a temperature $T>15$ K the angular dependence of the spectrum is described by a spin Hamiltonian of axial symmetry. At $T<15$ K a lowering of the symmetry to rhombic and a splitting the resonance line for a field orientation $\mathbf{H}\|\mathbf{b}$ are observed. These effects are discussed in a model of two nonequivalent Jahn–Teller centers with intercoupled dynamic distortions in the cell. The low-temperature behavior of the resonance line is due to critical broadening in the region of short-range magnetic order. © *2002 American Institute of Physics.* [DOI: 10.1063/1.1511709]

1. INTRODUCTION

The features of the magnetic resonance of octahedral complexes of divalent copper have stimulated a wide-ranging research on the diverse manifestations of the Jahn–Teller effect, mainly in crystals with high (cubic) symmetry of the local environment of the magnetic ion. However, the Jahn–Teller effect has been studied much less in systems with a local symmetry lower than cubic, which leads to a lifting of the degeneracy of the doublet and triplet electronic states of the ground orbital term $^2D_{5/2}$. Nevertheless, it has been established[1–3] that if the low-symmetry components of the crystalline field are small, then the EPR spectrum of these centers at low temperatures is characterized by a spin Hamiltonian of rhombic symmetry, and the centers themselves continue to demonstrate the characteristic Jahn–Teller behavior.

Systems containing more than one Jahn–Teller center in the cell are of great interest, as are highly concentrated and magnetically undiluted compounds containing Jahn–Teller complexes, since such objects can manifest cooperative effects.[4,5] In this case the properties of the centers in a pseudodegenerate electronic state can also largely determine the resulting structure and the magnetic behavior of the crystal.

In this paper we present the results of a study of the EPR spectrum of the $[Cu(en)2H_2O]SO_4$ crystal, which at low temperatures exhibits the properties of a Jahn–Teller system together with the characteristic behavior of a magnetically concentrated magnet in the region of short-range magnetic order.

2. FEATURES OF THE CRYSTAL STRUCTURE OF $[Cu(en)2H_2O]SO_4$ AND THE EXPERIMENTAL TECHNIQUE

The crystal structure of $[Cu(en)2H_2O]SO_4$ (en is ethylenediamine, $C_2H_8N_2$) at room temperature is monoclinic, characterized by the space group $C2/c$ (C_{2h}^6), and contains four formula units in a unit cell with parameters $a=7.232$ Å, $b=11.725$ Å, $c=9.768$ Å, and $\beta=105.5°$ (Ref. 6). The structure is made up of chains of distorted octahedra containing divalent copper ions. The chains lie along the a direction in the cell, the octahedra are noticeably elongated in that direction, and the apical oxygen ions also belong to SO_4^{2-} complexes, which connect the octahedra in the chains. The basal plane of the octahedra is formed by two oxygen ions which also belong to water molecules, and two nitrogen atoms of the ethylenediamine complex, which together form an isoceles trapezoid. Thus the local environment of the Cu^{2+} ion has rhombic symmetry, at minimum. The projection of the structure onto the ab plane is shown in Fig. 1.

The main measurements of the resonance spectra were made in the temperature interval 2.3–60 K at a wavelength $\lambda=4$ mm. This high-frequency range was chosen in order to increase the resolving power ($\approx 10^{-4}$) of the spectrometer with respect to the g factor. The error of measurement of the temperature was not more than 0.1 K in the interval 2.3–15 K and ~0.5 K at $T>15$ K. Measurements were made on single crystals with typical dimensions of $2\times0.3\times0.5$ mm. The error of orientation of the crystal with respect to the external field in the studies of the angular dependences was not more than 2°.

A series of test experiments was run for $\lambda\approx 8$, 6, 3, and 2 mm.

3. EXPERIMENTAL RESULTS

At relatively high temperatures ($T\geqslant 20$ K) the EPR spectrum of $[Cu(en)2H_2O]SO_4$ consists of a single symmetric line, whose angular dependence in an external field is described by the axial spin Hamiltonian

$$\hat{H}=g_{\|}\mu_B H_z S_z+g_{\perp}\mu_B(H_x S_x+H_y S_y)$$

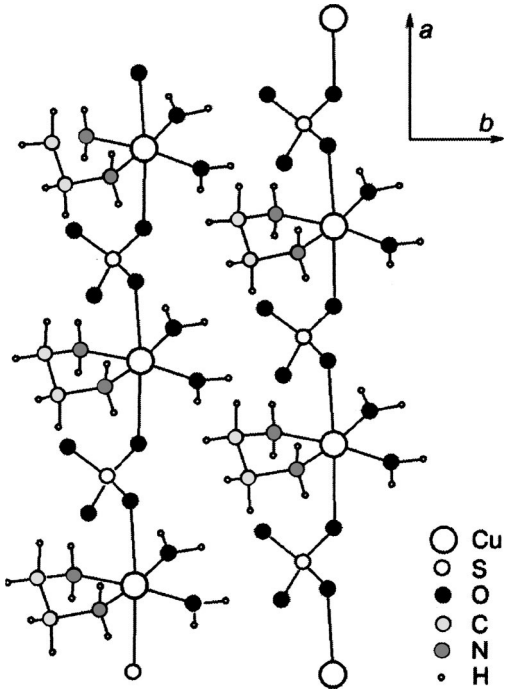

FIG. 1. Projection of the structure of $[Cu(en)2H_2O]SO_4$ on the ab plane.

with the effective g-factor values $g_{\parallel}=2.2909$ and $g_{\perp}=2.0671$. Here μ_B is the Bohr magneton, the Cu^{2+} ion has spin $S=1/2$, and the value of $g_{\parallel}$ corresponds to the external field orientation $\mathbf{H}\|\mathbf{a}$.

The hyperfine structure of the spectrum, which is due to the presence of a nuclear moment $I=3/2$ in the Cu^{2+} ion and is usually observed in systems with a low concentration of copper ions, is absent in $[Cu(en)2H_2O]SO_4$, a circumstance that is natural to link with the appreciable role of spin–spin interactions, which at 20 K form a rather narrow line of width $\Delta H\approx 25$ Oe.

As the temperature is lowered ($T<15$ K) the following substantial changes occur in the EPR spectrum.

1. The symmetry of the spectrum becomes rhombic and is characterized by three extremal values of the g factor. The directions of the principal axes z and x of the effective g-factor tensor coincide with the a and b directions of the cell, and the magnetic axis y is close to the c direction, making an angle $\beta-\pi/2$ with it.

2. For $\mathbf{H}\|\mathbf{x}$ a smooth splitting of the resonance line into two components of approximately equal energy occurs (Fig. 2), indicating the formation of two nonequivalent centers of the Cu^{2+} ions in the system. The values of the effective g factor for these centers at $T\leqslant 4.2$ K are $g_{x1}=2.0560$ and $g_{x2}=2.0528$.

3. For the orientations $\mathbf{H}\|\mathbf{z}$ and $\mathbf{H}\|\mathbf{y}$ no splitting of the resonance line is observed. At $T=4.2$ K the values of the effective g factor for these directions are $g_z=2.2725$ and $g_c=2.0663$.

4. Lowering the temperature leads to appreciable broadening of the resonance line for all orientations. This dependence is shown in Fig. 3 for the case $\mathbf{H}\|\mathbf{z}$.

4. DISCUSSION OF THE RESULTS

An attempt to explain the observed features of the resonance spectrum of $[Cu(en)2H_2O]SO_4$ can be made in terms

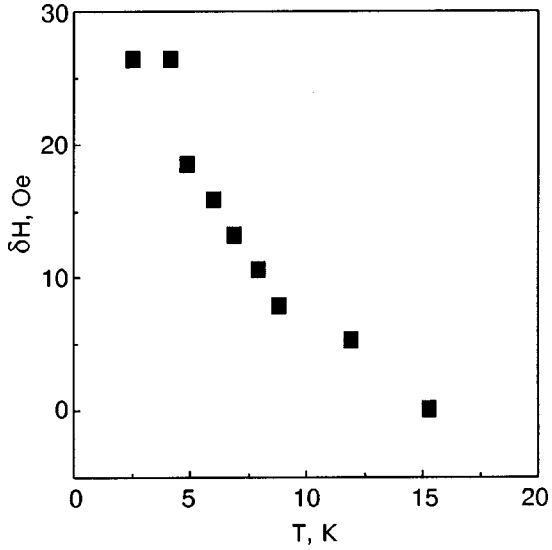

FIG. 2. Temperature dependence of the splitting of the resonance line of $[Cu(en)2H_2O]SO_4$ for an orientation of the external field $\mathbf{H}\|\mathbf{b}$.

of the features of the potential energy of a rhombic Jahn–Teller system. In Ref. 2 in a description of the Jahn–Teller effect in Tutton salts, a model was used in which, on account of the rhombic distortion of the local octahedral environment, the potential of the complex has a triple-well form, but the energy at the bottom of these wells becomes different. Here the following assumptions are made: the directions of the principal axes of the effective g-factor tensors, which are tied to the spatial diagonals of the octahedron of the local environments, are the same for states in all the potential wells; the extremal values of the g factor of these states is the same, and the directions of the distortions of the local octahedron change by a cyclic permutation on going from one state to another. At low temperature the system is localized in a state corresponding to the lowest potential well, and the parameters of the EPR spectrum characterize the ''static'' Jahn–Teller effect. Raising the temperature leads to occupa-

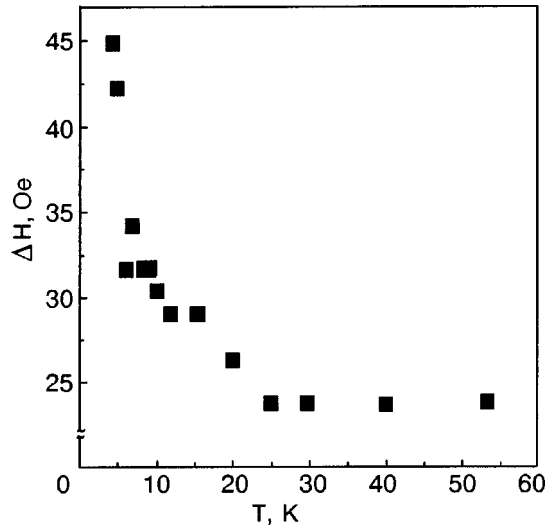

FIG. 3. Temperature dependence of the resonance linewidth of $[Cu(en)2H_2O]SO_4$ for $\mathbf{H}\|\mathbf{a}$.

tion of the high-lying states and the possibility of transitions between them; these correspond to a reorientation of the distortion axes of the complexes.

The rate $1/\tau$ of transitions between the states increases with increasing temperature and, since the EPR spectrum is observed at a fixed frequency ν, at a certain temperature such that $\nu \ll 1/\tau$ a complete averaging of the spectra will occur. The spectrum becomes isotropic, and this defines the ''dynamic'' Jahn–Teller regime. The averaging process occupies a certain temperature interval in which the observed magnetic parameters, primarily the values of the components of the g factor, vary in accordance with the Boltzmann factors for the occupation of the potential wells.

In Refs. 2 and 7 this model was applied to obtain a quantitative description of the temperature dependence of the components of the effective g factor and the parameters of the hyperfine interaction of the divalent copper ion, which is manifested in the dynamic Jahn–Teller effect. An alternative model for the dynamic vibronic coupling was also used for describing the temperature dependences $g(T)$ in a number of Tutton salts and other compounds in which, as a result of the Jahn–Teller effect, resonance spectra of isolated centers of rhombic symmetry are realized at low temperatures.[8]

It should be noted that the specific feature of the potential energy of Jahn–Teller complexes in Tutton salts is that the upper potential well is located considerably higher than the middle well. Therefore, in the investigated temperature interval the effects observed and analyzed here are actually due to a redistribution of the populations of only the two lower wells, and the temperature dependence and dynamic averaging are observed only for two components of the g factor and hyperfine structure parameter. As the temperature is raised, their values draw closer together, and the spectrum shows a tendency toward axial symmetry.

The EPR spectrum of $[Cu(en)2H_2O]SO_4$ is in many respects similar to the EPR spectra of copper-containing Tutton salts. As we said in Sec. 3, they also exhibit a smooth transition from rhombic to axial symmetry with increasing temperature, and only two components of the g factor vary, indicating that the two lower potential wells play the dominant role in the dynamics of the centers. An important difference is that at low temperatures there are two nonequivalent centers with coincident extremal directions of the effective g factor but with clearly different values of this parameter along the b direction, while for the other directions the g factors coincide and the absorption line becomes single.

This effect is indicative of the occurrence of a phase transition $[Cu(en)2H_2O]SO_4$ system at low temperatures. If as a result of this transition the dynamic distortions of the Jahn–Teller centers i and j that are formed are not intercoupled, then in accordance with the multiwell potential model[2,7] one expects that the g factors of these centers will have a temperature dependence of the form

$$g_{xi,j}(T) = g^0_{xi,j}\frac{K}{K+1} + g^0_{yi,j}\frac{1}{K=1};$$

$$g_{yi,j}(T) = g^0_{yi,j}\frac{K}{K+1} + g^0_{xi,j}\frac{1}{K+1},$$

where $g^0_{xi,j}$ and $g^0_{yi,j}$ are the values of the g factors in the respective directions for the two states of the center at the lowest temperature of the experiment, and $K = n_1/n_2 = \exp(\Delta E/kT)$ is the ratio of the populations of potential wells with an energy difference ΔE.

Here the expression for the temperature dependence of $\Delta g_x(T)$, which determines the splitting of the lines for $\mathbf{H}\|\mathbf{b}$, takes the form

$$\Delta g_x(T) = g_{xi}(T) - g_{xj}(T) = \Delta g^0_x(1 + e^{-\Delta E/kT})^{-1},$$

according to which $\Delta g_x(T)$ should decrease by a factor of two as the temperature is increased. This disagrees with the experimentally observed temperature dependence shown in Fig. 2, where the splitting of the line decreases to zero as the temperature is raised. Thus the model of isolated rhombic Jahn–Teller complexes does not agree with experiment.

One can therefore propose a model for the $[Cu(en)2H_2O]SO_4$ system wherein there are two nonequivalent octahedral complexes of the local environment of the Cu^{2+} ion, the dynamic distortions of which are intercoupled in the cell. The centers have rhombic symmetry of the spectrum with slightly different parameters g_b and a different energy of the potential wells. We note that the centrosymmetric cell of $[Cu(en)2H_2O]SO_4$, which contains four sites, admits their pairwise nonequivalence with respect to the twofold axis b, in agreement with the observed spectrum.

In this case the temperature dependence of the values of g_x for centers i and j become

$$g_{xi}(T) = g^0_{bi}\frac{K}{K+1} + g^0_{bj}\frac{1}{K+1};$$

$$g_{xj}(T) = g^0_{bj}\frac{K}{K+1} + g^0_{bi}\frac{1}{K+1},$$

and the temperature dependence of the line splitting for $\mathbf{H}\|\mathbf{b}$ corresponds to

$$\Delta g_x(T) = \Delta g^0_x \tanh\left(-\frac{\Delta E}{2kT}\right),$$

i.e., the difference of the g factors vanishes as temperature is increased. In Fig. 4 the experimental dependence of $\tanh^{-1}(\Delta g_x(T)/\Delta g^0_x)$ is plotted as a function of the inverse temperature. The fact that the points lie close to a straight line is consistent with a Boltzmann distribution of the population of the potential wells. The value obtained from this dependence for the energy splitting of the wells is $\Delta E = 12.2$ K, and on the whole the model of the dynamic Jahn–Teller effect for coupled centers more accurately describes the experimental results obtained for $[Cu(en)2H_2O]SO_4$.

It should be noted that in the multiwell models of Jahn–Teller centers the broadening of the resonance line with increasing temperature can be used to obtain information about the dynamics of the crystal lattice and, in particular, to estimate the values of the potential barrier between wells. For $[Cu(en)2H_2O]SO_4$ this possibility does not exist because of the low-temperature broadening of the resonance line, which can be noticed in Fig. 3; it may be an indication that the system is approaching a point of magnetic ordering. Indeed, an estimate of the energy of the exchange interaction in the system can be obtained from data on the value of the second

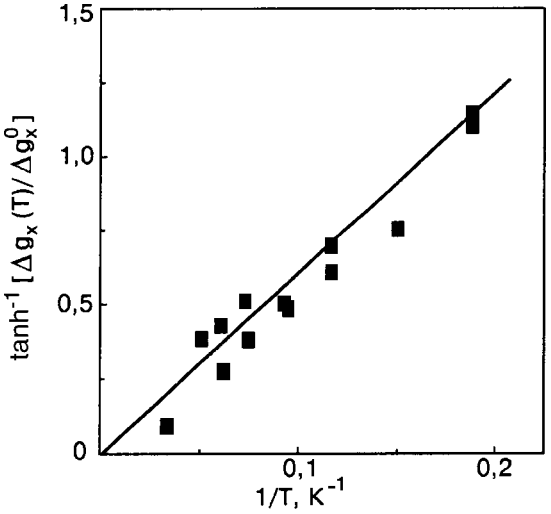

FIG. 4. Plot of $\tanh^{-1}(\Delta g_x(T)/\Delta g_x^0)$ versus $1/T$. The straight line corresponds to a value $\Delta E = 12.2$ K.

moment M_2 and the resonance linewidth ΔH observed in the experiment, in accordance with the known expression[9]

$$H_e = \frac{2M_2}{\Delta H}.$$

For $T > 30$ K, when the linewidth becomes temperature-independent and practically isotropic, these parameters are $M_2 = 5540$ Oe^2 and $\Delta H = 23.7$ Oe, which lead to a value $H_3 = 0.466$ kOe for the effective exchange field. This corresponds to a magnetic ordering temperature for this crystal of $T_N = 0.071$, which is below the working temperature range.

Thus in $[Cu(en)2H_2O]SO_4$ at $T < 15$ K a region of short-range magnetic order is realized in which critical broadening of the resonance line is observed, this broadening being a precursor of a magnetic phase transition point in this magnetically concentrated crystal.

5. CONCLUSIONS

The results of studies of the EPR spectrum of the magnetically concentrated compound $[Cu(en)2H_2O]SO_4$ at low temperatures permit the following conclusions.

1. The observed changes of the spectrum for $T < 15$ K, expressed in a lowering of its symmetry from axial to rhombic and splitting of the resonance line in the case of an external field orientation $\mathbf{H} \| \mathbf{b}$ can be attributed to a manifestation of the Jahn–Teller effect, which demonstrates a transition from the dynamic to the static regime of distortions of the octahedral complexes of the local environment of the Cu^{2+} ions.

2. The smooth splitting of the resonance lines observed for $\mathbf{H} \| \mathbf{b}$ is a consequence of the formation of two nonequivalent Jahn–Teller centers with different potential energies of the complexes, which in turn, attests to the occurrence of a second-order phase transition in the system at $T_c = 15$ K.

3. The temperature dependence of the resonance linewidth for $T < 15$ K corresponds to broadening in a critical region precursory to the establishment of long-range magnetic order in the crystal.

In closing, the authors gladly take this opportunity to thank V. V. Eremenko for his efforts in developing the cooperation between the B. Verkin Institute for Low Temperature Physics and Engineering, National Academy of Sciences of Ukraine and the P. I. Šafárik University in Košice, Slovakia in research on low-temperature magnetism.

We are grateful to I. S. Braude for x-ray orientation of the single crystal and to M. I. Kobets for making the high-frequency measurements of the spectrum.

*E-mail: aanders@ilt.kharkov.ua
**E-mail: feher@Kosice.upjs.sk

[1] G. L. Bir, Fiz. Tverd. Tela (Lenningrad) **18** 1627 (1976) [Sov. Phys. Solid State **18**, 946 (1976)].
[2] B. Silver and D. Getz, J. Chem. Phys. **61**, 638 (1974).
[3] I. B. Bersuker, *Electronic Structure and Properties of Coordination Compounds* [in Russian], Khimiya, Leningrad (1987).
[4] K. I. Kugel' and D. I. Khomskiĭ, Usp. Fiz. Nauk **136**, 621 (1982).
[5] M. D. Kaplan and B. G. Vekhter, *Cooperative Phenomena in Jahn–Teller Crystals*, Plenum Press, New York (1995).
[6] V. Menriques, M. Campos-Vallette, N. Lara, N. Gonzalez Tejeda, O. Wittke, G. Diaz, S. Diez, R. Muffoz, and L. Kriskovic, J. Chem. Crystallogr. **26**, 15 (1996).
[7] V. E. Petrashen, Yu. V. Yablokov, and R. L. Davidovich, Phys. Status Solidi B **101**, 117 (1980).
[8] M. J. Riley, M. A. Hitchman, and A. W. Mohammed, J. Chem. Phys. **87**, 3766 (1987).
[9] P. W. Anderson and P. R. Weiss, Rev. Mod. Phys. **25**, 269 (1953).

Translated by Steve Torstveit

Nonmonotonic temperature dependence of the spontaneous magnetization of the antiferromagnetic crystal $LiCoPO_4$

N. F. Kharchenko,* V. A. Desnenko, and Yu. N. Kharchenko

B. Verkin Institute for Low Temperature Physics and Engineering, National Academy of Sciences of Ukraine, pr. Lenina 47, 61103 Kharkov, Ukraine

R. Szymczak and M. Baran

Institute of Physics, Polish Academy of Sciences, Al. Lotnikow 32/46, PL-02-668, Warsaw, Poland
(Submitted April 17, 2002)
Fiz. Nizk. Temp. **28**, 896–904 (August–September 2002)

The temperature dependence of the magnitude of the weak ferromagnetic moment is measured in the many-sublattice antiferromagnetic magnetoelectric crystal $LiCoPO_4$. The dependence is found to be nonmonotonic—as the temperature is decreased below the Néel temperature T_N, the ferromagnetic moment initially increases and then decreases markedly. It reaches its highest value, close to 0.12 G, at a temperature of around 10.5 K, which is roughly $T_N/2$. The possible mechanisms for the appearance of weak ferromagnetism in $LiCoPO_4$ and the causes of the nonmonotonic temperature dependence of the spontaneous magnetic moment are discussed. Among the possible mechanisms, there is a preference for one in which the weak ferromagnetism is due to a nonuniform antiferromagnetic structure which is proposed for this crystal. © *2002 American Institute of Physics.* [DOI: 10.1063/1.1511710]

INTRODUCTION

This paper is a continuation of studies of the magnetic properties of the antiferromagnetic (AFM) magnetoelectric crystal $LiCoPO_4$, which is well known for its high (a record value for compounds of elements of the $3d$ group) magnetoelectric constant $\alpha_{xy}=9.2\times10^{-3}$ (30.6 ps/m).[1–7] Antiferromagnetic crystals of this family have been attracting particular attention recently. For example, the magnetoelectric and magnetic properties of the nickel and cobalt phosphates do not agree well with the symmetry of the magnetic structure determined by neutron diffraction methods for these AFM crystals. The presence of only off-diagonal nonzero components α_{xy} and α_{yx} of the magnetoelectric tensor[1,4] confirms the conclusion based on neutron diffraction measurements[8] that $LiCoPO_4$ has a collinear AFM structure with the Shubnikov symmetry group $Sh_{62}^{445}(Pnma')$. However, the hysteretic behavior of its magnetoelectric properties in a magnetic field and the presence of the characteristic magnetoelectric hysteresis loops of the ''butterfly'' type and also the possibility of bringing the crystal to a single-domain AFM state and of switching between collinear AFM states with opposite directions of the AFM vectors solely by means of a magnetic field[4–6] are inconsistent with the magnetic symmetry group found for $LiCoPO_4$ in Ref. 8. These properties indicate the possibility that weak ferromagnetism (WFM) exists in the crystal, but it has long eluded experimental observation in magnetic measurements.[8–10]

A more complex magnetic structure of $LiCoPO_4$ is also indicated by the behavior of the magnetic birefringence of linearly polarized light as a function of the magnitude of the magnetic field and the temperature—the change in the value of the birefringence is equal to the spontaneous value in an external magnetic field almost an order of magnitude smaller than the effective exchange field; the steplike change of the birefringence in a magnetic field much smaller than the field of the magnetic phase transition; the presence of a contribution to the birefringence which is linear in the field; and the pronounced hysteresis effects under conditions for which the sample should be found in a uniform single-domain AFM state.[11] Some possibilities for the formation of such a structure in $LiCoPO_4$ and $LiNiPO_4$ crystals are discussed in Ref. 6.

Recent magnetic measurements in $LiCoPO_4$ with a SQUID magnetometer have revealed features on the magnetization curve[12] which indicate that the antiferromagnetism in $LiCoPO_4$ is in fact uncompensated. And, although the observed spontaneous magnetic moment has a value only of the order of 0.12 G, its presence accounts for the fact that the AFM sample can be brought to a single-domain state by a magnetic field alone, without the application of an electric field. Unusual temperature dependence of the magnetization M in a static magnetic field has also been observed in $LiCoPO_4$. When a sample whose magnetic moment is initially directed opposite to the applied magnetic field is heated from helium temperature to 10 K in a magnetic field of 500 Oe, its magnetic moment increased in absolute value. This ''diamagnetic'' behavior indicates a nonmonotonic temperature dependence of the spontaneous moment, which is atypical for weak ferromagnets.[13–15] The goal of the present study was the experimental determination of the temperature dependence of the spontaneous magnetization of $LiCoPO_4$.

EXPERIMENT

The crystal structure of $LiCoPO_4$, like that of other isostructural lithium orthophosphates of transition elements, having the formula $LiMPO_4$ (M=Mn, Fe, Co, Ni) and be-

longing to the olivine family, is specified by the symmetry space group $Pnma = D_{2h}^{16}$. The unit cell contains 4 formula units. At room temperature the cell has the following dimensions: $a = 10.206$ Å, $b = 5.922$ Å, $c = 4.701$ Å.[10,16] The four cobalt ions are located in the four crystallographically equivalent c sites of the cell, which are arranged in pairs in two adjacent symmetry planes, the normal to which is parallel to the crystallographic axis $\mathbf{b} \| \mathbf{Y}$. The closest distance between Co^{2+} ions is in the corrugated layers oriented perpendicular to the axis $\mathbf{a} \| \mathbf{X}$. The Co^{2+} ions are surrounded by oxygen ions which form orientationally nonequivalent, rather strongly distorted octahedral sites with symmetry $m = C_s$. The exchange couplings between the ions of the transition elements in the crystals of this family have been analyzed in Ref. 17. The most strongly coupled pairs of ions, Co1–Co2 and Co3–Co4, are found in different corrugated layers. The exchange interaction between these ions acts via 125° antiferromagnetic Co–O–Co bonds. The next-nearest ions lie in the same layer. The exchange interaction between them acts via two pairs of bonds of the Co–O–P–O–Co type with 130° Co–O–P angles. Between the corrugated layers are PO_4 tetrahedra and LiO_6 octahedra, and therefore the exchange interaction between cobalt ions in the neighboring layers is much weaker than the interaction between nearest-neighbor ions in the layer. The weak coupling between ions of neighboring layers is due to pairs of Co–O–P–O–Co ion chains, which include 128°, 122°, and 95° Co–O–P links, and by Co–O–Li–O–Co ion chains. The bonds with Li^+ ions in them are weaker than the bonds acting via the P^{5+} ions.[17]

Since the ligand environment of Co^{2+} is substantially different from octahedral, the low-symmetry crystalline field causes substantial magnetic anisotropy, both at low and at high temperatures,[9] and a strong anisotropy of the g factor. In the doped crystal $LiMgPO_4$:Co the principal values of the g factor obtained in EPR studies were equal to 6.16, 4.14, and 2.53.[10] At low temperatures, when $T < D/k$, where D is the energy distance to the nearest excited state, the magnetic sites Co^{2+} in $LiCoPO_4$ are nearly Ising-like, and as a consequence of the hierarchy of exchange couplings, the behavior of the AFM structure of $LiCoPO_4$ can be described by a quasi-two-dimensional AFM Ising model. The dependence of the magnetization of the $LiCoPO_4$ single crystal in a magnetic field directed along the antiferromagnetic axis has a broad hump that is typical for two-dimensional systems, with a maximum at $T_{max} = 25$ K,[12] which is significantly higher than the the Néel temperature $T_N = 21.9$ K. However, the ratio T_{max}/T_N is only 1.14, substantially lower than the value 1.537 obtained for a square Ising lattice[18] but significantly higher than the value 1.025 for a simple cubic AFM Ising lattice.[19]

Measurements were made on a single-crystal sample of $LiCoPO_4$ in the form of a parallelepiped with dimensions of $0.96 \times 1.22 \times 1.76$ mm and a mass of 7.46 mg. The sample was provided to us by Prof. M. Mercier of the Technological University, Montlucon, France and Prof. H. Schmid of Geneva University. Experiments were done on the same sample independently on two devices: a Quantum Design MPMS-5 magnetometer at the Institute of Physics, Polish Academy of Sciences (IP-PAS), and on a SQUID magnetometer developed at the B. Verkin Institute for Low Temperature Physics and Engineering, National Academy of Sciences of Ukraine, Kharkov (ILT-NASU).

It follows from the magnetic measurements[12] that the coercive field for the hysteresis curve of the magnetization of the sample at a temperature of 15 K is 20–40 kOe. Therefore, one would expect that, up to the Néel temperature, the temperature dependences of the spontaneous magnetic moment could be extracted from the temperature dependence of the magnetization of the sample when it had been pre-cooled in a magnetic field applied along the **b** axis in two opposite directions. The dependence of the magnetization on the magnetic field strength at temperatures less than the Néel temperature is described to good accuracy by a third-degree polynomial. The contribution of the cubic term to the magnetization becomes important at temperatures greater than 10 K.[12] Although at 5 K this contribution is negligible at fields of up to 30 kOe, at a temperature of around 10 K it becomes substantial at a field of only 20 kOe. Therefore, it must be taken into account when extracting the spontaneous magnetization from the $M(T)$ curves for $H > 10$ kOe. Prior to the measurements the sample was cooled from a temperature of around 40 K, roughly double the Néel temperature, to helium temperature in a magnetic field directed along the crystallographic axis **b**. Measurements of the temperature dependence of the magnetic moment of the sample were made as the sample was heated in a magnetic field applied in the same direction as during cooling and then with the opposite direction of the field. During the measurements the temperature was set to an accuracy of 0.02 K or better.

RESULTS

The WFM moment was extracted from the results of measurements of the temperature dependence of the magnetization on the MPMS-5 magnetometer at magnetic field strengths of 50, 10, and 0.5 kOe. The temperature dependence of M/H is presented in Fig. 1. Prior to the measurements at $H = 0.5$ kOe the sample was cooled in the residual field of the solenoid, which was not over 20 Oe and was directed opposite to the field in which the measurements

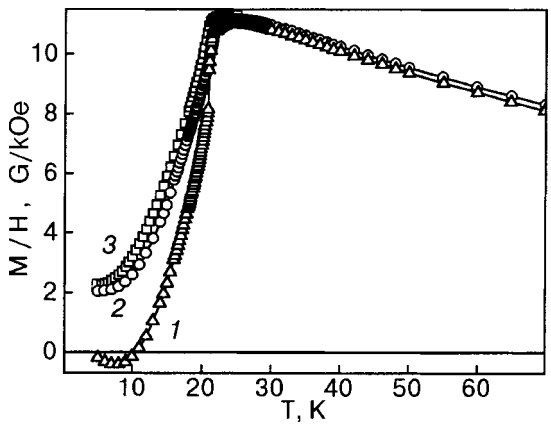

FIG. 1. Temperature dependence of the ratio of the magnetization to the magnetic field strength for different fields H [kOe]: 0.5 (*1*), 10 (*2*), and 50 (*3*). Prior to the measurements the sample was cooled to helium temperatures in fields H_{FC} [kOe]: ≈ -0.02 (residual field of the solenoid) (*1*), $+10$ (*2*), and $+50$ (*3*). $\mathbf{H} \| \mathbf{b}$.

would be taken. The orientation and magnitude of the field during the cooling of the sample prior to the measurements in fields of 10 and 50 kOe were the same as during the measurements.

The experimentally obtained values of the magnetization in the different fields are substituted into a system of three equations:

$$M(T)_i = M_0(T) + \chi_{\parallel}(T)H_i + \beta(T)H_i^3, \quad (1)$$

where $i=1, 2, 3$ and $H_1=0.5$ kOe, $H_2=10$ kOe, $H_3=50$ kOe, which was then solved for the spontaneous magnetization $M_0(T)$, the magnetic susceptibility $\chi_{\parallel}(T)$, and the nonlinear susceptibility $\beta(T)$ on the assumption that these values are independent of the strength of the field. The resulting function $M_0(T)$ is shown in Fig. 2 (curve *1*). Also shown are the functions $M_0(T)$ obtained from the same samples by solving Eqs. (1) without the cubic term for the pairs of $M(T)$ curves in fields of 0.5 and 10 kOe (curve *2*) and 0.5 and 50 kOe (curve *3*). We see that the influence of the term cubic in H is important at 50 kOe, and curve *3* cannot represent the function $M_0(T)$. We note that the temperature dependence of the spontaneous magnetization obtained from the M/H curves for $H=0.5$ kOe and $H=10$ kOe have a slight jump at 15 K. From these same data we also obtain nonzero values of M_0 for temperatures $T>T_N$. Since spontaneous magnetization should be absent at these temperatures, it can be assumed that the steplike changes of M_0 at 15 K were caused by uncontrolled noise.

To convince ourselves of the reliability of the temperature dependence obtained for the spontaneous magnetization, we made measurements of the magnetization of this same $LiCoPO_4$ sample as a function of temperature in low magnetic fields on a SQUID magnetometer at ILT-NASU. The fields strength was 300, 200, 100, 50, and 0 Oe. Measurements of $M(T)$ in this case, as before, were made in a magnetic field oriented along the crystallographic axis **b** after the sample had been cooled from a temperature above T_N to 4.2 K. The direction of the fields during cooling and measurement were the same (+FC) or opposite (−FC). The sequence of operations was as follows. In a magnetic field

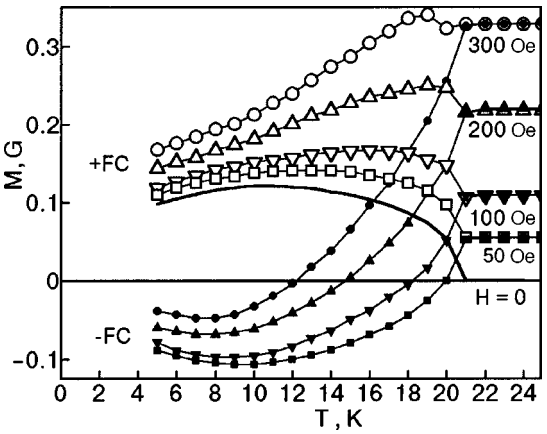

FIG. 3. Temperature dependence of the magnetization of the $LiCoPO_4$ crystal in a magnetic field $\mathbf{H}\|\mathbf{b}$ obtained after the sample had been cooled in fields H_{-FC} and H_{+FC}. The solid curve is for a sample that had been cooled in the Earth's magnetic field.

$H_{-FC}=-50$ Oe the crystal was cooled from 30 to 4.2 K, and then the field was decreased to zero and a field $H=+50$ Oe was applied, and the $M_{-FC}(T)$ curves were measured during heating. After a temperature of 30 K was reached, the sample was again cooled to 4.2 K in a field $H_{+FC}=+50$ Oe, and measurements of $M_{+FC}(T)$ were made in this field. The curves obtained for the temperature dependence of the magnetization of the $LiCoPO_4$ crystal are presented in Fig. 3.

Since the cubic contribution in a field $H\sim 300$ Oe is not more than 1.5×10^{-6} G (2×10^{-3}% of the maximum value of M_0), this contribution was not taken into account in determining $M_0(T)$. The temperature dependence of the spontaneous magnetization was determined as half the difference of the functions $M_{+FC}(T)$ and $M_{-FC}(T)$ obtained at magnetic fields strengths H_i equal to 50, 100, 200, and 300 Oe:

$$M_0(T)_i = \frac{M_{+FC}(T)_i - M_{-FC}(T)_i}{2}. \quad (2)$$

The calculated values of $M_0(T)$ are presented in Fig. 4. Here the dashed curve shows the corrected function $M_0(T)$

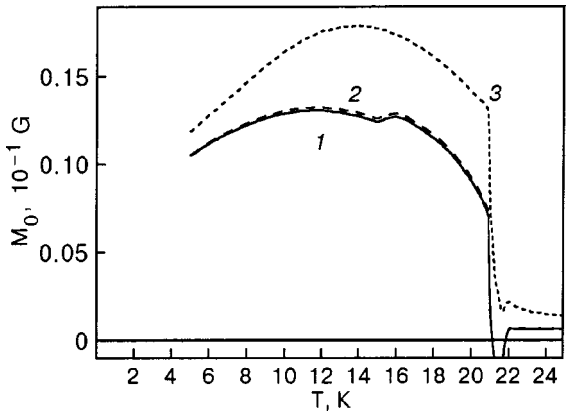

FIG. 2. Temperature dependence of the spontaneous magnetization obtained from the M/H curves in Fig. 1. M_0 is found as the solution of a system of three equations of the type (1) with $i=1$, 2, and 3 (curve *1*); $i=1$ and 2 (curve *2*); $i=1$ and 3 (curve *3*). For curves *2* and *3* the extraction of the spontaneous magnetization was done without taking into account the term cubic in H in Eq. (1).

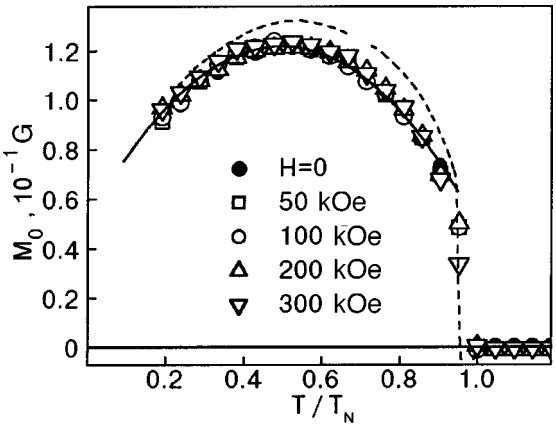

FIG. 4. Temperature dependence of the spontaneous magnetization extracted from the $M(T)_H$ curves shown in Fig. 3. The dashed curve shows the corrected dependence $M_0(T)$ determined from the experiments in high magnetic fields. The solid curve is the parabola $f(T)=0.122-6.5\times10^{-4}(T-10.4)^2$.

obtained from a series of experiments done at IP-PAS (a constant quantity equal to the value of the step observed near 15 K was subtracted from the data for $T>16$ K).

Comparing the results obtained independently in the two experiments, one can see that the values of the spontaneous moment are close—their difference is not more than 10%—and the character of the behavior of the $M_0(T)$ curves is the same—$M_0(T)$ is nonmonotonic and has a broad maximum near 11 K. Thus these two mutually complementary experiments confirm the conclusion that the antiferromagnetism of lithium cobalt phosphate is uncompensated, and the temperature dependence of the spontaneous magnetic moment differs from the behavior of $M_0(T)$ ordinarily observed in weak ferromagnets. The function $M_0(T)$ is almost symmetric about the maximum $M_0^{\max}$, which is reached at a temperature close to $(1/2)T_N$, and in a wide temperature interval 5–18 K ($0.2<T/T_N<0.9$) it has a parabolic character. The solid curve in Fig. 4 is a plot of the function $f(T)=0.122-6.5\times10^{-4}(T-10.4)^2$.

DISCUSSION

Let us consider the possibility of a spontaneous magnetic moment arising in the orthorhombic $LiCoPO_4$ crystal from the standpoint of the symmetry of the crystal. The possible antiferromagnetic modes in crystals described by the group $Pnma(D_{2h}^{16})$ can have the structure $\mathbf{L}_1=\mathbf{S}_1-\mathbf{S}_2+\mathbf{S}_3-\mathbf{S}_4$, $\mathbf{L}_2=\mathbf{S}_1-\mathbf{S}_2-\mathbf{S}_3=\mathbf{S}_4$, and $\mathbf{L}_3=\mathbf{S}_1+\mathbf{S}_2-\mathbf{S}_3-\mathbf{S}_4$, or **G**, **A**, and **C**, respectively, in the notation adopted in earlier papers on the description of the antiferromagnetism of magnetic *c* sites in other crystals of the same symmetry.[7,13] Table I shows the permutation of the *c* sites by operations of the symmetry group *Pnma* and indicates the parity of the AFM vector with respect to these operations. For the site numbering scheme adopted in Table I, which corresponds to that of Ref. 6 and is different from that in Refs. 7 and 13, the strongest AFM exchange coupling occurs in the pairs of nearest-neighbor ions Co1, Co2 and Co3, Co4.

It has been established by neutron diffraction methods that $LiCoPO_4$ has AFM ordering of the L_{2y} type, in which the spins of the cobalt ions are oriented along the **b** axis.[8] For this ordering of the spins the operation of spatial inversion in the *Pnma* group becomes odd—the direction of the AFM vector L_{2y} on inversion is changed to the opposite. The loss of a center of symmetry at the transition to the magnetic group *Pnma′* makes it possible for a magnetoelectric effect to appear but forbids the appearance of ordinary weak ferromagnetism. Oddness under the inversion operation in the crystal-chemical symmetry group forbids the appearance in the thermodynamic potential of the usual invariants of the form $L_{2i}M_i$, which would correspond to Dzyaloshinskiĭ–Moriya interactions.[13,21,22] The observation of a WFM moment in the magnetoelectric crystal $LiCoPO_4$ is not inconsistent with the answer, in the negative, to the question asked in the title of Ref. 20: can WFM and the magnetoelectric effect coexist in an AFM crystal? Although Ref. 20 talks about the incompatibility of these phenomena, in that paper the case when only uniform single-mode (or single-vector) AFM ordering is present was understood, in which case the operations of the crystal-chemical symmetry can be divided into even and odd with respect to their action on the AFM vector. The presence of WFM in $LiCoPO_4$ attests to its complex AFM structure, which may be represented as a superposition of one or two odd and one even AFM mode. The center of inversion of the crystal-chemical cell of $LiCoPO_4$ is odd with respect to the AFM vectors $\mathbf{L}_2$ and $\mathbf{L}_3$ but even with respect to $\mathbf{L}_1$. Therefore the mode $\mathbf{L}_1$ should be present in the AFM structure of $LiCoPO_4$.

Upon the appearance of a WFM moment $\mathbf{M}_0\|\mathbf{b}\|\mathbf{Y}$ the magnetic group of the crystal will lose the symmetry operations $\overline{2}_x/\tau_1$ and $2_z/\tau_3$, which connect the ions from different corrugated layers. It would seem that the absence of a symmetry relation between the magnetic moments of the ions from different layers coupled weakly to one another could lead to weak ferrimagnetism and to a diversity of possible variants of the temperature behavior of the resulting spontaneous moment. However, in $LiCoPO_4$ the cobalt ions occupy only crystallographically equivalent sites. No structural changes occur upon magnetic ordering, and the magnetic sites retain their equivalence; consequently, only weak ferromagnetism but not ferrimagnetism can arise in $LiCoPO_4$.

If it is assumed that the AFM structure of the $LiCoPO_4$ crystal is uniform and its weak ferromagnetism is due to noncollinearity of the magnetic moment vectors of the sublattices or to a slight difference of their lengths, then the weak-ferromagnetic moment in it can be described only with the aid of fourth-order invariants. In this case the appearance of WFM may be due to interactions not lower than fourth-order in the spins—biquadratic and four-spin interactions.[23] In the presence of the fundamental mode of antiferromagnetic ordering—the antiferromagnetic vector $L_{2y}=S_{1y}-S_{2y}-S_{3y}+S_{4y}$, the appearance of a WFM moment along the **b** axis can be described by several 4th-order invariants. They can be composed by starting from the table of transformations of the projections of the magnetic vectors (see Table II) and may be grouped into the following three groups:

1) invariants of three-dimensional noncollinear two-vector AFM structures with vectors $\mathbf{L}_1$ and $\mathbf{L}_2$,

$$L_{2y}M_yL_{1z}L_{2x},\quad L_{2y}M_yL_{1x}L_{2z}; \tag{3}$$

TABLE I. Transformation of the *c* sites and the change of the directions of the antiferromagnetic vectors in the $LiCoPO_4$ crystal under the operations of the symmetry group *Pnma*.

Co site No.	$\frac{2_x}{\tau_1}$	$\frac{2_y}{\tau_2}$	$\frac{2_z}{\tau_3}$	$\bar{1}$	$\frac{\bar{2}_x}{\tau_1}$	$\frac{\bar{2}_y}{\tau_2}$	$\frac{\bar{2}_z}{\tau_3}$
1	4	3	2	3	2	1	4
2	3	4	1	4	1	2	3
3	2	1	4	1	4	3	2
4	1	2	3	2	3	4	1
AFM vector							
$\mathbf{L}_1$	−	+	−	+	−	+	−
$\mathbf{L}_2$	+	−	−	−	−	+	+
$\mathbf{L}_3$	−	−	+	−	+	+	−

TABLE II. Transformation of the projections of the magnetic vectors and the unit vectors by the generators of the group $Pnma$.

Vector projections	$\bar{1}$	$\frac{\bar{2}_y}{\tau_2}$	$\frac{2_z}{\tau_3}$	Vector projections	$\bar{1}$	$\frac{\bar{2}_y}{\tau_2}$	$\frac{2_z}{\tau_3}$
M_x, L_{1z}	+	−	−	L_{2x}, L_{3z}	−	−	+
M_y	+	+	−	L_{2y}	−	+	+
M_z, L_{1x}	+	−	+	L_{2z}, L_{3x}	−	−	−
L_{1y}	+	+	+	L_{3y}	−	+	−
x	−	+	−	P_x	−	+	−
y	−	−	−	P_y	−	−	−
z	−	+	+	P_z	−	+	+

2) invariants of planar noncollinear three-vector AFM structures in which the magnetic moments of the ions lie in the (001) plane or in the (100) plane, with nonzero AFM vectors $\mathbf{L}_1$, $\mathbf{L}_2$, and $\mathbf{L}_3$,

$$L_{2y}M_yL_{1x}L_{3x},\ L_{2y}M_yL_{1z}L_{3z}; \tag{4}$$

3) an invariant of a collinear three-vector structure,

$$L_{2y}M_yL_{1y}L_{3y}. \tag{5}$$

The observed nonmonotonic temperature dependence of the WFM moment is indicative of a competition among different mechanisms leading to WFM in a uniform AFM crystal. If the WFM were due to interactions described by invariants of groups (3) and (4), it would be hard to expect nonmonotonic temperature dependence of the WFM moment in the absence of competition among different mechanisms. The effective fields due to the presence of ''transverse'' components of the AFM vectors $\mathbf{L}_2$, $\mathbf{L}_1$, and $\mathbf{L}_3$ and which lead to weak ferromagnetism can give rise to a temperature dependence of the WFM moment governed by the temperature dependence of the product $L_{2y}L_{\alpha i}L_{\beta j}$, which can qualitatively resemble a dependence of the form $M_\alpha(T)^3$, where $M_\alpha(T)$ is the sublattice magnetization. In this case one would expect to see the usual temperature dependence of the WFM moment, going to saturation as the temperature approaches absolute zero. In the presence of competing mechanisms, however, one can expect nonmonotonic temperature dependence of M_0 but with a maximum near the Néel temperature. In this case the temperature dependence of the WFM moment will be similar to that observed in YVO_3 crystals,[14,15] where the WFM moment described by the usual second-order Dzyaloshinskiĭ invariant changes strongly with temperature on account of a competition between the single-ion anisotropy and the antisymmetric exchange interaction.

If, on the other hand, the WFM is longitudinal, preserving the collinearity of the AFM structure, and is described by a single invariant of the third group (5), then one can expect a very strong temperature dependence similar to that of $(\chi_\parallel)^2M(T)_i$ and qualitatively similar to the temperature dependence of the longitudinal components of the magnetoelectric tensor, e.g., α_{33} in the antiferromagnet Cr_2O_3 (Ref. 28). Although such dependence also reflects the main feature of the temperature dependence of the magnetic moment observed in $LiCoPO_4$—a substantial decrease in value when the crystal is cooled to a temperature much less than T_N, it does not fully describe the experimental temperature dependence of the WFM moment. At temperatures much less than T_N one cannot expect substantial changes of the longitudinal WFM moment with temperature. The maximum value of the WFM moment should be reached at a temperature which is also close to the Néel temperature. The observed behavior of $M_0(T)$ is characterized by substantial changes with temperature even for $T/T_N<0.25$. Therefore it is necessary to consider other possible causes of the WFM moment.

One such possible cause of the WFM is due to the proposed presence in $LiCoPO_4$ of a nonuniform regular or irregular weak antiferromagnetic order. The possibility that modulated WFM structures which are described by invariants linear in the first spatial derivatives of the magnetic vectors and which are similar to Lifshitz invariants can arise in AFM crystals having an odd center of inversion has been considered in many papers (see, e.g., Refs. 6 and 23–26). The symmetry of the $LiCoPO_4$ crystal allows an invariant of the type $M_y(dL_{2y}/dx)-L_{2y}(dM_y/dx)$.[6] A nonzero resultant magnetic moment in this case might appear in the presence of nonuniformities of the modulation of the antiferromagnetic structure in the sample. However, both in the first neutron diffraction studies and in the recent ones[29] it has been established that the fundamental mode L_{2y} of the antiferromagnetic structure in $LiCoPO_4$ is uniform. If, on the other hand, it is assumed that the magnetic moments of the sublattices deviate from the **b** direction by small angles, so that the magnetic structure of the crystal is characterized by two or more AFM modes, and it is also assumed that the weak AFM modes are modulated in the direction of the **a** axis, along which the exchange couplings are especially weak, then, as is seen from Table II, the following invariants are symmetry-allowed:

$$\frac{L_{2y}M_ydL_{2x}}{dx}\frac{dL_{1z}}{dx},\quad \frac{L_{2y}M_ydL_{2z}}{dx}\frac{dL_{1x}}{dx},$$

$$\frac{L_{2y}M_ydL_{3z}}{dx}\frac{dL_{1z}}{dx},\quad \frac{L_{2y}M_ydL_{3x}}{dx}\frac{dL_{1x}}{dx}. \tag{6}$$

They can describe the appearance of a nonzero averaged WFM moment $\mathbf{M}_0\|\mathbf{b}\|\mathbf{Y}$. For such a modulation the fundamental AFM mode L_{2y} can be essentially uniform, while only the transverse projections (L_{1x} and L_{2z}, or L_{1x} and L_{3x}, or L_{1z} and L_{2x}, or L_{1z} and L_{3z}) of the AFM vectors are modulated completely and in phase with each other. In that case at low temperatures one can expect a stronger temperature dependence due to the usual temperature evolution of the character of the modulation of such structures from harmonic to solitonlike.[27] Since the WFM moment in this case is proportional to the volume of those parts of the crystal in which the variation of the antiferromagnetic vectors occur, it is natural that as the temperature is lowered, after a transition of the harmonically modulated structure to a solitonic structure (to the so-called ''soliton lattice'' of modulation) the WFM moment will decrease on account of a decrease of both the number and thickness of the walls between incommensurate domains. The increase of the gradient of the projec-

tions dL_{ki}/dx in the walls cannot compensate for of the decrease of the total volume of the walls. The symmetry of the crystal and the type of its antiferromagnetic ordering also admit other uniform and nonuniform invariants which could describe the appearance of weak ferromagnetism. Among them are uniform and gradient invariants containing the z projection of a hypothetical toroidal moment, which transforms in the same way as the y projection of the fundamental AFM vector L_{2y} (Ref. 6).

It is also necessary to consider the possibility of a weak spontaneous magnetic moment arising due to irregular local magnetic nonuniformities with frustrated exchange couplings, which can arise in 2D antiferromagnets.[30,31] Upon thermal excitation of such nonuniformities the temperature dependence of the spontaneous magnetization should be especially strong. It will be possible to determine the true mechanism for the appearance of weak ferromagnetism in $LiCoPO_4$ only after doing precise experimental studies of various physical properties which are sensitive to the magnetic structure of the crystal. Among these, besides neutron diffraction, are investigation of the hysteresis effects observed in the magnetooptical studies, and the search for spontaneous electrical polarization and unconventional magnetic (magnetization quadratic in the field) and magnetooptical effects (the linear magnetooptical effect, etc.).

CONCLUSION

The presence of weak ferromagnetism in $LiCoPO_4$ has been confirmed by two independent experiments. The presence of a spontaneous ferromagnetic moment in regular $LiCoPO_4$ crystals is evidence of a disagreement of the real magnetic symmetry with the magnetic group $Pnma'(Pnma/Pnm2_1)=Sh_{62}^{445}(D_{2h}^{16}/C_{2V}^{7})$ that was determined earlier by the neutron diffraction method. Since the center of symmetry of the crystal-chemical cell of the crystal after AFM ordering becomes odd with respect to the AFM vector, the weak ferromagnetism cannot be due to the usual interactions of the Dzyaloshinskiĭ–Moriya type—single-ion anisotropy and antisymmetric exchange. The cause of the weak ferromagnetism in $LiCoPO_4$ may be interactions of at least fourth order in the spins. The presence of weak ferromagnetism indicates that the antiferromagnetic structure of $LiCoPO_4$ is mixed—it can be described not by one but by two or three antiferromagnetic vectors, one of which contains the fundamental AFM mode while the others describe modes of weak antiferromagnetism.

The observed temperature dependence of the WFM moment of $LiCoPO_4$ is atypical of weak ferromagnets. In view of the strong temperature dependence of the spontaneous magnetic moment of lithium cobalt phosphate at low temperatures, we conclude that among the possible mechanisms for the appearance of the WFM moment in $LiCoPO_4$ there is a preference for that in which the formation of the spontaneous magnetic moment is due to a regular or irregular nonuniform solitonlike AFM structure.

The authors thank Prof. M. Mercier (Technological University, Montlucon, France) and Prof. H. Schmid (Geneva University, Switzerland) for providing the $LiCoPO_4$ single crystal. The authors thank Prof. H. Schmid for interest in this study and lively participation in it through e-mails, Dr. D. Vaknin (Ames Laboratory, USA) for providing unpublished results of neutron diffraction studies of $LiCoPO_4$, and Dr. M. M. Bogdan (ILT-NASU) for helpful discussions of the results of this study.

This work could not have been completed without the assistance rendered previously to one of the authors (N.F.Kh.) by the International Soros Science Education Program (ISSEP), Grant No. SPU062067.

This article was prepared for the jubilee of V. V. Eremenko. We are grateful to him for organizing a fruitful collaboration between the laboratories of the IP-PAS and the ILT-NASU, lasting for many years. One of the authors (N. F. Kh.) is especially indebted to V. V. Eremenko for introducing him to big science many years ago.

*E-mail: kharchenko@ilt.kharkov.ua

[1] M. Mercier, J. Gareyte, and E. F. Bertaut, C. R. Acad. Sci. Paris B **264**, 979 (1967).
[2] D. E. Cox, in *Magnetoelectric Interaction Phenomena in Crystals*, edited by A. J. Freeman and H. Schmid, Gordon and Breach, London–New York–Paris (1975), p. 111.
[3] H. Schmid, in *Magnetoelectric Interaction Phenomena in Crystals*, edited by A. J. Freeman and H. Schmid, Gordon and Breach, London–New York–Paris (1975), p. 121.
[4] J.-P. Rivera, Ferroelectrics **161**, 147 (1994).
[5] H. Wiegelmann, *Magnetoelectric Effects in Strong Magnetic Fields*, PhD Thesis, University of Konstanz, Konstanzer Dissertationen, Bd. **461**, Hartung-Gorre, Konstanz (1995).
[6] I. Kornev, M. Bichurin, J.-P. Rivera, S. Gentil, H. Schmid, A. G. Jansen, and P. Wyder, Phys. Rev. B **62**, 12247 (2000).
[7] E. A. Turov, A. V. Kolchanov, V. V. Men'shenin, I. F. Mirsaev, and V. V. Nikolaev, *Symmetry and Physical Properties of Antiferromagnets* [in Russian], Fiz.-Mat. Lit., Moscow (2001).
[8] R. P. Santoro, D. J. Segal, and R. E. Newnham, J. Phys. Chem. Solids **27**, 1192 (1966).
[9] J.-P. Rivera and J. Korean, Phys. Soc. **32**, S1855 (1998).
[10] A. Goni, L. Lezama, G. E. Barberis, J. L. Pizzarro, M. I. Arriortua, and T. Rojo, J. Magn. Magn. Mater. **164**, 251 (1996).
[11] M. F. Kharchenko, O. V. Miloslavska, Yu. M. Kharchenko, H. Schmid, and J.-P. Rivera, Ukr. J. Phys. Opt. **1**, 16 (2000).
[12] N. F. Kharchenko, Yu. N. Kharchenko, R. Szymczak, M. Baran, and G. Shmid, Fiz. Nizk. Temp. **27**, 1208 (2001) [Low Temp. Phys. **27**, 859 (2001)].
[13] E. A. Turov, *Physical Properties of Magnetically Ordered Crystals* [in Russian], Izd. AN SSSR, Moscow (1963).
[14] Y. Ren, T. T. M. Palstra, D. I. Khomskii, E. Pellegrin, A. A. Nugroho, A. A. Menovsky, and G. A. Sawatsky, Nature (London) **396**, 441 (1998).
[15] Y. Ren, T. T. M. Palstra, D. I. Khomskii, and G. A. Sawatsky, Phys. Rev. B **62**, 6577 (2000).
[16] Kugel, Z. Kristallogr. **209**, 755 (1994).
[17] J. M. Mays, Phys. Rev. **131**, 38 (1963).
[18] M. F. Sykes and M. E. Fisher, Physica (Amsterdam) **28**, 919 (1962).
[19] M. E. Fisher and M. F. Sykes, Physica (Amsterdam) **28**, 939 (1962).
[20] E. A. Turov, Usp. Fiz. Ṇauk **164**, 325 (1994).
[21] I. Dzyaloshinskii, Zh. Éksp. Teor. Fiz. **5**, 1259 (1957) [Sov. Phys. JETP **27**, 1027 (1957)].
[22] T. Moriya, Phys. Rev. **120**, 91 (1960).
[23] V. G. Bar'yakhtar, E. P. Stefanovskiĭ, and D. A. Yablonskiĭ, Fiz. Tverd. Tela (Leningrad) **28**, 504 (1986) [Sov. Phys. Solid State **28**, 281 (1986)].
[24] I. E. Chupis, Fiz. Nizk. Temp. **12**, 330 (1986) [Sov. J. Low Temp. Phys. **12**, 188 (1986)].
[25] I. E. Chupis and N. Ya. Aleksandrova, Ukr. Fiz. Zh. **32**, 111 (1987).
[26] V. G. Bar'yakhtar and E. P. Stefanovskiĭ, Fiz. Nizk. Temp. **22**, 904 (1996) [Low Temp. Phys. **22**, 693 (1996)].
[27] E. L. Nagaev, *Magnets with Complicated Exchange Interactions* [in Russian], Nauka, Moscow (1988).
[28] G. T. Rado, in *Magnetoelectric Interaction Phenomena in Crystals*, edited by A. J. Freeman and H. Schmid, Gordon and Breach, London–New York–Paris (1975), p. 3.

[29] It was recently observed in some careful new neutron diffraction studies on $LiCoPO_4$ that the magnitic moments of the Co^{2+} ions are inclined at a small angle to the crystallographic **b** axis: D. Vaknin, J. L. Zarestky, L. L. Miller, J.-P. Rivera, and H. Schmid, Phys. Rev. B **65**, (2002) [to be published].

[30] M. M. Bogdan, A. S. Kovalev, and A. A. Stepanov, Fiz. Nizk. Temp. **18**, 838 (1992) [Low Temp. Phys. **18**, 591 (1992)].

[31] E. C. Marino, Phys. Rev. B **65**, 054418 (2002).

Translated by Steve Torstveit

STRONGLY CORRELATED SYSTEMS AND HIGH TEMPERATURE SUPERCONDUCTIVITY

Features of the magnetic properties of rare-earth intermetallides RMn_2Ge_2 (Review)

N. P. Kolmakova and A. A. Sidorenko

Bryansk State Engineering University, 241035 Bryansk, Russia

R. Z. Levitin*

Physics Department, M. V. Lomonosov Moscow State University, Vorob'evy Gory, 119899 Moscow, Russia
(Submitted December 24, 2001; revised February 24, 2002)
Fiz. Nizk. Temp. **28**, 905–925 (August–September 2002)

The magnetic and other physical properties of the ternary intermetallic compounds RMn_2Ge_2 (R is a rare earth) are of great interest on account of effects due to the coexistence of the $3d$ (manganese) and $4f$ (rare-earth) magnetic subsystems. The layered structure, the high sensitivity of the exchange parameters to the interatomic distances, the antiferromagnetic exchange interaction in the manganese subsystem in intermetallides containing heavy rare earths, and also the appreciable crystal-field effects in the rare-earth subsystem make for complex magnetic phase diagrams in these compounds. A review is given of the experimental and theoretical research on the magnetic properties and magnetic phase diagrams of the intermetallic compounds RMn_2Ge_2, including measurements in high and ultrahigh magnetic fields. A theoretical model is proposed which takes into account the features of the crystal structure and the hierarchy of exchange interactions in intermetallides containing heavy rare earths; this model is in many cases capable of describing the magnetic properties of these intermetallides over a wide range of magnetic fields and temperatures, and it permits determination of the interaction parameters for RMn_2Ge_2 compounds with R=Gd and Dy from a comparison of the experimental and calculated magnetization curves and $H-T$ phase diagrams. © *2002 American Institute of Physics.* [DOI: 10.1063/1.1511711]

1. INTRODUCTION

Ternary intermetallic compounds containing rare earths (R) and transition elements (T) have attracted a great deal of interest in recent years. This is because the inclusion of a third element (X) in the formula for the intermetallide allows one to vary the type of crystal structure, interatomic distances, concentration of conduction electrons, etc., making it possible to obtain materials with new magnetic properties.

Among the many ternary intermetallides the compounds RT_2X_2 with X=Ge or Si have held a steady research interest, as can be seen from the number of scientific publications devoted to them in recent years (see, e.g., the review[1]). This attention is due to the fact that the intermetallides RT_2X_2 manifest a great diversity of physical characteristics. Among these compounds one can find superconductors and heavy-fermion systems, variable-valence effects, etc.[1] The magnetic properties of these intermetallides are also extremely interesting, although one cannot yet say that the magnetism of the intermetallic compounds RT_2X_2 is conclusively understood.

The magnetic properties of RT_2X_2 intermetallides containing manganese are especially interesting, since only in RMn_2X_2 does magnetic ordering arise in the $3d$ manganese subsystem at comparatively high temperatures.[1] The features of the crystal structure and exchange interactions of RMn_2X_2 are conducive to spontaneous magnetic phase transitions in many of these compounds, and several of those transitions have not yet been adequately explained. The magnetic phase transitions in a magnetic field have been studied even less. The magnetoelastic properties of RMn_2X_2 intermetallides have also been studied in insufficient detail. Very recently it was pointed out that because of the features of the crystal structure, these intermetallides are natural superlattices and can be used as model objects for studying the processes occurring in superlattices; this circumstance has heightened the interest in these objects.

The intermetallic compounds RMn_2X_2 that have been studied in greatest detail are those with X=Ge. In this article we give a brief review of the nature and the features of the magnetic ordering in intermetallides of the RMn_2Ge_2 type, based on both information available in the literature and the experimental and theoretical research of the authors. A theoretical model is proposed which in many cases is capable of describing the spontaneous and induced magnetic phase transitions in these compounds.

2. CRYSTAL STRUCTURE OF THE INTERMETALLIC COMPOUNDS RT_2X_2

Intermetallic compounds of the type RT_2X_2 are formed by the rare earths (R) thorium, uranium, yttrium, barium, and calcium, transition elements (T) of the $3d$, $4d$, and $5d$ groups, and germanium or silicon (X). These intermetallides containing manganese and other $3d$ materials crystallize in the well-known body-centered tetragonal structure that was

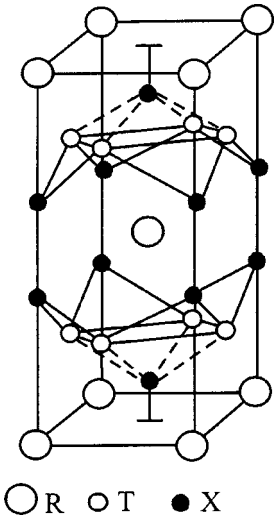

FIG. 1. Crystal structure of the $ThCr_2Si_2$ type.

first determined for $ThCr_2Si_2$ in Ref. 2 and have space group $I4/mmm$. The unit cell of this structure contains two formula units and is illustrated in Fig. 1.

An important feature of the compounds RMn_2X_2 with a structure of the $ThCr_2Si_2$ type is that this structure consists of layers of rare earths, transition elements, and germanium (or silicon) lying perpendicular to the tetragonal axis c and arranged in the sequence

–R–X–T–X–R–X–T–X–R–.

The layers of X and T atoms form a sandwich structure with a rare-earth atom situated between neighboring sandwiches. Each R atom is surrounded by eight X atoms and eight T atoms, which are located at the corners of a cube. The interatomic distances R–X and R–T are smaller than the sum of the corresponding ionic radii but larger than the sum of the covalent radii.

3. MAGNETIC PROPERTIES AND MAGNETIC STRUCTURE OF THE INTERMETALLIC COMPOUNDS RMn_2Ge_2

As we said in the Introduction, numerous studies have shown that in the majority of the RT_2Ge_2 intermetallic compounds the transition metal T does not have a magnetic moment. An exception is manganese, which is magnetically ordered at relatively high temperatures.[1] Thus from a magnetic standpoint the RMn_2Ge_2 intermetallides consist of two different subsystems: the R subsystem and the Mn subsystem. A feature of the magnetic properties of the RMn_2Ge_2 intermetallides is that these subsystems become magnetically ordered at different temperatures: at high temperatures only the manganese subsystem is ordered; the ordering of the rare-earth subsystem occurs at much lower temperatures. The main magnetic characteristics of the RMn_2Ge_2 intermetallides, according to the data of different experiments, are presented in Table I.

Neutron diffraction and magnetic studies of RMn_2Ge_2 compounds with light rare earths[9,10] have shown that with decreasing temperature in those compounds the manganese subsystem undergoes first a transition from the paramagnetic to an antiferromagnetic state (the Néel temperature T_N) and then, as the temperature is decreased further, a transition to a ferromagnetic state (the Curie temperature T_C). The Néel temperature of these compounds lies in the range 390–410 K, and $T_C \approx 330$ K.

The magnetic ordering of the rare-earth subsystem in RMn_2Ge_2 compounds with the light rare earths Pr and Nd occurs at a temperature T_t of the order of 100 K.[10] The compound $SmMn_2Ge_2$ has the most complex magnetic behavior.[13,15] Like the other intermetallides with light rare earths, this compound undergoes a transition from the paramagnetic to an antiferromagnetic state and then from the antiferromagnetic to a ferromagnetic state as the temperature is lowered. However, unlike the intermetallides with La, Pr, and Nd, when $SmMn_2Ge_2$ is cooled below a temperature $T_{t1} \approx 150$ K the manganese subsystem undergoes a transition from a ferromagnetic to an antiferromagnetic state (meanwhile, the Sm subsystem is magnetically disordered). When the temperature is decreased further to $T_t \approx 100$ K an inverse transition of the Mn subsystem to a ferromagnetic state occurs, accompanied by ferromagnetic ordering of the Sm subsystem, so that a resultant ferromagnetic structure is formed.

The RMn_2Ge_2 intermetallides with heavy rare earths are simpler from a magnetic point of view. On cooling to the Néel temperature T_N, antiferromagnetic ordering arises in their Mn subsystem.[1] The value of T_N is equal to 410 K for the Tb compound and increases with increasing atomic number of the rare earth, to $T_N \approx 478$ K for $TmMn_2Ge_2$ (Refs. 19 and 21). The compound $GdMn_2Ge_2$ stands out some, with $T_N \approx 365$ K.[5,18] However, an anomaly of the magnetization of this intermetallide has been detected[17] at a temperature $T_N \approx 480-500$ K. The nature of this anomaly is not clear.

On further cooling of RMn_2Ge_2 intermetallides with heavy rare earths to T_t, magnetic ordering occurs in the rare-earth subsystem.[19,21] This temperature is approximately equal to 95 K for the Gd and Tb compounds, around 40 K for $DyMn_2Ge_2$, and considerably lower for compounds with Ho ($T_t = 2.15$ K), Er ($T_t = 5.5$ K), and Tm ($T_t = 8.5$ K).[21] We note that in the compounds containing Gd, Tb, and Dy the onset of magnetic order in the R subsystem is a first-order phase transition and is accompanied by a transition of the Mn subsystem from the antiferromagnetic to the ferromagnetic state, so that the resulting magnetic structure becomes ferrimagnetic. In the remaining compounds with heavy rare earths the magnetic ordering of the rare-earth subsystem is a second-order phase transition; here the Mn subsystem remains antiferromagnetic to the lowest temperatures investigated (~ 2 K).[21]

Previously it has been assumed that the magnetic structure of the Mn subsystem consists of ferromagnetically ordered manganese planes of the (001) type, and the resulting ferro- or antiferromagnetic structure is realized for a parallel or antiparallel orientation of the magnetic moments of neighboring planes, respectively. However, recent neutron diffraction studies[8–10] have shown that the situation is more complicated. From neutron diffraction measurements both on pure RMn_2Ge_2 compounds and on mixed compounds of the $(Y, La)Mn_2Ge_2$ and $(R, R')Mn_2Ge_2$ type it follows that collinear magnetic ordering of the Mn subsystem occurs only in compounds with the heavy rare earths Tb, Dy, Ho, Er, Tm, and Y (the intermetallide $GdMn_2Ge_2$ was not studied by neu-

TABLE I. Main magnetic characteristics of the compounds RMn_2Ge_2: T_N is the Néel temperature, T_C the Curie temperature, T_t the temperature of ordering of the R subsystem, Θ_p the paramagnetic Curie temperature, M_{eff} the effective moment, M_s the spontaneous magnetization at 4.2 K, m_{Mn} and m_{R} the magnetic moments of the Mn and R atoms at 4.2 K, $g_J J$ the magnetic moment of R^{3+}, and EA the axis of easy magnetization.

R	T_N, K	T_C, K	T_t, K	Θ_p, K	M_{eff}, μ_B	M_s, μ_B	m_{Mn}, μ_B	m_{R}, μ_B	$g_J J$, μ_B	EA
La	413 [3] 410 [4]	310 [5,6] 306 [7] 326 [8]		270 [6] 225 [9]	3,5 [6] 4,7 [7] 3,39 [9]	3,1 [6] 3,0 [5,7]	3,065 [9] 1,55 [6]			[001]
Pr	414 [3] 415 [4]	330 [10] 329 [11] 334 [5]	100 [10] 80 [11] 40 [5]	260 [10]	6,1 [10]	5,9 [11] 3,7 [10] 3.9 [5]	2,80 [10] 1,55 [11]	2,95 [10] 2,77 [11]	3,2	[001]
Nd	418 [3] 415 [4]	330[10] 336 [12] 334 [5]	100 [10] 40 [5]	280 [10]	6,0 [10]	5,7 [12] 5,2 [10] 6,0 [5]	2,70 [10] 1,55 [3]	2,35 [10]	3,28	[001], $\perp$ c**
Sm	389 [3] 385 [4]	348 [13] 350 [14] 341 [15]	60; 196* [13 100; 153 [14] 100; 153 [15]		3,4 [7]	3,0 [7]	1,7 [13]		0,71	[001], [110]***
Gd	365 [5,16]		95 [5,16,17,18]	100 [19]	8,8 [19]	3,6 [19]	2,0 [18] 1,7 [17]	7,0 [17]	7	[001]
Tb	414 [19] 413 [20]		95 [19] 110 [20] 105 [21]	100 [19]	10,4 [19] 9,6 [7]	5,3 [19] 6,0 [7]	2,21 [21] 2,3 [20] 1,7 [19]	8,81 [21] 8,0 [19] 7,8 [20]	9	[001]
Dy	438 [19,22] 430 [23,24] 385 [5,7]		40 [19] 47 [5,7]	100 [19]	10,8 [19] 9,9 [5,7]	6,2 [19]	2,2 [24] 2,0 [22]	10,2 [18,24] 3,5 [5,7]	10	[001]
Ho	459 [19] 403 [5,7]		4,2 [19] 2,1 [21] 37 [5,7]	100 [19]	10,0 [19] 8,5 [5,7]	5,5 [5,7]	2,38 [21]	6,9 [21]	10	[001]
Er	475 [19] 390 [7]		5,5 [21] 8,5 [7] 4,2 [19]	224 [19]	9,4 [19] 9,0 [7]	8,3 [19] 6,0 [7]	2,3 [7] 2,34 [21]	6,81 [21] 7,7 [7]	9	$\perp$ c
Tm	487 [21] 458 [7]		8,5 [21]		6,2 [7]		2,28 [21]	6,63 [21]	7	[001]
Y	427 [3] 437 [25] 395 [7]			394 [3] 385 [7]	3,34 [3] 3,8 [7]	0,11 [25]	2,23 [21] 2,95 [7]			

Notes: *In $SmMn_2Ge_2$ on cooling to this temperature a transition occurs from the ferromagnetic phase to an antiferromagnetic phase in the manganese subsystem; **below 250 K; ***below 100 K.

tron diffraction because of the large neutron absorption cross section of gadolinium). At the same time, in intermetallides with light rare earths more complex magnetic structures are formed in the manganese subsystem. These magnetic structures have the feature that in many of the compounds a magnetic ordering which combines ferro- and antiferromagnetic components arises in planes of the (001) type; in addition, in some of the compounds there can be long-period noncollinear structures. Figure 2 shows the different types of magnetic structures of the Mn subsystem which are characteristic of the $(Y, La)Mn_2Ge_2$ system and of other RMn_2Ge_2 intermetallides.[8,10,26] In the compound YMn_2Ge_2 there is a collinear antiferromagnetic structure of the AF*il* type. This is the type of structure that the Mn subsystem has in intermetallides containing heavy rare earths at temperatures above T_t. Below T_t the Mn subsystem in compounds containing Tb, Dy, and, apparently, Gd undergoes a transition to a collinear ferromagnetic structure of the F type.[21] The AF*il*-type antiferromagnetic structure of the Mn subsystem in compounds containing Ho, Er, and Tm persists to the lowest temperatures ($\sim$2.2 K). In the compound $LaMn_2Ge_2$ at high

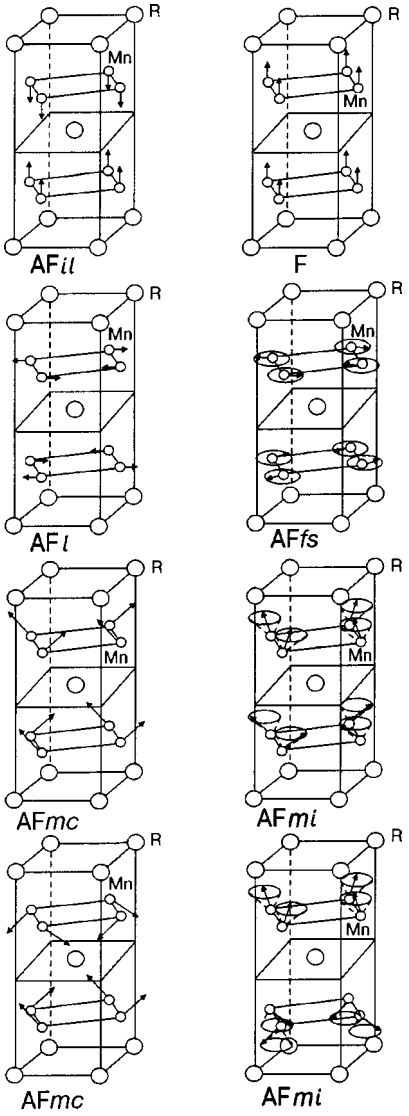

FIG. 2. Magnetic structures of the manganese subsystem observed in RMn_2Ge_2 intermetallic compounds.

temperatures ($T_N > T > T_C$) there is a planar spiral antiferromagnetic structure of the AF*fs* type, which at a temperature below T_C undergoes a transition to an incommensurate structure of the F*mi* type with a ferromagnetic component along the tetragonal axis. In the compounds $PrMn_2Ge_2$ and $NdMn_2Ge_2$ for temperatures above T_C the Mn subsystem has a collinear antiferromagnetic structure of the AF*l* type in which the magnetic moment is perpendicular to the *c* axis. Below T_C these compounds have a commensurate ferromagnetic structure of the F*mc* type, with a ferromagnetic component along the *c* axis. At still lower temperatures ($T < 280$ and 250 K for Pr and Nd, respectively) a helical ferromagnetic structure of the F*mi* type arises in the Mn subsystem.

The magnetic ordering in the rare earth subsystem is also differential in different compounds. In intermetallides containing Pr, Nd, Gd, Tb, Dy, and Er at a temperature below T_t the R subsystem has a collinear ferromagnetic structure. The magnetic moments of Nd and Er lie in the (001) plane, and in the rest of these compounds the magnetic moment of the rare earth is oriented along the tetragonal axis.[10,21] In $HoMn_2Ge_2$ below T_t there are two different coexisting sinusoidally modulated magnetic structures in the Ho subsystem.[21] In $TmMn_2Ge_2$ the Tm moments lie in the basal plane.[21] Along the *c* axis the ferromagnetic Tm (001) layers alternate in the sequence $++--$. The Mn moments deviate slightly from the *c* axis, and the components of the Mn moments in the (001) layer alternate from layer to layer in the same sequence as for the moments of Tm.

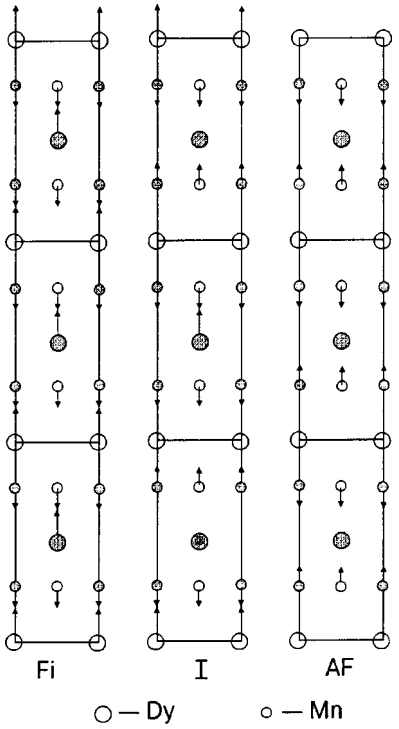

FIG. 3. Magnetic structures of the compound $DyMn_2Ge_2$ (the shaded atoms are shifted relative to the plane of the figure by half a lattice parameter).

It has also been found as a result of magnetic and neutron diffraction studies[22,24] that the magnetic structure in $DyMn_2Ge_2$ at $T < T_1 = 33–35$ K is ferrimagnetic: the magnetic moments of the manganese and dysprosium subsystems are collinear to the tetragonal axis and antiparallel to each other (Fig. 3, the Fi phase). Above $T_2 = 37.5–40$ K the manganese subsystem is antiferromagnetic, and the dysprosium subsystem is in a paramagnetic state (Fig. 3, the AF phase). According to the data of Ref. 22, for $T_1 < T < T_2$ the ferrimagnetic and antiferromagnetic phases coexist with a phase in which the magnetic moments of the manganese subsystem alternate in the sequence $--+---+$, and the dysprosium subsystem is partially ordered: 1/3 of the dysprosium atoms are magnetically ordered, and 2/3 are found in a paramagnetic state (Fig. 3, phase I).

The compound $SmMn_2Ge_2$ has not been studied by neutron diffraction. However, studies of the mixed silicon-based compound $Nd_{0.35}La_{0.65}Mn_2Si_2$ (Ref. 26), in which temperature-induced spontaneous magnetic phase transitions like those in $SmMn_2G_2$ were observed, have shown that in this compound the Mn system has different magnetic structures at different temperatures, much as has been observed in germanium-based intermetallides with light rare earths (see Fig. 2). Below $T_N \approx 395$ K the compound $Nd_{0.35}La_{0.65}Mn_2Si_2$ is characterized by the structure AF*l*, in

the temperature interval between $T_C \approx 295$ K and $T_{t1} \approx 220$ K by the structure Fmc, for $T_{t1} > T > T_{t2} \approx 50$ K it has the AFmc structure, and for $T < T_{t2}$ it again has the Fmc structure (the magnetic structures mentioned are illustrated in Fig. 2). It is possible that the Mn subsystem in $SmMn_2Ge_2$ has these same structures.

In intermetallides with light rare earths the R–Mn exchange interaction is ferromagnetic, and as a consequence of this the resulting magnetic structure below the magnetic ordering temperature of the rare-earth subsystem is ferromagnetic. In intermetallides with heavy rare earths, on the contrary, the R–Mn exchange interaction is antiferromagnetic, so that the resulting magnetic structure is ferrimagnetic.

Neutron diffraction studies[8,10] have determined the magnetic moments of Mn at $T = 4.2$ K in the compounds $LaMn_2Ge_2$, $PrMn_2Ge_2$, and $NdMn_2Ge_2$, which have the values 3.06, 2.8, and $2.7\mu_B$, respectively, which are much larger than the values obtained from the magnetic measurements. This difference can be explained by the circumstance that in the compounds studied the Mn subsystem has a noncollinear structure, as the neutron diffraction studies have revealed.

In compounds with heavy rare earths the magnetic moment of manganese is approximately $1.7-2\mu_B$, according to magnetic measurements on single crystals.[19,27] At the same time, from the neutron diffraction data the moment of the manganese is almost the same in all these compounds, having a value $2.3\mu_B$.[21] We note that according to the neutron diffraction data the magnetic moment of manganese in compounds with light rare earths is much larger than the moment of manganese in the compounds with heavy rare earths. A possible explanation of this is that the manganese is found in different electronic states in the compounds with light and heavy rare earths. This effect may be due to the change in the distance between manganese atoms as one goes from La to Tm. We see from Table I that the magnetic moments of the rare earths are close to the theoretical values $g_J J \mu_B$ for the free Re^{3+} ions (except Nd and Ho). Some differences may be attributed to the influence of the crystalline field on the state of the R^{3+} ions. In Ref. 28 it was observed that the magnetic moment of manganese ($\Delta m_{Mn}/m_{Mn} \approx 16\%$ in $TbMn_2Ge_2$) decreases upon the transition of the manganese subsystem from the ferro- to the antiferromagnetic state in compounds of the system $Nd_xTb_{1-x}Mn_2Ge_2$ for $x = 0-0.4$.

Magnetic studies have shown[6,11,12,17,27] that the axis of easy magnetization (EA) in RMn_2Ge_2 compounds with R = La, Pr, Gd, Tb, Dy, Ho, and Tm is oriented along the tetragonal axis, while in $ErMn_2Ge_2$ the EA is parallel to the [110] direction.[19,21] In the compound $NdMn_2Ge_2$ at temperatures above $T_{sr} = 250$ K the EA is the c axis, while for $T < T_{sr}$ the EA is reoriented in the (001) plane,[12] so that a spin-reorientation phase transition occurs. In $SmMn_2Ge_2$ at temperatures above $T_t = 100$ K the EA is parallel to the c axis, and for $T < T_t$ the EA is oriented along the [110] axis.[13]

The magnetization curves of RMn_2Ge_2 single crystals along the easy and hard magnetization directions show[19] that compounds in which the rare earth atoms have a nonzero orbital moment have a large magnetic anisotropy (Table II). It is seen from the table that the magnetic anisotropy of $GdMn_2Ge_2$ (the Gd^{3+} ion is found in an S state) is an order of magnitude smaller than the magnetic anisotropy of the other compounds with magnetic rare earths. This indicates that the large magnetic anisotropy is due to the rare earth ions and apparently, as in the other R–T intermetallides, has a single-ion nature.

TABLE II. Values of the magnetic anisotropy constants of RMn_2Ge_2 compounds at $T = 4.2$ K (according to the data of Refs. 11 and 19).

R	K_1, erg/cm^3	EA
La	$2.2 \cdot 10^6$	[001]
Pr	$5.3 \cdot 10^7$	[001]
Gd	$5.4 \cdot 10^6$	[001]
Tb	$8.4 \cdot 10^7$	[001]
Dy	$1.3 \cdot 10^8$	[001]
Ho	$1.3 \cdot 10^8$	[001]
Er	$-4.2 \cdot 10^8$	[110]

4. EXCHANGE INTERACTIONS IN RMn_2Ge_2 INTERMETALLIC COMPOUNDS

We have shown that the compounds RMn_2Ge_2 have various magnetic structures, and various magnetic phase transitions occur in them as the temperature is varied. The formation of these structures and transitions is intimately related to the competition among the different types of exchange interactions, with the different mechanisms contributing to them (the RKKY exchange interaction via conduction electrons, and superexchange between the magnetic atoms via germanium). Generally speaking, the exchange interactions in the RMn_2Ge_2 intermetallides can be divided into four classes:

a) Mn–Mn in the layer;

b) interlayer Mn–Mn (in the simplest case between nearest manganese planes);

c) Mn–R;

d) R–R.

Numerous studies have shown (see, e.g., the review[1]) that the strongest is the exchange interaction between Mn ions in the layer, which is mainly determined by the magnetic ordering temperature of the intermetallides RMn_2Ge_2. In compounds with heavy rare earths this interaction is ferromagnetic. In compounds with light rare earths an antiferromagnetic ordering arises in the layer at high temperatures (above T_C). This is due to the onset of an antiferromagnetic component of the intralayer exchange, which depends on the Mn–Mn interatomic distance d_{Mn-Mn} in the layer. According to Ref. 26, the critical distance d_c is approximately 2.87 Å. In compounds with heavy rare earths one has $d_c > d_{Mn-Mn}$, and therefore in those intermetallides the antiferromagnetic component is absent, and the manganese in the layer is ordered ferromagnetically. In intermetallides with light rare earths, for which $d_c < d_{Mn-Mn}$, the antiferromagnetic compo-

nent of the exchange gives rise to an antiferromagnetic (collinear or noncollinear) magnetic ordering in the layer. We note, however, that the origin and features of the antiferromagnetic component of the exchange interaction in the layer has been insufficiently well studied and is in need of further investigation.

The exchange interaction between manganese planes is an order of magnitude smaller than the Mn–Mn exchange interaction in the layer. As has been shown by many authors (see, e.g., Ref. 13 and the references cited therein), this interaction is also strongly dependent on the Mn–Mn interatomic distance in the layer and changes sign at a certain critical value $d_{c1}=2.86$ Å. In compounds with light rare earths the Mn–Mn interatomic distance at room temperature is larger than d_{c1}, and the exchange interaction between nearest manganese planes is ferromagnetic. In configurations with heavy rare earths, on the contrary, this interaction is antiferromagnetic, since the Mn–Mn interatomic distance is less than d_{c1}. As a result, in compounds with light rare earths the manganese subsystem has a ferromagnetic structure, and in intermetallides with heavy rare earths at temperatures above the magnetic ordering temperature of the rare earths the manganese subsystem is found in an antiferromagnetic state. The dependence of the manganese–manganese interplane exchange on the interatomic distance has been confirmed by numerous studies both on $SmMn_2Ge_2$ and on several mixed compounds.[25,29,30] In $SmMn_2Ge_2$ the Mn–Mn interatomic distance in the layer is close to d_{c1}. At room temperature $d>d_{c1}$ in this compound, and $SmMn_2Ge_2$ is a ferromagnet. On cooling, because of the change of the interatomic distances with temperature, d becomes smaller, and there is a transition of the manganese subsystem to an antiferromagnetic state on account of the change in sign of the Mn–Mn interlayer exchange interaction. Further decrease in temperature leads to magnetic ordering of the Sm subsystem, which induces a return of the ferromagnetic ordering of the manganese subsystem. An analogous transition of the manganese subsystem is observed in compounds with Gd, Tb, and Dy as the temperature is lowered to T_t.

We note that because of the dependence of the Mn–Mn interplane exchange interaction on the interatomic distance in the layer, d (or, in other words, on the crystal lattice parameter a), appreciable magnetoelastic anomalies appear on the temperature dependence of the parameter a at the spontaneous magnetic phase transitions due to the transition of the manganese subsystem from the ferro- to the antiferromagnetic state.[31] This is clearly seen in Fig. 4, which shows the temperature dependence of the parameters of the crystal structure of several RMn_2Ge_2 intermetallides from Ref. 31.

The Mn–R exchange interaction has approximately the same value as the exchange interaction between nearest manganese planes. The competition of these two interactions determines the magnetic properties of these compounds at low temperatures. In compounds with Gd, Tb, and Dy at the magnetic ordering temperature of the R subsystem, the Mn subsystem undergoes a transition from the antiferromagnetic to a ferromagnetic state on account of the fact that the Mn–R exchange interaction is larger than the antiferromagnetic exchange interaction between nearest manganese planes. In compounds with Ho, Er, and Tm the antiferromagnetism in

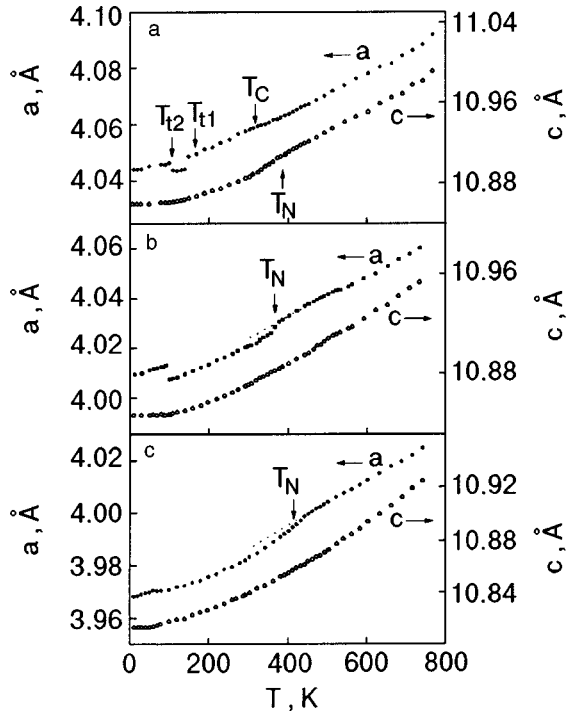

FIG. 4. Temperature dependence of the crystal structure parameters of the compounds RMn_2Ge_2: R = Sm (a), Gd (b), Dy (c).

the Mn subsystem persists to the lowest temperatures, since in these compounds the Mn–R exchange interaction is smaller than the manganese interplane exchange interaction. The magnetic ordering of the R subsystem in compounds with Gd, Tb, and Dy is due to the Mn–R exchange interaction, while in compounds with Ho, Er, and Tm the magnetic ordering of the R subsystem is caused by the R–R exchange interaction proper, which is an order of magnitude smaller than the Mn–R exchange interaction.

We conclude this Section by noting that the nature of the magnetism of a $3d$ subsystem in intermetallides of the RT_2X_2 type is unclear at the present time. In Refs. 32 and 33 an attempt was made to explain the difference of the properties of the manganese and other $3d$ subsystems in these intermetallides in the framework of an itinerant magnetism model. The band structure of the intermetallides $LaMn_2Ge_2$, YMn_2Ge_2, and $LaCo_2Ge_2$ was calculated, and it was shown that the value of the density of states at the Fermi level in YMn_2Ge_2 and $LaMn_2Ge_2$ is relatively large, and the Stoner criterion for itinerant ferromagnetism is satisfied for those compounds. For $LaCo_2Ge_2$ the density of states at the Fermi level is considerably smaller, and for that intermetallide the Stoner criterion is not satisfied, and therefore the Co subsystem is nonmagnetic. Thus calculations in a band model can explain the presence of magnetic ordering in the manganese subsystem and its absence in the cobalt subsystem of the compound RT_2Ge_2. However, analysis of the magnetic moments of the manganese in the magnetically ordered and paramagnetic states led the authors of Ref. 1 to conclude that the magnetism of the manganese subsystem in RM_2Ge_2 intermetallides cannot be described completely in a band model. This question needs further investigation.

5. DESCRIPTION OF THE MAGNETIC PROPERTIES OF RMn_2Ge_2 INTERMETALLIDES IN THE YAFET–KITTEL MODEL FOR FERRIMAGNETS WITH AN ANTIFERROMAGNETIC INTRASUBLATTICE EXCHANGE INTERACTION

Thus the RMn_2Ge_2 intermetallic compounds have two magnetic sublattices: manganese and rare-earth. In the intermetallides with heavy rare earths the exchange interaction between these subsystems is antiferromagnetic, and therefore these intermetallides can be treated as two-sublattice ferrimagnets. An important feature of RMn_2Ge_2 with heavy rare earths is that the exchange interaction between neighboring manganese layers is also antiferromagnetic, and these compounds can therefore be treated as two-sublattice ferrimagnets with an antiferromagnetic exchange interaction in one of the sublattices. The properties of these ferrimagnets were first calculated by Yafet and Kittel,[34] who showed that in the exchange approximation for $H=0$ in addition to the ordinary collinear ferrimagnetic (Fi) phase, in which the magnetic moments of the sublattices are oriented antiparallel to each other, there can arise a triangular (T) magnetic phase in which the sublattice with the antiferromagnetic intrasublattice exchange interaction (the unstable sublattice) splits up into two equivalent subsublattices, the magnetic moments of which are oriented the same relative to the magnetic moment of the stable sublattice and at an angle to each other. Subsequently it was established[35] that in the presence of a field, such a ferrimagnet can have, besides the T phase, in which the magnetic moments of the sublattices are oriented at an angle to each other, and the ferromagnetic (F) phase, in which the magnetic moments of the sublattices are parallel to each other, an additional phase in which the magnetic moments of the subsublattices are antiparallel (an antiferromagnetic (AF) phase).

The Yafet–Kittel model has been used[36–38] to describe the properties of the intermetallides of the systems $Gd_{1-x}Y_xMn_2Ge_2$ and $Gd_{1-x}La_xMn_2Ge_2$. For such systems the thermodynamic potential at low temperatures can be written in the form

$$\Phi = -\lambda_{12}\mathbf{M}\cdot(\mathbf{m}_1+\mathbf{m}_2) - \lambda'_{22}\mathbf{m}_1\cdot\mathbf{m}_2 - \frac{1}{2}\lambda_{22}(m_1^2+m_2^2) - \frac{1}{2}\lambda_{11}\mathbf{M}^2 - \frac{K}{2m^2}(m_{1z}^2+m_{2z}^2) - H(\mathbf{M}+\mathbf{m}_1+\mathbf{m}_2). \quad (1)$$

Here the first term describes the exchange interaction of the stable (magnetic moment $\mathbf{M}$) and unstable (magnetic moment $\mathbf{m}_1+\mathbf{m}_2$) sublattices ($\lambda_{12}<0$), the second term describes the exchange between the sublattices ($\lambda'_{22}<0$), the third the exchange within the sublattices ($\lambda_{22}>0$), the fourth the exchange interaction within the stable sublattice ($\lambda_{11}>0$), the fifth the magnetic anisotropy of the unstable sublattice (the z axis coincides with the axis of the crystal, $m=|\mathbf{m}_1|=|\mathbf{m}_2|$), and the last term describes the Zeeman energy. We emphasize that in this case the nearest-neighbor approximation is used, i.e., only the exchange interactions of neighboring planes of a given type are taken into account. In systems with gadolinium, which is an S ion, one can neglect the magnetic anisotropy of the gadolinium subsystem (the case of a non-S ion is analyzed in the next Section) and assume that only the unstable manganese sublattice has anisotropy, and for it the direction of easy magnetization, according to the experimental data, is parallel to the axis of the crystal (magnetic anisotropy constant $K>0$) for the systems under study.

From the conditions of minimum thermodynamic potential one can determine the equilibrium magnetic structures and construct the magnetic phase diagrams and magnetization curves. It follows from the thermodynamic potential (1) that (see Ref. 36 for more details) in the absence of field this system, for a sufficiently strong intersublattice exchange interaction, will go to a collinear Fi phase with the magnetic moments of the sublattices directed collinearly with the axis of the crystal. Decreasing the intersublattice exchange will lead to a second-order transition from the Fi phase to the triangular T phase, with an orientation of the magnetic moment of the stable sublattice parallel to the axis of the crystal. Upon further decrease of the exchange interaction between sublattices, the magnetic moment of the stable sublattice undergoes a jumplike reorientation to a direction perpendicular to the axis of the crystal, and a new triangular phase T′ arises. Finally, if the exchange field acting on the unstable sublattice is equal to zero, then an antiferromagnetic structure arises in that sublattice, with an orientation of the magnetic moments of the subsublattices collinear with the axis of the crystal. The spontaneous magnetic structures arising in a two-sublattice ferrimagnet with negative exchange in one of the sublattices and uniaxial anisotropy in that sublattice are shown in Fig. 5.

Thus in the presence of anisotropy of the unstable sublattice, the triangular structure that was shown by Yafet and Kittel to arise in an isotropic ferrimagnet with magnetic instability will split up into two triangular structures with a perpendicular orientation of the magnetic moment of the stable sublattice. The transition from phase T to T′ is due to the fact that in the T phase a decrease of the intersublattice exchange will lead to a decrease of the angle between the axis of the crystal and the directions of the magnetic moments of the subsublattices, causing an increase in the magnetic anisotropy energy and stimulating a transition to the T′ phase, in which the magnetic anisotropy energy decreases.

Let us now analyze the behavior of an anisotropic ferrimagnet with magnetic instability in a magnetic field. We consider the situation in which the magnetic moment of the stable sublattice is greater than the magnetic moment of the unstable sublattice. For simplicity we limit consideration to the case when the total moment of the crystal in the initial

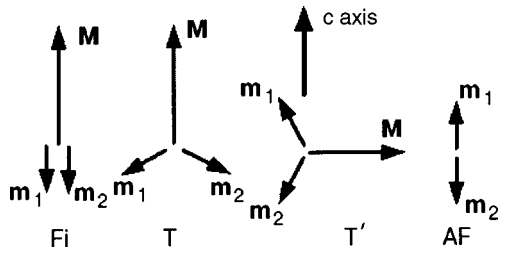

FIG. 5. Possible spontaneous magnetic phases of a ferrimagnet with an antiferromagnetic exchange interaction in the unstable sublattice with allowance for the magnetic anisotropy of that sublattice.

state is oriented along the axis of the crystal (phases Fi and T) and the external field is also directed along that axis. Then the problem reduces to finding the behavior of a uniaxial antiferromagnet in an effective field equal to the sum of the external field and the molecular field acting on the unstable sublattice on account of the stable sublattice. If $M>2m$ then for a comparatively small magnetic anisotropy ($K<-2\lambda'_{22}m$) the following sequence of phases arises with increasing field: Fi$\leftrightarrow$T$\leftrightarrow$AF$\leftrightarrow$T$\leftrightarrow$F. The transitions between the triangular and antiferromagnetic phases is first-order, and the rest are second-order magnetic phase transitions. The magnetization curve in this case is shown schematically in Fig. 6, and the transition fields are as follows:

$$\begin{aligned} H_{\mathrm{Fi}\leftrightarrow\mathrm{T}}&=2\lambda'_{22}m-\lambda_{12}M+2K,\\ H_{\mathrm{T}\leftrightarrow\mathrm{AF}}&=-\lambda_{12}M-\sqrt{(-2\lambda'_{22}m^2+K)K},\\ H_{\mathrm{AF+T}}&=-\lambda_{12}M+\sqrt{(-2\lambda'_{22}m^2+K)K},\\ H_{\mathrm{T}\leftrightarrow\mathrm{F}}&=-2\lambda'_{22}m-\lambda_{12}M-2K. \end{aligned} \tag{2}$$

If the magnetic anisotropy constant increases, then for $K>-2\lambda'_{22}m$ the canted phases become energetically unfavorable—the system becomes Ising-like.

For a field orientation perpendicular to the axis of the crystal, the following sequence of phases is realized at fields higher than the technical saturation field (when the magnetic moment of the stable sublattice is oriented perpendicular to the axis of the crystal): Fi$'\leftrightarrow$T$'\leftrightarrow$F$'$ (the prime indicates that the magnetic moment of the stable lattice is oriented perpendicular to the axis of the crystal). The critical fields for these second-order transitions are described by the expression

$$H=-\lambda_{12}M\pm\lambda'_{22}m\left(2-\frac{K}{\lambda'_{22}m^2}\right),$$

where the plus sign pertains to the transition Fi$'\leftrightarrow$T$'$ and the minus sign to T$'\leftrightarrow$F$'$. We note, however, that the ferrimagnetic structure does not arise if the technical saturation field is larger than the critical field of the transition Fi$'\leftrightarrow$T$'$ (Ref. 36).

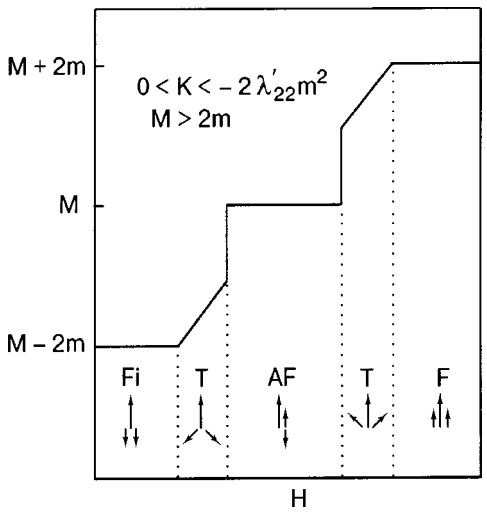

FIG. 6. Magnetization curve of an anisotropic ferrimagnet with an antiferromagnetic exchange interaction in the unstable sublattice in a field along the axis of the crystal.

We should point out that the formulas presented above pertain to low temperatures, where the field dependence of the magnetic moments of the stable and unstable sublattices do not need to be taken into account. At higher temperatures, where the field dependence of these moments must not be neglected, the calculation is done numerically (see Refs. 36, 38, and 39). For this the free energy of the different phases is calculated with both the internal energy and the entropy contribution taken into account, and the phase with the minimum free energy under the given conditions is found.

We recall that in the calculations it is necessary to take into account the strong dependence of the Mn–Mn interplane exchange interaction (the parameter λ'_{22}) on the interatomic distances in the plane (or on the lattice parameter a). This effect leads to a dependence of λ'_{22} on the temperature and concentration and in a number of cases can have a substantial influence on the magnetic properties. If it is assumed that the dependence $\lambda'_{22}(a)$ is linear,

$$\lambda'_{22}=\rho(a-a_c)$$

($a_c=4.045$ Å for RMn_2Ge_2), then this effect can be taken into account in the framework of the Kittel exchange inversion model.[40] (This question is discussed in more detail in Refs. 37 and 38.)

The approximation described above was used to analyze the experimental data for the system of intermetallides $Gd_{1-x}Y_xMn_2Ge_2$ (Ref. 36). Replacing gadolinium with yttrium leads to a decrease of the magnetic moment of the stable (gadolinium) sublattice and thereby decreases the molecular field acting on the unstable (manganese) on account of the stable sublattice and thus alters the ground state of the unstable sublattice. It should be noted that the concept of a ''stable'' gadolinium sublattice must be employed with some caution, since replacing even a small amount of the gadolinium with yttrium can alter the character of the long-range exchange in the spin subsystem of gadolinium and lead to the formation of new magnetic phases.[41] In the present case, however, the details of the interactions in the Gd sublattice are overwhelmed by the stronger intersublattice interaction, and the gadolinium subsystem can be regarded as stable.

The measurements[36] were made on ''free'' powders, the particles of which could rotate in an external field. It was shown that at all of the concentrations studied ($0\leqslant x\leqslant 0.5$) the samples had a spontaneous magnetization at low temperatures and underwent a metamagnetic transition in a field (Fig. 7).

The temperature dependence of the magnetization of the gadolinium–yttrium intermetallides is shown in Fig. 8. These compounds can be divided into three groups according to the character of the curves. The magnetization of compounds with a low yttrium concentration ($x=0$, 0.1, 0.2) decreases monotonically with increasing temperature before falling off sharply after a certain temperature T_1 is reached. In the compounds with $x=0.3$ and 0.4 the magnetization varies weakly at low temperatures, then increases sharply after a certain temperature T_2 is reached; this is followed by a monotonic decrease up to a temperature T_3, above which the magneti-

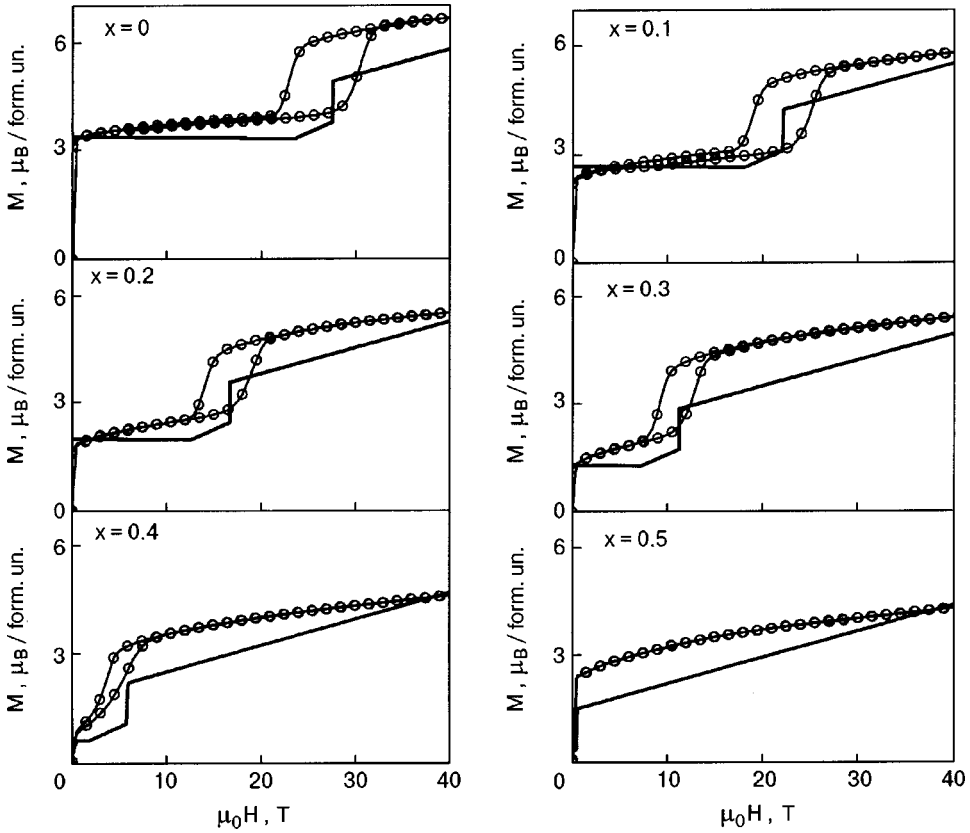

FIG. 7. Magnetization curves for free powders of the intermetallides $Gd_{1-x}Y_xMn_2Ge_2$ at 4.2 K. The points are experimental data, and the curves are calculated.

zation depends weakly on temperature. Finally, for $x=0.5$ the magnetization falls off monotonically with increasing temperature. Analysis of the magnetic data and the results of x-ray diffraction measurements of the crystal structure parameters of these compounds show that the transitions at temperatures T_1 and T_2 are first-order magnetic phase transitions, while that at T_3 is a second-order phase transition. Above T_c a weak magnetic state is observed at all the concentrations studied. The $T-x$ magnetic phase diagram of the intermetallides $Gd_{1-x}Y_xMn_2Ge_2$ is shown in Fig. 9.

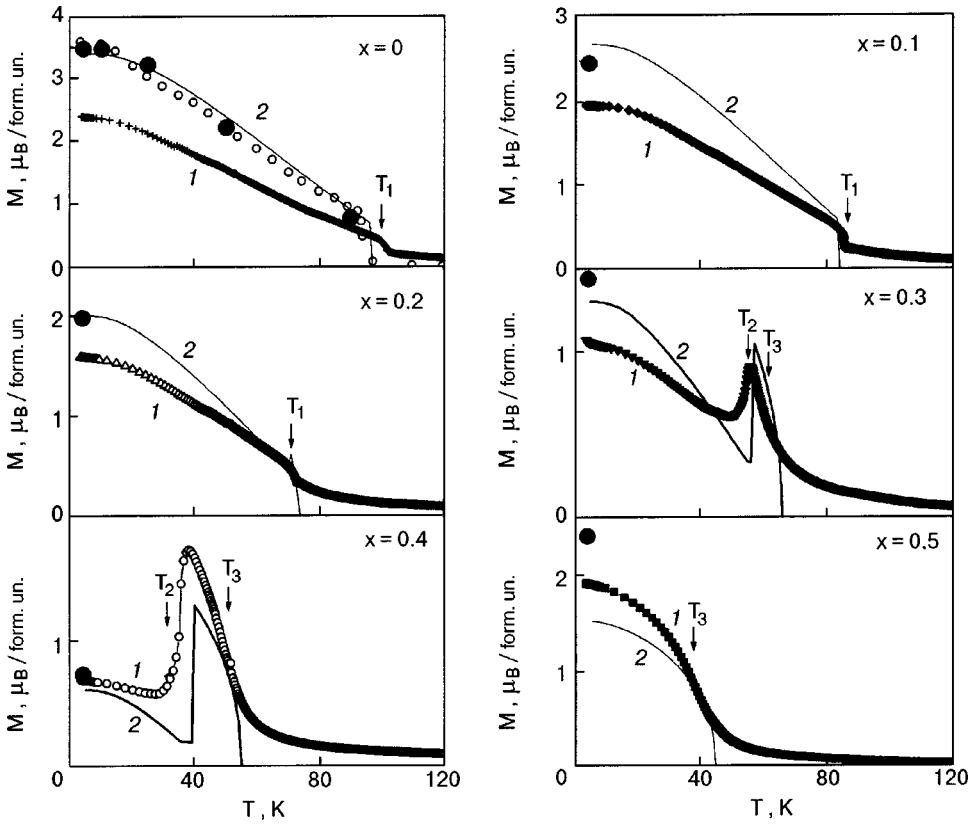

FIG. 8. Temperature dependence of the magnetization of $Gd_{1-x}Y_xMn_2Ge_2$ intermetallides: experimental data in a field of 0.83 T for free powders (*1*); theoretical dependences (*2*); ●—values of the spontaneous magnetization obtained from measurements in high magnetic fields (see Fig. 7). For the compound with $x=0$ the spontaneous magnetization data of Ref. 27 for a single crystal are also shown (○); T_i are the critical temperatures of the phase transitions.

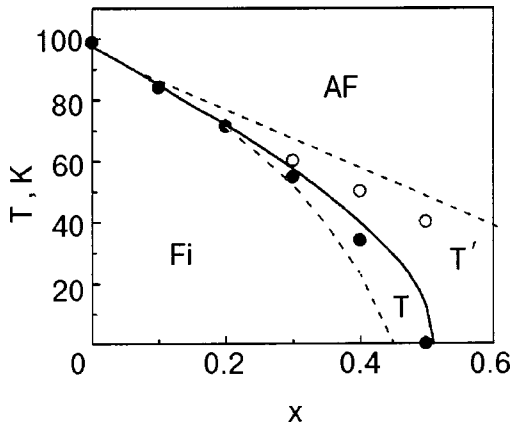

FIG. 9. Magnetic $T-x$ phase diagram for $Gd_{1-x}Y_xMn_2Ge_2$ intermetallides: ○, ●—experimental data for second- and first-order phase transitions, respectively. The calculated phase diagrams are shown by the dashed (second-order transition) and solid (first-order transition) curves.

The experimental data can be explained in terms of a modified Yafet–Kittel model in the following way. At low temperatures the gadolinium-rich compounds ($x \leqslant 0.4$) have a rather large intersublattice exchange interaction. This leads to ferromagnetic ordering of the manganese subsystem and, consequently, those intermetallides are collinear ferrimagnets. At $x=0.5$ the intrasublattice exchange interaction is insufficient for collinear ferromagnetic ordering of the unstable manganese subsystem—the triangular phase appears, and the total moment increases (see Fig. 8). As the temperature is raised, the decrease in the magnetization of the gadolinium subsystem leads to a decrease in the molecular field acting on the unstable manganese subsystem, and in compounds with $x=0$, 0.1, and 0.2 this subsystem undergoes a transition to an antiferromagnetic state at a temperature T_1, and the gadolinium subsystem becomes paramagnetic. We note that this behavior has been confirmed previously for a number of RMn_2Ge_2 intermetallides by neutron diffraction studies.[1,10] In compounds with $x=0.3$ and 0.4 there is a second-order transition from the Fi phase to the T phase on heating and then, as the temperature is increased further to T_2 there is a second-order transition from that phase to a triangular phase T′; here the magnetization increases in a jump (the compound with $x=0.5$ is already in the T′ phase at 4.2 K, and therefore the second-order transition is absent). Finally, at a temperature T_3 the manganese subsystem becomes antiferromagnetic while the gadolinium subsystem goes to a paramagnetic state.

The modified Yafet–Kittel model can also describe the metamagnetic transition observed in the free powders at high magnetic fields (Fig. 7). In Ref. 36 it was shown that the following sequence of phases should be observed in free powders with increasing field: Fi↔T↔T′↔T↔F, and that the transitions between triangular phases are first-order phase transitions while the rest are second-order. It can be assumed that the metamagnetic transition is due to a transition from the phase T to T′.

The modified Yafet–Kittel model is capable of not only a qualitative but also a quantitative description of the experimental data for the $Gd_{1-x}Y_xMn_2Ge_2$ intermetallides. The theoretical curves calculated in this model are shown by the curves in Figs. 7–9. In the theoretical calculations the necessary exchange parameters are determined from the concentration dependence of the field of the metamagnetic transition at 4.2 K in the system $Gd_{1-x}Y_xMn_2Ge_2$ and from the temperatures of the spontaneous magnetic phase transitions and Néel temperature in $GdMn_2Ge_2$. The magnetic anisotropy constant K was determined from data on the field dependence of the magnetization of the $GdMn_2Ge_2$ single crystal along the axis of hard magnetization at 4.2 K from Ref. 18 (the details of the calculation are given in Ref. 36): $\lambda_{12}=-7.7\ \mathrm{T}/\mu_B$, $\lambda'_{22}=-10.9\ \mathrm{T}/\mu_B$, $\lambda_{22}=245\ \mathrm{T}/\mu_B$, $\lambda_{11}=2.2\ \mathrm{T}/\mu_B$, and $K=15.8\ \mathrm{T}\cdot\mu_B$. These parameters were also used in calculating the magnetization curves of the $GdMn_2Ge_2$ single crystal for comparison with the experimental data (Figs. 10 and 11). It may be seen that the agreement of the theory with experiment is quite good.

Since the sizes of the Gd and Y atoms are close to each other, in analyzing the magnetic properties of $Gd_{1-x}Y_xMn_2Ge_2$ one can in a first approximation ignore the dependence of the exchange interaction between neighboring Mn planes on the concentration x. In contrast to the system with yttrium, in the intermetallides $Gd_{1-x}La_xMn_2Ge_2$ the concentration dependence of the interatomic distances is extremely large, since the atomic radii of Gd and La are very different. Therefore the magnetic properties of the yttrium- and lanthanum-substituted intermetallides of gadolinium are qualitatively different. However, in spite of this, a rather good description of the experimental data on the magnetization and magnetic phase diagrams of the $Gd_{1-x}La_xMn_2Ge_2$ system can be achieved using the data obtained for the gadolinium–yttrium intermetallides, if the dependence of the Mn–Mn interlayer exchange interaction on the interatomic distances is taken into account.[37,38]

In Fig. 12 the experimental temperature dependence of the magnetization of $Gd_{1-x}La_xMn_2Ge_2$ is compared with the dependence calculated in the Yafet–Kittel model. It is seen that satisfactory agreement is obtained between the theoretical and experimental data and, most importantly, that the theoretical model describes well the sequence of spontaneous transitions Fi→AF→Fi→paramagnetic phase (P) observed experimentally at high temperatures in compounds with $x<0.1$. The Fi→AF transition is due to the fact that at higher temperatures the magnetic moment of the gadolinium subsystem decreases, and at the temperature of this transition the manganese subsystem goes to an antiferromagnetic state, while the gadolinium subsystem becomes paramagnetic. On further increase in temperature the crystal lattice parameter a increases on account of thermal expansion, and at the temperature of the reentrant transition AF↔Fi the interplane exchange interaction becomes ferromagnetic. We note that for $x>0.1$ this interaction is ferromagnetic in the entire temperature range ($a>a_c$), and the intermetallides with such a La concentration behave as ordinary ferrimagnets. A comparison of the theoretical and experimental $T-x$ phase diagrams (Fig. 13) attests to their good agreement.

Thus the modified Yafet–Kittel model permits description of the magnetic properties of the mixed intermetallides over f a wide range of concentrations and temperatures in the region of moderately high magnetic fields. We agree, though, that this is a simplified model, since it includes only the

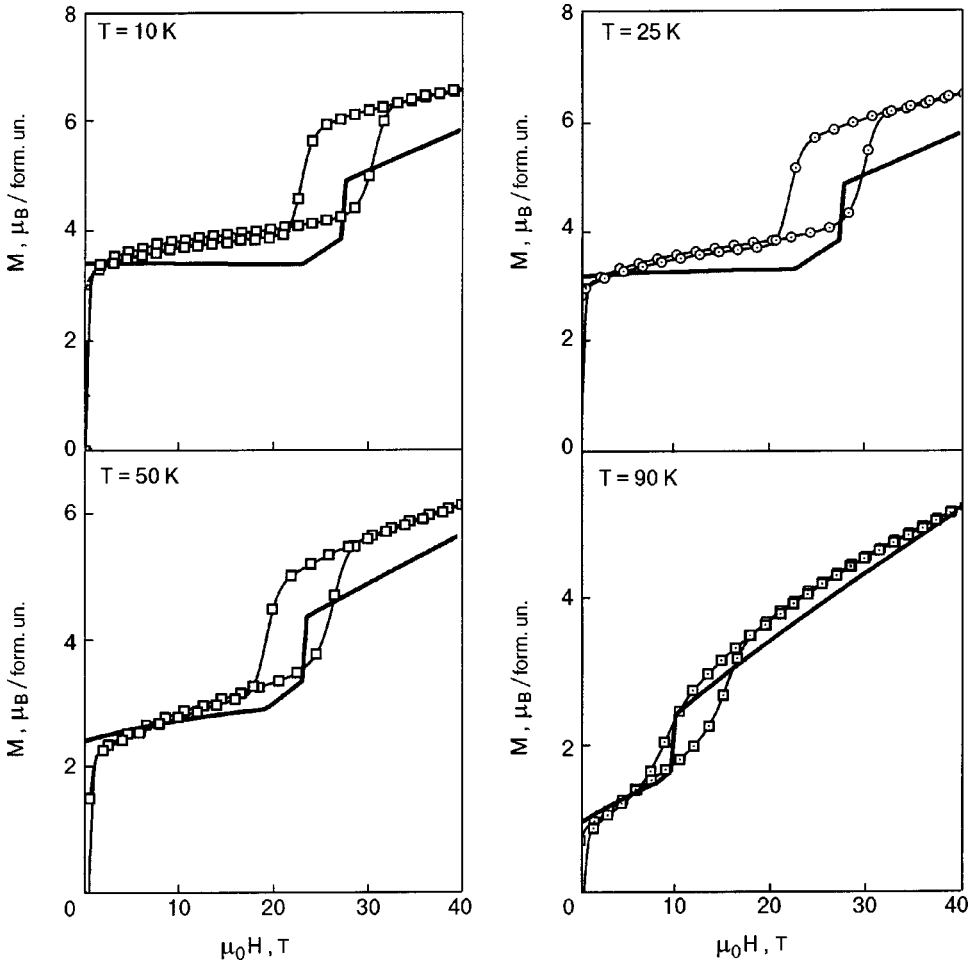

FIG. 10. Field dependence of the magnetization of $GdMn_2Ge_2$ intermetallides for different temperatures. The symbols are experimental data, and the curves are calculated.

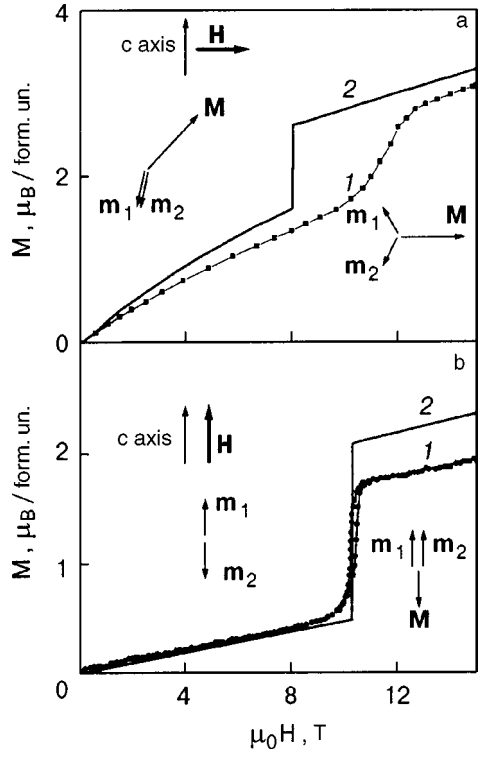

FIG. 11. Experimental (*1*), for a single crystal from Ref. 18, and calculated (*2*) magnetization curves of the intermetallic compound $GdMn_2Ge_2$ at 77 K for $\mathbf{H}\perp\mathbf{c}$ (a) and at 290 K for $\mathbf{H}\perp\mathbf{c}$ (b).

exchange interactions in the planes and between nearest-neighbor planes. It is incapable of describing the long-period magnetic structures observed in the RMn_2Ge_2 intermetallides with light rare earths. Difficulties arise in using this model to describe the magnetic phase diagram of the $GdMn_2Ge_2$ single crystal in high magnetic fields, etc. For this reason we have attempted to complicate the model and move beyond the framework of the Yafet–Kittel approximation in interpreting the magnetic properties of these intermetallides.

6. BEYOND THE YAFET–KITTEL APPROXIMATION

Yet another example of a shortcoming of the model set forth in the preceding Section, as an analysis of the available experimental data shows, is its inability to give even a qualitative description of the magnetic properties of the compound $DyMn_2Ge_2$. Magnetic and neutron diffraction studies on the single crystal have shown[24] that in $DyMn_2Ge_2$ the magnetic moments of Mn order antiferromagnetically at $T_N = 431$ K. According to the data of Ref. 24 and also of Refs. 22 and 43, where neutron diffraction studies were done on powders, in the low-temperature region $DyMn_2Ge_2$ has two first-order magnetic phase transitions: at a temperature T_1, which according to the data of these studies lies in the interval from 33 to 35 K, and at T_2, from 37.5 to 40 K. For $T < T_1$ $DyMn_2Ge_2$ is characterized by an Fi structure, analogous to that described above for $GdMn_2Ge_2$. For $T > T_2$ the compound has an AF structure with disordered dysprosium

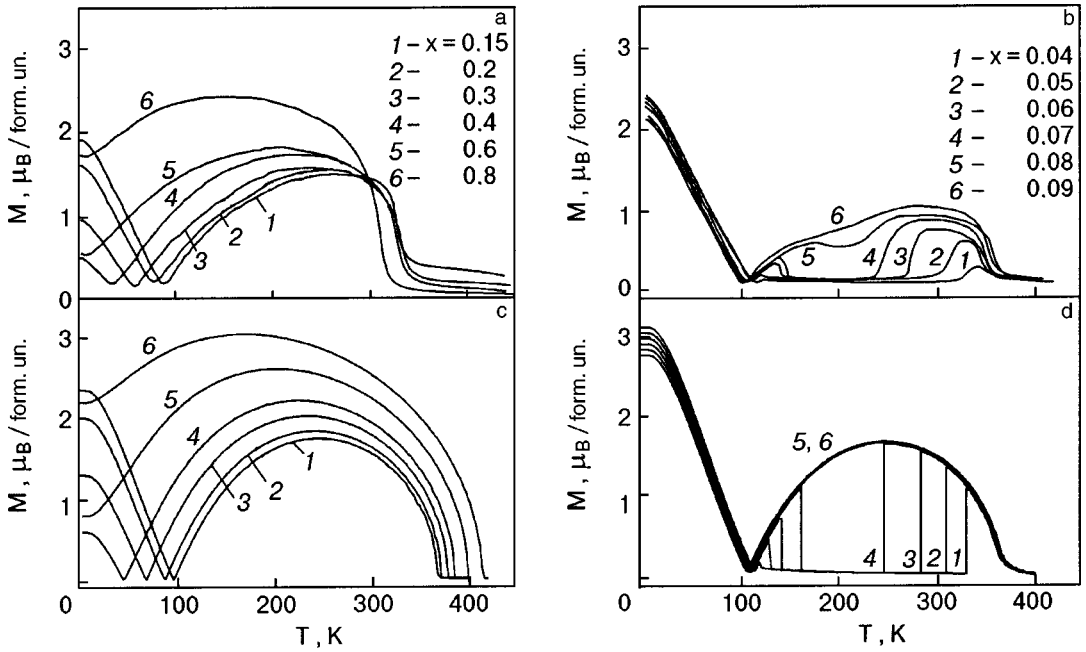

FIG. 12. Experimental (a,b) and theoretical (c,d) temperature dependence of the magnetization of $Gd_{1-x}La_xMn_2Ge_2$ intermetallides.

moments. For the temperature interval between T_1 and T_2 the data of Refs. 22, 24, and 43 are inconsistent. According to Ref. 22, three phases coexist in this interval: Fi, I and AF (see Fig. 3), and the magnetic unit cell is characterized by a tripling along the tetragonal axis, i.e., $a'=a$ and $c'=3c$. According to Ref. 43, below T_2 the AF phase does not exist, as can be seen from the temperature dependence of the integrated intensity of the corresponding line. The authors of Ref. 43 believe that a single incommensurate phase exists between T_1 and T_2, with a wave vector $\mathbf{k}\approx(0,0,0.65)$ according to a preliminary determination. The measurements of the magnetization curves on $DyMn_2Ge_2$ single crystals in fields up to 15 T (Ref. 24) and 5 T (Ref. 44) have revealed the presence of first-order transitions in all of the investigated temperature range, up to 70 K.

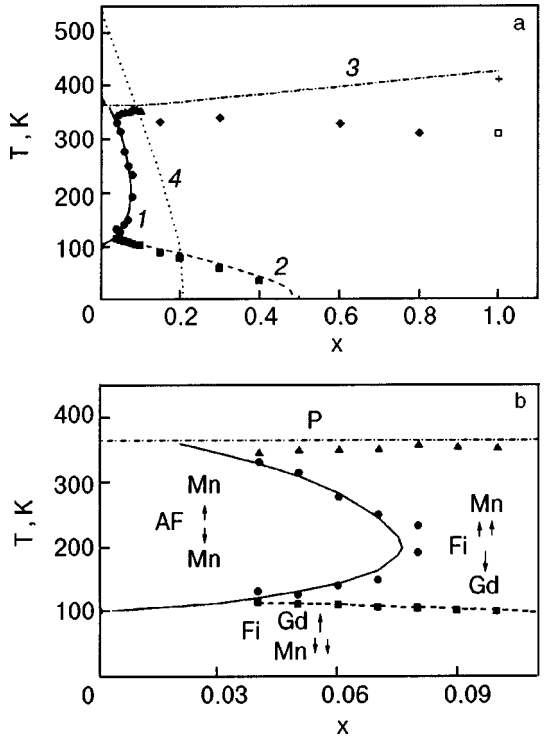

FIG. 13. a—The $T-x$ magnetic phase diagram of the $Gd_{1-x}La_xMn_2Ge_2$ intermetallides in a field of 0.8 T (the points are experimental data, the curves are calculated): first-order phase transition Fi↔AF (●, *1*); magnetic compensation temperature (■, *2*); the second-order transition to the paramagnetic state (Néel temperature T_N) (3); temperature of the destruction of ferrimagnetic order (the Curie temperature T_C) (▲, ♦); the line of the change of sign of the Mn–Mn interlayer exchange interaction (*4*); the temperatures T_N and T_C are from Ref. 8 (+, □). b—The experimental part of the phase diagram from Ref. 42 for $x<0.1$ in comparison with the results of the calculation.

The model described above is incapable, in particular, of explaining the existence of the magnetic structure observed in the temperature interval between T_1 and T_2, the value of the jump in magnetization at the second-order phase transition at low temperatures in a field oriented along the tetragonal axis of the crystal,[24] etc. Therefore in Ref. 45 the model was refined to include the exchange interactions between the next-nearest magnetic layers. This is a natural refinement, since the exchange interaction in the intermetallides under study is brought about not only by the superexchange via germanium but also via conduction electrons, and it is long-ranged. The Dy^{3+} ion, in contrast to Gd^{3+}, is not an S ion, and so there will be substantial crystal-field effects. When these factors are taken into account, nonequivalent positions of the magnetic moments can arise in the crystal, both in the dysprosium and manganese magnetic subsystems. The presence of these nonequivalent positions and the exchange interactions between different layers of magnetic atoms were taken into account in writing the effective Hamiltonians in Ref. 45.

The effective Hamiltonian for the Dy^{3+} ion located in the ith position can be written in the molecular field approximation as

$$\mathcal{H}_{\mathrm{Dy}}^{(i)}=B_2^0O_2^0+B_4^0O_4^0+B_4^4O_4^4+B_6^0O_6^0 + B_6^4O_6^4-g_J\mu_B\mathbf{J}^{(i)}(\mathbf{H}+\mathbf{H}_m^{(i)}), \quad (4)$$

where B_n^m are the parameters of the crystalline field of tetragonal symmetry, O_n^m are equivalent operators, g_J is the Landé factor, and $\mathbf{J}^{(i)}$ is the angular momentum operator of the Dy^{3+} ion. The molecular field $\mathbf{H}_m^{(i)}$ is given by the expression

$$H_{mj}^{(i)}=\sum_l \lambda_{11}^{(l)}M_j^{(l)}+\sum_k \lambda_{12}^{(k)}m_j^{(k)},\ j=x,y,z. \quad (5)$$

The components of the ith dysprosium magnetic moment $\mathbf{M}^{(i)}$ and the kth manganese magnetic moment $\mathbf{m}^{(k)}$ are given by $M_j^{(i)}=\mu_B g_J\langle J_j^{(i)}\rangle$ and $m_j^{(i)}=\mu_B g\langle S_j^{(k)}\rangle$, where g is the g factor of Mn, $\mathbf{S}^{(k)}$ is the spin angular momentum operator of Mn, and $\lambda_{11}^{(l)}$ and $\lambda_{12}^{(k)}$ are the parameters of the Dy–Dy and Dy–Mn exchange interactions, respectively. The parameters of the Dy–Dy and Dy–Mn exchange interactions between atoms belonging to different layers appear in all the expressions additively,[45] and so it makes sense to use the summed parameters λ_{11} and λ_{12}.

For the kth magnetic moment of the d subsystem of manganese the effective Hamiltonian $\mathcal{H}_{\mathrm{Mn}}^{(k)}$ in the molecular field approximation with only the exchange interactions taken into account is equal to

$$\mathcal{H}_{\mathrm{Mn}}^{(k)}=-g\mu_B\mathbf{S}^{(k)}H_{\mathrm{Mn}}^{(k)}. \quad (6)$$

The effective field acting on the kth magnetic moment of the Mn subsystem in an external magnetic field $\mathbf{H}$ oriented at an angle φ to the $\mathbf{c}$ axis of the crystal is equal to

$$H_{\mathrm{Mn}}^{(k)}=H\cos(\varphi-\eta_k)+H_m^{(k)},$$

$$H_m^{(k)}=\sum_{n=k,k\pm1,\ldots}\lambda_{22}^{(n)}m^{(n)}\cos(\eta_n-\eta_k) + \lambda_{12}\sum_i (M_z^{(i)}\cos\eta_k+M_x^{(i)}\sin\eta_k), \quad (7)$$

where η_k is the polar angle of the kth manganese moment, and $\lambda_{22}^{(n)}$ are the parameters of the Mn–Mn exchange interaction between atoms belonging to the kth and nth layers. The anisotropy of the manganese subsystem, since it is small compared to the exchange, is included in the thermodynamic potential as an additive term.

The thermodynamic potential per formula unit in the molecular field approximation is given by the following expression (N is the number of nonequivalent formula units):

$$\Phi=\frac{1}{N}\left\{-k_BT\sum_{i=1}^{N}\ln Z_i+\frac{1}{2}\sum_{i=1}^{N}\mathbf{M}^{(i)}\mathbf{H}_m^{(i)}-k_BT \times\sum_{k=1}^{2N}\ln\frac{\sinh[(2S+1)x_k/2]}{\sinh(x_k/2)}+\frac{1}{2}\sum_{k=1}^{2N}\mathbf{m}^{(k)}\mathbf{H}_m^{(k)} +\sum_{k=1}^{2N}K\sin^2\theta_k\right\}. \quad (8)$$

The partition function Z_i for the ith dysprosium moment was calculated in Ref. 45 by numerical diagonalization of the Hamiltonian $\mathcal{H}_{\mathrm{Dy}}^{(i)}$ with the solution of the corresponding self-consistent problems, $x_k=\mu_B gH_{\mathrm{Mn}}^{(k)}/k_BT$; here and K is the anisotropy constant for the manganese subsystem. The second and fourth terms in expression (8) are the usual correction terms in molecular field theory.

The problem of determining the set of parameters of the compound $DyMn_2Ge_2$ when interpreting experimental data on the magnetic properties of this compound on the basis of the thermodynamic potential (8) was solved in Ref. 45.

At helium temperatures $DyMn_2Ge_2$ has three first-order phase transitions from the initial phase Fi in a field along the tetragonal axis. At $H\approx7$ T a transition occurs to phase I, in which every third layer of the manganese subsystem has a magnetic moment reoriented along the field direction. The higher-field phases are the AF phase, with antiferromagnetic ordering in the manganese subsystem, and the F phase, in which the magnetic moments of both subsystems are oriented along the field. The values of the three critical fields are: $H_{\mathrm{Fi}\leftrightarrow\mathrm{I}}=7$ T, $H_{\mathrm{I}\leftrightarrow\mathrm{AF}}=32$ T, and $H_{\mathrm{AF}\leftrightarrow\mathrm{F}}=110$ T (Ref. 45) can be used to determine the three exchange parameters of the compound: λ_{12} (Dy–Mn), λ'_{22} (Mn–Mn in neighboring layers), and λ''_{22} (Mn–Mn in next-nearest layers). At low temperatures and high fields along the tetragonal axis the critical fields of these transitions are given by the expressions

$$H_{\mathrm{Fi}\leftrightarrow\mathrm{I}}=-\lambda_{12}M+(\lambda'_{22}+\lambda''_{22})m,$$

$$H_{\mathrm{I}\leftrightarrow\mathrm{AF}}=-\lambda_{12}M+(\lambda'_{22}-2\lambda''_{22})m, \quad (9)$$

$$H_{\mathrm{AF}\leftrightarrow\mathrm{F}}=-\lambda_{12}M-(\lambda'_{22}+\lambda''_{22})m.$$

For $M=10\mu_B$ and $m=2.2\mu_B$ (Ref. 24) the exchange parameters have the values $\lambda_{12}=-5.85$ T/μ_B, $\lambda'_{22}=-20$ T/μ_B, and $\lambda''_{22}=-3.5$ T/μ_B. The total low-temperature magnetization curve calculated with these parameters for the compound $DyMn_2Ge_2$ in the case when the field is applied along the tetragonal axis is shown in Fig. 14. Also shown there are the experimental curve measured in a field of up to 15 T in Ref. 24 and the high-field peaks of the differential magnetic susceptibility obtained in Ref. 45.

From the values of $T_N=440$ K and the known values of λ'_{22} and λ''_{22} one can find the parameter of the Mn–Mn exchange interaction in the layer: $\lambda_{22}\approx2\times10^3$ T/μ_B. The $H-T$ phase diagram calculated on the basis of Eq. (8) is presented in Fig. 15 together with the experimental data obtained in Refs. 24, 44, andm 45. We see that the calculated temperature dependence of the critical field $H_{\mathrm{Fi}\leftrightarrow\mathrm{I}}$ is in good agreement with the experimental dependence obtained on a single crystal in Ref. 24. The field $H_{\mathrm{I}\leftrightarrow\mathrm{AF}}$ according to the calculation depends more weakly on temperature than does that obtained from the measurements on free powders in Ref. 45. The extremely good agreement of the experimental[24] and calculated magnetization curves for the AF phase in a field parallel to the tetragonal axis can be seen in Fig. 16d.

For a field direction perpendicular to the tetragonal axis a first-order phase transition from the Fi to the triangular phase occurs at the critical field; in the triangular phase the magnetic moment of dysprosium is oriented along the field direction, while the Mn moments lie at obtuse angles to it. The corresponding theoretical magnetization curves calculated with the use of the crystal-field parameters determined in Ref. 45 ($B_2^0=200$, $B_4^0=-3.5$, $B_6^0=-50$, and $B_4^4=-390$ cm^{-1}) are shown in Figs. 16a and 16b. It is seen that the calculated susceptibility in the Fi phase agrees with

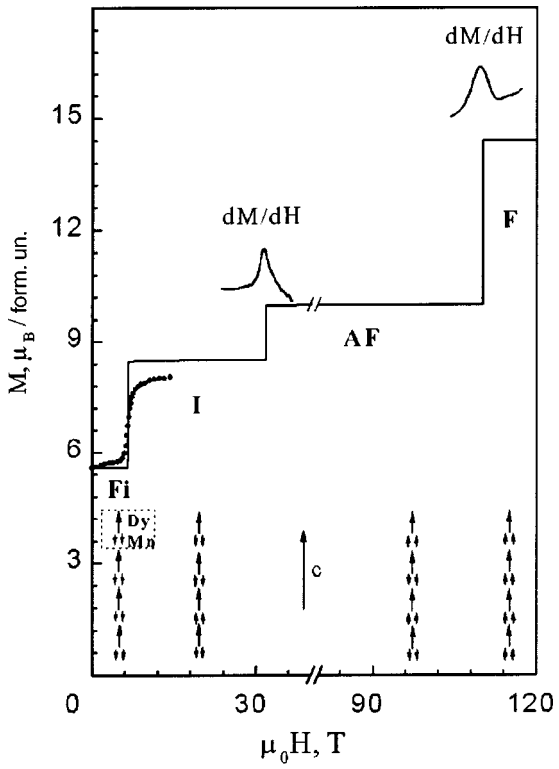

FIG. 14. Low-temperature magnetization of the compound $DyMn_2Ge_2$ as a function of the field applied along the tetragonal axis. The curve is calculated, the filled circlets are the experimental data for a single crystal at 4.2 K from Ref. 24. For the phase transitions I↔AF and AF↔F the peaks of dM/dH obtained in Ref. 45 for $T=7$ and 5 K, respectively, are shown above the magnetization curve. The arrows indicate the magnetic moments of dysprosium and manganese in the layers. The dotted box encloses one formula unit.

the experimental dependence at both temperatures. The decrease of the critical field with increasing temperature is also correctly described (in both the experiment and theory the field of the phase transition is smaller at 20 K than at 4.2 K). The calculated jump in the magnetization is larger than that observed in experiment. Figures 16c and 16d show the magnetization curves for a field direction in the basal plane in the temperature region where the initial phase is AF. It is seen that at $T=60$ K (Fig. 16c) the theoretical curve is in good agreement with the experimental curve obtained in Ref. 44 in measurements on a single crystal in the form of a slab, with allowance for the demagnetizing fields. For $T=77$ K (Fig. 16d) the agreement between the calculated and experimental (from Ref. 24) magnetization curves is poorer.

Thus when the exchange interaction between next-nearest manganese layers is taken into account together with the antiferromagnetic exchange interaction of nearest manganese layers, one can describe the magnetic properties of $DyMn_2Ge_2$ over a wide range of magnetic fields.

We have attempted to apply this model to solve the problems of the first-order high-field transition in $GdMn_2Ge_2$. The second-order phase transition in $GdMn_2Ge_2$ observed near 100 T in measurements of the differential magnetic susceptibility in ultrahigh magnetic fields[46] should be interpreted in the framework of the phase diagram of this compound for $\mathbf{H}\|\mathbf{c}$ as an AF↔T transition, since this is the only possible high-field first-order transition (see Fig. 6). The value of the critical field of this transition, calculated using the values determined for the parameters of $GdMn_2Ge_2$ in the modified Yafet–Kittel model (see Sec. 5), came out to be ~70 T, i.e., much less than the experimental value. This raises the question of whether the agreement of the experimental and calculated values of the field of this transition might be improved by taking into account the interaction between next-nearest Mn planes, as was the situation in the dysprosium compound. However, our calculations showed that the Mn–Mn exchange across an intervening layer does not appear in the expression for the critical fields of this phase diagram. This means that the problem requires further investigation.

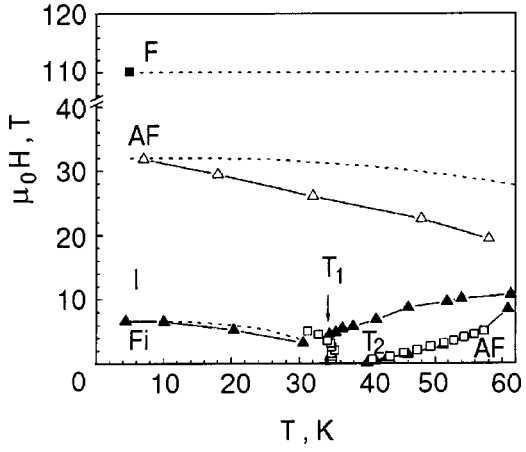

FIG. 15. Magnetic phase diagram $H-T$ for $DyMn_2Ge_2$. The dashed curves are calculated, the rest is experimental data from Ref. 45 (■, △), Ref. 24 (▲), and Ref. 44 (□).

CONCLUSION

This review of the magnetic properties of layered intermetallic compounds RMn_2Ge_2 has shown a great diversity of magnetic structures, magnetic phase diagrams, and various spontaneous and field-induced phase transitions in pure, diluted, and mixed compounds. It follows from an analysis of the magnetic properties of intermetallides with heavy rare earths that these compounds can be considered to be ferrimagnets with an antiferromagnetic exchange interaction in the manganese subsystem. In a number of cases their properties are satisfactorily described in the extremely simple model of a two-sublattice ferrimagnet with antiferromagnetic intrasublattice exchange (the Yafet–Kittel model) with allowance for the magnetic anisotropy. However, such a model is not always adequate, since it takes into account only the exchange interaction between nearest neighbors, and one must consider more complicated models. For example, for describing the properties of $DyMn_2Ge_2$ it is necessary to take into account the exchange between next-nearest manganese layers. Apparently the antiferromagnetic component of the intraplane exchange interaction in the manganese subsystem is also important; it might make it possible to explain the long-period noncollinear magnetic structures observed in a number of RMn_2Ge_2 intermetallides with light rare earths.

We note that RMn_2Ge_2 compounds are natural superlattices, and some interesting questions concerning that property are beyond the scope of this review. In particular, there is an extremely significant giant magnetoresistance effect

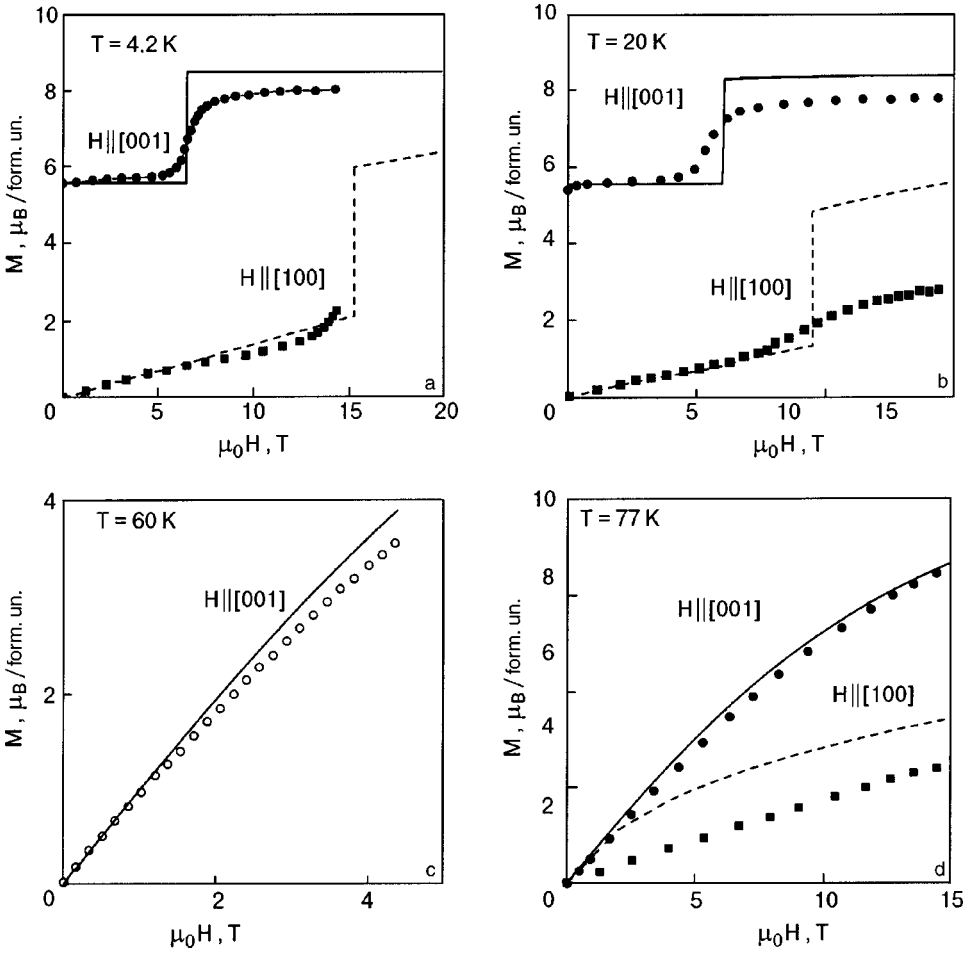

FIG. 16. Magnetization of the compound $DyMn_2Ge_2$ as a function of magnetic field applied along the indicated directions for various temperatures T [K]: 4.2 (a), 20 (b), 60 (c), and 77 (d). The points are experimental data of Ref. 24 (●, ■) and Ref. 44 (○); the curves are calculated.

that is manifested at metamagnetic transitions induced by a magnetic field. In Refs. 47 and 48, for example, an unusually large (up to 15%) jump in the magnetoresistance in a field was observed in (Gd, La)Mn_2Ge_2 compounds near 200 K.

This study was supported by the Foundation for Support of Science Schools (Project No. 00-15-96695).

*E-mail: levitin@plms.phys.msu.su

[1] A. Szytula and J. Lecieijewicz, *Handbook on Physics and Chemistry of Rare Earths*, Vol. 12, edited by K. A. Gschneidner Jr. and L. Eyring, North Holland, Amsterdam (1989), p. 133.
[2] Z. Ban and M. Sikirica, Acta Crystallogr. **18**, 594 (1965).
[3] G. Venturini, J. Alloys Compd. **232**, 133 (1996).
[4] I. Nowik, Y. Levi, I. Felner, and E. R. Bauminger, J. Magn. Magn. Mater. **140–144**, 913 (1995); **147**, 373 (1995).
[5] K. S. V. L. Narashimhan, J. Appl. Phys. **46**, 4957 (1975).
[6] T. Shigeoka, N. Iwata, H. Fujii, and T. Okamoto, J. Magn. Magn. Mater. **53**, 83 (1985).
[7] A. Szytula and I. Szott, Solid State Commun. **40**, 199 (1981).
[8] G. Venturini, B. Malaman, and E. Ressouche, J. Alloys Compd. **241**, 135 (1996).
[9] G. Venturini, R. Welter, E. Ressouche, and B. Malaman, J. Alloys Compd. **210**, 213 (1994).
[10] R. Welter, G. Venturini, E. Ressouche, and B. Malaman, J. Alloys Compd. **218**, 204 (1995).
[11] N. Iwata, T. Ikeda, T. Shigeoka, H. Fujii, and T. Okamoto, J. Magn. Magn. Mater. **54–57**, 481 (1986).
[12] T. Shigeoka, N. Iwata, and H. Fujii, J. Magn. Magn. Mater. **76–77**, 189 (1988).
[13] H. Fujii, T. Okamoto, T. Shigeoka, and N. Iwata, Solid State Commun. **53**, 715 (1985).
[14] E. M. Gyorgy, B. Batlogg, J. P. Remeika, R. B. van Dover, R. M. Fleming, H. E. Blair, G. P. Espinosa, A. S. Cooper, and R. G. Maines, J. Appl. Phys. **61**, 4237 (1987).
[15] M. Duraj, R. Duraj, A. Szytula, and Z. Tomkowicz, J. Magn. Magn. Mater. **73**, 240 (1988).
[16] I. Felner and I. Nowik, J. Phys. Chem. Solids **39**, 763 (1978).
[17] T. Shigeoka, H. Fujii, H. Fujiwara, K. Yagasaki, and T. Okamoto, J. Magn. Magn. Mater. **31–34**, 209 (1983).
[18] H. Kobayashi, H. Onodera, and H. Yamamoto, J. Magn. Magn. Mater. **79**, 76 (1989).
[19] T. Shigeoka, J. Sci. Hiroshima Univ.: Ser. A, **48**, 103 (1984).
[20] J. Leciejewicz and A. Szytula, Solid State Commun. **49**, 361 (1984).
[21] G. Venturini, B. Malaman, and E. Ressouche, J. Alloys Compd. **240**, 139 (1996).
[22] G. Venturini, B. Malaman, K. Tomala, A. Szytula, and J. P. Sánchez, Phys. Rev. B **46**, 207 (1992).
[23] T. Ono, H. Onodera, M. Ohashi, H. Yamaguchi, and Y. Yamaguchi, J. Magn. Magn. Mater. **123**, 133 (1993).
[24] H. Kobayashi, H. Onodera, Y. Yamaguchi, and H. Yamamoto, Phys. Rev. B **43**, 728 (1991).
[25] Yin-gang Wang, Fuming Yang, Changpin Chen, N. Tang, and Qidong Wang, J. Phys.: Condens. Matter **9**, 8539 (1997).
[26] G. Venturini, R. Welter, E. Ressouche, and B. Malaman, J. Magn. Magn. Mater. **150**, 197 (1995).
[27] N. Iwata, K. Hattori, and T. Shigeoka, J. Magn. Magn. Mater. **53**, 318 (1986).
[28] L. Morellon, P. A. Algarabel, M. R. Ibarra, and C. Ritter, Phys. Rev. B **55**, 12363 (1997).
[29] M. Duraj, R. Duraj, and A. Szytula, J. Magn. Magn. Mater. **79**, 61 (1989).
[30] H. Fujii, M. Isoda, T. Okamoto, T. Shigeoka, and N. Iwata, J. Magn. Magn. Mater. **54–57**, 1345 (1986).
[31] I. Yu. Gaĭdukova, Guo Guanghua, S. A. Granovskiĭ, I. S. Dubenko, R. Z. Levitin, A. S. Markosyan, and V. E. Rodimin, Fiz. Tverd. Tela (St. Petersburg) **41**, 2053 (1999) [Phys. Solid State **41**, 1885 (1999)].
[32] S. Asano and J. Yamashita, Prog. Theor. Phys. **49**, 373 (1972).
[33] S. Ishida, S. Asano, and J. Ishifa, J. Phys. Soc. Jpn. **55**, 936 (1986).

[34] Y. Yafet and C. Kittel, Phys. Rev. **87**, 290 (1952).
[35] N. P. Kolmakova, S. A. Kolonogiĭ, R. Z. Levitin, and H. W. Nekrasova, Fiz. Tverd. Tela (St. Petersburg) **41** 1797, (1999) [Phys. Solid State **41**, 1694 (1999)].
[36] A. Yu. Sokolov, Guo Guanghua, S. A. Granovskiĭ, R. Z. Levitin, Kh. Vada, M. Shiga, and T. Goto, Zh. Éksp. Teor. Fiz. **116**, 1346, (1999) [JETP **89**, 723 (1999)].
[37] Guo Guanghua, R. Z. Levitin, V. V. Snegirev, D. A. Filippov, and A. Yu. Sokolov, Zh. Éksp. Teor. Fiz. **117**, 1127 (2000) [JETP **90**, 979 (2000)].
[38] Guo Guanghua, R. Z. Levitin, A. Yu. Sokolov, V. V. Snegirev, and D. A. Filippov, J. Magn. Magn. Mater. **214**, 301 (2000).
[39] Guo Guanghua, N. P. Kolmakova, R. Z. Levitin, M. Yu. Nekrasova, A. Yu. Sokolov, and D. A. Filippov, in *Proceedings of MISM'99* MSU, Moscow (1999), part 2, p. 233.
[40] C. Kittel, Phys. Rev. **120**, 335 (1960).
[41] V. V. Eremenko, A. B. Beznosov, E. L. Fertman, P. P. Pal-Val, and V. P. Popov, Adv. Cryog. Eng. **46**, 413 (2000).
[42] A. Sokolov, H. Wada, M. Shiga, and T. Goto, Solid State Commun. **105**, 289 (1998).
[43] H. Kobayashi, M. Ohashi, H. Onodera, T. Ono, and Y. Yamaguchi, J. Magn. Magn. Mater. **140–144**, 905 (1995).
[44] H. Wada, Y. Tanabe, K. Hagiwara, and M. Shiga, J. Magn. Magn. Mater. **218**, 203 (2000).
[45] Guo Guanghua, M. V. Eremin, A. Kirste, N. P. Kolmakova, A. S. Lagutin, R. Z. Levitin, M. von Ortenberg, and A. A. Sidorenko, Zh. Éksp. Teor. Fiz. **120**, 910 (2001) [JETP **93**, 796 (2001)].
[46] A. Kirste, R. Z. Levitin, M. von Ortenberg, V. V. Platonov, N. Puhlmann, V. V. Snegirev, D. A. Filippov, and O. M. Tatsenko, Fiz. Tverd. Tela (St. Petersburg) **43**, 1661 (2001) [Phys. Solid State **43**, 1731 (2001)].
[47] T. Fujiwara, H. Fujii, and T. Shigeoka, Physica B **281–282**, 161 (2000).
[48] E. V. Sampathkumaran, S. Majumdar, R. Mallik, R. Vijayaraghavan, H. Wada, and M. Shiga, J. Phys.: Condens. Matter **12**, L399 (2000).

Translated by Steve Torstveit

Anomalies of the electronic heat capacity of thulium cuprates in the pseudogap phase region

E. B. Amitin,* K. R. Zhdanov, M. Yu. Kameneva, Yu. A. Kovalevskaya, L. P. Kozeeva, and I. E. Paukov

Institute of Inorganic Chemistry, Siberian Branch of the Russian Academy of Science, pr. Lavrent'eva 3, 630090 Novosibirsk, Russia

A. G. Blinov

Novosibirsk State University, ul. Pirogova 2, 630090, Russia
(Submitted January 22, 2002)
Fiz. Nizk. Temp. **28**, 926–933 (August–September 2002)

Precision measurements of the heat capacity of thulium 1-2-3 cuprate with oxygen concentrations $x=6.92$ and $x=6.7$ are made in the temperature range 6–300 K. After the lattice components of the heat capacity of the samples are subtracted off, a comparison of the results makes it possible to determine the contribution to the heat capacity due to the formation of the pseudogap phase for the sample with $x=6.7$. The temperature dependence of this contribution has an anomaly near the boundary of the transition from the pseudogap phase to the normal metallic phase. The experimental results correlate with the theoretical ideas about the rearrangement of the electronic structure upon the transition of the system to the pseudogap phase region. © *2002 American Institute of Physics.* [DOI: 10.1063/1.1511712]

INTRODUCTION

A number of papers devoted to the study of the features that arise in various properties of a material upon the formation of a so-called pseudogap phase (PGP) in underdoped yttrium 1-2-3 and lanthanum 2-1-4 cuprate high-T_c superconductors (HTSCs) have come out in recent years. These systems manifest unusual properties as the charge carrier concentration p decreases from a certain critical value p_c (see Fig. 1), which corresponds to or is close to the optimal doping point (ODP), where a phase transition from the superconducting to the normal metallic state occurs. With decreasing carrier concentration ($p<p_c$) a new state of matter, which has come to be called the pseudogap phase, arises in a temperature interval $T_c(p)<T<T^*(p)$.

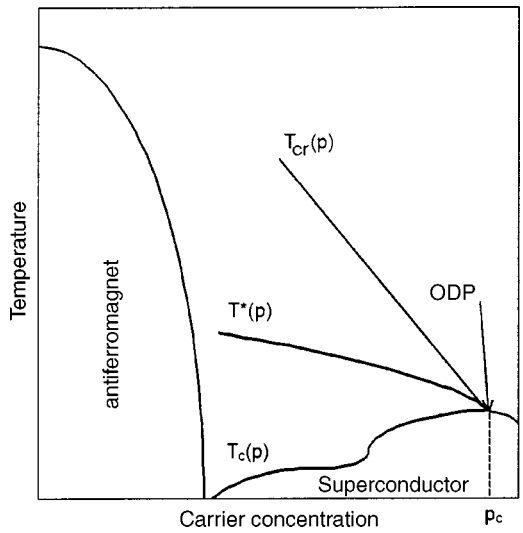

FIG. 1. Schematic illustration of the phase diagram.

Hundreds of papers have been devoted to the study of the unusual manifestations of the PGP in various properties of HTSCs. The most convincing proofs of the existence of the PGP have been obtained by direct methods—angle-resolved photoemission spectroscopy (ARPES) and electron tunneling.[1–3] The data from those studies indicate an appreciable decrease in the electronic density of states in the PGP region, where the electronic density of states in the neighborhood of the Fermi level has a V-shaped minimum. This V-shaped minimum becomes rounder as the temperature is increased and the boundary line is crossed. The system is transformed from the pseudogap state into a normal metallic state. Historically in the study of boundary phenomena in the normal phase of cuprate HTSCs in an underdoped state the boundary of the region in which a sharp deviation from the Korringa rule for NMR spin–lattice relaxation was taken as the boundary of the PGP.[4,5] Subsequent studies have established that the result obtained for the boundary of the PGP depends on the property used to determine it. It is known that the boundary $T_{\rm cr}$ determined by NMR methods from the Knight shift or by spin–lattice relaxation methods passes substantially higher on the temperature axis than the low-temperature boundary $T^*(p)$ determined from the thermodynamic and kinetic properties. The experimental facts have led many authors to assume that regions of strong and weak pseudogaps exist.[6] We shall adopt the notation proposed in Ref. 6. The upper boundary determined as the boundary of crossover phenomena in the NMR studies is denoted as $T_{\rm cr}$. The lower boundary can have the conventional notation $T^*(p)$.

Actually the existence of clearly defined boundaries separating different phases remains an open question. Some authors assume that no definite boundary exists and consider $T^*(p)$ to be proportional to the energy width of the

pseudogap.[7] In that case the upper and lower boundaries are the boundaries of two different forms of pseudogap—weak and strong. The authors of those papers assume that on crossing the line $T^*(p)$ the behavior of the electronic heat capacity can exhibit weak anomalies due to the rearrangement of the electronic density of states. Other authors (see, e.g., Ref. 8) take these boundaries to be lines of phase transitions. Chakravarti *et al.*[8] have proposed the presence of weak lattice modifications occurring in cuprates at the transition through the boundary $T^*(p)$ as a consequence of symmetry changes in the system of d electrons. In this case certain anomalies of the thermodynamic properties can be observed at $T^*(p)$. It can be quite complicated to sort out the nature of the possible features.

Two main mechanisms for the formation of the PGP have been considered in the literature.

The first mechanism involves the formation of Cooper pairs above the superconducting transition temperature. Here incoherent paired states are formed. As the temperature is lowered, the concentration of these pairs increases until, at the point T_c, a transition of the incoherent pairs to a correlated superconducting state occurs.[9,10]

The second mechanism assumes the formation of pseudogap states (PGS) on account of the interactions of the charge carriers with fluctuations of antiferromagnetic or charge-related short-range order (charge- or spin-density waves).[11–13]

Calculations show[14] that the interaction with the fluctuations can lead to a V-shaped dip in the density of states at the Fermi level. The choice of one model or the other for the formation of the PGS is a rather complex problem. Many authors assume that the second mechanism is more plausible than the first. Indeed, the experimental facts indicate that as the system approaches the tetra–ortho transition and moves farther away from the ODP, the distance between the boundary lines $T^*(p)$ and $T_c(p)$ on the temperature axis of the phase diagram increases substantially. At the same time, it would seem that similar pairing mechanisms in the PSS region and the superconducting phase should lead to a similar trend of the two boundary lines. In this sense the second mechanism, in which the intensity of the magnetic and charge fluctuations should play the governing role, can account for the experimentally observed behavior.

In addition to the direct studies of the features of the electronic states in the PGS of 1-2-3 and 2-1-4 cuprate HTSCs by the ARPES and electron tunneling methods, a significant contribution to the development of new ideas can be made by studying the thermodynamic properties of these compounds, particularly the electronic component of the heat capacity. The first studies of the unusual features of the thermodynamic characteristics in these systems were done by Junod's group in the early 1990s.[15,16] The main papers on the study of the new thermodynamic effects due to the formation of the PGP were written by Loram *et al.* in the latter half of that decade.[17–21] Interest in these studies has steadily grown, since much remains unclear in the theoretical description of the observed effects. The determination of the electronic contribution to the heat capacity meets with considerable difficulties. The electronic component of the heat capacity, C_{el}, in the normal state (above T_c) amounts to no more than 2–3% of the total value of the heat capacity. The component C_{el} due to the formation of a PGP is even smaller; it amounts to only 0.2–0.3% of the total heat capacity. In this situation even a small error in the the separation of the heat capacity into components (lattice, anharmonic, and magnetic) can lead to significant errors in the determination of the main parameters of the electronic properties of cuprate systems.

For determining the electronic components of the heat capacity in the yttrium cuprates $YBa_2Cu_3O_{6+x}$ in the PGS region, Loram *et al.* used the lattice heat capacity C_{ph} of the insulator $YBa_2Cu_3O_6$ as a base and took into account the possible differences of the lattice components in the cuprates under study. These corrections were made in the form of an expansion in Einstein functions. The expansion parameters for C_{ph} were determined in the low-temperature region ($T \approx 40$ K). Extrapolating of these components to the PGS region allowed those authors to separate out the electronic components of the heat capacity of the underdoped cuprates under study. It should be noted that the value of C_{ph} determined in this way should also include the difference of the magnetic and anharmonic contributions. Approximating this difference and extrapolating it by Einstein functions into the PGS region can lead to substantial errors in the determination of the electronic components of the heat capacity.

In view of what we have said above, we think it is more correct to determine the electronic contributions due to the formation of the PGS from a comparison of the experimental data for an underdoped sample and a sample in the ODP region. In this paper we present the results of such a comparison.

CHARACTERISTICS OF THE SAMPLES AND THE EXPERIMENTAL TECHNIQUE

A ceramic sample of $TmBa_2Cu_3O_x$ was obtained by the standard technique of solid-phase synthesis from the oxides Tm_2O_3 (Tm-3 grade), BaO, and CuO (OSCh—"especially pure"—grade). For a preliminary purging of volatile impurities prior to synthesis, the thulium and copper oxides were annealed at temperatures of 750 and 700 °C, respectively. The synthesis was done in corundum crucibles in the temperature interval 800–900 °C with a step of 25 °C. Before the start of the synthesis and before each temperature step-up the sample was carefully ground in an agate mortar. The annealing time at each temperature was 25 hours. Saturation of the sample to the optimum value ($x = 6.92$) was done at a elevated oxygen concentration. A subsequent reduction of the oxygen concentration to $x = 6.7$ was achieved by annealing in a standard atmosphere at $T = 590$ °C, followed by quenching in liquid nitrogen and a homogenizing low-temperature anneal at 100 °C for 2 days. The mass of the sample was ≈16 g. A $TmBa_2Cu_3O_x$ sample was chosen because the concentration of impurity Al, which enters the ceramic during synthesis in the corundum crucibles, is smaller by a factor of ten in that compound as compared to $YBa_2Cu_3O_x$. According to the data of an x-ray phase analysis (XPA), the $TmBa_2Cu_3O_x$ sample was close to single-phase, containing not more than 2–3% of the impurity phases Tm_2BaCuO_5 and $BaCuO_2$. The XPA data showed that the impurity content did not change when the oxygen concentration was changed. It should be noted that analysis

of the structure factors, which are sensitive to the uniformity of the oxygen distribution (the orthorhombicity parameters and the half-width of the basal reflections) showed a high degree of uniformity of the samples both at $x=6.92$ and at $x=6.70$.

Our studies of the temperature dependence of the heat capacity of the thulium cuprates $TmBa_2Cu_3O_{6.92}$ and $TmBa_2Cu_3O_{6.70}$ were done using an automated low-temperature vacuum adiabatic calorimeter.[22] The difference from the measurements done in Ref. 22 was that the nickel calorimetric cell was replaced by a similar one made of silvered copper. The cell had a volume of $\approx 6\ \mathrm{cm}^3$ and was graduated in the temperature interval 6–310 K, and the reliability of its operation was checked by a measurement on a standard substance—highly pure benzoic acid. The results obtained are in good agreement with reliable published data.[23–25] The accuracy of the measurements was $\pm 2\%$ at temperatures of 6–10 K, 0.5% in the interval 10–30 K, 0.2% from 30 to 60 K, and 0.1% in the interval from 60 to 310 K. The temperature rise in an individual calorimetric run was not over 5 K in the temperature interval 100–300 K. In that temperature interval the average scatter of the experimental values of the heat capacity over several series of measurements was around 0.02%. When the temperature was lowered to 10 K the scatter increased to a value of the order of 1%. For each sample we did 300–400 calorimetric runs.

EXPERIMENTAL RESULTS AND DISCUSSION

Determination of the harmonic components of the lattice heat capacity

The measured values of the heat capacity $C_p(T)$ can be decomposed into lattice, anharmonic, electronic, and magnetic components:

$$C_p = C_{\mathrm{ph}} + C_{\mathrm{uh}} + C_{\mathrm{el}} + C_{\mathrm{magn}}. \tag{1}$$

In the temperature interval of interest to us, the main contribution to the heat capacity comes from the lattice component C_{ph}. It will be described using the method of Ref. 26. It is known that there are three acoustic and $3(r-1)$ optical branches in the crystal. The contribution to the heat capacity from the acoustic branches, C_{ac}, will be described as a Debye contribution $C_{\mathrm{ac}}/R = 3D(\theta_0/T)$ with a phonon density of states $\gamma_{\mathrm{ac}}(\omega) = 9\omega^2/\omega_0^3$, where R is the gas constant, ω_0 is the limiting frequency of the acoustic modes, expressed in kelvins ($\omega_0 = \theta_0$), and

$$D(x) = \frac{3}{x^3}\int_0^x \frac{x^4 e^{-x}}{(1-e^{-x})^2}\,dx$$

is the Debye function. We shall assume that the optical modes are grouped into bands. In each band the photon density of states is taken to be constant: $\gamma_i(\omega) = m_i/(\omega_{i2} - \omega_{i1})$, where m_i is the number of branches in the ith band, and ω_{i1} and ω_{i2} are the lower and upper boundaries of the band. Then the contribution to the heat capacity from such a band is given by

$$\frac{C_i}{R} = \frac{m_i T}{\omega_{i2} - \omega_{i1}}\int_{i1/T}^{i2/T} \frac{x^2 e^{-x}}{(1-e^{-x})^2}\,dx.$$

It is clear that the sum of all m_i is determined by the number of atoms in the unit cell and is the sum of all the optical modes $\Sigma m_i = 3(r-1)$. At low temperatures the expression for the contribution from such an optical band has the form

$$\frac{C_i}{R} = \frac{m_i \omega_{i1}}{\omega_{i2} - \omega_{i1}}\left(\frac{\omega_{i1}}{T}\right)\exp\left(-\frac{\omega_{i1}}{T}\right).$$

It is seen from this expression that if at low temperatures the contribution from the low-lying phonon branches is subtracted, the corresponding component of the heat capacity will be governed by the exponential factor. Then the contribution from the high-lying optical modes is exponentially small and can be neglected. This leads to the following algorithm for determining the photon density of states from the calorimetric data. First the parameter ω_0 of the acoustic part of the phonon spectrum is determined. This can be done by considering the standard low-temperature approximation of the calorimetric data by an expression of the type $C_p(T) = \gamma T + \beta T^3$ and fitting the coefficient of the cubic term. With the use of the parameter ω_0 determined in this way, the contribution from the acoustic modes is calculated and subtracted from the values of the heat capacity obtained in the experiment. The remainder is due to optical modes. Here the low-temperature values of the heat capacity are determined solely by the lower optical band. When the parameters of this band are determined, the contribution of these modes to the heat capacity is calculated and also subtracted from the experimental values. The remainder of the heat capacity is used to determine the parameters of the next optical band. The process is repeated until all of the optical branches have been fit. The total phonon density of states is equal to the sum of all its components: $\gamma(\omega) = \gamma_{\mathrm{ac}}(\omega) + \Sigma\gamma_i(\omega)$. At each step of the determination of the parameters of the optical bands the values used for the heat capacity were obtained only at low temperatures, where the anharmonic contribution could be neglected.

This procedure was used to determine the photon density of states $\gamma(\omega)$ of our samples. The parameters of each optical mode were chosen such that the contribution from it described the experimental values over as large a temperature interval as possible. The function $\gamma(\omega)$, in turn, was used not for analysis of the phonon spectrum but for calculation of the lattice heat capacity. Since the phonon spectrum determines the heat capacity of the crystal in an integral manner, small inaccuracies in $\gamma(\omega)$ should not lead to large errors in the determination of the lattice heat capacity. Apparently the error in the studies by Loram *et al.* was just as small.

Contribution to the electronic heat capacity due to the PGP

The electronic heat capacity should include a contribution due to the usual Fermi-particle component C_s, which should be dominant in the sample with $x=6.92$. In the sample with $x=6.70$, in addition to the contribution C_s there should exist a contribution C_{PGS} due to the onset of a pseudogap state in underdoped samples. It should be kept in mind that for the sample with $x=6.92$ there may be a small contribution from the PGS, since the PGS in 1-2-3 cuprates vanishes at $x = 6.985 \pm 0.015$.

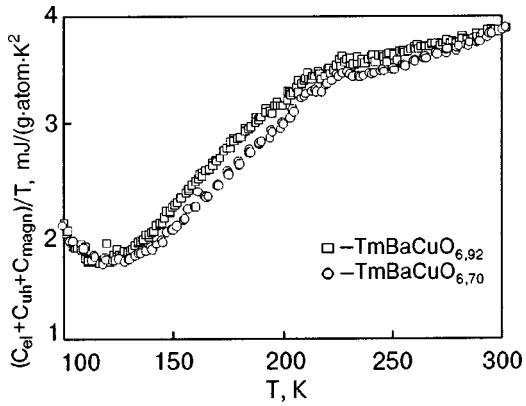

FIG. 2. Temperature dependence of the electronic, anharmonic, and magnetic contributions to the heat capacity of thulium cuprate samples.

Figure 2 shows the remainders of the heat capacity for the samples with $x=6.92$ and $x=6.70$ after subtraction of the harmonic contributions from the experimental values of the heat capacity. We assume that the anharmonic and magnetic components of the heat capacity in the two samples are practically the same. Our experimental data were analyzed as follows. After subtraction of the lattice components of the heat capacity we constructed the function $f(T)$ (see Fig. 3), where

$$f(T)=\frac{C_{\rm uh}(x=6.92)}{T}\,\gamma_{\rm el}(x=6.92)+\frac{C_{\rm mag}(x=6.92)}{T}\,\frac{C_{\rm uh}(x=6.70)}{T}\,\gamma_{\rm el}(x=6.70)+\frac{C_{\rm mag}(x=6.70)}{T}. \tag{2}$$

If it is assumed that the anharmonic and magnetic contributions to the heat capacity in the samples studied are so close to each other that their difference can be neglected, then in this case

$$f(T)=\Delta\gamma_s-\gamma_{\rm PGS}(x=6.70). \tag{3}$$

The first term on the right-hand side in Eq. (3) is positive and increases weakly with increasing temperature.[27] In the temperature interval 200–300 K its value is nearly constant. The function $\Delta\gamma_s(T)$ does not have any extrema. Consequently, the extremal wavelike features in $f(T)$ are due to the second term in Eq. (3). The presence of a minimum in the function $f(T)$ is due to the existence of a maximum in the function $\gamma_{\rm PGS}(x=6.70)$ in the temperature interval 200–250 K. As the temperature approaches $T=300$ K the value of f falls off; this corresponds to a transition from the PGP to the normal metallic state.

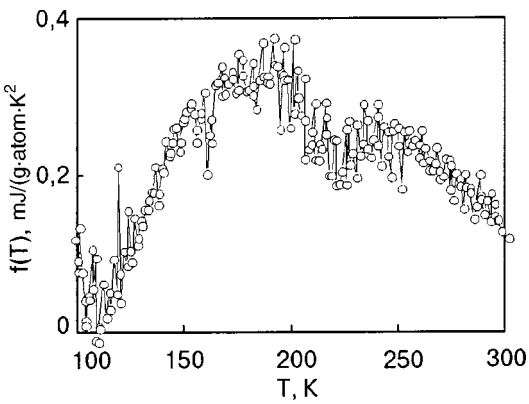

FIG. 3. Temperature dependence of the function f.

Discussion

In the paper by Moca and Janko[27] an analysis is made of the temperature dependence of the electronic component of the heat capacity according to the data of Loram's group. As a theoretical model they considered the mechanism of formation of uncorrelated Cooper pairs in the PGS region. In this case, as was assumed by the authors of Ref. 27, $\gamma_{\rm el}$ should consist of two components:

$$\gamma_{\rm el}(T)=\gamma_s(T)+\gamma_p(T). \tag{4}$$

The first term on the right-hand side of Eq. (4) is due to the single-particle contribution of the Fermi particles. This contribution is analogous to the first term in Eq. (3). The second term in (4) is due to the mechanism for the onset of the PGS through the formation of uncorrelated Cooper pairs. According to Ref. 27, the temperature dependence of γ_p is determined by the factor $(T^*/T)^3\exp(-2T^*/T)$ and has the form of a curve with a smeared maximum near $T\approx T^*$. Based on their analysis of Loram's data, the authors of Ref. 27 made the conjecture that as the oxygen concentration in these systems increases, the position of the point of the maximum on the temperature dependence of $\gamma_{\rm el}(T)$ is shifted to lower temperatures. At an oxygen concentration $x=6.7$ the maximum on the $\gamma_{\rm el}(T)$ curve, according to the estimates of Ref. 27, lies at $T=125\pm5$ K. However, no signs of an extremum in the temperature region 120–130 K are seen on the curves in Fig. 3.

With the systematic error due to the inaccuracy of determination of the harmonic and anharmonic contributions, the error in the calculation of the electronic component of the heat capacity can be some tens of percent, values which amount to tenths of a percent of the total heat capacity. We give these estimates to make it clear to the reader how hard it is to determine correctly the character of the features in the temperature dependence of the electronic component of the heat capacity in cuprate systems.

The temperature interval 200–250 K is unusual for the investigated cuprates, since the boundary between the regions of the PGP and normal metallic phase passes through in this temperature region for the samples with oxygen concentration $x=6.7$. Analysis of the experimental data of Loram's group does not establish the presence of such anomalies in this region for 1-2-3 cuprates. At the same time, in Ref. 28 those same authors presented data for the 2-1-4 lanthanum cuprate, in which the characteristic wavelike temperature dependence of the heat capacity is observed in the indicated temperature interval.

It may be thought that these formations could be due to impurity effects. Indeed, in this temperature interval, at 212.6 and 229.5 K, there are two phase transitions in cupric oxide—one of the initial components of the synthesis of cuprate HTSCs.[29] Special tests for the presence of cupric oxide were done on the samples by the XPA method, and no signs of CuO were detected in the samples at the sensitivity of the method (2–3%). Using the data of Junod *et al.*[29] one can show that for such anomalies to be manifested it would be necessary for the samples to contain at least 4–5% cupric oxide. We note that our data, presented in Fig. 3, should likewise be free of such anomalies. Indeed, if our samples did contain any amount of cupric oxide, it should have been the same in both samples. The sample with the oxygen concentration $x=6.70$ was obtained from the initial sample ($x=6.92$) by annealing at 590 °C. Since the decomposition of cupric oxide begins at $T=1061$ °C, it can be concluded that the function f should not manifest any anomalies due to effects of phase transitions in CuO. It might be assumed that annealing at 590 °C gives rise to appreciable disorder of the oxygen in a layer with chainlike oxygen structures, and that leads to the formation of CuO inclusions. However, careful x-ray structural studies have shown that the reflections from these planes are not broadened as they would be if such disorder were present.

Our data indicate that the values of the observed anomalies in the temperature dependences of the heat capacity decrease as the oxygen concentration approaches the neighborhood of the ODP. These facts suggest that the observed features are due to boundary phenomena at the transition from the PGP to the normal metallic phase.

Some theoretical studies that have come out in recent years have examined the features of the states of electronic systems in which exchange occurs with charge or spin fluctuations of the short-range order.[7,30] It was shown that these interactions can be responsible for the formation of a pseudogap structure in the neighborhood of the Fermi surface. A feature of the interactions of the charge carriers with fluctuations of the short-range order in these systems is the absence of self-averaging. Calculations done in the mean field approximation do not give a complete description of the properties of the system. When the fluctuation effects in the PGP region were correctly taken into account, it was found that in addition to the V-shaped dip in the density of states, sharp peaks can also form.[7,30] It is natural to expect that the dependence of the effective density of states $N(E)$ in the neighborhood of the Fermi level near the boundary of the PGP can be extremely complex and very sensitive to a change in state of the system. In that case the transition from the PGP region to the normal metallic phase can be accompanied by complex anomalies in various physical characteristics. This should be particularly true for properties that depend on the density of states of the charge carriers. We assume that the anomalies which we observed in the behavior of the electronic component of the heat capacity bear a direct relation to this. Apparently the anomalies of the temperature dependence of the heat capacity which were observed in Ref. 28 on the $C_p(T)$ curves of lanthanum 2-1-4 cuprates are also features of this kind.

We assume that our experimental results on thulium cuprates and the results of measurements made on lanthanum 2-1-4 cuprates in Ref. 28 can serve as qualitative confirmation of the theoretical results of Sadovskiĭ *et al.*[7,30]

Some of the authors of this article recall with pleasure the time when we taught with Viktor Valentinovich Eremenko at Kharkov State University.

This study was supported in part by the Russian Foundation for Basic Research (Grant 00-02-17914) and by the scientific programs ''High-Temperature Superconductivity'' (Grant No. 98009) and ''Universities of Russia'' (Grant No. 1785), and by the FAP ''Integration'' (Grant No. 274).

*E-mail: amitin@casper.che.nsk.su

[1] M. Randeria and J. C. Campuzano, cond-mat/9709107.
[2] M. Randeria, cond-mat/9710223.
[3] H. Ding, T. Yokoya, J. C. Campuzano, T. Takahashi, M. Randeria, M. R. Norman, T. Mochiku, K. Kadowaki, and J. Giapintzakis, Nature (London) **382**, 51 (1996).
[4] A. J. Millis, H. Monien, and D. Pines, Phys. Rev. B **42**, 167 (1990).
[5] K. Gorny, O. M. Vyaselev, J. A. Martindale, V. A. Nandor, C. H. Pennington, P. C. Hammel, W. L. Hults, J. L. Smith, P. L. Kuhns, A. P. Reyes, and W. G. Moulton, Phys. Rev. Lett. **82**, 177 (1999).
[6] J. Schmalian, D. Pines, and B. Stojkovich, Phys. Rev. B **60**, 667 (1999).
[7] M. V. Sadovskiĭ, Usp. Fiz. Nauk **171**, 539 (2001).
[8] S. Chakravarty, R. B. Laughlin, D. K. Morr, and Ch. Nayak, ArXiv:cond-mat/0005443 v2, 6 Sept 2000.
[9] V. B. Geshkenbein, L. B. Ioffe, and A. I. Larkin, Phys. Rev. B **55**, 3173 (1997).
[10] V. P. Gusynin, V. M. Loktev, and S. G. Sharapov, Zh. Éksp. Teor. Fiz. **115**, 1243 (1999) [JETP **88**, 685 (1999)].
[11] J. Schmalian, D. Pines, and B. Stojkovich, Phys. Rev. Lett. **80**, 3839 (1998).
[12] É. Z. Kuchinskiĭ and M. V. Sadovskiĭ, Zh. Éksp. Teor. Fiz. **115**, 1765 (1999) [JETP **88**, 968 (1999)].
[13] A. I. Posazhennikova and M. V. Sadovskiĭ, Zh. Éksp. Teor. Fiz. **115**, 632 (1999) [JETP **88**, 347 (1999)].
[14] M. Sadovskiy and E. Z. Kuchinskiy, Physica C **341–348**, 879 (2000).
[15] A. Junod and T. Graf, Physica B **165–166**, 1335 (1990).
[16] A. Junod, A. Bezinge, and J. Muller, Physica A **152**, 50 (1988).
[17] W. Y. Liang, J. W. Loram, K. A. Mirza, N. Athanassopoulou, and J. R. Cooper, Physica C **263**, 277 (1996).
[18] J. W. Loram, K. A. Mirza, J. R. Cooper, and J. L. Tallon, Physica C **282–287**, 1405 (1997).
[19] J. W. Loram, K. A. Mirza, J. R. Cooper, W. J. Liang, and J. M. Wade, J. Supercond. **7**, 234 (1994).
[20] J. W. Loram and J. L. Tallon, Physica C **349**, 53 (2001); cond-mat./0005063.
[21] J. W. Loram, J. L. Tallon, and G. V. M. Williams, Physica C **338**, 9 (2000).
[22] V. G. Bessergenev, Ju. A. Kovalevskaya, I. E. Paukov, M. A. Starikov, H. Opperman, and W. Reichelt, J. Chem. Thermodyn. **24**, 85 (1992).
[23] N. P. Rybkin, M. P. Orlova, and A. K. Baranyuk, Izmeritel'naya Tekhnika, No. **7**, 29 (1974).
[24] K. Moriya, T. Matsuo, and H. Suga, J. Chem. Thermodyn. **14**, 1143 (1982).
[25] M. Sorai, K. Kayi, and Y. Kaneko, J. Chem. Thermodyn. **24**, 167 (1992).
[26] K. R. Zhdanov, F. S. Rakhmenkulov, V. E. Fedorov, and A. V. Mishchenko, Fiz. Tverd. Tela (Leningrad) **30**, 1119 (1988) [Sov. Phys. Solid State **30**, 649 (1988)].
[27] C. P. Moca, and B. Janko, E-prints arXiv: cond-mat/0105202 v1.
[28] J. W. Loram, K. A. Mirza, J. R. Cooper, and J. L. Tallon, J. Phys. Chem. Matter. **59**, 2091 (1998).
[29] A. Junod, D. Eckert, and G. Triskone, J. Phys. Chem. Matter. **1**, 8021 (1989).
[30] M. V. Sadovskiĭ and É. Z. Kuchinskiĭ, Zh. Éksp. Teor. Fiz. **117**, 613 (2000) [JETP **90**, 535 (2000)].

Translated by Steve Torstveit

Optical spectroscopy of antiferromagnetic correlations and the stripe state in the superconductor $YBa_2Cu_3O_{6+x}$

V. N. Samovarov, V. L. Vakula, M. Yu. Libin, and S. A. Uyutnov

B. Verkin Institute for Low Temperature Physics and Engineering, National Academy of Sciences of Ukraine, pr. Lenina 47, 61103 Kharkov, Ukraine

G. G. Sergeeva*

Kharkov Physicotechnical Institute National Science Center, ul. Akademicheskaya 1, 61108 Kharkov Ukraine

(Submitted January 15, 2002; revised February 13, 2002)
Fiz. Nizk. Temp. **28**, 934–951 (August–September 2002)

Results of measurements of the temperature dependence of the absorption spectra of $YBa_2Cu_3O_{6+x}$ films in the antiferromagnetic and metallic (superconducting, $T_c=88$ K) phases are presented. The temperature evolution of the absorption bands, which are diagnostic for the electron and spin correlations and the degree of metallization (oxygen–copper hybridization), is investigated in the energy region 1.3–2.6 eV. It is shown that in the metallic phase in the pseudogap state below $T^*=120\pm10$ K there is a sharp rise of these absorption bands characteristic of the antiferromagnetic (AF) phase, including the electron–two-magnon $(A+J)$ band, which reflects the development of strong AF correlations. In contrast to the insulator, here the $(A+J)$ band has a fine structure due to the creation of both interacting and noninteracting magnons, and it coexists with the bands due to the strong metallization. The results demonstrate phase separation at $T_c<T<T^*$, with the formation of a stripe superstructure consisting of metallic and insulating (with short-range antiferromagnetic ordering) regions. This superstructure is preserved in the superconducting state, and an additional enhancement of the AF correlations occurs at the superconducting transition. Taken together, the results provide independent optical evidence of the undoubted participation of AF correlations in the superconductivity. © *2002 American Institute of Physics.*
[DOI: 10.1063/1.1511713]

INTRODUCTION

Optical spectroscopy is now one of the most informative methods of studying magnetic interactions and correlations in magnetically ordered crystals and doped antiferromagnets. The development of electron spectroscopy of magnets owes much to the work of V. V. Eremenko and his students. The influence of antiferromagnetic (AF) ordering on the absorption spectra of magnets was first detected in the 1960s, in a study of manganese carbonate $MnCO_3$, and this effect was later confirmed and investigated for a wide diversity of AF insulators.[1] In Ref. 2 the spin-wave parameters in the α phase of solid oxygen were first determined from subtle experiments on the absorption spectra. In many respects Refs. 1 and 2 formed a basis for the development of the magnetooptics of absorption, luminescence, birefringence, and photoinduced phenomena in insulating magnets. A generalization of the results on the low-temperature spectroscopy of magnets is reflected in Eremenko's famous monograph[3] and in the book[4] written by him and his students.

For copper oxide high-T_c superconductors (HTSCs), which are doped antiferromagnets, the question of the diagnostics of AF correlations became particularly topical in connection with the fact that one of the possible scenarios for the superconducting (SC) pairing involves the participation of AF fluctuations.[5–9] It should be noted that the possibility of superconductivity with the participation of AF spin waves had been demonstrated theoretically long before that by I. A. Privorotskiĭ.[10]

For HTSCs, as was the case for antiferromagnets, the first question was whether the optical spectra are sensitive to a phase transition, in this case, to superconductivity. In the general view this problem has a long history. For low-temperature superconductors repeated experimental attempts to detect an influence of the superconducting transition on the equilibrium optical spectra in the visible region of frequencies $\hbar\omega\approx2$ eV have given a negative result. In one of the first such studies, B. I. Verkin and B. L. Lazarev back in 1948[11] attempted to detect an influence of the superconducting transition on the transmission and reflection spectra of tin and mercury. Their careful measurements did not reveal any anomalies at the superconducting transition, and they arrived at the conclusion that the electromagnetic response should be sought ''at frequencies close to the frequency characterizing the binding energy inherent to the electronic liquid in the superconductor.'' For tin and lead the analogous experiments were done in foreign laboratories in the early 1950s in the period when the BCS concepts were being substantiated (see the discussion in the paper by J. E. Hirsch[12]). Again, no anomalies of any kind were observed at the superconducting transition. The negative results on observation of an optical response gave development to the idea of the existence of an energy gap Δ_S in the electronic spectrum of a supercon-

ductor. After the gap nature of superconductivity was established and, as a result, the observation of low-frequency response to a superconducting state at ''gap'' frequencies $\hbar\omega \leqslant \Delta_S$, the idea of optical diagnostics of superconductivity in the region $\hbar\omega \gg \Delta_S$ was for many years considered illogical.

The situation was fundamentally altered with the discovery of high-temperature superconductivity. A sensitivity of the optical luminescence spectra to superconductivity was first observed in cuprate HTSCs. This observation was made practically simultaneously in papers by the groups of V. G. Stankevich[13] and V. V. Eremenko.[14] It was established that the superconducting transition has a direct influence on the cathodoluminescence[14] and photoluminescence[13] spectra of YBCO in the region 2–3 eV. Then, and this is very important, in joint studies by the group of I. Ya. Fugol' and her German colleagues[15,16] a significant optical response of the equilibrium absorption to the the superconducting transition was observed for the first time in YBCO films. Measurements were made at frequencies ≈ 2 eV, i.e., for energies much higher than the energy of the superconducting gap, $\Delta_S \approx 10^{-2}$ eV. It was found that the spectra varied substantially with temperature in the normal phase but become temperature-independent below T_c. In other words, a jump of the temperature derivative of the absorption coefficient was observed.[1)] This effect must be acknowledged as extremely unexpected, since it had not been predicted previously and there was no such branch of optical spectroscopy for low-temperature superconductors.

For various cuprate HTSCs based on Y, La, and Bi, sensitivity of the optical reflection and absorption spectra to superconductivity has been confirmed over a wide range of frequencies, from 0.3 to 3 eV: in the SC phase for $T < T_c$ the reflection and absorption spectra become temperature-independent.[17–19] This naturally gave rise to an interesting idea—to separate out the optical feature due to the magnetic degrees of freedom in the spectrum of cuprates and track its evolution as the temperature is lowered from room temperature to T_c and in the SC phase itself. This problem, which was ultimately directed toward elucidating the role of magnetic interactions in the formation of high-temperature superconductivity, turned out not to be simple. Substantial results in this area have been obtained comparatively recently for lightly doped YBCO films in the studies by V. V. Eremenko and co-workers,[20,21] in which an electron–two-magnon absorption band $A+J$ near 2.15 eV was identified. It was shown that the $(A+J)$ band, which reflects the development of short-range AF correlations, appears on cooling of metallic YBCO films and persists in the SC phase.

The role of AF correlations in the SC pairing for copper-oxide HTSCs is among the most hotly debated questions, and no less so is the nature of the pseudogap (PG) state in the temperature region $T_c < T < T^*$ which precedes superconductivity with d-wave pairing (see, e.g., Refs. 5–9 and 22). A generally accepted point of view as to the nature and interrelationship of SC and the PG states does not yet exist. However, the hypothesis that the superconductivity in these compounds is due to a preliminary phase separation of the samples into insulating (with short-range AF ordering) and metallic quasi-one-dimensional stripes (the stripe phase) is finding more and more confirmation.[23–26] Stripes of a metallic character with a quasi-one-dimensional motion of holes are separated by insulating stripes and together form a stripe superstructure that fluctuates in time ($\sim 10^{-10}$ s) and space. The width of each stripe amounts to several lattice constants for the Cu^{2+} ions. The method of inelastic neutron scattering is thought to be the most sensitive to the stripe structure,[24] but in a brief communication[27] V. V. Eremenko and co-workers demonstrated that optical spectroscopy can identify the formation of a stripe superstructure in YBCO.

In the present study we have measured the temperature dependence of the absorption spectra of insulating films of $YBa_2Cu_3O_{6+x}$ with $x = 0.3–0.35$ and superconducting $YBa_2Cu_3O_{6+x}$ films with optimal doping, with $x \approx 0.85$ and $T_c = 88$ K. In the region 1.2–2.6 eV we have tracked the temperature evolution of the different absorption bands, which are diagnostic of the electron and spin correlations and also of the degree of pd hybridization in the active CuO_2 plane. The optical data show that the degree of pd hybridization increases strongly on metallization (doping) but it varies weakly with temperature and is not a decisive factor for the appearance of superconductivity. More subtle effects unfold with the participation of the magnetic subsystem on cooling of a metallic film below $T^* = 120 \pm 10$ K. In the PG state for $T < T^*$ the electron–two-magnon $(A+J)$ absorption band, the fine structure of which consists of two maxima at 2.145 and 2.28 eV, rises quite sharply. These maxima can be attributed to the additional excitation at the electronic A transition of mutually interacting ($3J$ resonance) and noninteracting ($4J$ resonance) magnons, where J is the exchange energy. This picture is a direct indication of the development of strong AF correlations below T^*. Here the $(A+3J)$ component, which is characteristic of the AF phase, coexists with the B absorption band characteristic of a metal. This effect reflects the presence of phase separation in the PG state into stripes of insulating (with short-range antiferromagnet order) and metallic regions. The phase separation that arises persists in the SC phase, and at the SC transition an enhancement of the AF correlations (intensification of the $3J$ and $4J$ resonances) occurs. On the whole, our results are entirely sufficient to support the conclusion that as the temperature is lowered in the normal state, the electron energy ''prepares'' for the appearance of superconductivity through the development AF correlations, which persist in the SC phase. Thus the method of optical absorption spectroscopy, which does not have an analog for classical superconductors, leads to the independent conclusion that AF correlations undoubtedly play a role in the formation of superconductivity in YBCO.

1. EXPERIMENT

Measurements of the absorption spectra were made on three $YBa_2Cu_3O_{6+x}$ films, which will be denoted as YS370, BH609, and BH611. The film of the YS series was grown by the dc sputtering of targets at the Physics Institute of the University of Erlangen, Germany, and the films of the BH series were grown by laser ablation at the Research Center of the Siemens Corp. in Erlangen. All of the films were grown on (100) $SrTiO_3$ substrates, had an orientation of the c axis of the crystal perpendicular to the substrate, and had a thickness $\ell = 2300$ Å. The films YS370 and BH609 are insulat-

ing, with lattice periods of 11.842 and 11.820 Å, respectively, along the c axis. These values correspond to doping indices $x \approx 0.3$ and $x \approx 0.35$, i.e., the films are close to the insulator–metal transition. The film BH611 is metallic, with a lattice period along the c axis of 11.695 Å, which corresponds to a doping index $x \approx 0.85$. According to magnetic measurements the superconducting transition temperature for the film BH611 is equal to 88 K, and the transition width is around 1 K. The resistivity of this film for the ab plane of the crystal, $\rho_{ab}(100\ \mathrm{K})$, is approximately 100 $\mu\Omega \cdot$cm.

The experimental technique of measuring the absorption spectra [the absorption coefficient $\alpha(\omega)$] is described in sufficient detail in Refs. 20 and 21. We mention only the key points. Optical measurements were made in unpolarized light ($\mathbf{E} \| ab$ plane of the crystal), and the irradiation of the films was done with the use of an MDR-12 monochromator in an automated mode of data registration and spectral scanning. For $T \approx 300$ K the absolute absorption spectra are given, in units of the optical density $\alpha\ell(\omega)$. The data taken on cooling of the films are presented in the form of the difference spectrum $\Delta(\alpha\ell) = \alpha\ell(\omega, T) - \alpha\ell(\omega, T_0)$, where T_0 is the initial temperature from which the films were cooled. The values of $\Delta(\alpha\ell)$ were determined from the relation $\Delta(\alpha\ell) = \ln[t_0(\omega)/t(\omega)]$, where $t_0(\omega)$ and $t(\omega)$ are the measured transmission spectra of the films at the temperatures T_0 and T. This relation holds well even without allowance for the temperature variations of the reflection coefficient $R(\omega)$. In the energy region 1.2–3 eV, where the measurements were made, the reflection is small in the insulator and metallic phases of YBCO: $R \approx 10\%$ for both polarizations in the ab plane.[28] The temperature variations of the reflectance on cooling of the films is also small, $\Delta R/\Delta T \approx 10^{-4}\ \mathrm{K}^{-1}$ (Ref. 29), which is noticeably smaller than the temperature variations of the transmittance. Therefore the use of the expressions given above for determining $\Delta(\alpha\ell)$ from the transmission spectra is completely reliable.

2. CLASSIFICATION OF OPTICAL TRANSITIONS AND THE PRINCIPLES OF ANALYSIS OF THE ABSORPTION SPECTRA

For complete apprehension of the physical picture it is helpful to set forth the accepted classification of transitions and to specify the approaches we have followed in the analysis of the optical features.

In the IR and visible regions of the spectrum, for $\hbar\omega < 3$ eV, the absorption spectrum of YBCO is determined by a set of interband and intraband transitions and also dd transitions in the Cu^{2+} ion. Altogether the spectrum is an extremely complex multicomponent spectrum whose interpretation requires a definite picture of the distribution of the density of states $N(E)$ together with the scheme of splitting of the dd transitions in the field of the oxygen ligands. The identification of the spectra absorption spectra was based on the system of electronic transitions shown schematically in Fig. 1. This picture reflects the most fundamental features of the structure of the electronic states of cuprate HTSCs.

Interband transitions with charge transfer

These transitions reflect the peculiarity of the distribution of the density of states $N(E)$ in 2D-correlated copper–oxygen systems.[6,30] The lower pd hybridized Hubbard band (LHB) is separated from the upper Hubbard band (UHB) formed from the copper d orbitals by an optical gap E_g. The nature of the gap is due to the transfer of charge from oxygen to copper in the insulator $YBa_2Cu_3O_{6+x}$ ($x < 0.4$) the gap has a value $E_g \approx 1.7$ eV.[31] In the metallic phase of YBCO the gap is preserved all the way to the optimal doping region ($x \approx 0.9$), but on overdoping, when the cuprate HTSCs become 3D metals and begin to lose their superconducting properties, the gap is filled by band states. Interband transitions with charge transfer [charge-transfer (CT) transitions] for $\hbar\omega > E_g$ correspond to a continuous component of the absorption spectrum, which is denoted in terms of the optical density as $(\alpha\ell)_{CT}$.

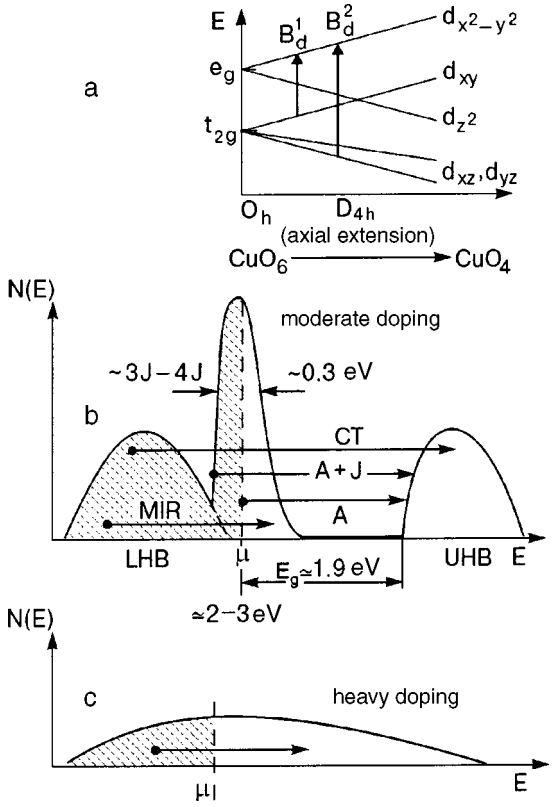

FIG. 1. Splitting of the d levels of the Cu^{2+} ion in a crystalline field of tetragonal symmetry D_{4h} under axial extension by internal fields (a). The distribution of the density of states $N(E)$ at moderate (b) and heavy (c) doping. The arrows indicate optical transitions considered in the analysis of the measured absorption spectra of YBCO in the visible frequency range. The figures are drawn without adherence to scale (see the text for notation).

A transitions from the correlation peak of the density of states

Other types of interband optical transitions arise on account of the existence of a narrow correlation peak (the A peak) of the density of states at the top of the LHB. In correlated systems the A peak of the density of states arises independently of the chosen approach for obtaining the spectral distribution $N(E)$: the single-band Hubbard model with[32] and without[30] allowance for the AF fluctuations, the Zhang–Rice polaron model of copper–oxygen singlets,[33] and the Kondo collective resonance model.[34] In the framework of the tJ approach the appearance of the A peak in the structure of $N(E)$ is a consequence of the interaction of the

charge carriers with the AF fluctuations that develop intensively in cuprate oxides in the temperature region below the exchange interaction energy, $J \approx 4t^2/U \approx 10^3$ K, where $t \approx 0.2-0.3$ eV is the amplitude of the intersite transition, and $U \approx 2-3$ eV is the value of the effective Hubbard energy. In this case the width of the A peak is governed by processes of creation (vanishing) of magnons in the motion of holes and has a characteristic value of $3J-4J$.[8,32] In the absorption spectra the A peak of the density of states should be manifested in the form of an A band with a width scale of J, located at $E \approx E_g$ [referred to below as the $(\alpha\ell)_A$ component].

We note that the parameters of the A peak in 2D systems are anisotropic. For example, along the Γ–M direction of the Brillouin zone the carriers interact intensively with AF fluctuations and, as a consequence, have a large mass (*hot quasiparticles*), but for other directions of the 2D Brillouin zone the interaction is greatly weakened (*cold quasiparticles*) (see Ref. 9 and references cited therein). Since our measurements were made with the use of unpolarized light, the absorption due to transitions from the heavy-hole band, according to known rules, dominates over the absorption due to transitions from the light-hole band.

($A+J$) transitions with additional excitation of the magnon subsystem

Yet another type of optical transitions arises if excitation of the magnon AF subsystem occurs simultaneously with the A transitions. The energy of these $(A+J)$ transitions exceeds that of the A transitions by an amount equal to the energy of the $3J-4J$ two-magnon excitations in YBCO, and should be manifested in the absorption spectra as a narrow $(A+J)$ band (the component $(\alpha\ell)_{A+J}$).

Intraband MIR transitions

In the metallic phase of YBCO, when the Fermi level lies in the region of the A peak of the density of states, continuum intraband transitions can occur from the depths of the valence band LHB to a region of hole states which is opening up with doping. The low-frequency boundary of these MIR (mid-infrared) transitions has a value close to the width of the A peak, i.e., 0.3–0.4 eV, the absorption maximum comes at 0.5–0.6 eV, and the high-frequency wing falls off slowly on account of the large width of the valence band, and can therefore span even the visible region to $\hbar\omega = 3$ eV.[6,19,20]

dd transitions in the Cu^{2+} ion

In the unit cell of YBCO the Cu^{2+} ion is located in the base of a CuO_5 pyramid, where it is surrounded by 5 oxygen ligands: 4 atoms in the CuO_2 plane, and 1 atom of apical oxygen. A qualitative scheme of the splitting of the d orbitals of Cu^{2+} in an octahedral environment is presented in Fig. 1, where the initial e_g doublet and t_{2g} triplet in the CuO_6 octahedron are split on account of the weakening of the axial field of the apical oxygen atoms, including the removal of one of them. In the limiting case when both apical oxygen atoms are missing, the splitting corresponds to that of the plane square complex CuO_4. For a polarization $\mathbf{E} \| ab$ the largest contribution to the absorption should be given by the transitions $d_{xy} \rightarrow d_{x^2-y^2}$ and $d_{yz,xz} \rightarrow d_{x^2-y^2}$ to the orbital $Cu^{2+}(d_{x^2-y^2})$ with a hole state. However, in the absorption spectra the dd transitions are forbidden by a symmetry rule for the d orbitals. In copper-containing oxides the finite degree of pd hybridization (degree of covalency) lifts the restriction on the dd transitions.[35] In the insulating phase of YBCO and other cuprates the dd transitions are observed in the form low-intensity bands with absorption coefficients $\alpha \approx 10^4$ cm^{-1} (Refs. 20 and 36); this is apparently due to the weakened pd hybridization.[35] At the same time, in the Raman scattering spectra the dd transitions are very well expressed. For example, in the Raman spectra the transition $d_{xy} \rightarrow d_{x^2-y^2}$ is clearly seen in the insulating phase of $YBa_2Cu_3O_{6+x}$ ($x \leqslant 0.4$) in the form of narrow band centered near 1.5–1.56 eV with a half-width ≈ 0.1 eV.[37] In the metallic phase, because of the enhancement of the pd hybridization the absorption coefficient for the dd transitions increases to values comparable to the coefficients for the allowed CT transitions, $\alpha \approx 10^5$ cm^{-1} (Refs. 20 and 21), but in the Raman spectra the transition $d_{xy} \rightarrow d_{x^2-y^2}$ is greatly weakened upon metallization.[37] The transitions $d_{xy} \rightarrow d_{x^2-y^2}$ and $d_{xz,yz} \rightarrow d_{x^2-y^2}$ have been observed[20,21] in the form of narrow bands at 1.5 and 2.4 eV in the absorption spectrum of the metallic phase of YBCO at moderate doping ($x \leqslant 0.7$). In the notation adopted in Ref. 20, these dd transitions are denoted at $B_d^1(d_{xy} \rightarrow d_{x^2-y^2})$ and $B_d^2(d_{xz,yz} \rightarrow d_{x^2-y^2})$, and the optical density coefficients are $(\alpha\ell)_{1B}$ and $(\alpha\ell)_{2B}$.

Thus the spectral composition of the absorption of YBCO in the region 1–3 eV (see Fig. 1) should be determined by the sum of six components.

1. The continuum interband component $(\alpha\ell)_{CT}$ for $\hbar\omega \geqslant E_g$ for transitions with charge transfer from oxygen to copper, the CT component.

2. The continuum component from the short-wavelength wing of the intraband MIR component $(\alpha\ell)_{MIR}$. The MIR and CT components give a continuous background of absorption in the frequency region 1–3 eV.

3. The narrow-band $(\alpha\ell)_A$ component of the A transitions from the correlation maximum of the density of states across the optical gap without excitation of the magnetic degrees of freedom, the A band.

4. The narrow-band $(\alpha\ell)_{A+J}$ component of the $(A+J)$ transitions from the correlation maximum of the density of states across the optical gap with an additional excitation of the magnetic degrees of freedom, the $(A+J)$ band.

5. The narrow-band $(\alpha\ell)_{1B}$ component for the dd transitions $d_{xy} \rightarrow d_{x^2-y^2}$ due to the pd hybridization in the CuO_2 plane, the B_d^1 band.

6. The narrow-band $(\alpha\ell)_{2B}$ component for the dd transitions $d_{xz,yz} \rightarrow d_{x^2-y^2}$ due to pd hybridization in the direction transverse to the CuO_2 plane, the B_d^2 band.

The results of the present study and also those of Refs. 20 and 21 show that the absorption components under consideration can provide an effective ''tool box'' for studying the evolution of the correlation, magnetic, and covalent contributions to the carrier spectrum with changes in the temperature and doping level of YBCO.

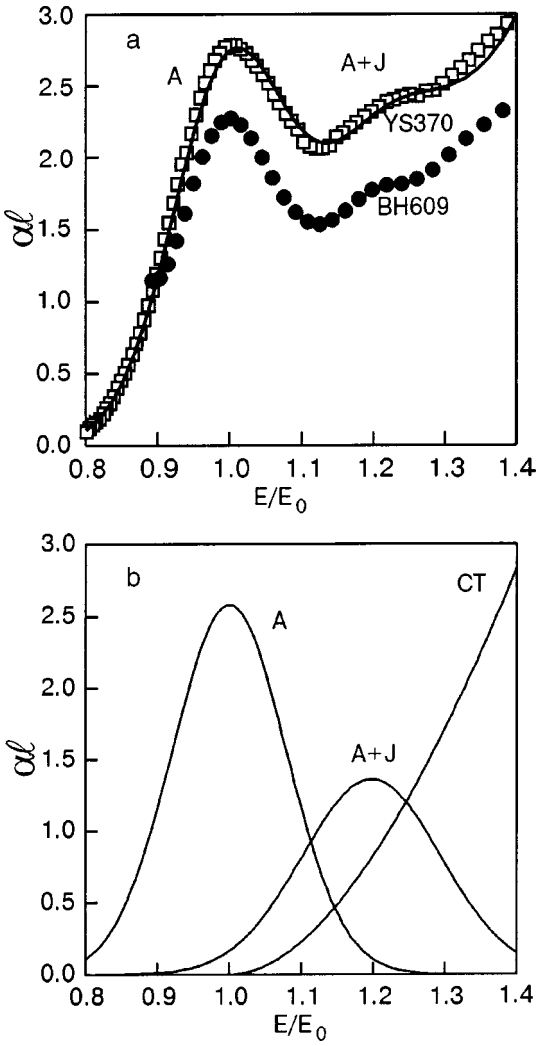

FIG. 2. Absolute absorption spectra of insulating films of $YBa_2Cu_3O_{6+x}$ with $x \approx 0.3$ (the film YS370) and $x \approx 0.35$ (the film BH609) at 300 K. The solid curves show the model description of the spectrum (a). The decomposition of the measured spectrum for the film BH609 into spectral components (b).

3. INSULATOR PHASE OF YBCO

Figure 2 shows the absorption spectrum of the insulating films YS370 with $x \approx 0.3$ and BH609 with $x \approx 0.35$ in the spectral region 1.4–2.8 eV at 300 K. The results are plotted in the coordinates $\alpha\ell - E/E_0$ (optical density versus reduced energy), where E_0 is the position of the strong A peak of the absorption. As we see in Fig. 2a, the character of the spectra and the position of the main features practically coincide in the two films and, hence, do not depend on the method used to grow the films. The correlation A peak of the absorption, with an intensity $(\alpha\ell)_A = 2.2–2.7$, comes at an energy $E_0^A \approx 1.77$ eV. On the high-frequency side of the A peak, near 2.12 eV, the $(A+J)$ peak is clearly manifested. These two bands are situated on a background of the continuum CT component (the intraband MIR component is absent in the insulating phase). The $A+J$ band is centered at $E_0^A + \hbar\omega_{2m}$ and is separated from the A band by the energy of the two-magnon excitation $3J$, which, according to the absorption and Raman-scattering data for the insulating and slightly metallized phases of YBCO, has a value $\hbar\omega_{2m} = 0.33–0.35$ eV.[6,38–40]

For a quantitative description of the measured data we have carried out a model decomposition of the absorption spectrum of the film BH609 into three components: $(\alpha\ell)_{\text{fit}} = (\alpha\ell)_A + (\alpha\ell)_{A+J} + (\alpha\ell)_{CT}$. The A and $A+J$ bands were described by Gaussian contours, and the interband CT component by a quadratic energy dependence:

$$(\alpha\ell)_{\text{fit}} = \sum_i \frac{\mu_i}{\sigma_i\sqrt{\pi}} \exp\left[-\frac{(E-E_0^i)^2}{2\sigma_i^2}\right] + \frac{\mu_{CT}(E-E_g)^2}{E}, \quad (1)$$

where $i = A,\ A+J$. The frequency dependence for the interband CT absorption, $(\alpha\ell)_{CT} \propto (E-E_g)^2$, is typical for transitions due to the "tails" of the density of states inside the optical gap and also to strong scattering of charge carriers.[41] In Hubbard systems the existence of such tails is a direct consequence of the interrelationship of the densities of states of the UHB and LHB.[30] In the case of pronounced tails of the density of states in YBCO this frequency dependence has been verified in optical experiments.[42]

The model decomposition of the measured spectrum for the film BH609 is shown in Fig. 2b. The parameters of this decomposition, which can give a description of the experimental spectrum to an accuracy of 4% or better throughout the entire range of measurements (the values of the parameters of the analogous decomposition for the film YS370 are given in parentheses), are:

1. Gaussian A band: $E_0^A = 1.77$ eV (1.75 eV), standard deviation $\sigma_A = 0.14$ eV (0.12 eV), amplitude component $\mu_A = 0.64$ eV (0.44 eV).

2. Gaussian $(A+J)$ band: $E_0^{A+J} = 2.12$ eV (2.06 eV), standard deviation $\sigma_{A+J} = 0.17$ eV (0.17 eV), $\mu_{A+J} = 0.41$ eV (0.30 eV).

3. Interband CT component: $E_g = 1.77$ eV (1.75 eV), amplitude coefficient $\mu_{CT} = 14$ eV^{-1} (12.1 eV^{-1}).

We see that the dd bands are absent from the absorption spectrum of the insulating phase at 300 K. In this connection we note that they can be discerned only on heating of an insulating (semiconducting) YBCO film.[20] They appear at 1.56 eV (B_d^1) and 2.4 eV (B_d^2) in the form comparatively weak spectral features with an amplitude $(\alpha\ell)_B \approx 0.1$ and a coefficient $\mu_B \approx 0.02$ eV. Films at the boundary of the insulator–metal transition are found in an activational conduction regime, and the enhancement of the B_d^1 and B_d^2 bands follows the growth of metallization as the temperature is raised. We have also observed the appearance of these bands in experiments on photometallization (photodoping) of YBCO films with $x \approx 0.35$ cooled to 80 K. Those experiments clearly showed that the dd bands B_d^1 and B_d^2 can act as optical probes of the metallization, as is confirmed by our data for the metallized film BH611, presented in the next Section.

Let us consider the interesting question of the changes of the absorption spectra of insulating films with temperature as they are cooled into the region of the AF phase. For YBCO films with index $x \approx 0.3–0.35$ the temperature of the AF transition lies near $T_N \approx 250–200$ K.[43] It is extremely difficult to establish a more accurate quantitative correspondence of T_N with the doping index x because of the rapid fall-off of the function $T_N(x)$ with increasing x at the boundary of the insulator–metal transition. Let us examine the difference

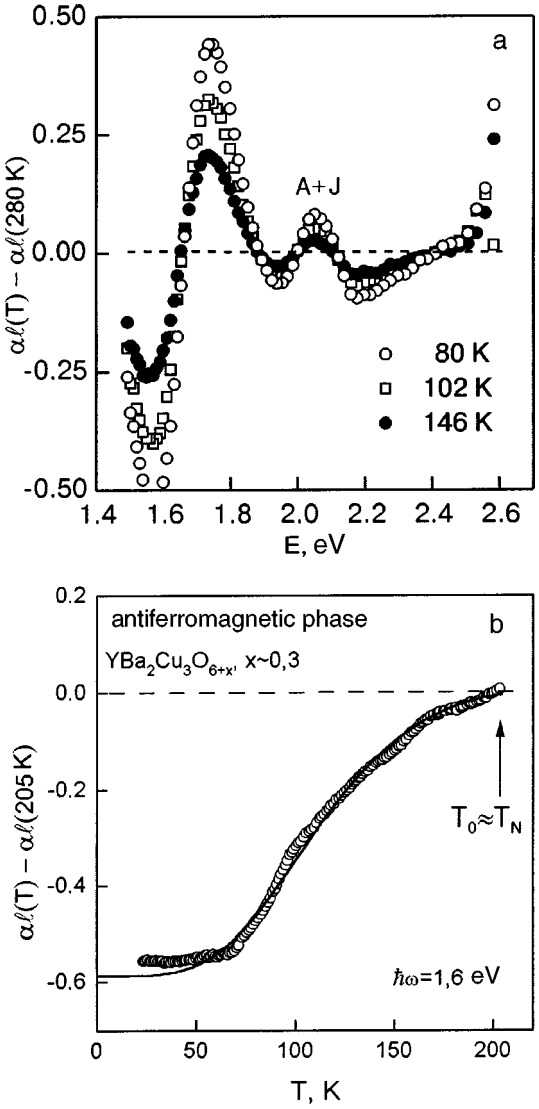

FIG. 3. Difference spectra of the absorption $\Delta(\alpha\ell)=\alpha\ell(T)-\alpha\ell(T_0)$ measured for the film YS370 with $x\approx 0.3$ relative to an initial temperature $T_0=280$ K (a). The temperature behavior of the absorption coefficient $\Delta(\alpha\ell)=[\alpha(T)-\alpha(205\ \mathrm{K})]$ relative to the temperature $T_0=205$ K ($T_0\approx T_N$) in the AF phase of the film YS370. The photon energy is 1.6 eV. The solid curve shows the theoretical dependence (b).

spectra $\Delta(\alpha\ell)=\alpha\ell(\omega,T)-\alpha\ell(\omega,T_0)$ in reference to the initial temperature T_0 in the region 1.5–2.6 eV. Figure 3a shows the results of measurements of $\Delta(\alpha\ell)$ on cooling of the film YS370 from $T_0=280$ K to 146, 102, and 80 K. It is clearly seen that in the AF phase the absorption at the maxima of the A and $(A+J)$ bands increases, i.e., $\Delta(\alpha\ell)>0$. At the same time, the red wing of the A band in the region $\hbar\omega<1.65$ eV is greatly weakened, and here $\Delta(\alpha\ell)<0$, i.e., the contour of the A band narrows on cooling (the A band may have an asymmetric contour). Noticeable changes of the A and $(A+J)$ bands with temperature occur against the background of relatively weak changes for the CT component. We note immediately that the strong temperature dependence of the A and $(A+J)$ bands in the AF phase attest to a direct interrelationship of these bands with the AF degrees of freedom. An indication of this may be seen from the data shown in Fig. 3b, which demonstrate the changes of the absorption coefficient with temperature, $\Delta(\alpha\ell)$, relative to $T_0=205$ K, for a photon energy of 1.6 eV, i.e., on the low-frequency wing of the A band. It is seen that as the temperature is lowered from $T_0=205$ K ($T_0\approx T_N$), the derivative of the temperature-related changes increases rapidly but then decreases sharply to zero in the region below 50–60 K. This behavior of the spectral parameters of the absorption bands formed by exciton–magnon interactions is typical and is well known for classical AF insulators having a spin gap, e.g., for the two-dimensional $[NH_3(CH_2)_2NH_3]MnCl_4$, the quasi-one-dimensional $CsMnCl_3\cdot 2H_2O$, and the three-dimensional MnF_2 (Refs. 4 and 44).

Theoretical studies of the temperature dependence of the absorption in these materials have shown that the standard deviation of the bands in the AF phase is well described by a law $\sigma(T)\propto T^{n-1}\exp(-\Delta_N/k_BT)$, where Δ_N is the value of the spin-wave gap, and $n=2,3$ denotes the dimensionality of the system (for a gapless AF state in the case of a 3D crystal $\sigma(T)\propto T^3$; Ref. 44). This dependence leads to strong changes of the absorption band with temperature in the AF phase, but with a nearly thresholdlike transition, in the case of low-dimensional systems, to a temperature-independent part $\sigma=\mathrm{const}$ for $T<\Delta_N/k_B$. The solid curve in Fig. 3b shows the theoretical dependence $\Delta(\alpha\ell)_{\mathrm{fit}}=\alpha\ell(T)-\alpha\ell(T_0=205\ \mathrm{K})$ for the difference absorption of the Gaussian A band at $\hbar\omega=1.6$ eV, constructed with the use of $\sigma(T)$ for the 2D case ($n=2$). Here it is assumed that the area under the contour of the A line is conserved as the temperature is lowered from 300 K, i.e., for the Gaussians $\alpha\ell(T)$ and $\alpha\ell(T_0)$ it is assumed that $\mu_A=\mathrm{const}$. At the same time, the standard deviation is described by the expression $\sigma(T)=\sigma(T=0)+\gamma T\exp(-\Delta_N/k_BT)$, where γ is a normalizing constant. In order to link γ with the adjustable fitting parameters $\sigma(T=0)$ and Δ_N, it was assumed for the Gaussian $\alpha(T_0=205\ \mathrm{K})$ that $\sigma(T_0)=\sigma(300\ \mathrm{K})$. Good agreement of the experimental data and the theoretical curve is achieved for the following values of the parameters: $\sigma(T=0)=0.04$ eV, $\Delta_N=6$ MeV. The value of Δ_N specifies a temperature ≈ 65 K below which the changes of the A band with temperature in the AF phase should be insignificant. The value obtained for Δ_N agrees with the independent measurements of the spin-wave gap $\Delta N=3-6$ MeV in the insulating phase of YBCO which were made by neutron methods (see the discussion in Ref. 45). Thus the data in Fig. 3 show that the A band of absorption and the $(A+J)$ band related to it are formed as a result of the electron–magnon interaction. Here the standard deviation of the A band is apparently determined by the long-wavelength magnons, and the position and parameters of the electron–two-magnon $(A+J)$ band are due to magnons at the edge of the Brillouin zone, where the magnon density of states is close to a maximum.

Let us discuss in more detail the temperature dependence of the $(A+J)$ band. Figure 4 shows the data on $\Delta(\alpha\ell)_{A+J}=\alpha\ell(\omega,T)-\alpha\ell(\omega,140\ \mathrm{K})$ for the $(A+J)$ line in the AF phase of the film YS370, measured relative to the temperature $T_0=140$ K. It is seen that the $(A+J)$ band in the AF phase does not have a fine structure and is described well by a single Gaussian contour, shown by the solid curve in Fig. 4. The narrow $(A+J)$ band lies on a background of continuous variations of the interband absorption band, for which $\Delta(\alpha\ell)_{CT}=\alpha\ell_{CT}(\omega,T)=\alpha\ell_{CT}(\omega,140\ \mathrm{K})\approx -0.05$.

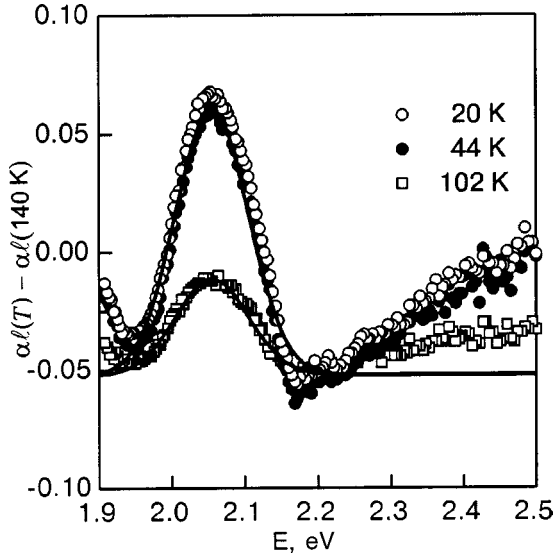

FIG. 4. Difference spectra of the absorption $\Delta(\alpha\ell)=\alpha\ell(T)-\alpha\ell(T_0)$, measured relative to $T_0=140$ K for the AF phase of the YS370 film in the region of the $(A+J)$ maximum. The solid curves show the model Gaussians.

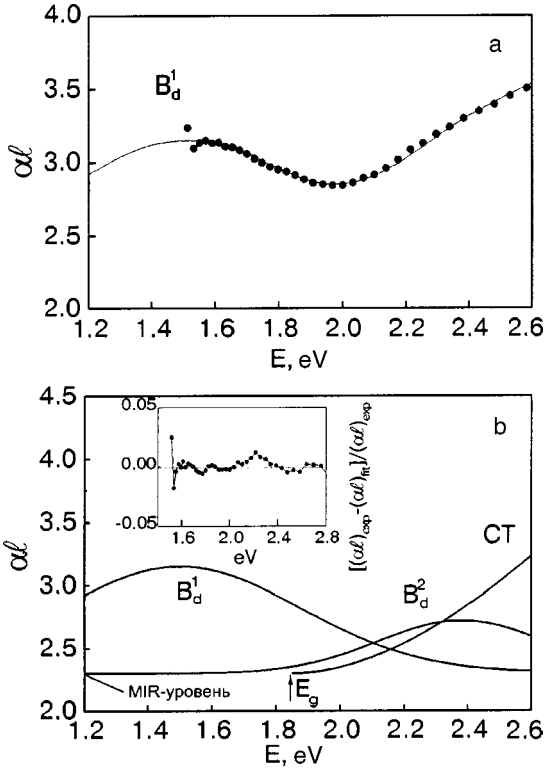

FIG. 5. Absolute absorption spectrum of the metallized film BH611 with $x\approx0.85$ at 300 K. The solid curve shows the model dependence (a). The decomposition of the model absorption spectrum into 4 components. The inset shows the relative difference of the experimental and model spectra (b).

The difference spectrum $\Delta(\alpha\ell)_{A+J}$, like the contour of the A band, should be determined by the difference of two Gaussians at different temperatures. If the standard deviation of the Gaussian varies slowly with temperature in the region of the AF phase, then the difference $\Delta(\alpha\ell)_{A+J}$ is practically a pure Gaussian with $\sigma_{A+J}=$const and an amplitude coefficient $\Delta\mu_{A+J}=\mu(T)-\mu(140\text{ K})$. This is explained by the fact that for magnon excitations with energy ε at the Brillouin zone edge the strong inequality $T\ll\varepsilon/k_B$ holds, and for the $(A+J)$ band the standard deviation can indeed be assumed temperature-independent in the entire AF phase region. From the approximating curves in Fig. 4 one can say that for $T<T_N$ the standard deviation of the contour satisfies a value $\sigma_{A+J}=0.05$ eV, i.e., at the transition to the AF state it decreased severalfold in comparison with its value 0.17 eV at 300 K; in the AF phase itself on cooling from 140 to 20 K the standard deviation varies weakly. At the same time, as we see in Fig. 4, in the AF phase the oscillator strength of the $(A+J)$ transition increases noticeably with decreasing temperature. For example, on cooling from 140 to 102 K the increment to the amplitude coefficient is $\Delta\mu_{A+J}=\mu(102\text{ K})-\mu(140\text{ K})=0.0036\text{ eV}=0.012\mu(300\text{ K})$, and on further cooling to 44 K the change reaches $\Delta\mu_{A+J}=0.01\text{ eV}=0.033\mu(300\text{ K})$. Thus in the insulating phase upon the transition from short-range AF ordering at $T<T_N$ to long-range AF ordering at $T<_iT_N$ the standard deviation of the $(A+J)$ band decreases, while the amplitude of the band (the optical transition probability) increases and continues to increase all the way to 44 K. In the region $T\leqslant44$ K all the temperature dependence stops (see Fig. 4), just as in the case of the A transitions with which the electron–two-magnon $(A+J)$ transitions are genetically related. We again call attention to the fact that in the AF phase the Gaussian contour of the $(A+J)$ band is structureless throughout the entire range of temperatures investigated.

4. METALLIC PHASE OF YBCO

Let us now consider the absolute absorption spectra of the metallic phase of $YBa_2Cu_3O_{6+x}$ $(x\approx0.85)$ at near-optimal doping with $T_c=88$ K and the changes of the spectral composition of the absorption as the temperature is swept through the PG and SC states. Figure 5a shows the absolute absorption spectrum of the film BH611 at 300 K in the region 1.2–2.6 eV, and Fig. 5b shows a model decomposition of the spectrum into components. The spectrum contains four components: the B_d^1 band, the B_d^2 band, the CT component, and the MIR component, which is constant in the region 1.2–2.6 eV. The decomposition of the spectrum into these components allows one to describe the experimental data with an accuracy of 1% or better (the relative difference of the experimental and model (fit) spectra $[(\alpha\ell)_{\text{exp}}-(\alpha\ell)_{\text{fit}}]/(\alpha\ell)_{\text{exp}}$ is shown in the inset of Fig. 5b). The total model spectrum $(\alpha\ell)_{\text{fit}}=(\alpha\ell)_{1B}+(\alpha\ell)_{2B}+(\alpha\ell)_{CT}+(\alpha\ell)_{MIR}$ has the following parameters:

1) for a Gaussian B_d^1 band: $E_0^{1B}=1.5$ eV, standard deviation $\sigma_{1B}=0.38$ eV, amplitude coefficient $\mu_{1B}=0.57$ eV;

2) for a Gaussian B_d^2 band: $E_0^{2B}=2.38$ eV, $\sigma_{2B}=0.26$ eV, $\mu_{2B}=0.19$ eV;

3) for the CT component: $E_g=1.85$ eV, $\mu_{CT}=4.3\text{ eV}^{-1}$ (the increase in the value of the optical gap in comparison with the insulator gap may be due to the appearance of a hole band with a scale of 0.1 eV);

4) for the short-wavelength wing of the MIR component the absorption level is assumed constant, $(\alpha\ell)_{MIR}=2.3$.

Thus at 300 K the A and $(A+J)$ bands are absent from

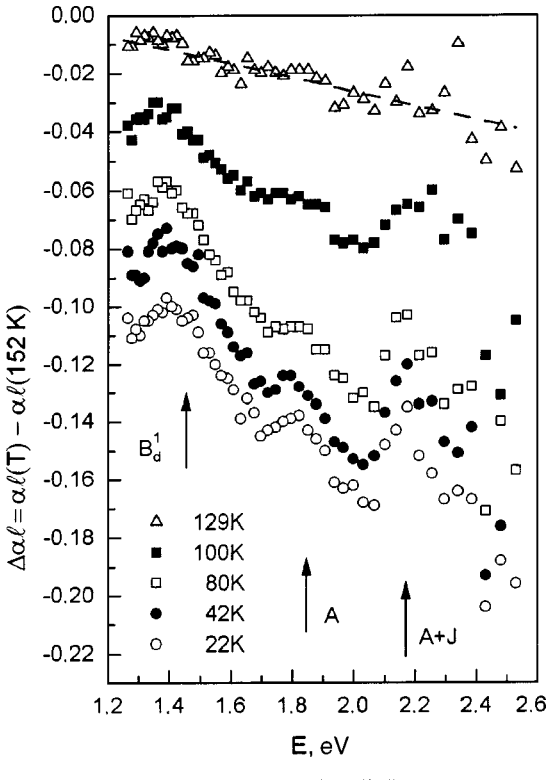

FIG. 6. Evolution of the spectral composition of the absorption of the metallized film BH611 ($T_c = 88$ K) on cooling relative to the initial temperature $T_0 = 152$ K. For clarity the data for the temperatures 22 and 42 have been shifted downward by 0.04 and 0.02 relative to the data for 80 K. The arrows indicate the bands that appear upon cooling.

the spectral composition of the absorption; this should be attributed to the strong suppression of the charge and spin correlations in the optimal doping phase. At the same time the *dd* bands B_d^1 and B_d^2 are very strong on account of the enhancement of the degree of *pd* hybridization (degree of covalency) in the metallic phase, both in the CuO_2 plane and in the transverse direction. The fact that the correlation *A* band and the "covalent" *B* bands behave in opposite ways on doping is evidence that the *pd* hybridization and the electronic correlations compete with each other. As the number of carriers increases, the *pd* hybridization increases, i.e., the degree of covalency of the crystal increases, while the electronic (Hubbard) correlations become weaker, i.e., the degree of ionicity of the crystal decreases. Here a strong damping of magnons occurs in the electron–hole pair formation channel and, as a result, there is no $(A+J)$ band.

To answer the question of what changes in the electronic interactions are necessary for the appearance of superconductivity, we must study the temperature evolution of the spectral composition of the absorption. Let us consider in this connection the difference spectra $\Delta(\alpha\ell) = (\alpha\ell)(\omega, T) - (\alpha\ell)(\omega, 152\ \mathrm{K})$, which characterize the changes of the spectral composition of the absorption of the film BH611 relative to that at the temperature $T_0 = 152$ K in the range of the B_d^1, *A*, and $(A+J)$ bands. The data for the temperatures $T = 129$, 100, 80, 42, and 22 K are presented in Fig. 6. In these measurements the frequency scanning was done with a step of 10 nm ($\approx 3.5 \times 10^{-2}$ eV). This rather large scanning step permits demonstration of the most general trends in the temperature dependence of the whole spectrum. In the next Section we present data obtained with a scanning step one-tenth as large, making it possible to reveal the fine structure of the $(A+J)$ band.

As we see in Fig. 6, with decreasing temperature the absorption of the film decreases in the spectral region of the measurements, 1.25–2.5 eV, i.e., $\Delta(\alpha\ell) < 0$. More importantly, no narrow-band features are present in the interval 129–152 K; only the continuous weakening of the absorption is observed, and the changes themselves, $\Delta(\alpha\ell) = -(0.01-0.03)$ are small. We stress that for $T > 152$ K and up to room temperature these changes are still smaller and have the same continuous character. For clarity, the energy behavior of this background component is shown by the dashed line. This wide-band change in the spectrum is due primarily to the weakening of the MIR and CT components. In the region $\hbar\omega \leqslant 1$ eV, as one can readily see, this background component changes sign, $\Delta(\alpha\ell) > 0$. This occurs because in the region $\hbar\omega < 1$ eV, where the MIR maximum is concentrated, the absorption increases with decreasing temperature.[6,19,20] We shall not discuss the redistribution of the intensities within the contour of the MIR absorption band itself but will focus our attention on the behavior of the narrow-band features of the spectrum.

For the temperature region $T > 130$ K it can be stated that the narrow-band absorption contours are temperature-independent, since $\Delta(\alpha\ell) \approx 0$ for them. Consequently, the contours of the B_d^1 and B_d^2 bands present in the spectrum at 300 K (see Fig. 5) do not change their parameters as the film is cooled, and the *A* and $A+J$ bands, which are formed by electron–magnon interactions, remain absent.

At 100 K, however, one observes a different picture (see Fig. 6). The bands B_d^1, *A*, and $A+J$ are quite clearly visible against the continuous background. When the temperature is lowered further to 80 K and below, these bands become more and more pronounced. In the SC phase these narrow-band feature persist, and with constant parameters, down to the final temperature of the measurements, 22 K.

Before turning to a quantitative analysis of the measured spectra, let us point out that the narrow-band features arise in the interval 100–130 K. The appearance of the *A* and $(A+J)$ bands, which are clearly expressed for the AF phase of the insulator, is direct evidence that in this temperature interval the metallized system shifts toward AF ordering. In other words, the fact that the bands *A* and $A+J$ appear at $T < 130$ K is due to the onset of short-range AF ordering with short-wavelength magnons, which can only exist in the metal.

In the most diverse experiments with YBCO at moderate and optimal doping, anomalies preceding superconductivity are observed at temperatures below a threshold value ≈ 160 K.[8,22,24] For example, for YBCO with $T_c \approx 85$ K, according to the data of resistive, NMR, and heat capacity measurements, this threshold temperature lies at $T^* \approx 110$ K. According to the neutron data for $YBa_2Cu_3O_{6.8}$ the value is $T^* = 115 \pm 15$ K, and for $T < T^*$ there is a decrease in the contribution to the imaginary part of the magnetic susceptibility from the spin excitations with energy less than 20 meV.[6,24] This allows us to speak of the formation of a spin pseudogap for $T < T^*$.

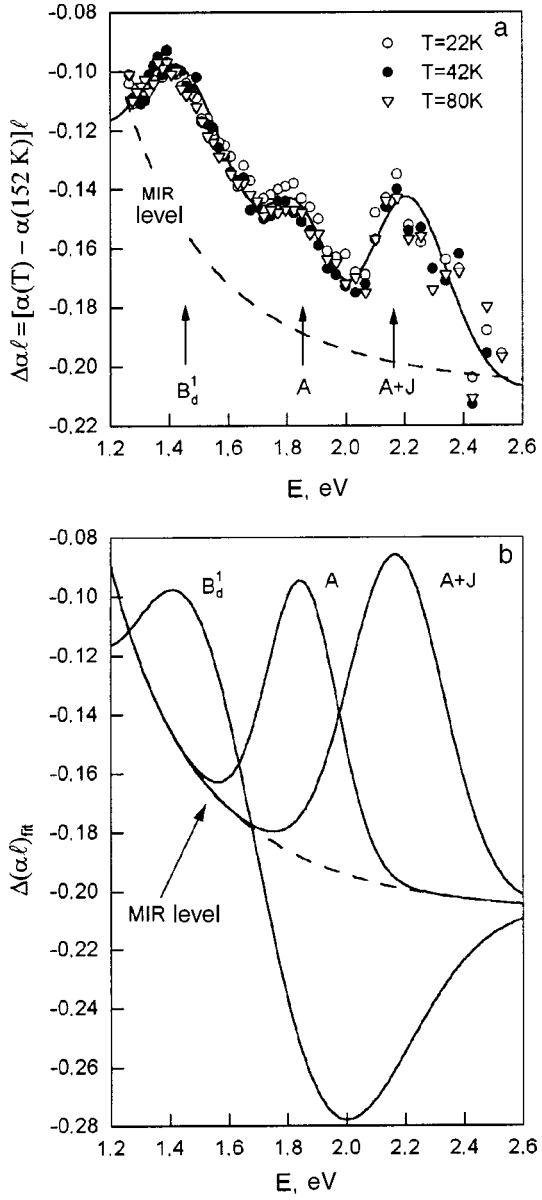

FIG. 7. Experimental data and model curves for the change of the absorption coefficient $\Delta(\alpha\ell)=\alpha\ell(T)-\alpha\ell(T_0)$ on cooling of the film BH611 ($T_c\approx 88$ K) from $T_0=152$ K to the SC phase. A direct comparison of the data with the model dependence (a). The decomposition of the model dependence into spectral components. As the zero level for the B, A, and $(A+J)$ components we have taken the MIR component of the absorption (the MIR level). The unusual form of the B component is due to the fact that it is determined as the difference between two Gaussians, one at 152 K and one at $T=22$, 42, or 80 K. The difference spectra for the A and $(A+J)$ components, which are absent at 152 K, are pure Gaussians (b).

Thus the special temperature interval 100–130 K which we have identified from the optical spectra is confirmed by a number of other measurements. Even in a qualitative treatment the observed appearance of A and $(A+J)$ bands in this interval can serve as independent proof of the decisive contribution of AF fluctuations to the nature of the PG state.

Let us turn to a quantitative analysis of the measured spectra. Figure 7 shows the model dependence describing the difference spectrum of the absorption in the region of the SC phase at 80, 42, and 22 K relative to 152 K. The decomposition of the model dependence into spectral components is shown. It is clear that the absorption contours at the three temperatures practically coincide, i.e., the SC phase "freezes" the absorption spectral composition that has arisen in the pseudogap state. The model curve in Fig. 7a was constructed with allowance for the following temperature-related changes:

$$\Delta(\alpha\ell)_{\rm fit}=\Delta(\alpha\ell)^{\rm fit}_{1B}+\Delta(\alpha\ell)^{\rm fit}_{A}+\Delta(\alpha\ell)^{\rm fit}_{A+J}+\Delta(\alpha\ell)^{\rm fit}_{MIR},$$

where the first three terms have the form $\Delta(\alpha\ell)^{\rm fit}_i=(\alpha\ell)^{\rm fit}_i(22\ {\rm K})-(\alpha\ell)^{\rm fit}_i(152\ {\rm K})$ for $i=1B$, A, $A+J$. The component $\Delta(\alpha\ell)_{MIR}$ was chosen as a function of frequency, permitting a description of the background component of the difference spectrum. Since the absorption bands A and $A+J$ are absent above 152 K, the components $\Delta(\alpha\ell)^{\rm fit}_A$ and $\Delta(\alpha\ell)^{\rm fit}_{A+J}$ at 22 K are pure Gaussians with adjustable parameters σ and μ. The behavior of $\Delta(\alpha\ell)^{\rm fit}_{1B}$ is given by the difference of two Gaussians at 22 and 152 K, and, following the data in Fig. 5, we have assumed that the Gaussians at 152 and 300 K are equal: $(\alpha\ell)^{\rm fit}_{1B}(152\ {\rm K})=(\alpha\ell)^{\rm fit}_{1B}(300\ {\rm K})$. Let us give the quantitative characteristics of the decomposition, which describes the experimental results extremely well.

1. For the MIR component $\Delta(\alpha\ell)^{\rm fit}_{MIR}=-0.21+0.25/E^4$ (the MIR level in Fig. 7), i.e., the change in sign of the temperature trend of the high-frequency wing of the MIR component occurs near $E=1.05$ eV, where $\Delta(\alpha\ell)^{\rm fit}_{MIR}=0$. We note that the change of the CT component with temperature can be assumed to be effectively included in the behavior of $\Delta(\alpha\ell)^{\rm fit}_{MIR}$.

2. For the A band the parameters of the Gaussian contour in the SC phase are: $E_0^A=1.85$ eV, standard deviation $\sigma_A=0.12$ eV, and amplitude coefficient $\mu_A=0.02$ eV. Consequently, the standard deviation of the contour of the A band in the film with $x\approx 0.85$ matches the value $\sigma_A=0.12-0.14$ eV in the paramagnetic phase (300 K) for films with $x\approx(0.3-0.35)$.

3. For the $(A+J)$ band the Gaussian parameters in the SC phase are $E_0^{A+J}=2.18$ eV, $\sigma_{A+J}=0.16$ eV, and $\mu_{A+J}=0.032$ eV. The standard deviation of this contour is again practically equal to the value $\sigma_{A+J}=0.17$ eV in the case of an insulating film with $x=(0.3-0.35)$ in the paramagnetic phase.

4. For the covalent B_d^1 band ($E_0^{1B}=1.5$ eV) the standard deviation decreases noticeably on cooling of the film, from $\sigma_{1B}=0.38$ eV at 300 K to 0.3 eV at 22 K, nearly a 30% decrease, but the amplitude coefficient changes less strongly: $\mu_{1B}=0.57$ eV (300 K) and 0.5 eV (22 K). It should be emphasized that the narrowing of the dd absorption bands is a characteristic feature of antiferromagnets on passage through the AF transition.[3,4] At the same time, the small changes of μ_{1B} with temperature indicate that the degree of pd mixing reached at 300 K through chemical doping is preserved as the temperature is lowered. In Ref. 21, where the optical characteristics of the B_d^1 band of a YBCO film with $x\approx 0.7$ were measured, it was also observed that the changes of the level of pd hybridization with temperature are small. At the same time, even a small increase in the index x from 0.7 to 0.9, for which T_c rises from 74 to 90 K, leads to an increase of the coefficient μ_{1B} by more than a factor of 5.[20,21]

Thus the quantitative characteristics of the measured spectra indicate that the standard deviation of the A and $(A+J)$ bands in the PG state and directly in the SC state practically coincide with that for the insulating phase with well-developed AF correlations. Since the electron–magnon bands A and $A+J$ coexist in the PG state with a pronounced covalent B_d^1 band, the AF fluctuations develop under conditions of strong pd hybridization. In the insulating phase, as was shown in Fig. 3, no such coexistence is observed. However, the degree of pd hybridization in the metal is almost independent of temperature ($\mu_{1B} \approx$ const), i.e., the hybridization is not a decisive factor in the formation of superconductivity. More subtle mechanisms responsible for superconductivity involve the development of AF fluctuations in the PG state, as is evidenced by the observed appearance of the A and $(A+J)$ bands for $T \leqslant T^* = 120 \pm 10$ K.

In this connection it is natural to ask, how might such essentially contrary states as the fluctuation insulator (antiferromagnet) and the metallic state with strong pd hybridization be compatible, both in the PG and in the SC states? To answer this question we examined the fine structure of the $(A+J)$ band for optical evidence of phase separation (the appearance of a stripe superstructure) at $T < T^*$.

5. STRUCTURE OF THE $(A+J)$ ABSORPTION BAND IN THE METALLIC PHASE OF YBCO

In the experiments the fine structure of the $(A+J)$ absorption band was revealed in a scanning of the spectra with a step of 1 nm, which corresponds to approximately 3×10^{-3} eV, in the frequency range 2–2.4 eV, where the $(A+J)$ band is located. As the sample was cooled in the temperature range 170–20 K we measured the difference spectra $\Delta(\alpha\ell)_{A+J} = \alpha\ell(\omega, T_1) - \alpha\ell(\omega, T_2)$ at rather narrow intervals between T_2 and T_1.

Figure 8 shows the difference spectra of $\Delta(\alpha\ell)_{A+J}$ for the film BH611 with $x \approx 0.85$ in five temperature intervals ($T_1 \leqslant T \leqslant T_2$). The data labeled *1* pertain to the interval 150 K$\leqslant T \leqslant$170 K, i.e., for the region $T > T^*$. It is seen that in this interval the narrow-band $(A+J)$ component is once again absent, which, as we have said, was also the case at 300 K. Data set *2* pertain to the interval 155–112 K, which includes the value $T^* \approx 120$ K. It is clearly seen that when the temperature passes through the point of formation of the PG state the electron–two-magnon maximum does not arise simply but appears in the form of a doublet structure with maxima at $E_{01}^{A+J} = 2.145$ eV and $E_{02}^{A+J} = 2.28$ eV. (In the region of energies below 2 eV the growth of the absorption is due to the appearance of the A band.) Thus more detailed measurements show that the $(A+J)$ band has a fine structure in the PG state. The solid curve shows the sum of two Gaussians of this doublet, with parameters $\sigma_1^{A+J} = 0.053$ eV, $\sigma_2^{A+J} = 0.045$ eV and $\mu_1^{A+J} = 0.0024$ eV, $\mu_2^{A+J} = 0.0015$ eV. We stress that for the PG state the standard deviation of each doublet is practically the same as that for the AF phase of the insulator. On further cooling in the interval from $T_2 = 113$ K to $T_1 = 98$ K ($T_c < T < T^*$) there is no change of the doublet with temperature (data set *3*), i.e., $\Delta(\alpha\ell)_{A+J} = 0$. However (see data set *4*), on passage through the SC transition ($T_c = 88$ K), in the temperature interval 100–70 K, there is an additional increase in the amplitude of each maximum, i.e., an increase in the probability of electron–two-magnon excitation. The amplitude increments are $\Delta\mu_1^{A+J} = 0.0018$ eV and $\Delta\mu_2^{A+J} = 0.0007$ eV, or $\approx 50\%$ of the initial amplitudes of the components arising in the PG state in the interval 112–155 K. The standard deviation of the contour (magnon damping) does not change on passage through T_c. Further cooling from 71 to 20 K, now in the SC phase, does not lead to any changes with temperature ($\Delta(\alpha\ell)_{A+J} = 0$; data set *5*), i.e., the doublet structure itself and its parameters are preserved unchanged in the whole region of the SC state.

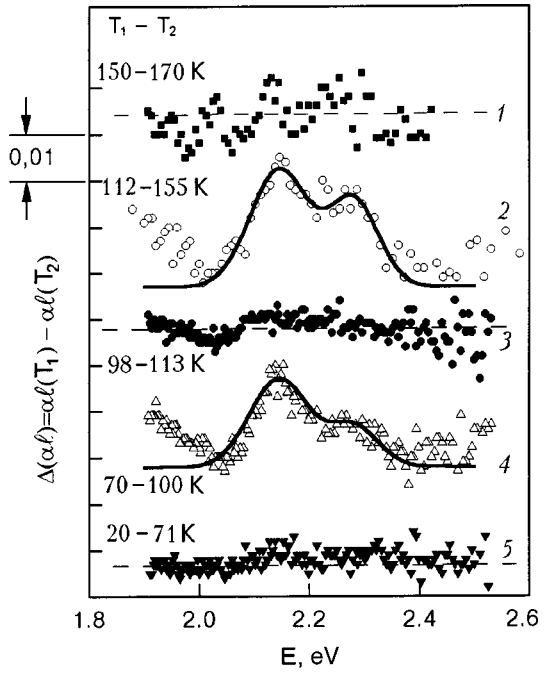

FIG. 8. Change with temperature of the absorption spectra $\Delta\alpha\ell = \alpha\ell(T_1) - \alpha\ell(T_2)$ for a superconducting YBCO film. The temperatures T_1 and T_2 for each region of the measurements are given to the left of the experimental data. Data set *2* corresponds to the region of opening of the pseudogap state and data set *4* to the region of the superconducting state. The solid curves are model curves in the form of sums of two Gaussians.

We said in the previous Section that the appearance of the $(A+J)$ band as the temperature is lowered is evidence that the metallized phase of YBCO is shifted toward short-range AF ordering. However, in the paramagnetic and AF states of the insulator the $A+J$ band do not exhibit fine structure (see Fig. 4). Consequently, the short-range AF ordering in the metal is of a peculiar nature. The analysis of these data in the next Section will show that the fine structure of the $(A+J)$ band reflects the appearance, in the SG and SC states, of phase separation in the form a stripe superstructure consisting of an alternation of insulating and metallic quasi-one-dimensional stripes. This spatial structure permits the compatibility of well-developed AF fluctuations (insulating stripes) in the metal, on the one hand, and mobile hole carriers that do not destroy the AF fluctuations (metallic stripes with strong oxygen–copper hybridization), on the other.

6. DISCUSSION AND CONCLUSIONS

The many nontrivial properties of copper-oxide HTSCs in the normal and SC phases are a manifestation of the fundamental peculiarities of low-dimensional systems in which

there are well-developed scalar (charge) and vector (spin) correlations. In the final analysis, it is these correlations that determine the optical properties that are observed in cuprate HTSCs but not in classical metals and doped semiconductors. In the present paper the main goal was to elucidate the nature of the pseudogap state that precedes superconductivity and of the actual superconducting state of YBCO. Let us discuss the main results, paying particular attention to the narrow-band features of the spectrum.

1. In the absorption spectra of YBCO in the visible frequency region one can discern the following narrow bands with a standard deviation of around 0.1 eV, and with the following diagnostic possibilities:

— the contribution of the correlation peak of the density of states (the correlation A band at $\hbar\omega \approx E_g$);

— the contribution of the AF correlations (electron–two-magnon band $A+J$ at $\hbar\omega \approx E_g + \hbar\omega_{2m}$);

— the degree of pd mixing (degree of covalency) in the active CuO_2 plane (the B_d^1 band for dd transitions at $\hbar\omega \approx 1.5$ eV). As the data of the present study and also those of Ref. 20 show, the B_d^1 band can serve as an optical probe of the metallization both at the insulator–metal transition and also in the metallic phase itself.

2. In the insulator phase of YBCO the integrated intensity of the B_d^1 band is at least an order of magnitude lower than the intensities of the A and $(A+J)$ absorption bands. This is a consequence of the weak metallization of CuO_2 and the existence in YBCO of localized ''copper'' holes. At the same time, in the spectra of the paramagnetic and AF states of the insulator the A and $(A+J)$ bands are very pronounced as a consequence of the developed AF correlations. At the transition to the AF phase with long-range order for $T<T_N$ the absorption at the maxima of these bands $(\alpha\not{\prime})_{A,A+J} \propto \mu/\sigma$ is enhanced substantially. These bands are sensitive to both short- and long-range AF correlations. The existence of A and $(A+J)$ bands in cuprate HTSCs apparently is of a general nature: their analogs can be observed at 300 K in the optical conduction spectra (near the fundamental edge of absorption with charge transfer) in a number of insulators containing CuO_2 planes.[6]

3. With increasing doping index the correlation A band and the two-magnon $(A+J)$ band broaden and rapidly weaken. Traces of these bands at 300 K can be discerned only in the lightly and moderately doped metallic YBCO film with $x \leqslant 0.7$. At optimal doping ($x \approx 0.85$) they are absent, reflecting the suppression of charge and spin correlations in the metal at 300 K. Moreover the integrated intensity of the B_d^1 band increases by almost a factor of 5 at the transition from the YBCO insulator with $x \approx 0.35$ to the metallic phase with $x \approx 0.7$ (Ref. 20) and, as the data of the present study show, by almost a factor of 20 at the transition to the optimal doping phase. Nevertheless, at 300 K the enhancement of the pd hybridization and the weakening of the AF correlations do not lead to superconductivity, i.e., the oxygen–copper hybridization (covalency) is a necessary but not sufficient factor for the appearance of superconductivity. As measurements of the absorption spectra show, it is in the magnetic subsystem of YBCO where the more subtle processes responsible for superconductivity develop as the temperature is lowered.

4. On cooling of metallized YBCO films the spectral composition of their absorption does not change down to a certain critical region near $T^* > T_c$. For optimally doped YBCO the parameters of the B_d^1 band do not change, and A and $(A+J)$ bands are absent from the spectrum, just as at 300 K. It can be stated that in the interval $T^* < T \leqslant 300$ K the temperature does not affect the degree of pd mixing, and the AF correlations remain strongly suppressed. In other words, the weak AF fluctuations do not have a substantial influence on the motion of the hole carriers, which occurs in a space with rather uniform copper–oxygen covalent bonds.

5. The spectral (physical) picture changes fundamentally on cooling in the interval $T_c < T \leqslant T^*$, where YBCO has a transition to a pseudogap (according to the neutron data) state that precedes superconductivity. For YBCO with optimal doping a value $T^* = 120 \pm 10$ K is obtained from the optical data in the present study, in good agreement with the neutron data ($T^* = 115 \pm 15$ K).[24] At the ''doorstep'' of superconductivity for $T \leqslant T^*$ the A and $(A+J)$ absorption bands, which are characteristic of the paramagnetic and AF states of YBCO, appear rather rapidly in the spectral composition. The standard deviation of these newly appearing bands is $\sigma_{A,A+J} = 0.12-0.16$ eV, in agreement with the values $\sigma_{A,A+J} = 0.12-0.17$ eV for a paramagnetic insulator state at 300 K, in which the AF fluctuations of the short-range order are quite pronounced. At the same time, for $T \leqslant T^*$ there is a noticeable narrowing of the B_d^1 band by almost 30%, as is characteristic for dd transitions upon the transition of magnetically ordered materials to the AF phase.[3,4] Thus our data undoubtedly attest to the fact that the PG state is due to the existence of developed AF fluctuations. Since the values of the standard deviations of the A and $(A+J)$ bands are the same as for insulating YBCO, the wavelength of the magnetic excitations should be less than the correlation length $\xi_{AF} \approx 10$ Å for AF fluctuations in the metallized CuO_2 plane.[6] In this case fluctuational spin waves exist in regions with dimensions smaller than ξ_{AF}. Within such a region the situation below T^* is completely analogous to the short-range AF ordering of an insulator near T_N.

The nature of the A and $(A+J)$ bands in the metal and, primarily, of the $A+J$ feature, which is most sensitive to AF fluctuations is in agreement with the neutron scattering data for YBCO. For example, according to these data, when the temperature is lowered in the region $T \leqslant T^*$, together with the formation of a spin pseudogap, enhancement of the fluctuations of the magnetic moment $\langle m_{\rm res}^2 \rangle$ occurs. The fluctuations $\langle m_{\rm res}^2 \rangle \propto \chi''_{\rm res}(\omega) d$ correspond to the formation of a resonance peak for the imaginary part of the magnetic susceptibility $\chi''_{\rm res}$ at the acoustic AF mode frequency $\hbar\omega_{\rm res} \approx 40$ meV.[24] Here, as our optical data show, the integrated intensity of the B_d^1 band in the SC state does not change, i.e., the degree of pd mixing is conserved. When all is said and done, an unusual picture emerges, in which strong AF correlations (the A and $(A+J)$ bands) coexist with strong metallization (the B_d^1 band). This sort of coexistence is not observed in the insulator or in the metallic phase above T^*, including at 300 K. It is logical to propose the following physical picture for the interpretation of this coexistence. The hole carrier creates around itself a region of strong covalent bonding (with shortened lengths of the hybridized

Cu–O bonds), where the electronic and spin correlations are suppressed, but outside of this region the matrix of pronounced AF correlations persists. Such a formation, according to Ref. 46, can be called a correlation polaron dressed in a coat of AF fluctuations. However, this is only a first step toward understanding the phase separation in the PG state of YBCO. A more precise picture follows from analysis of the fine structure of the $(A+J)$ band.

6. Careful measurements show that in the pseudogap state the $(A+J)$ band has a doublet structure and consists of two narrow maxima with energies $E_{01}^{A+J}=2.145$ eV and $E_{02}^{A+J}=2.28$ eV. The standard deviation of each of them (≈ 0.05 eV) is the same as that of the single $(A+J)$ contour in the AF phase of the insulator at low temperatures. The first maximum $(A+3J)$ is separated from the strictly electronic A transition ($E_0^A=1.85$ eV) by an amount 0.3 eV, and the second maximum $(A+4J)$ by 0.43 eV, these being in units of the exchange energy $3J$ and $4J$. These data can be analyzed from two points of view: first, in comparison with the results on inelastic neutron scattering in YBCO, and, second, for analysis of the cause of the appearance of the $4J$ resonance in the optical absorption spectra of the metallic phase when it is absent in the AF insulator phase.

According to the neutron data,[8,24] in YBCO slightly above T_c the peak of inelastic scattering on spin fluctuations is split on account of the formation of an incommensurate superstructure (the stripe structure). The difference of the wave vectors responsible for the splitting of the neutron peak equals $\Delta k=0.2$ Å^{-1} for the optimal doping region. In a first approximation this value corresponds to an energy difference $\Delta E=\Delta k\hbar v=0.12$ eV, where $\hbar v=0.6$ eV·Å is the spin-wave velocity in YBCO.[6,47] The values of the neutron and optical splittings ΔE are in good agreement with each other.

Let us now consider the formation of the stripe superstructure from the standpoint of establishing the cause of the $4J$ resonance, which is particularly revealing of the pattern of separation into insulating and metallic phases. In the YBCO insulator, according to our data (see Fig. 4) and the Raman scattering data of Refs. 48 and 49, the most interesting is the $3J$ resonance involving the creation of two interacting magnons with binding energy J. The probability of creation of two noninteracting magnons with total energy $4J$ by a photon in the an insulator is small. For example, in the Raman scattering spectra of cuprate HTSCs the $4J$ resonance is observed only in the form of a weak feature in the insulator phase, leading to a slight asymmetry of the two-magnon scattering band.[48] It must be noted that in cuprate HTSCs, according to the theoretical conclusions, the probability of excitation of the $3J$ and $4J$ resonances should increase sharply for photons with energies close to the optical gap with charge transfer, E_g (Ref. 48). In the case of formation of a stripe superstructure it becomes possible to excite magnons from different insulating stripes separated by a metallic stripe. Here, because of the significant decrease of the magnon interaction the amplitude of the $4J$ resonance should increase. Since the time for an optical transition with the absorption of light ($\approx 10^{-14}$ s) is substantially shorter than the lifetime ($\approx 10^{-10}$ s; Ref. 24) of the fluctuating stripe structure, optical diagnostics give a quasistationary picture of this structure.

Thus our optical data are unambiguous evidence that the PG state is a superstructure with spatially separated regions of the the metallic and insulating types, in the insulating regions of which there exist fluctuational spin waves. This structure arises extremely rapidly at $T=T^*$, and with further decrease in temperature down to T_c its parameters remain practically unchanged. We note that the neutron data, because of the large temperature scanning step, do not reveal these important details of the temperature evolution of the stripe structure.[24]

7. Upon passage through the SC transition, the spectral composition of the absorption formed in the pseudogap state all remains as it was, i.e., the stripe structure is preserved. However, at the SC transition at T_c an additional increase by about 50% in the amplitudes of the $3J$ and $4J$ resonances occurs. The standard deviation of each resonance does not change. The increase of the integrated intensity of the resonances near T_c occurs just as abruptly as upon the formation of the PG state. This circumstance can be interpreted as a transformation of the pseudogap in the spectrum of magnetic interactions into a real spin gap for magnon states with energies less than 20 meV.[24] The enhancement of the resonances can also be interpreted as being a consequence of the appearance of a more regular stripe structure below T_c. In this case there should be an additional redistribution of the magnetic density of states throughout the entire Brillouin zone. At temperatures approximately 10 K lower than T_c there are no longer any changes occurring in the spectral composition and the parameters of the absorption bands. It can be said that under conditions of a developed superconducting order parameter the physical picture of the stripe superstructure ''freezes in,'' much as this happens in the PG state.

8. Thus it must be acknowledged that the optical absorption spectra of YBCO films in the visible frequency range give independent and rather convincing evidence in favor of the participation of the magnetic AF subsystem in the formation of the stripe structure of the pseudogap and superconducting states. An enhancement of the AF correlations occurs at the SC transition. Apparently the superconducting transition occurs as two-dimensional, with a large temperature region of two-dimensional superconducting fluctuations. The superconductivity most likely develops on account of the establishment of a global phase coherence between the metallic stripe phases. A careful examination of the electronic processes and interactions of the magnetic, phonon, hole subsystems in HTSCs[50,51] shows the necessity of invoking a magnetoelastic polaron model for describing the normal and superconducting properties of HTSCs under conditions of phase separation. The optical absorption data, like those given above and those published in Refs. 6, 49, and 50 can be interpreted in the framework of a polaron model of quasiparticle excitations in these compounds (this topic will be the subject of a separate paper). We also note that since the optical measurements can be done in polarized light, our results promise to provide a new method of studying the anisotropy of the AF correlations in the pseudogap state and also the anisotropy of the superconducting order parameter.

This paper was prepared for the jubilee of Viktor Valentinovich Eremenko.

This study was supported in part by the Government Foundation for Basic Research of the Ministry of Education and Science of Ukraine.

*E-mail: gsergeeva@kipt.kharkov.ua

[1)]According to Hirsch's theory [Physica C **364–365**, 37 (2001)], sensitivity of the optical spectra to superconductivity in hole-type HTSCs is due to the fundamental asymmetry of the pairing of electrons and holes (hole polarons) in the superconducting state.

[1] V. V. Eremenko and A. I. Belyaeva, Usp. Fiz. Nauk **98**, 27 (1969).
[2] V. V. Eremenko, Yu. G. Litvinenko, and T. I. Garber, JETP Lett. **7**, 298 (1968).
[3] V. V. Eremenko, *Introduction to the Opical Spectroscopy of Magnets* [in Russian], Naukova Dumka, Kiev (1975).
[4] V. V. Eremenko, N. F. Kharchenko, Yu. G. Litvinenko, and V. M. Naumenko, *Magneto-Optics and Spectroscopy of Antiferromagnets*, Springer-Verlag, Berlin (1992).
[5] A. Millis, P. Montoux, and D. Pines, Phys. Rev. B **42**, 167 (1990).
[6] M. Imada, A. Fujimori, and Y. Tokura, Rev. Mod. Phys. **70**, 1039 (1998).
[7] G. G. Sergeeva, Yu. P. Stepanovskiĭ, and A. V. Chechkin, Fiz. Nizk. Temp. **24**, 1029 (1998) [Low Temp. Phys. **24**, 771 (1998)].
[8] S. G. Ovchinnikov, Usp. Fiz. Nauk **167**, 1043 (1997).
[9] T. Timusk and B. Statt, Rep. Prog. Phys. **62**, 61 (1999).
[10] I. A. Privorotskiĭ, Zh. Éksp. Teor. Fiz. **43**, 2255 (1962) [Sov. Phys. JETP **16**, 1593 (1963)].
[11] B. I. Verkin and B. G. Lazarev, Izv. AN SSSR Ser. Fiz. **12**, 598 (1948).
[12] J. E. Hirsch, Physica C **199**, 305 (1992).
[13] V. G. Stankevich, N. Yu. Svechnikov, K. V. Kaznacheev, R. A. Kink, Kh. É. Niédrais, V. N. Golubev, V. Ya. Kosyev, Yu. N. Simirskiĭ, and M. B. Tsetlin, JETP Lett. **47**, 385 (1988).
[14] V. V. Eremenko, I. Ya. Fugol', V. N. Samovarov, and V. M. Zhuravlev, JETP Lett. **47**, 618 (1988).
[15] I. Ya. Fugol', V. N. Samovarov, Yu. I. Rybalko, V. M. Zhuravlev, and P. Berberikh, Sverkhprovodimost' (KIAE) **4**, 109 (1991) [Superconductivty **4**, 94 (1991)].
[16] I. Fugol, G. Saemann-Ischenko, V. Samovarov, Yu. Rybalko, V. Zhuravlev, Y. Ströbel, B. Holzarfel, and P. Berberich, Solid State Commun. **80**, 201 (1991).
[17] H. L. Dewing and E. K. H. Salje, Supercond. Sci. Technol. **5**, 50 (1992).
[18] I. Ya. Fugol', V. N. Samovarov, A. M. Ratner, V. M. Zhuravlev, G. Zaĭmann-Ishchenko, M. Lippert, B. Khol'tsapfel', and O. Maĭer, Fiz. Nizk. Temp. **18**, 1338 (1992) [Low Temp. Phys. **18**, 932 (1992)].
[19] C. H. Rüscher and M. Götte, Solid State Commun. **85**, 393 (1993).
[20] V. V. Eremenko, V. N. Samovarov, V. N. Svishchev, V. L. Vakula, M. Yu. Libin, and S. A. Uyutnov, Fiz. Nizk. Temp. **26**, 739 (2000) [Low Temp. Phys. **26**, 541 (2000)].
[21] V. V. Eremenko, V. N. Samovarov, V. L. Vakula, M. Yu. Libin, and S. A. Uyutnov, Fiz. Nizk. Temp. **26**, 1091 (2000) [Low Temp. Phys. **26**, 809 (2000)].
[22] V. M. Loktev, R. M. Quick, and S. G. Sharapov, Phys. Rep. **349**, 1 (2001).
[23] V. J. Emery, S. A. Kivelson, and O. Zachar, Phys. Rev. B **56**, 6120 (1997).
[24] P. Dai, H. A. Mook, and F. Dogan, Phys. Rev. Lett. **80**, 1738 (1998); P. Dai, H. A. Mook, S. M. Hayden, G. Aeppli, T. G. Perring, R. D. Hunt, and F. Dogan, Science **284**, 1344 (1999).
[25] J. Zaanen, Nature (London) **404**, 714 (2000).
[26] A. Bianconi, D. Di Castro, G. Bianconi, A. Pifferi, N. L. Saini, F. C. Chou, D. C. Johnston, and M. Colapietro, Physica C **341–348**, 1719 (2000).
[27] V. V. Eremenko, V. N. Samovarov, V. L. Vakula, M. Yu. Libin, S. A. Uyutnov, and V. M. Rashkovan, Fiz. Nizk. Temp. **27**, 1327 (2001) [Low Temp. Phys. **27**, 981 (2001)].
[28] S. L. Cooper, D. Reznik, A. Kotz, M. A. Karlov, R. Lin, M. V. Klein, W. C. Lee, J. Giapintzakis, D. M. Ginsberg, B. W. Veal, and A. P. Paulikas, Phys. Rev. B **47**, 8233 (1993).
[29] M. J. Holcomb, C. L. Perry, J. P. Collman, and W. A. Little, Phys. Rev. B **53**, 6734 (1996).
[30] E. Dagotto, Rev. Mod. Phys. **66**, 763 (1994).
[31] S. L. Cooper, G. A. Thomas, A. J. Millis, P. E. Sulewski, J. Orenstein, D. H. Rapkine, S-W. Cheong, and P. L. Trevor, Phys. Rev. B **42**, 10785 (1990).
[32] N. Bulut, Turk. J. Phys. **20**, 548 (1996).
[33] F. C. Zhang and T. M. Rice, Phys. Rev. B **37**, 3759 (1988).
[34] Th. Pruschke, M. Jarrell, and I. K. Freericks, Adv. Phys. **44**, 187 (1995).
[35] V. M. Loktev, Fiz. Nizk. Temp. **20**, 173 (1994) [Low Temp. Phys. **20**, 139 (1994)].
[36] J. D. Perkins, R. J. Birgeneau, J. M. Graybeal, M. A. Kastner, and D. S. Kleinberg, Phys. Rev. B **58**, 9390 (1998).
[37] D. Salamon, P. Abbamonte, Ran Liu, M. V. Klein, W. C. Lee, D. M. Ginsberg, I. I. Tartakovskii, and B. W. Veal, Phys. Rev. B **53**, 886 (1996).
[38] J. Lorenzana and G. A. Sawatzky, Phys. Rev. B **52**, 9576 (1995).
[39] D. Reznik, S. L. Cooper, M. V. Klein, W. C. Lee, D. M. Ginsberg, A. A. Maksimov, A. V. Puchkov, I. I. Tartakovskii, and S-W. Cheong, Phys. Rev. B **48**, 7624 (1993).
[40] A. A. Maksimov, D. A. Pronin, S. V. Zaĭtsev, I. I. Tartakovskiĭ, M. V. Klein, and B. W. Veal, Zh. Éksp. Teor. Fiz. **116**, 684 (1999) [JETP **89**, 366 (1999)].
[41] V. V. Sobolev and V. V. Nemoshkalenko, *Electronic Structure of Solids near the Fundamental Absorption Edge* [in Russian], Naukova Dumka, Kiev (1992).
[42] V. D. Okunev and Z. A. Samoĭlenko, Fiz. Tverd. Tela (Leningrad) **33**, 2811 (1991) [Phys. Solid State **33**, 1588 (1991)].
[43] J. M. Tranquada, J. Less-Common Met. **153**, 181 (1989).
[44] A. V. Eremenko, I. S. Kachur, V. G. Piryatinskaya, and V. V. Slavin, Fiz. Nizk. Temp. **18**, 380 (1992) [Low Temp. Phys. **18**, 258 (1992)].
[45] V. L. Aksenov and V. V. Kabanov, Phys. Rev. B **49**, 3524 (1994).
[46] J. B. Goodenough and J. Zhou, Phys. Rev. B **49**, 4251 (1994).
[47] Yu. A. Izyumov, N. M. Plakida, and Yu. N. Skryabin, Usp. Fiz. Nauk **159**, 621 (1989).
[48] A. V. Chubukov and D. M. Frenkel, Phys. Rev. Lett. **74**, 3057 (1995).
[49] M. A. Kastner and R. J. Birgeneau, Rev. Mod. Phys. **70**, 897 (1998).
[50] M. Grüninger, D. van der Marel, A. Damascelli, A. Zibold, H. P. Geserish, A. Erb, M. Klsser, Th. Wolf, T. Nunner, and T. Korr, Physica C **313–318**, 286 (1999).
[51] G. G. Sergeeva, Vopr. At. Nauki Tekh. (Kharkov), No. 6, 375 (2001); G. G. Sergeeva and V. L. Vakula, cond-mat/0207052.

Translated by Steve Torstveit

Low-temperature electric conductivity of $YBa_2Cu_3O_{7-\delta}$ ceramic high-T_c superconductors with different oxygen concentrations

V. A. Finkel[a)]

National Science Center, Kharkov Institute of Physics and Technology, ul. Akademicheskaya 1, 61108 Kharkov, Ukraine

(Submitted February 1, 2002; revised May 7, 2002)
Fiz. Nizk. Temp. **28**, 952–957 (August–September 2002)

The electric conductivity of $YBa_2Cu_3O_{7-\delta}$ ceramic high-T_c superconductors with different oxygen contents ($6.28 \leqslant 7-\delta \leqslant 6.95$) is measured in the temperature range $\sim 20-273$ K. It is shown that the temperature dependence of the resistivity can be described by the relation $\rho = \alpha_0(1+\beta T + e^{\gamma/T})$ at all oxygen concentrations. It is found that in the framework of resonant tunneling theory one can obtain information about the anisotropy of the electric conductivity of HTSCs from the results of experiments performed on polycrystalline samples.
 [DOI: 10.1063/1.1511714]

Research on the kinetic properties of high-temperature superconducting (HTSC) $YBa_2Cu_3O_{7-\delta}$ began immediately after the discovery of the 90 K superconductivity of this compound.[1] In the 15 years that has passed since that time, tens if not hundreds of studies have been devoted to measurements of the electrical conductivity of single-crystal, film, and ceramic samples of $YBa_2Cu_3O_{7-\delta}$. These studies are basically done in two areas.

1. Studies of the influence of so-called weakly bound oxygen in the O4 and O5 positions of the orthorhombic (in the O-I and O-II phases) or tetragonal (in the T phase) crystal lattice of $YBa_2Cu_3O_{7-\delta}$ on the processes of charge transport in the normal state. Studies of this sort are done, as a rule, on ceramic samples (see, e.g., Refs. 2–5).

2. Studies of the anisotropy of the kinetic properties of $YBa_2Cu_3O_{7-\delta}$. These studies are done exclusively on HTSC single crystals (see, e.g., Refs. 6–10).

The results of the research in these two areas are fundamentally different.

1. The data obtained on ceramic samples have led to the establishment of only the general characteristic of the influence of oxygen in the O4 and O5 positions on the electrophysical properties of $YBa_2Cu_3O_{7-\delta}$: an increase in the resistivity ρ and a lowering of the critical temperature of the superconducting transition T_c with decreasing oxygen index $7-\delta$, changes in the form of the function $\rho(T)$ from a linear growth of the resistivity with temperature ($\rho = A + BT$) in the O-I phase with $7-\delta \to 7$ to a ''semiconductor'' trend ($\rho \sim e^{C/T}$) in the nonsuperconducting T phase with $7-\delta \to 6$; the temperature dependence of the resistivity of the intermediate phase O-II is of a transitional character from $\rho = A + BT$ to $\rho \sim e^{C/T}$. The critical temperature T_c of HTSC $YBa_2Cu_3O_{7-\delta}$ decreases with decreasing oxygen index in the O-I phase, depends weakly on $7-\delta$ in the O-II phase, and goes to zero at the boundary between the O-II and T phases.

2. Studies done on $YBa_2Cu_3O_{7-\delta}$ single crystals with a composition close to $YBa_2Cu_3O_7$ have shown that the resistivity ρ_{ab} in the basal plane ab (001) of the orthorhombic lattice decreases in an almost linear manner with decreasing temperature, while the resistivity ρ_c along the principal axis c ($\langle 001 \rangle$) increases. We us point out immediately that because of the morphological features of the growth of $YBa_2Cu_3O_{7-\delta}$ crystals (thin slabs cut by ab planes) it is extremely difficult to make measurements along the c axis, and all of the data have been obtained, to some degree, with the use of the indirect method of Montgomery;[11] the results are often in disagreement as to the character of the dependence $\rho_c(T)$. The results of the few studies that have been done on $YBa_2Cu_3O_{7-\delta}$ single crystals with a reduced oxygen concentration[7,9] indicate that the anisotropy of the resistivity increases with decreasing oxygen index. The results of such studies are extremely important for establishing the nature of high-temperature superconductivity,[12] since analysis of the data on the character of the temperature and concentration dependence of $\rho_c/\rho_{ab}(T, 7-\delta)$ can in principle decide between different models of charge transport in high-T_c superconductors (HTSCs).

It would seem that only the results of electrophysical measurements on single crystals of $YBa_2Cu_3O_{7-\delta}$ could be of fundamental value for establishing the character of the charge transport in different directions of the crystal lattices of HTSCs and settling the question as to the nature of the phenomenon of high-temperature superconductivity. The goal of this paper is to show that measurements of the resistivity of ceramic (polycrystalline) samples can also in a number of case yield useful information about the anisotropy of the conductivity of HTSC crystals for purposes of choosing a realistic model of the charge transport. In this paper we develop further the idea of investigating the anisotropic properties of HTSCs on polycrystalline samples, the possibility of which has been used previously[13–15] for studying the anisotropy of the lower critical fields H_{c1} of HTSC $YBa_2Cu_3O_{7-\delta}$.

In this paper we have carried out the following program of studies:

1) the conductivity of a rather representative series of ceramic samples of HTSC $YBa_2Cu_3O_{7-\delta}$ ($6.28 \leqslant 7-\delta \leqslant 6.95$) has been studied experimentally in the temperature range $\sim 20-273$ K;

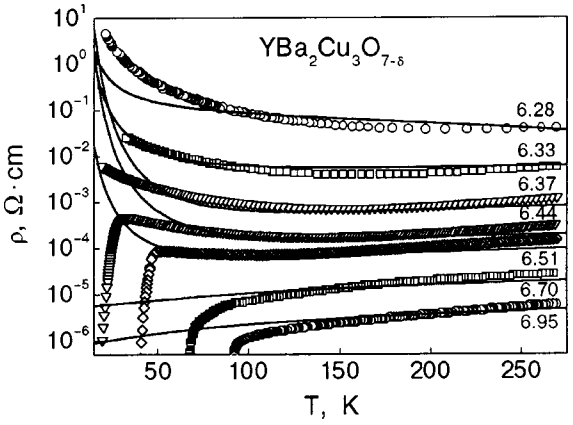

FIG. 1. Temperature dependence of the resistivity of samples of HTSC $YBa_2Cu_3O_{7-\delta}$ with different oxygen content.

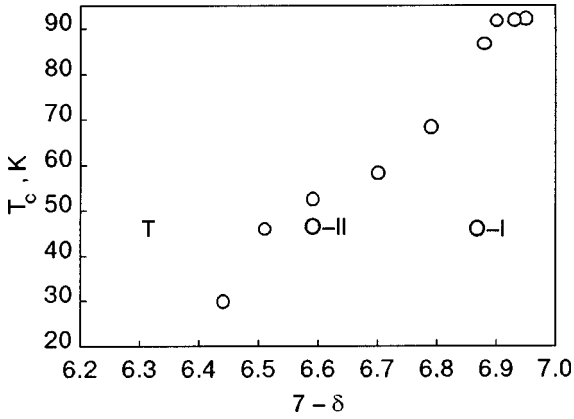

FIG. 2. Plot of T_c versus the oxygen index $(7-\delta)$ for HTSC $YBa_2Cu_3O_{7-\delta}$.

2) a model has been developed for describing the temperature dependence of the resistivity of $YBa_2Cu_3O_{7-\delta}$ in the normal state at all values of the oxygen index $7-\delta$ over a wide range of temperatures;

3) the data obtained are discussed on the basis of the existing theoretical ideas about the charge transport in HTSCs.

Measurements were made on ceramic samples with dimensions of $2\times2\times20$ mm, obtained from a single batch of $YBa_2Cu_3O_{7-\delta}$ powder. The samples were prepared for the measurements by pressing the powder and then sintering in air at 945 °C for 24 h, followed by slow cooling to room temperature. In order to obtain samples with different values of the oxygen index $7-\delta$ the samples were quenched from different temperatures in liquid nitrogen. The oxygen concentration was monitored by gravimetric and x-ray diffraction methods (in the latter case from the values of the lattice parameters).[16]

The resistivity of the $YBa_2Cu_3O_{7-\delta}$ samples was studied on a programmable data acquisition (PDA) unit based on a personal computer.[17] The PDA unit for measuring the temperature dependence of the electrophysical and magnetic properties in the range 10–300 K was based on a Leybold RGD-210 cryogenerator. The temperature sensor was a platinum resistance thermometer.

The results of the effective resistivity measurements on samples with different oxygen concentrations are presented in Fig. 1 (not all of the $\rho(T)$ curves are shown). The character of the evolution of the $\rho(T)$ curves with changing oxygen index is in good agreement with the known T–$(7-\delta)$ diagram of the $YBa_2Cu_3O_{7-\delta}$ system:[18] for $6.7\leqslant 7-\delta \leqslant 6.95$ (the O-I phase) the $\rho(T)$ curves have a practically linear character, for $6.28\leqslant 7-\delta\leqslant 6.37$ (the T phase) the resistivity grows with decreasing temperature, and for $6.44 \leqslant 7-\delta\leqslant 6.59$ (the O-II phase) a combination of the two tendencies is observed. The dependence of T_c on the oxygen index (Fig. 2) is also consistent with the character of the T–$(7-\delta)$ diagram — one observes a sharp drop of T_c with decreasing $7-\delta$ in the existence region of the O-I phase and a tendency for a ''plateau'' to appear in the O-II phase, and, of course, in the T phase superconductivity does not occur.

On the whole the temperature dependence of the resistivity and critical temperatures of HTSC $YBa_2Cu_3O_{7-\delta}$ agree qualitatively with the results of previous studies.[2–5]

To construct a model for describing the temperature dependence of the resistivity of $YBa_2Cu_3O_{7-\delta}$ in the normal state, one should obviously proceed from the fact that the charge transport process at all values of the oxygen index occurs via two different channels: in the ab plane, where the metallic conductivity arises on account of the doping of the CuO_2 planes by holes, and along the c axis (by an activational mechanism; see below). Approximating the real three-dimensional microstructure of a ceramic sample by a one-dimensional chain of series-connected single crystals with $\mathbf{E}\perp\mathbf{c}$ (metallic conductivity) and $\mathbf{E}\|\mathbf{c}$ (activational conductivity), we can write the following model expression for describing the $\rho(T)$ dependence in HTSC $YBa_2Cu_3O_{7-\delta}$ with different concentrations of the weakly bound oxygen over a wide range of temperatures (except the region of fluctuation conductivity near T_c):

$$\rho=\alpha_0(1+\beta T+e^{\gamma/T}), \tag{1}$$

which contains both a linear term responsible for ''metallic'' conductivity in the ab plane and an exponential term responsible for the ''activational'' conductivity along the c axis.[1)] The description of the real microstructure, i.e., the relation of differently oriented crystals in the ceramic, is obviously invested in the factor α_0.

The undeniably approximate expression (1), which does not take into account, in particular, the enhancement of the antiferromagnetic fluctuations with decreasing oxygen index,[19] satisfactorily describes the temperature dependence of the resistivity of the ceramic samples of HTSC $YBa_2Cu_3O_{7-\delta}$ (the solid curves in Fig. 1): outside of the fluctuation region, the experimental points conform well to the calculated curves. The results of a processing of the data obtained are given in Table I.

Thus over a wide range of oxygen concentrations the temperature dependence of the resistivity of HTSC $YBa_2Cu_3O_{7-\delta}$ can be described by a single relation (1) which includes both mechanisms of charge transport — the ''metallic'' and the ''activational.'' We note immediately that in the stability region of the O-I phase $(6.7\leqslant 7-\delta\leqslant 6.95)$ the ''activation'' parameter γ in relation (1) takes on a clearly ''nonphysical'' value: $\gamma<0$. This is apparently because fluctuation effects have not been taken into account.

TABLE I. Coefficients of the equation $\rho=\alpha_0(1+\beta\tau+e^{\gamma/T})$ for the temperature dependence of the resistivity of samples of high-temperature superconducting $YBa_2Cu_3O_{7-\delta}$.

$7-\delta$	T_c, K	α_0, $\Omega\cdot$cm	β, K^{-1}	γ, K
6.95±0.02	92.22±0.05	0.00007±0.0000068	0.01958±0.00215	−105.35±26.35
6.95±0.02	92.16±0.05	0.00009±0.0000069	0.02165±0.00203	−99.81±21.95
6.93±0.02	91.9±0.05	0.00009±0.00002	0.02057±0.00508	−116.88±65.26
6.9±0.02	91.66±0.05	0.00009±0.00004	0.01685±0.00874	−126.55±144.12
6.88±0.02	86.62±0.05	0.00033±0.00024	0.0099±0.00932	−130.25±243.56
6.79±0.02	68.28±0.05	0.00033±0.00024	0.0099±0.00932	−130.25±243.56
6.7±0.02	58.2±0.05	0.00049±0.00008	0.00825±0.00181	−138.94±59.42
6.59±0.02	52.49±0.05	0.00051±0.00002	0.01389±0.00063	−19.142±5.838
6.51±0.02	46.02±0.05	0.00033±0.0000021	0.02768±0.00023	111.80±0.753
6.44±0.02	25.95±0.05	0.00037±0.000006	0.03669±0.00076	171.66±1.76
6.37±0.02	n/a	0.0009±0.00002	0.02661±0.00077	161.39±2.05
6.33±0.02	n/a	0.00421±0.00005	0.00762±0.00022	100.74±0.95
6.28±0.02	n/a	0.03734±0.00047	−0.00459±0.00012	59.21±0.38

The results presented above can be described in terms of the concepts of resonant tunneling as the mechanism of charge transport along the c axis in HTSCs.[12] In essence these ideas reduce to the following: in samples of HTSC $YBa_2Cu_3O_{7-\delta}$ with $7-\delta<7$ the $\ldots$–Cu–O–Cu–$\ldots$ chains along the b axis are broken, but the remaining oxygen atoms can create localized states for electrons and draw them out of the CuO_2 planes; this is what leads to the transport of holes between planes along the c axis. In order for this "resonant tunneling" mechanism to be effective, it is necessary that a potential well with a localized state exist inside the potential barrier, with the well located exactly at the center of the barrier, and that the electron energy be equal to the energy of the bound state in the well. Both conditions are automatically satisfied in the case of $YBa_2Cu_3O_{7-\delta}$, and the $\rho_c(T)$ dependence has an exponential character.[12]

The theory of resonant tunneling gives the following expression for the anisotropy of the resistivity:

$$\frac{\rho_c}{\rho_{ab}}=AT\cosh^2\frac{T_0}{T}, \tag{2}$$

where A is a constant that depends on the electronic interaction parameters ($A\sim v^2$, where v is the velocity at the Fermi boundary) and on the oxygen index $7-\delta$, and T_0 is the characteristic activation energy, which is determined by the energy position of the level via which the resonant tunneling process takes place.

With allowance for the standard equation in crystal physics for the averaged value of a property (described by a tensor of rank two) of crystals of intermediate symmetry, e.g., the resistivity

$$\rho=\frac{2}{3}\rho_{ab}+\frac{1}{3}\rho_c, \tag{3}$$

it follows from relations (1) and (3) that

$$\rho_{ab}=\frac{3}{2}\alpha_0(1+\beta T), \quad \rho_c=3\alpha_0 e^{\gamma/T}. \tag{4}$$

Then

$$\frac{\rho_c}{\rho_{ab}}=2\frac{e^{\gamma/T}}{1+\beta T}, \tag{5}$$

and relation (2) can be rewritten in the form

$$2\frac{e^{\gamma/T}}{1+\beta T}=AT\cosh^2\frac{T_0}{T}. \tag{6}$$

Figure 3 shows the results of a processing by formula (6) of the data obtained for HTSC $YBa_2Cu_3O_{7-\delta}$ samples of different composition. We see that the results of the measurements are approximated fairly well by the equation of the theory of resonance tunneling. Moreover, the temperature de-

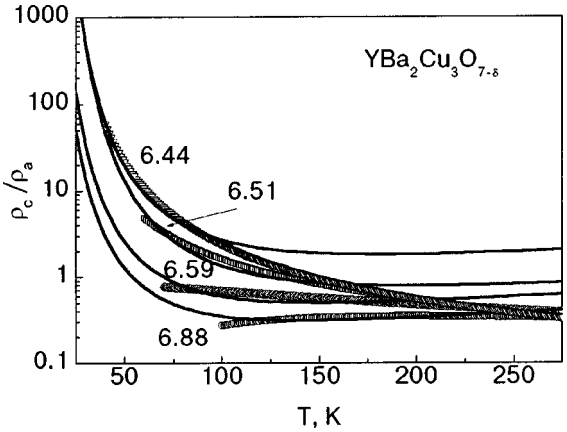

FIG. 3. Temperature dependence of the anisotropy of the resistivity (ρ_c/ρ_{ab}) of HTSC $YBa_2Cu_3O_{7-\delta}$. The "experimental" points on the graph correspond to the left-hand side of Eq. (6), and the solid curves are the results of an approximation of these data in accordance with the right-hand side of that equation.

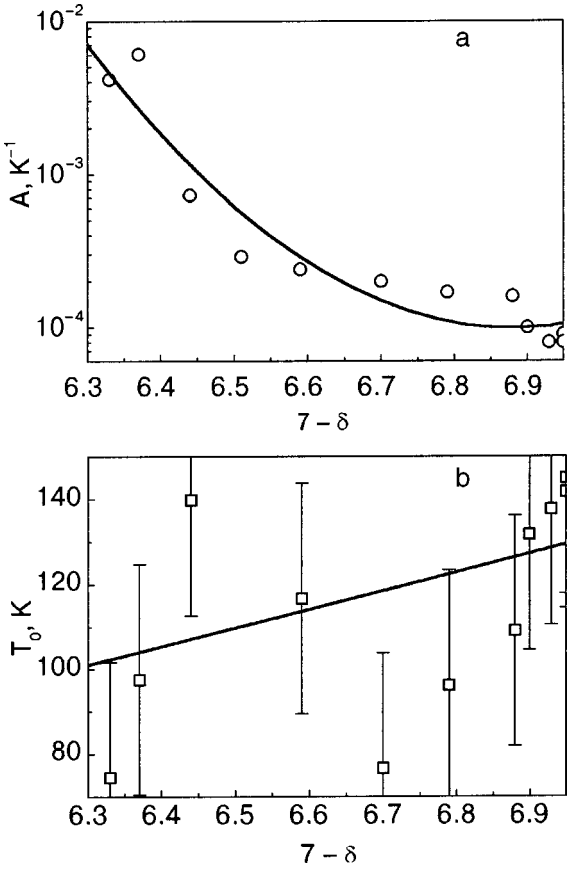

FIG. 4. Concentration dependence of the parameters A (a) and T_0 (b) of the equation $\rho_c/\rho_{ab}=AT\cosh^2(T_0/T)$.

pendence of the anisotropy of the energy $\rho_c/\rho_{ab}(T)$ obtained from measurements on ceramic samples of $YBa_2Cu_3O_{7-\delta}$ are close to the results of direct measurements on single crystals.[9,12]

From a processing of the experimental data we constructed the concentration dependence of the parameters A and T_0 of the theory (Fig. 4). The plots of $A(7-\delta)$ in Fig. 4a and $T_0(7-\delta)$ in Fig. 4b are on the whole reasonable: the constant A, due mainly to the transport of charges (holes) in the . . . –Cu–O–Cu– . . . chains, increases noticeably with decreasing oxygen index (and this agrees with the data showing a decrease in the carrier concentration with decreasing oxygen index[20,21]), while the variation of the activation energy T_0 for the tunneling transport of holes between planes of the CuO_2 chains is relatively small.

Thus in this paper, on the basis of measurements of the temperature dependence of the resistivity of ceramic samples of HTSC $YBa_2Cu_3O_{7-\delta}$ with different oxygen concentrations in the temperature range ~20–273 K, we have established the following:

— the $\rho(T)$ dependence for any content of weakly bound oxygen can be described by an expression containing terms corresponding to the two mechanisms of charge transport;

— on the basis of the results of the measurements on polycrystalline samples one can estimate the value of the resistivity anisotropy $\rho_c/\rho_{ab}(T)$ of a high-T_c superconductor.

We note in conclusion that the technique of studying the anisotropy of the kinetic properties of HTSCs on polycrystalline samples, the possibility of which was demonstrated in this study, is not claimed to be a universal approach, especially as a substitute for measurements on oriented single crystals. However, in a number of cases such a technique might be the only way of estimating the anisotropy of the resistivity of HTSCs.

The author is grateful to A. A. Blinkin, V. V. Derevyanko, and Yu. Yu. Razdovskiĭ for assistance in doing the experiments.

This work was supported by the Science and Technology Center of Ukraine (Project STCU No. 2266).

[a)]E-mail: finkel@kipt.kharkov.ua

[1)]On the assumption that two mechanisms of charge transport operate simultaneously – the so-called "metallic" mechanism in the CuO_2 planes and the "activational" mechanism along the c axis — one can write the resistivity of an untextured polycrystalline object as the normalized sum of the resistivities associated with these two mechanisms: $\rho=\alpha_0(1+\beta T)+\alpha_0' e^{\gamma/T}$. The data sets obtained for $\rho(T)$ were approximated by a minimal (three-parameter) form with $\alpha=\alpha_0'$, i.e., relation (1).

[1] C. W. Chu, P. H. Hor, R. L. Meng, L. Gao, Z. J. Huang, and Y. Q. Wang, Phys. Rev. Lett. **58**, 405 (1987).
[2] J. R. Cooper, S. D. Obertelli, A. Carrington, and J. W. Loram, Phys. Rev. B **44**, 12 086 (1991).
[3] L. Sun, Y. Wang, H. Shen, and X. Cheng, Phys. Rev. B **38**, 5114 (1988).
[4] S. Zhu, X. Zhang, Z. Xu, H. Wang, and H. Xia, Phys. Lett. **6**, 185 (1989).
[5] V. M. Arzhavitin, A. A. Blinkin, V. V. Derevyanko, Yu. Yu. Razdovskiĭ, A. G. Rudenko, V. A. Finkel', and Yu. N. Shakhov, Sverkhprovodimost' (KIAE) **6**, 2095 (1993).
[6] S. W. Tozer, A. W. Kleinsasser, T. Penny, D. Kaiser, and F. Holtzberg, Phys. Rev. Lett. **59**, 1768 (1987).
[7] Y. Iye, T. Tamegai, T. Sakakibara, T. Goto, N. Miura, H. Takeya, and H. Takei, Physica C **153–155**, 26 (1988).
[8] M. A. Obolenskiĭ, A. V. Bondarenko, V. I. Beletskiĭ, V. N. Morgun, V. P. Popov, N. N. Chebotaev, A. S. Panfilov, A. I. Smirnov, O. A. Mironov, S. V. Chistyakov, and I. Yu. Skrylev, Fiz. Nizk. Temp. **16**, 1103 (1990) [Sov. J. Low Temp. Phys. **16**, 639, (1990).
[9] V. N. Zverev and D. B. Shovkun, JETP Lett. **72**, 73 (2000).
[10] T. Ito, K. Takenaka, and S. Uchida, Phys. Rev. Lett. **70**, 3995 (1993).
[11] H. C. Montgomery, J. Appl. Phys. **42**, 2971 (1971).
[12] A. A. Abrikosov, Usp. Fiz. Nauk **186**, 683 (1998).
[13] V. A. Finkel' and V. V. Toryanik, Fiz. Nizk. Temp. **23**, 824 (1997) [Low Temp. Phys. **23**, 618 (1997)].
[14] V. A. Finkel', Fiz. Nizk. Temp. **25**, 554 (1999) [Low Temp. Phys. **25**, 410 (1999)].
[15] V. A. Finkel' and V. V. Derevyanko, Fiz. Nizk. Temp. **26**, 128 (2000) [Low Temp. Phys. **26**, 92 (2000)].
[16] V. A. Finkel, V. M. Arzhavitin, A. A. Blinkin, V. V. Derevyanko, and Yu. Yu. Razdovskii, Physica C **235–240**, 303 (1994).
[17] V. V. Toryanik, V. A. Finkel', and V. V. Derevyanko, Fiz. Khim. Obrabot. Mater., No. 5, 55 (1995).
[18] E. Bonetti, E. G. Campari, and S. Mantovari, Physica C **196**, 7 (1992).
[19] B. P. Stojcovic and D. Pines, Phys. Rev. B **55**, 8576 (1997).
[20] V. V. Eremenko, V. N. Samovarov, V. N. Svishchev, V. L. Vakula, M. Yu. Libin, and S. A. Uyutnov, Fiz. Nizk. Temp. **26**, 739 (2000) [Low Temp. Phys. **26**, 541 (2000)].
[21] V. V. Eremenko, V. N. Samovarov, V. L. Vakula, M. Yu. Libin, and S. A. Uyutnov, Fiz. Nizk. Temp. **26**, 1091 (2000) [Low Temp. Phys. **26**, 809 (2000)].

Translated by Steve Torstveit

Metallic properties of lead dioxide. Band structure and NMR of ^{207}Pb at low temperatures

L. A. Boyarskiĭ* and S. P. Gabuda

Institute of Inorganic Chemistry, Siberian Branch of the Russian Academy of Sciences, pr. Akad. Lavrent'eva 3, 630090 Novosibirsk, Russia; Novosibirsk State University, ul. Pirogova 2, 630090 Novosibirsk, Russia

S. G. Kozlova

Institute of Inorganic Chemistry, Siberian Branch of the Russian Academy of Sciences, pr. Akad. Lavrent'eva 3, 630090 Novosibirsk, Russia

R. N. Pletnev

Institute of Solid State Chemistry, Urals Branch of the Russian Academy of Sciences, ul. Pervomaĭskaya 91, 620219 Ekaterinburg, Russia

(Submitted January 2, 2002)
Fiz. Nizk. Temp. **28**, 958–962 (August–September 2002)

The local magnetic fields at the ^{207}Pb nuclei in lead dioxide with the rutile structure (β-PbO_2) are measured by the NMR method at temperatures down to 20 K. It is shown that the values of the local fields and the character of their temperature dependence correspond to the Knight mechanism for the shifts of the NMR spectra in metals. The band structure of this compound is calculated with allowance for relativistic corrections. A conjecture is made as to the nature of the metallic conductivity of this oxide on the basis of the results obtained. [DOI: 10.1063/1.1511715]

INTRODUCTION

This paper is devoted to basic research on the properties of strongly correlated electron systems. The problems of strongly correlated electron systems are related to a number of extremely important problems in modern low-temperature condensed-matter physics, such as, for example, the mechanism of high-temperature superconductivity, the properties of matter containing heavy fermions, and new materials of the fullerene class.

Of particular interest are the different nonuniform states of the electron subsystem in such substances as high-T_c superconductors, perovskite crystals, and oxides of heavy and transition metals. The various manifestations of such states have been widely discussed in the literature in recent years: the appearance of a pseudogap phase in HTSCs, antiferromagnetic correlations in the underdoped cuprates, ladder-type charge structures in oxides doped with alkali metals, etc.

However, it would be well to list the questions that still remain unanswered in spite of their importance for the construction of a general theory of strongly correlated electron systems. These are the nature of the formation of the pseudogap phase in HTSCs, the structure of antiferromagnetic formations in underdoped HTSCs, and the mechanism giving rise to nonuniform spin and charge states in substances which are in some sense model materials (for the problem of high-temperature superconductivity): oxides of heavy and transition metals. A number of questions of a more general nature also arise. For example, why are oxides of related metals in some cases metals and in others insulators? Why, within the limits of the same class of substances, does the stoichiometric composition of one substance (niobium stannide) correspond to a deep minimum of the potential energy while for another substance (niobium germanide) it is possible to achieve total correspondence of the synthesized material to the stoichiometric formula only in the presence of an aluminum dopant? These results were obtained back in the early 1970s, including the use of shock-wave synthesis. The mechanism of formation of a number of compounds having close to the stoichiometric composition was proposed by Khomskii[1] (the so-called internal autodoping mechanism), but there is no clear answer to the question of why such a mechanism is operative in some cases and in others not.

The search for a solution to the problems listed requires a comprehensive approach both to the choice of objects of study and the selection of the optimal techniques. However, in one article we have space for only one particular problem: we shall focus our attention on the properties of oxides. It is known that the dioxides of a number of transition metals (VO_2, NbO_2, MoO_2, WO_2, TcO_2, ReO_2) are characterized by metallic properties.[2–8] In accordance with the model of Ref. 1, the high conductivity of those compounds is to a certain extent due to the partial contribution of the $2p$ electrons of O^{2-} to the density of states at the Fermi level. It is also known that a metal–insulator phase transition is observed with decreasing temperature in transition metal oxides; this transition is accompanied by distortion of the crystal lattice and the onset of a nonuniform cation charge density distribution.[9]

It is known that, of the higher oxides of p elements, only the oxides of the p elements of group VI of the periodic table

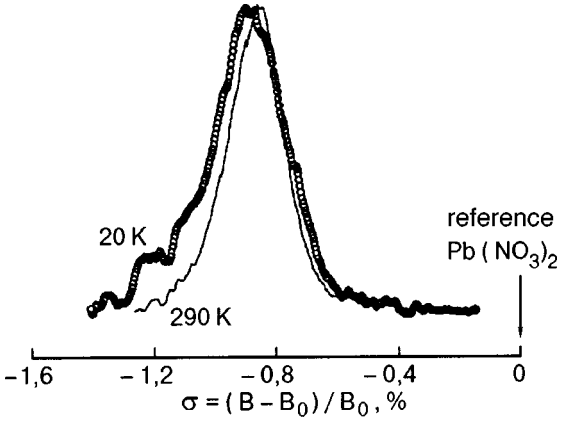

FIG. 1. NMR spectra of ^{207}Pb in PbO_2 at different temperatures.

(Tl, Pb, Bi), including lead dioxide PbO_2 (plattnerite), have the potential to be metals (or semimetals). As indirect evidence of their metallic nature one can cite the characteristic brownish-black color of these oxides, their tendency to form nonstoichiometric compounds, and the ease with which oxygen is detached from them. However, data on the band structure and on the low-temperature electronic properties of plattnerite have not been obtained before now. In this paper we present the results of an analysis of the electronic properties of PbO_2 on the basis of the measurements of the NMR shifts of ^{207}Pb at low temperatures and also the data of a band structure calculation for β-PbO_2.

EXPERIMENT

The polycrystalline samples of PbO_2 for the measurements were synthesized by two different methods: oxidation of lead monoxide PbO (ChDA grade) by hypochlorite or by the reaction of minium Pb_3O_4 (KhCh grade) with concentrated nitric acid. The fine-crystalline samples were brownish-black in color and according to x-ray phase analysis corresponded to β-PbO_2 with the rutile structure (plattnerite); no impurity phases were detected.

The β-PbO_2 samples are characterized by a relatively high electrical conductivity. To increase the Q factor of the rf circuit for making the radio spectroscopic measurements, the samples were flooded with melted paraffin, which greatly reduced the electrical contacts between crystallites. It should be noted that the parameters of the samples studied did not depend substantially on the method of synthesis. Preliminary results of a study of the NMR spectra were published previously.[10] It was found that there is a nonuniform distribution of oxygen-ion vacancies in the samples, which leads to the presence of a number of oxides with a composition close to the stoichiometric dioxide but not equal to it.

The NMR spectra of ^{207}Pb were recorded on a Bruker spectrometer with a superconducting solenoid at temperatures of 290 and 20 K in a field $B_0=9.1$ T. Each spectrum was a sum of 15 subspectra obtained at equally spaced frequencies (with a step of 80 kHz). Each of the the subspectra is the Fourier transform of the spin echo half signal. The time delay between the two pulses forming the echo signal was 35 μs, the number of integrations was 20000, and the repetition time of the train was 10 ms. Typical NMR spectra of ^{207}Pb in β-PbO_2 are presented in Fig. 1.

As can be seen in Fig. 1, the NMR spectra of ^{207}Pb in β-PbO_2 are shifted to lower magnetic fields B relative to the field value B_0 at which the NMR signal of ^{207}Pb is observed in solid lead nitrate $Pb(NO_3)_2$, which was chosen as a reference standard. The value of the shift $(B-B_0)$ corresponds to a certain additional magnetic field induced at the ^{207}Pb nuclei in the sample under study. The local magnetic field varies in proportion to the applied external field B, and it can therefore be characterized by the value of the relative shift of the peak of the NMR signal: $\sigma=(B-B_0)/B_0$. As a result of the measurements of the NMR spectra we obtained the values $\sigma=-(0.850\pm0.002)\%$ at 290 K, and $\sigma=-(0.904\pm0.002)\%$ at 20 K. We note that the calculated values of the shifts σ for β-PbO_2 are clearly found outside the limits of the scale of chemical shifts of the NMR spectra of ^{207}Pb for the Pb^{4+} ions in lead (IV) compounds, including the insulating oxides Pb_3O_4 ($\sigma=-0.240\%$), Ba_2PbO_4 ($\sigma=-0.215\%$), and Sr_2PbO_4 ($\sigma=-0.235\%$), for which, besides, no temperature dependence of the shifts σ has been observed outside the measurement error.[11,12]

On the other hand, the values of σ obtained for β-PbO_2 are close to the value $\sigma=-0.82\%$ measured previously for the metallic perovskite $BaPbO_3$ and also to the value $\sigma=-1.345\%$ (at 100 K) measured for the perovskitelike superconductor $Ba(Pb_{0.85},Bi_{0.15})O_3$, with a superconducting transition temperature of $T_c=7$ K.[13] Thus, judging from the value of the shifts, the binary dioxide of lead β-PbO_2 also belongs to the class of oxides with pronounced metallic properties, for which the formation of induced local magnetic fields and the resulting shifts of the NMR spectra are due to the Knight mechanism.[13,14] Particular attention should be paid to the pronounced temperature dependence of the Knight shift in β-PbO_2, which is apparently due to the characteristic growth of the conductivity with decreasing temperature in metals.

BAND STRUCTURE CALCULATIONS

The band structure calculation for β-PbO_2 was done using the software ADF-Band (Scientific Computing and Modelling, Vrije University, The Netherlands), based on the use of the density-functional theory.[12,15] The exchange and correlation interactions in the calculations were approximated by the VWN functional proposed in Ref. 16. Relativistic effects (the scalar and spin–orbit interactions) were taken into account in the zero-order regular approximation (ZORA).[17] As the basis wave functions we used Slater-type orbitals (relativistic and nonrelativistic): the Pb atom was represented by the $5d$, $6s$, $6p$, and $6d$ orbitals, and the O atom by the $2s$ and $2p$ orbitals.

The calculations in which the nonrelativistic orbitals were used gave a band structure typical of an insulator, with a band gap of 2.72 eV. When the relativistic corrections were taken into account (in the ZORA) the Fermi level turned out to be located inside the filled band formed mainly by the $2p$ states of O^{2-} (Fig. 2). Here the density of states at the Fermi

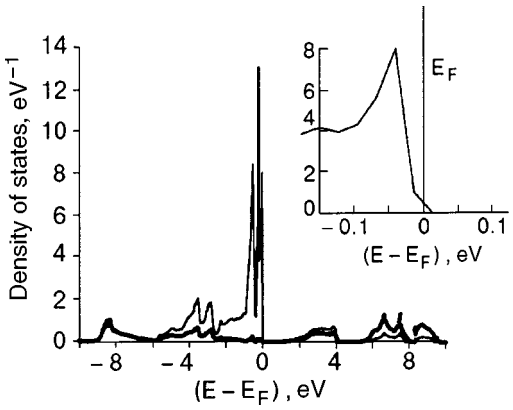

FIG. 2. Partial density of states in PbO_2 (per formula unit): the heavy line is for Pb ($5d$, $6s$, $6p$); the fine line is for O ($2s$, $2p$). Inset: The density of states of PbO_2 near the Fermi energy.

level, which is responsible for the appearance of the Knight shift, is created mainly by the $2p$ states of the O^{2-} anions, in complete agreement with the model of Ref. 1. Thus the results of a band structure calculation for plattnerite can be reconciled with the measured shifts of the NMR spectra of ^{207}Pb only when relativistic corrections are taken into account in the zeroth approximation).

Analysis of the results can clarify the physical mechanism for the appearance of metallic properties in PbO_2 on account of the relativistic corrections. The main contribution is from relativistic effects that lower the energy of the $6s$ state of the Pb^{4+} ion (by 2.93 eV) and raise the energy of the levels of the spin–orbit doublet of the $5d$ states: by 2.33 eV for $5d_{3/2}$ and by 5.14 eV for $5d_{5/2}$. Consequently, the relativistic corrections lead to a decrease (by 8 eV) of the splitting between the filled $5d^{10}$ state of the Pb^{4+} ions and the nearest unfilled $6s$ state of this ion. As a result, a weak overlap of the $5d$ and $6s$ bands arises in the PbO_2 crystal, making the mechanism for the appearance of metallic properties in this system (characterized by an even number of electrons in the unit cell) close to the mechanism for the appearance of such properties in the alkaline-earth metals.

CONCLUSION

Turning to the experimental results, we note that the large value of the NMR shift of ^{207}Pb in PbO_2 and its substantial temperature dependence can apparently be explained in terms of a model of strong electron–nuclear coupling of the ^{207}Pb nuclei with the conduction electrons in compounds with a metallic character of the bonding,[14,18] a fact which confirms the results of the band structure calculation for PbO_2. The values found for the shifts are comparable in order of magnitude with the Knight shifts of the NMR of ^{207}Pb in metallic lead:[19] $\sigma_K = -1.465\%$ (290 K) and $\sigma_K = -1.400\%$ (extrapolation of the data obtained in Refs. 19 to 20 K). We note that the metallic lead and lead dioxide PbO_2 are characterized by opposite signs of the coefficients of the temperature dependence of their Knight shifts: in Pb the Knight shift decreases with decreasing temperature, while in PbO_2 it increases. The difference in the character of the temperature dependence of the Knight shifts of Pb and PbO_2 is explained by the presence of two terms of opposite sign in them.[18,20,21] The first of these terms is the direct contact contribution due to the Fermi electrons in the s states. The second (polarization) contribution is due to the exchange interaction of the electrons of the unfilled p shells with the electrons of the inner (filled) s shells and their partial polarization, which gives rise to an additional hyperfine contact field at the nucleus (with the opposite sign).

We note that in the case of PbO_2 the polarization contribution can be neglected in a rough approximation, since the Pb^{4+} and O^{2-} ions are characterized by closed shells, and the observed Knight shift is determined by the contact interaction of the ^{207}Pb nuclei with the conduction electrons and by the nonzero density of $2p$ states of the O^{2-} ions at Fermi level. In this case the increase of the Knight shift of the NMR of ^{207}Pb in PbO_2 at low temperatures can be attributed to a decrease in the Pb-O distances and to an increase in the direct contact contribution of the $2p$ electrons of oxygen to the density of states at the Fermi level, in agreement with the band calculations and the model of Ref. 1. On the other hand, for metallic lead, with its unfilled $6p$ shells, it is necessary to take into account both the contact and the polarization contributions, which are characterized by extremely complicated temperature dependences,[20,21] the calculation of which is an independent problem.

As to the nature of the metallic conduction in lead dioxide, it is apparently appropos to make the following observations. Back in the 1960s, in developing a theory of itinerant magnetism of metals, J. Friedel introduced the concept of virtual levels arising in the conduction band in a fluctuational manner.[22] The features of the band structure, like the nonuniform distribution of the charge density in the material, make it quite probable for such levels to arise in the unoccupied conduction band of lead dioxide. The resonant smearing of the levels into a narrow band makes for an additional conductivity in the case of a normal metal (for lead dioxide, however, this would be the main contribution). We also note that analysis of the experimental data permits the conclusion that not only the $6p$ but also the $5d$ electrons from the filled shell of lead can take part in the formation of the virtual electronic levels. Fluctuation effects of similar sort are not infrequently encountered in nature. For example, we might mention the existence of fluctuating antiferromagnetic correlations in underdoped high-T_c superconductors.[23,24] Although that effect pertains to a different area of condensed matter physics, the commonality of the mechanisms cannot be doubted.

The authors are grateful to S. V. Verkhovskiĭ and A. I. Pogudin for assistance in making the measurements. One of the authors (L. A. B.) wishes to express his deep gratitude to Viktor Valentinovich Eremenko for his steadfast and well-meaning interest in our research.

The study was done with the support of the FAP ''Integration'' (Grant 274), the ''Universities of Russia'' program (Grant 1785), and the Russian Federation (Grant 99-03-32477).

*E-mail: boy@casper.che.nsk.su

[1] D. Khomskii, cond-mat/ 0101164 (2001).
[2] V. Eyert, cond-mat/0106137 (2001).
[3] D. Adler, Rev. Mod. Phys. **40**, 714 (1968).
[4] J. B. Goodenough, in *Progress in Solid State Chemistry*, edited by H. Reiss, Pergamon Press, Oxford (1971), p. 145.
[5] A. Zylbersztejn and N. F. Mott, Phys. Rev. B **11**, 4383 (1975).
[6] R. M. Wentzcovitch, W. W. Schulz, and P. B. Allen, Phys. Rev. Lett. **72**, 3389 (1994); *ibid.* **73**, 3043 (1994).
[7] T. M. Rice, H. Launois, and J. P. Pouget, Phys. Rev. Lett. **73**, 3042 (1994).
[8] M. Imeda, A. Fujimori, and Y. Tokura, Rev. Mod. Phys. **70**, 1039 (1998).
[9] L. A. Boyarskiĭ, S. P. Gabuda, and S. G. Kozlova, Fiz. Nizk. Temp. **26**, 197 (2000) [Low Temp. Phys. **26**, 147 (2000)].
[10] L. A. Boyarskiĭ, S. V. Verkhovskiĭ, S. P. Gabuda, S. G. Kozlova, and I. V. Postnov, Élektronnyĭ Zhurnal ''Issledovano v Rossii'' 599 (2001); http://zhurnal.ape.relarn.ru/articles/2001/053.pdf.
[11] S. P. Gabuda, S. G. Kozlova, V. V. Terskikh, C. Dubovski, G. Neue, and D. L. Perry, Solid State NMR **15**, 103 (1999).
[12] C. G. Kozlova, *Correlation and Exchange Interactions in Heavy-Metal Oxides and Fluorides (NMR and Quantum-Chemical Calculations)* [in Russian], Doctoral Thesis, Novosibirsk (2001).
[13] N. F. Benschop, Physica C **235–240**, 2527 (1994).
[14] C. P. Slichter, *Principles of Magnetic Resonance*, 3rd ed., Springer-Verlag, Berlin (1990), Mir, Moscow (1981).
[15] Amsterdam Density Functional (ADF) Program, Release 2000.02; Vrije Universteit, Amsterdam, The Netherlands (2000).
[16] S. H. Vosko, L. Wilk, and M. Nusair, Can. J. Phys. **58**, 1200 (1980).
[17] C. Chang, M. Pelissier, and P. Durand, Phys. Scr. **34**, 394 (1986); J. L. Heully, I. Lindgren, E. Lindroth, S. Lundqvist, and A. M. Martensson-Pendril, J. Phys. B **19**, 2799 (1986).
[18] S. P. Gabuda and R. N. Pletnev, *Applications of NMR in Solid State Chemistry* [in Russian], Izd. Ekaterinburg, Ekaterinburg (1996).
[19] G. Neue, C. Dybovski, M. L. Smith, M. A. Hepp, and D. L. Perry, Solid State Nucl. Magn. Reson. **6**, 241 (1996).
[20] W. E. Pickett, K. M. Ho, and M. L. Kohen Phys. Rev. B **19**, 1734 (1979).
[21] L. R. Testordi and L. F. Mattheiss, Phys. Rev. Lett. **41**, 1612 (1978).
[22] J. Friedel, G. Leman, and S. Olzewski, J. Appl. Phys. **32**, 325S (1961) [Russian translation in *Theory of Ferromagnetism of Metals and Alloys*, Izd. Inostr. Lit., Moscow (1963), p. 283].
[23] J. Rossat-Mignod, L. P. Regnault, C. Vettier, P. Bourges, P. Burlet, J. Bossy, J. Y. Henry, and G. Lapertot, Physica C **185–189**, 86 (1991).
[24] E. B. Amitin, A. G. Blinov, L. A. Boyarsky, V. Ya. Dikovsky, K. R. Zhdanjv, M. Yu. Kameneva, O. M. Kochergin, V. N. Naumov, and G. I. Frolova, Phys. Rev. B **51**, 15388 (1995)

Translated by Steve Torstveit

DEFECTS IN CRYSTALS

Instability zones and short-lived defects in the physics of crystals

V. M. Koshkin*

Kharkov Polytechnical Institute National Engineering University, ul. Frunze 21, 61002 Kharkov, Ukraine
(Submitted February 1, 2002)
Fiz. Nizk. Temp. **28**, 963–977 (August–September 2002)

A review is given of the role played in the problems of solid-state physics by the various manifestations of instability zones for interacting defects and the presence of equilibrium and radiation-induced unstable vacancy–interstitial-atom pairs. The unstable pairs determine the features of the diffusion process and of a number of thermal properties of metals, semiconductors, and insulators, including superionic crystals, and also determine the radiation stability of solids. © *2002 American Institute of Physics.* [DOI: 10.1063/1.1511716]

1. INTRODUCTION

This article presents a review of various processes in the physics of crystals from the standpoint of a model of short-lived unstable defect pairs consisting of a vacancy and interstitial atom. These processes result from the presence of zones of absolute instability of the interacting defects and, in turn, govern many of the equilibrium and radiation properties of metals, insulators, and semiconductors.

Equilibrium unstable pairs (UPs) are manifested mainly at temperatures quite close to the melting point but, generally speaking, can be observed at any temperatures.

The kinetics of the accumulation and healing of radiation defects, especially in pure substances, is governed by the instability zones (IZs), in particular, in low-temperature irradiation by low-energy particles, with energies only slightly above the Seitz threshold. In this paper we discuss the origin of the IZs and their role in the thermodynamics of the UPs, which are a third type of equilibrium defect in crystals, in addition to Schottky defects (SDs) and Frenkel pairs (FPs). Equilibrium UPs, together with SDs and FPs, determine the thermal properties and diffusion in solids. We consider the role of IZs in the accumulation of nonequilibrium (radiation-induced) defects. In particular, a crystallographic criterion of radiation stability is presented, along with a large number of experimental data for materials with extremely high radiation stability. The technical applications of radiation-stable metals, insulators, and semiconductors are discussed.

2. INTERACTING DEFECTS: ZONES OF ABSOLUTE RECOMBINATION AND ABSOLUTE SQUEEZING

2.1. The classic paper by Gibson, Goland, Milgram and Vineyard,[1] in which the methods of molecular dynamics were first applied to the study of radiation phenomena in metals, revealed an unusual phenomenon. It was found that if an interstitial atom i is located in the vicinity of a vacancy v, then i recombines with v without activation at any arbitrarily low temperature. In Ref. 1 these regions around v were called zones of spontaneous recombination or zones of instability of i with respect to v. The possibility of such an instability of defects was predicted by Frenkel some twenty years before, in 1943, but only by a single phrase in his famous book.[2] After the publication of Ref. 1 many authors reported both experiments and computer simulations confirming the existence of recombination instability zones (RIZs) in metals, semiconductors, and insulators, which appear during irradiation by high-energy particles. The characteristic radii of the IZs range from a few angstroms to tens of angstroms (see Refs. 3–5). The cause of these zones of absolute instability was elucidated in Refs. 3 and 6 and is as follows. The periodic potential of the lattice for an interstitial atom has an amplitude U_m which is the activation energy for the migration of i. Low-temperature experiments show that in the majority of crystals of the most diverse natures the values of U_m for an intrinsic i is of the order of 10^{-1}–10^{-2} eV, e.g., in copper it is 0.05 ± 0.02 eV, in germanium 0.02 ± 0.02 eV, in KBr and KCl from 0.03 0.06 eV for charged i to 0.1 eV for neutral i (see Refs. 3 and 5).

Vacancies are considerably less mobile, and the activation energies for their displacements are >1 eV in the majority of crystals. Now let i and v interact with each other, and superpose their interaction potential on the periodic migration potential of interstitials. It is easy to show that nearest energy minimum for an interstitial atom to a vacancy is found, generally speaking, not in the nearest interstitial position to v but far away from it: the interaction potential ''cuts off'' the nearest extrema up to a distance r_0 from v. In this region there are no extrema, and the interstitial atom (or ion) ''slides down'' toward the vacancy in an activationless manner. This is a recombination instability zone.

In the case of a Coulomb interaction

$$r_0^{\mathrm{es}}=\alpha(q_i q_v a/\varepsilon U_m)^{1/2}, \tag{1}$$

where q_i and q_v are the charges of i and v, a is the interatomic distance, ε is the dielectric constant, and α is a factor of order unity which depends on the choice of the periodic potential.

A Coulomb IZ arises in insulators and semiconductors but not in metals, where the electrostatic interaction is

screened and only an elastic interaction, with a potential $U_{iv}=G\Delta V_i\Delta V_v/r^3$, is possible.[7] The radius of the IZ in that case is

$$r_0^{\rm el}=\alpha^{1/2}(3G\Delta V_i\Delta V_v a/U_m)^{1/4}, \tag{2}$$

where G is the shear modulus, and ΔV_i and ΔV_v are the changes in the volume of the crystal upon the introduction of an isolated i or v. Interstitial atoms always expand the lattice, and vacancies almost always draw the matrix in toward them. The different signs of the displacements near the defects creates their attraction.

We should emphasize that while Eq. (1) is suitable for quantitative calculations, Eq. (2) is only good for estimates unless the radii of the elastic IZs are not more than 2–3 interatomic distances, but in most metals the IZs are larger than that.

Calculations according to Eqs. (1) and (2) describe the experimental data on IZs quite well.[3,5] Of course, everything is determined by small quantities—the migration energies of interstitial atoms or ions.

Let us estimate the lifetime of an ion found at the boundary of an IZ of radius $r_0^{\rm es}$ in the presence of a Coulomb $i-v$ interaction.[3,8] The time required for i to return to its site is easily determined from the difference of the Coulomb potentials at the point r and in the initial position $r_0^{\rm es}$, knowing the charges ($q_i=q_v$) and the mass M of the the ion, if it is assumed that within the IZ the ion moves as a free particle ($W(r)$ is the velocity of the particle):

$$\mathcal{T}=\int_{r_0}^{0}W^{-1}(r)dr=\frac{\pi}{2\sqrt{2}}\frac{\sqrt{M}}{q}r_0^{3/2}. \tag{3}$$

Estimates according to Eq. (3) for $r=20$ Å and a mass of 60 amu give $\sim 10^{-11}$ s, which is only one or two orders of magnitude greater than the characteristic time for lattice vibrations. The calculations by Oksengendler[9] with allowance for the scattering of the moving particle on atoms inside the IZ give practically the same estimate for the lifetime of i.

2.2. The interaction of any defects will give rise to IZs. It should be noted that in the presence of repulsion between defects a zone of absolute squeezing (SIZ) arises in which, as in an RIZ, a mobile defect cannot be localized.[10,11] Of course, expressions (1) and (2) also describe SIZs around defects.

Instability zones also arise around dislocations. They, of course, have a cylindrical shape.

In the case of charged dislocations D and defects d one has

$$r_{Dd}^{\rm es}=\alpha^2(2e^2a\sigma/\varepsilon U_m), \tag{4}$$

where e is the charge of an electron and $e\sigma$ is the linear charge density at the dislocation. In the case of an elastic interaction of D and d a somewhat more awkward expression is obtained.[3,12]

Instability zones also arise in the interaction of dislocations with each other, only instead of the energies of migration of i the relevant quantity is the height of the Peierls barrier, which for plastic solids, metals and many ionic crystals, is of the order of 0.05–0.1 eV.[3]

Estimates show that IZs around dislocations can extend for several tens of angstroms, and so the formulas can be used for quantitative calculations.

Below we shall trace the role of IZs in the physics of crystals.

3. THERMODYNAMICS OF UNSTABLE PAIRS AND THEIR PLACE AMONG OTHER EQUILIBRIUM DEFECTS

3.1. In spite of their very short lifetimes, there exists an equilibrium concentration of $v-i$ pairs. If a thermally excited atom does not leave the RIZ of its vacancy, then it will return to its place in an activationless manner within its lifetime. The birth event of an UP is the same as for a Frenkel pair (FP), but, unlike the latter, when the v and i that are created become independent, in an UP the interstitial recombines with the same vacancy with which it is corrected by birth. The UPs die at the same point where they were born. Therefore, unlike the free energy of equilibrium FPs, in the partition function of a system with UPs it is necessary to take into account this strict correlation, viz: the number of states f of the interstitial in the IZ.[3,8,13] In the zeroth approximation at low temperature (i.e., for a small concentration of equilibrium defects) and small RIZs, the concentration of Frenkel defects and UPs are independent and are expressed as

$$C_{PF}=\beta^{1/2}\exp(-E_{PF}/2kT), \tag{5}$$

$$C_{UP}=f\exp(-E_{UP}/kT), \tag{6}$$

respectively, where E_{PF} and E_{UP} are the energies of formation of a Frenkel pair and an unstable pair, and β is the ratio of the number of lattice sites to the number of interstitial positions.

In the next approximation[3,8] it becomes obvious that FPs and UPs compete, and for large IZs the UPs prevail, provided, of course, that E_{UP} is not too much larger than E_{PF}:

$$C_{PF}=\beta^{1/2}[1-f\exp(-E_{UP}/kT)]\exp(-E_{PF}/2kT). \tag{7}$$

The energy of formation of an equilibrium FP is equal to the sum of the energies of formation of the independent i and v. The energy of formation of an unstable pair is the sum of the same energies, but in view of the short distances between the interstitial atom and vacancy in an unstable pair, it is smaller by the amount of the interaction energy between them. Estimates of the lifetime of a UP (3) show that the relaxation of the lattice occurs before recombination, and one can therefore introduce an average energy of formation E_{UP}. In the case of the Coulomb interaction one has $E_{UP}=E_{PF}-e^2/\varepsilon r_{iv}$ (r_{iv} is the average $i-v$ distance in the UP).

Then the concentration ratio is

$$\frac{C_{UP}}{C_{PF}}=f\exp\left[\frac{1}{2kT}\left(\frac{2e^2}{r_{iv}}-E_{PF}\right)\right]. \tag{8}$$

Estimates show that for sufficiently large RIZs the competition of FPs and UPs is won by the latter. It is this third type of defect (additional to Schottky and Frenkel defects) that turns out to be the predominant type of equilibrium defect in many crystals at high temperatures, where by "high" temperatures we mean temperatures not very far from the melting point of the substance. This can be a temperature of the order of a thousand (e.g., for copper or silicon) or tens of

kelvins (for frozen gases). A computer model for the investigating thermal excitations in metals, which was created recently by Nordlund and Averbak,[14] showed that UPs are in fact significant in copper at premelting temperatures.

3.2. What place do UPs occupy among the other equilibrium lattice defects (see Refs. 3, 4, and 7)? The lowest-energy defect is a lattice vibration: the excited atom executes small harmonic vibrations about its site. At a larger amplitude the vibration becomes anharmonic. When a very high energy is localized in the vicinity of a given site on account of fluctuations, the atom can go out to a distance of the order of the interatomic distance or more. If the atom remains within the RIZ and returns to the vacancy that it has left, then this excitation is similar to a vibration about the site, but its amplitude is so large that it would be senseless to describe the motion of such an interstitial atom in terms of an anharmonic correction. If the energy of the local excitation exceeds the threshold for formation of an unstable pair but is less than that necessary to leave the boundaries of the RIZ and form a Frenkel pair with independent i and v, then a short-lived unstable pair arises. Thus the UP is a special type of lattice defect intermediate between a harmonic vibration and the Frenkel pair.

Below we discuss the consequences of the presence of unstable pairs and the experimental data confirming their determining role in many equilibrium properties of crystals.

4. EQUILIBRIUM UNSTABLE PAIRS AND THE PHYSICAL PROPERTIES OF CRYSTALS

4.1. One of the fundamental differences between unstable pairs and other equilibrium defects (Frenkel pairs or Schottky vacancies) is that an unstable pair cannot be quenched. Indeed, unlike FPs and Schottky defects (SDs), the lifetime of an unstable pair is very short and is independent of temperature, and the interstitial atom and vacancy of a given unstable pair recombine specifically with each other. Therefore, in crystals where the predominant type of defect is unstable pairs, a rapid quenching should leave all the properties unchanged. This has been demonstrated for the example of the semiconductors In_2Te_3 and Ga_2Te_3 with a loose-packed crystal lattice,[3,15] where it was shown by investigations of the most diverse physical properties (see below) that UPs were the main type of equilibrium defects. In Ref. 15 careful estimations were made of the possibilities of defects escaping to sinks, and it was shown that at the quenching rates used (not less than 100 K/s) less than 1% of the defects would manage to escape to sinks if they were long-lived. Control experiments on the quenching of other semiconductors (Ge, CdTe, ZnSe), in which the predominant equilibrium defects are SDs, were done under the same conditions,[15] and it was found that the quenching of these other substances led to radical changes of all their measured parameters, in complete agreement with the known published data.

Kraftmakher[16] called attention to the fact that the quenching of the majority of metals, which, as we know, leads to the freezing of defects, reveals a paradoxical fact: the concentration of frozen defects turns out to be several orders of magnitude lower than the equilibrium concentration for the high temperature from which the quenching took place. Kraftmakher developed a unique modulation technique for determining the concentration of equilibrium defects at premelting temperatures and reliably showed that the aforementioned difference is a general effect for metals. Also presented in Ref. 16 were data on the large disagreement of the heat capacity and the stored enthalpy on quenching. This is the same effect.

It seems that the unquenchability of defects is a direct consequence of the fact that a significant fraction of the equilibrium defects consists of unstable pairs (see the detailed analysis in Refs. 17 and 18).

4.2. It is known that in the temperature region where the equilibrium concentrations of any point defect (FP, SD, or UP) is rather large, the contribution of their formation to the heat capacity becomes substantial.[16,19] Using the model of Refs. 3, 4, 8, and 13, which describes the coexistence of all three types of defects, it is possible to interpret this effect, keeping in mind that at high temperatures UPs and FPs come into play, with energies of formation that are larger than that of SDs, which are prevalent in metals at lower temperatures. Tere is another paradox in the thermal properties of metals, noted in Refs. 16 and 19: the concentrations of defects determined from dilatometric measurements and from the heat capacity under equilibrium conditions at a high temperature come out different. Kraftmakher showed[16] that these differences are indicative of the presence of interstitials. As we have seen above, in spite of the short lifetimes of UPs, the relaxation of the lattice around v and i does have time to take place, and therefore in the x-ray diffraction experiments the lattice constant is determined by the difference of the effects of i and v. Thus the UP model can also eliminate this paradox in the high-temperature physics of metals.[17,18]

4.3. Finally, diffusion. Of course, UPs cannot contribute directly to the mass transfer, since they die at the same point where they were born. Nevertheless, their participation in a diffusion event can play an important role. An elementary diffusion event in the case of a long-lived SD, for example, consists in the following. A marked atom ''waits'' until an already formed vacancy migrates into a position adjacent to it and then, with a certain probability, hops over into it. Therefore the activation energy for diffusion by the vacancy mechanism consists of two components: the formation energy of v and its migration energy. In the case of an UP, the situation is different. The marked atom ''waits'' until an unstable pair is formed near it, within a distance less than the size of the RIZ of this atom and vacancy. Then in competition with the interstitial atom i belonging to this vacancy, the atom gets a chance to hop over into the vacancy. This mechanism of diffusion, which was proposed in 1974,[20] eliminates the migration, and the activation energy for diffusion in crystals in which UPs are predominant should therefore be equal to the energy of their formation and should not depend on the jump energy of the diffusing atom. Studies of semiconductors of the In_2Te_3 type, where UPs are the predominant type of equilibrium defect, have shown that the activation energy for self-diffusion and heterodiffusion in them is always the same.[21] Later, similar diffusion mechanisms were proposed in Refs. 22 and 23, the authors of which also were forced to propose an instability of Frenkel pairs.

The anomalies in the temperature dependences of the

coefficients of self-diffusion in metals were also discussed in the brilliant review by Kraftmakher.[16] It turns out that in many metals at high temperature the activation energy for diffusion increases sharply without any phase transitions, and this activation energy can exceed the enthalpy of formation of defects, determined from the temperature coefficient of the heat capacity, by a factor of two or even three times.

This surprising fact can also be interpreted consistently on the basis of the UP model. Indeed, as the temperature increases, so do the concentrations of both SDs and UPs, and, consequently, the probability of an encounter, which is proportional to the product of their concentrations, increases as well. If an encounter does occur, then the interstitial atom belonging to the UP can hop over into the Schottky vacancy. The diffusion coefficient in this case will be

$$D \sim \exp[-(E_{\mathrm{Sch}}+E_{UP})/kT], \tag{9}$$

i.e., the activation energy for diffusion at high temperature is the sum of the energies of formation of a Schottky vacancy and an unstable pair. A joint processing of the data on the temperature dependences of the heat capacity and of the diffusion coefficients shows quite satisfactory agreement.[17,18]

Thus the UP model can be used successfully to describe many phenomena corrected with the equilibrium concentration of defects in crystals.

5. UNSTABLE DEFECTS IN THE RADIATION PHYSICS OF CRYSTALS

5.1. As we have seen, all three types of point defects—Schottky vacancies, Frenkel pairs, and unstable pairs—are manifested in the equilibrium properties of crystals. The lowest energy of formation of all equilibrium defects is that of the SDs, and we need to demonstrate that the FPs and UPs can be predominant under certain conditions. In the case of radiation damage of a solid, everything is quite the contrary. The primary defects are now FPs and UPs, which are related in their origins. Indeed, the attacking high-energy particle, in transferring energy and momentum to an atom of the lattice and knocking it out of its site, of necessity creates v and i in equal numbers (see Ref. 24). Even if the formation of defects is a secondary result of the decay of optical excitation of an atom (so-called subthreshold effects), which takes place mainly in ionic and cryocrystals, again it is $i-v$ pairs that are created.[25] The IZs turn out to govern the kinetics of the accumulation of radiation defects: the RIZ is the cross section for their recombination.[3,5,24]

One of the basic parameters in the radiation physics of crystals is the Seitz threshold E_S, which has a value of the order of 20–30 eV. This is the energy that the primary knock-on atom (PKA) must acquire in order to occupy a stable position in an interstitial site. For a long time it was assumed that this would be a position in the nearest coordination sphere of the vacancy created. The discovery of IZs made it necessary to modify the interpretation of E_S: it is the energy of a PKA necessary for the latter to leave the perimeter of the RIZ, since otherwise i would recombine with v in an activationless manner.[3,24]

The simplest kinetic equation describing the process of accumulation of point defects under the action of ionizing radiation with allowance for the number of positions f of the interstitials within the RIZ and the fact that the concentration of radiation-produced i and v are equal[24] has the form

$$dC_d/d\Phi = \chi[1-w_0C_d], \tag{10}$$

where w_0 is the volume of the RIZ and χ is the number of defects introduced by a unit fluence Φ of defect-forming particles.

The solution to equation (10),

$$C_d = w_0^{-1}[1-\exp(-w_0\chi\Phi)], \tag{11}$$

shows that with increasing w_0 both the rate of accumulation of defects and their limiting concentration

$$C_{\mathrm{sat}} = 1/w_0 \tag{12}$$

fall off. (In Eqs. (10)–(14) the concentration is the number of particles per unit volume.)

This is how things stand with the irradiation by particles of small mass and/or at not very high energies, when the PKA acquires an energy only slightly in excess of E_S. In this case only point defects form, and the meaning of Eq. (10) is that the rate of accumulation of defects is proportional to that volume of the crystal which remains free of the RIZs of those vacancies which have already accumulated by the given time. Saturation sets in when the RIZs of the accumulated v cover the entire volume of the crystal. (Below we shall recall the situation when the UPs initiated by irradiation can become stabilized at significantly higher concentrations.)

5.2. One of the main ways of determining the RIZ volumes experimentally involves the processing of data with the use of Eqs. (10) and (11). A great number of data have been accumulated on the sizes of the IZs. The characteristic radii of RIZs in metals are often of the order of ten or even fifteen times larger than the atomic radii.[3,5,27,28] At the same time, as have seen, the RIZs in metals are determined exclusively by elastic $v-i$ interactions, and such large sizes of the IZs cannot be described by means of Eq. (2). They can be interpreted quantitatively if not only the elastic attraction of v and i is taken into account but also the elastic repulsion potential of like defects, $i-i$ and $v-v$.[10,11] The zones of absolute squeezing (SIZs) must be taken into account in order to explain the circumstance that the effective volume of a crystal available for localization of defects generated by the radiation should be decreased by that fraction of the volume in which the defects cannot coexist, not only because of recombination but also on account of expulsion. Two interstitials, for example, crowd each other out from the SIZ into the RIZs of vacancies, the attraction of which leads to mutual annihilation of two partners v and i. And the interstitial that has expelled its partner remains alive until another one expels it. Thus, there is a severe ultraspecific struggle.

Generalization of the linear Thompson equation (10) with allowance for the repulsion of like defects gives a saturation concentration

$$C_{\mathrm{sat}} = 1/(w_0+w_1), \tag{13}$$

where w_1 is the volume of the EIZ of the interstitials.

Since an interstitial i usually carries considerably larger elastic stresses than a vacancy v, the contribution of the $i-i$ interactions exceeds the direct effect of the RIZ.[10] Thompson[24] showed that the general form of the dependence

of the concentration of accumulated defects on the fluence of irradiation remains formally the same as in the case described even when the crystal is irradiated by heavy particles at high energies (fast neutrons, protons, ions, highly relativistic electrons), which form not only isolated $v-i$ pairs but also cascades of atomic collisions with the multiple creation of such pairs. Generally speaking, expressions (10)–(13) describe an extremely perfect crystal containing such a small number of dislocations, grain boundaries, and blocks that the escape of point defects to those sinks can be neglected. Strictly speaking, this is the low-temperature limit, when the thermally stimulated migration (diffusion) of defects is not taken into account, but when it is taken into account it is obvious that the larger the RIZ and SIZ, the lower the saturation concentration C_{sat}, which characterizes the radiation stability of the structure. The larger the values of w_0 and w_1, which take into account both the RIZ and SIZ, the smaller the value of C_{sat}, and the fewer the lattice defects that manage to survive after the action of the ionizing radiation.

A most important characteristic of crystals, their radiation stability, is largely determined by the sizes of the instability zones of defects—the RIZs and SIZs.

6. RADIATION STABILITY: EXPERIMENTS AND CRITERIA

The radiation stability of materials is extremely important in the age of atomic energy and space flight. It is necessary to create materials which, when subjected to enormous fluxes of ionizing radiation, maintain their operational parameters, both functional and protective. Is this possible in principle? It is necessary only to find a way to ensure the self-healing of defects.

6.1. As we have seen, the radiation stability is determined by the sizes of the IZs. How will the radiation resistance change if vacancies are introduced in the crystal prior to irradiation, with each vacancy forming its RIZ for interstitials i? The kinetic equation (10) for the concentration of radiation defects takes the form[29]

$$dC_d/d\Phi = \chi[1 - w_0(C_{v0} + C_d)], \tag{14}$$

where C_{v0} is the preirradiation vacancy.

It is clear from Eq. (14) that with increasing C_{v0} the value of C_{sat} decreases. This is a consequence of the recombination of i from the radiation-excited pairs with the previously existing vacancies. The physical meaning of Eq. (14) is that the i introduced by the radiation can recombine with structural vacancies v present in the sample, leading to the annihilation of these particles, so that a vacancy introduced by irradiation replaces the vacancy initially present, and their total concentration remains the same: the vacancies simply exchange places.

There are several classes of metallic alloys in which the concentration of vacancies is determined by the composition of the alloy, e.g., Hume-Rothery alloys in which the concentration of equilibrium vacancies C_{v0} is determined by the relationship between the electron concentrations and the filling of the states in the Brillouin zones in the corresponding alloy (alloys in the systems Ni–Al, Ni–In, Ni–Sn, etc.). In these alloys the concentration C_{v0} does not depend on temperature influences and therefore these alloys can serve as a basis for radiation-stable metal structures: it would seem that the coalescence of defects and radiation swelling could be eliminated if the RIZs of the existing structural vacancies covered the entire volume of the crystal: recombination process occur immeasurably faster than diffusion processes. Estimates show that pre-irradiation vacancies in the amount of 0.1% would be sufficient to completely prevent the accumulation of radiation defects—their self-healing is practically complete.[29]

Equation (14) describes processes occurring upon the spatially uniform introduction of point radiation defects: the cascade damage by heavy particles lessens the attractiveness of this idea. However, this seems like a promising way of developing structural metals, particularly since the RIZs are substantial even in damage cascades (see below).

Let us mention an exceedingly important point concerning all radiation damage effects in crystals. Equations (10)–(14) describe the accumulation of those i which after excitation have overcome the Seitz threshold, i.e., have escaped to beyond an RIZ. In fact, a very large fraction of the PKAs that have acquired an energy less than E_S remain within an RIZ and, with a probability of unity, recombine with the vacancies they have left behind in a time of the order of 10^{-10} s. The fraction that these made up depends on the energy of the PKA and the size of the RIZs. Under any circumstances, the larger the RIZs, the higher the radiation stability of the crystal, both on account of instantaneous recombination and on account of the slower processes described by equations of the type (10) and (14), e.g., the behavior of those PKAs that have escaped to beyond the RIZ.

The destiny of the PKAs remaining within the RIZs, which recombine with their vacancies v and return the energy they have acquired back to the crystal, was investigated in Ref. 30 on the basis of the UP model:[3,13] Indenbom[30] assumed that the energy released in the recombination of i and v becomes a source of short-wavelength phonons, which stimulate the annealing of radiation defects.

Can radiation stability be ensured for semiconductors and insulators, whose properties are immeasurably more sensitive to the effects of radiation? In contrast to the metals considered above, in which the initial v are disordered, in nonmetallic compounds the exchange of places between different atoms or ions is ruled out altogether or it creates defects that radically alter all the physical characteristics. It would seem that the problem of finding radiation-stable semiconductors is hopeless.

6.2. Meanwhile, back in 1969 (the first open publications were Refs. 13 and 31–33) it was revealed that semiconductors of the In_2Te_3 type have extremely high radiation stability both against to gamma radiation, which creates only point radiation defects, and to the action of fast neutron fluxes (in a nuclear reactor) and highly relativistic electrons with energies of up to 300 MeV. In recent years this phenomenon has been comprehensively investigated. It has been shown that the electrical conductivity of such semiconductors, its temperature dependence, the optical absorption in the ultraviolet, visible, and infrared regions, the the photoconductivity spectra, the lifetimes of photoexcited charge carriers, the thermopower, the thermally stimulated conductivity, and the mechanical properties suffer practically no changes after irradiation by fluxes of fast neutrons to fluences of

10^{18} cm^{-2} and of electrons with energy up to 300 MeV to fluences of up to 10^{17} cm^{-2}. (The fluxes indicated were those that were achieved in the experiments and by no means represent the limiting fluences for radiation stability of these semiconductors!) Both the irradiation and the measurements were done at temperatures ranging from 80 to 300 K. Measurements have also been made directly in the channel of a nuclear reactor. The stability of all the parameters of semiconductors of the In_2Te_3 type has been confirmed in all the experiments: radiation defects hardly accumulate, if at all, during irradiation.

''Effects of absence'' require special experimental ''hygiene.'' Therefore in all the experiments with the crystals mentioned, samples of the classic semiconductors CdTe, ZnTe, and Ge were irradiated and investigated under the same conditions. The data obtained, which are in splendid agreement with published sources, confirmed that the classic semiconductors are not radiation stable and are degraded when irradiated even by low fluences.

A detailed review of the data on radiation stability can be found in Refs. 3, 4, and 26.

6.3. What is the reason for such unusual radiation stability of the semiconductors In_2Te_3, Ga_2Te_3, and Ga_2Se_3? It lies in the crystal structure of these substances. They all have the sphalerite lattice, the same as for II–VI and III–V semiconductors, but with a fundamentally important structural feature: one-third of the sites of the cation sublattice of the compounds III_2-VI_3 are vacant. Even without delving into the quantum chemistry of these compounds (see Ref. 3), it is easy to see that for the same sphalerite structure, the number of cations and the number of anions in II–VI and III–V are equal, while in II_2-VI_3 there are three anions for every two cations. The presence of stoichiometric vacancies (SVs) is determined by the valence relations and is independent of temperature. It would seem that if there is an enormous concentration of vacancies, everything will reduce to the problem of metals with inherent vacancies, which was considered in paragraph 6.1. But let us not be hasty with conclusions. In fact, it is likely that a cation knocked out of its site will fall into a SV and set up a chemical bond, while the vacancy of a radiation origin left behind will become stoichiometric. This would amount to only disordering of the SVs and the cations in the cation sublattice of III_2-VI_3. This apparently is what happens in experimental reality; there is indirect evidence of it. But what happens in the anion sublattice? The mechanism considered in paragraph 6.1 cannot be used to interpret the anomalously high radiation resistance of these semiconductor compounds. It has a different physics (see below).

6.4. Concerning the accumulation of radiation defects and radiation resistance under irradiation by heavy particles. Of course a very large fraction of the radiation defects created are annihilated immediately after creation, as is confirmed by the results of Ref. 34, in which the damage to a lattice under irradiation by heavy ions was simulated and, at the same time, from the data of diffuse x-ray scattering, experimental evidence was found of a very large UP fraction, whose annihilation time is independent of temperature. If we are talking only about the SVs of III_2-VI_3 in relation to irradiation by gamma rays or electrons with energies of the order of a few MeV, when the energy transferred to the PKA is only slightly larger than E_S and only point radiation defects form, the high radiation resistance could be completely explained by the large sizes of the RIZs and instability of FPs, both cationic and anionic, which is in fact observed in these loose-packed crystal structures (see Sec. 4) by virtue of the rather large IZs in these crystals. However, the radiation resistance against fast heavy particles, neutrons in particular, requires a completely different interpretation, of course, using the presence of RIZs.

The collision of a fast neutron with the nucleus of a lattice atom transfers to the atom an energy E many time larger than E_S. The simplest estimate, according to Kinchin–Pease (see Ref. 24), shows that the number of defects formed in this case is E/E_S. As was shown in the classic papers of Lindhard,[24] the average distance between the vacancy v formed and the PKA i, because of multiple scattering on the surrounding atoms of the lattice, is not large; in copper crystals, e.g., it is not more than 3–5 Å. This value is considerably smaller than the radius of a RIZ, and it would seem that all of the radiation defects could recombine at the time of creation. If this were the case, then there would be no problem of the radiation stability of materials in nuclear power technologies. In actuality the situation is different. There is the Silsbee effect: a focusing of atomic collisions (see Ref. 24). This is a classical effect that goes back to the billiard rules formalized by Coriolis and Sommerfeld. If a chain of billiard balls is arranged in a line and is struck by another ball strictly along the line, then the whole row is shifted by one interball distance and (almost!) all of the energy and momentum is acquired by the last ball in the chain. It will go far, in accordance with the force of the impact. Silsbee discovered the same thing in atomic chains: as it advances, losing energy, the PKA can initiate an interstitial atom far from the place where it initiated the focusing, leaving a vacancy at that point. The mean free path L $[hkl]$ of such an excitation (crowdion) can amount to tens of interatomic distances (h, k, and l are the Miller indices denoting the crystallographic direction of propagation of the crowdion). Torrens and Chadderton[35] showed that focusing can also occur along chains of different atoms if the mass of the atoms is not too different. Thompson and Nelson showed that the Silsbee effect is enhanced substantially in a lattice on account of the focusing ''atomic lenses'' consisting of symmetric atomic triangles and (more rarely) squares surrounding a given crystallographic direction. These lenses do not allow the advancing crowdion to deviate from its line of travel, restoring deviating atoms to the correct path. This is the so-called ''additional focusing'' effect, which is much more effective than the simple focusing effect: an interstitial atom can end up at a distance of several tens of atomic distances from the place where the vacancy due to its creation is located. There is no hope that defects so far apart will be within a RIZ and recombine with each other.

It would seem that radiation stability is unachievable...

But nature has also provided the inverse effect, the possibility of asymmetric, defocusing atomic lenses.[4,3,36] Such lenses occur in crystal structures where there is asymmetry of the local environment—not of a given atom, but of a given crystallographic direction in the lattice. It is therefore

clear that crystallographically anisotropic crystals are more radiation stable than are isotropic crystals, and this has been confirmed experimentally.[37] The asymmetry of the lenses is strongest in crystal structure, which, even macroscopically isotropic, have local asymmetry in the short-range ''coordination cylinders'' of a given crystallograpic direction (cylinders and not spheres, since we are talking about the propagation of crowdions). In crystals with stoichiometric vacancies the latter create an exceedingly strong asymmetry of the lenses, which instead of three identical atoms in a given lens have one of the atoms missing. Such a lens is defocusing: at such a place the advancing crowdion breaks up, and a classical interstitial i is formed. Such lenses suppress focusing. This was demonstrated in Ref. 36 with the aid of a very simplified modification of the molecular dynamics method. The criteria of radiation stability of an initially defect-free single crystal is[9,3,36]

$$L_{\langle hkl\rangle} < r_{0\langle hkl\rangle}, \tag{15}$$

where $L_{\langle hkl\rangle}$ is the mean free path of the crowdion, and $r_{0\langle hkl\rangle}$ is the size of the RIZ for the $i-v$ interaction in the crystallographic direction $\langle hkl\rangle$. In the presence of defocusing lenses the maximum distance between i and v is the distance between these lenses. In crystals of the In_2Te_3 type, as a result of the presence of SVs, the defocusing lenses along the principal focusing direction $\langle 111\rangle$ are located at distances not exceeding two interatomic distances. It is clear that in III_2-VI_3, even a focused interstitial i will remain within the RIZ of the vacancy it has left. In such lattices, defocusing lenses are present for all directions with low Miller indices, i.e., the directions for which focusing is even possible. There are three-component semiconductors, e.g., $ZnIn_2Te_4$ and $Hg_3In_2Te_6$, which also have lattices close to the sphalerite lattice but with a lower concentration of SVs (1/4 and 1/6 of all the cation sites, respectively). It was shown in Ref. 38 that the radiation resistance of such crystals is also substantially higher than for classic semiconductors without SVs.

Of course, the class of crystals with a loose-packed lattice does not exhaust all semiconductors with SVs. In particular, there is an enormous number of oxides whose structures have the same defocusing lenses. If the distance between these lenses is smaller than the radius of the RIZ in any of the possible focusing directions, then those crystals should also have very high radiation resistance, especially in view of the fact that the dielectric permittivity in oxides is lower than in covalent semiconductors, and this [see Eq. (1)] will tend to increase the size of the RIZs. Experimental data on the irradiation of a number of substances in a reactor have shown that the radiation resistance is in fact high in such crystals (e.g., Y_2O_3 and In_2O_3).[36] Criterion (15) can be used to propose a classification of crystals according to radiation resistance: if defocusing lenses are present at distances of not more than 3–4 interatomic distance in all crystallographic directions (for cubic crystals there are three of them), then the radiation stability will be especially high; if defocusing is absent in one of the three directions, then the radiation stability is lower; if absent in two directions, it is lower still. Crystals in which focusing is not suppressed at all have the lowest radiation resistance. Such a classification and a numerical radiation resistance scale were introduced in Ref. 39. On the basis of this classification one can choose substances for applications in radiation technologies.

Thus the radiation stability of crystals is determined by IZs and UPs.

7. COLLECTIVE EFFECTS WITH THE PARTICIPATION OF UNSTABLE PAIRS

7.1. Let us begin with phenomena in radiation physics. At very high intensities of the defect-forming radiation, short-lived UPs, by interacting with each other, can create long-lived defects. Indeed, if the spatial density of the UP excitations is so high that the RIZs overlap, then a situation can arise in which the interstitial i from one UP is simultaneously located in the RIZ of another. Then this i can annihilate with the vacancy from another UP, and the i from the latter, together with the v from the former, find themselves at a distance greater than the size of the RIZ. In this case a long-lived FP has been created from two UPs. However, the FPs that have arisen also interact with other raditation defects. As a result, with increasing concentration of nonequilibrium PKAs introduced by radiation per unit time (in the case of a uniform distribution of them, which is realized, for example, in the case of intense gamma irradiation), the overall concentration of FPs nevertheless decreases, and the concentration of UPs, which are not preserved on quenching, increases, reaching a nearly constant value at extremely high intensities.[40] This is rather unexpected: with increasing intensity of the introduction of radiation defects, the probability of accumulation of stable radiation defects can decrease. Such a scenario is also observed in cascades of radiation defects created by heavy particles, when the local concentration of radiation defects in a volume of the order of several hundred atomic volumes is huge, and collective effects arise; by the way, some aspects of the physics of these collective effects find agreement with the above-described features of the kinetics of the accumulation of radiation defects at a large but uniformly distributed concentration of them.

As was shown 40 years ago (see Ref. 24) and is confirmed by present-day studies,[34] the lattice damage after the impact of a heavy particle when the energy of the PKA is many times greater than E_S leads to a nonuniform distribution of defects: at the center of a cascade there are predominantly vacancies v, and at the periphery there are excess interstials i. If i and v in a radiation defect are charged, then the higher concentration of v at the center of the cascade will create an excess charge, so that the i on the periphery are found in an electrostatic field created by the excess v at the center, the total charge Z of which is the difference of the charges of v and i inside a sphere of any radius centered at the center of the cascade. It is easy to see that the RIZ of any i in such a field increases, according to (1), by a factor of $\sqrt{Z}$. This is the size of an instability macrozone.[41] It is clear that recombination of radiation defects in cascades is stimulated by this distribution of the defects. The overall picture is the same for cascade damage occurring in metals or in covalent semiconductors like Ge and Si, in which case the total elastic stress field around the core of the cascade creates a corresponding macro RIZ by analogy with (2). It is clear that this mechanism acts the more strongly the larger the ordinary

RIZs (1) and (2). We note that such a distribution of i and v in the cascades for which the distance between i and v in the central regions is substantially smaller than the RIZ does not, however, lead to complete annihilation, partly because the numbers of i and v are not equal. This limits the radiation resistance even for those crystals which meet criterion (15). A much stronger limitation is the probability of formation at the center of the cascade of amorphous regions or new crystalline phases that may have equilibrium analogs or may be particularly nonequilibrium.[42,43] As was shown by Bakai,[44] even the state diagrams of multicomponent alloys under steady defect-forming irradiation acquire different topological forms. This is apparently equivalent to the introduction of an additional quasi-thermodynamic degree of freedom, corresponding to the steady-state concentration of i and v.

We have discussed the possibilities of the annihilation of radiation defects. It must be kept in mind, however, that there are mechanisms that act to stabilize the unstable radiation defects. These are the aforementioned overlap of the RIZs, the formation of metastable states of electrons with the participation of UPs, and also the formation of complexes of components of the UP with impurities.[27,34,40]

The formation of metastable phases and the amorphization at the center of cascades, as well as the phenomena listed above which stabilize the unstable radiation defects, spoil radiation stability, so that any euphoria as to the prospects for radiation-stable materials, even for those materials whose crystal structure is favorable for radiation stability, must be tempered by these factors. Nevertheless, there is a quite definite way of creating and selecting materials with enhanced radiation stablility.

7.2. Collective interactions of UPs determine effects in superionic (SI) crystals. The phenomenon of SI conduction consists in the fact that in a number of nonmetallic crystals, a wide class of substances called solid electrolytes or superionic crystals, a phase transition occurs in which the ionic conduction increases in a jump by several orders of magnitude, sometimes reaching values of up to $1\ \Omega^{-1}\,\mathrm{cm}^{-1}$, and the activation energy for conduction decreases sharply. The fundamental review[45] discusses both the experimental physics and theoretical models of SI crystals. In the final analysis, any model of ionic conduction rests on the concepts of mobile interstitials originating from FPs. However, theories based on the idea of an interaction of FPs and explaining many effects in SI crystals (in particular, the preservation of one of two sublattices nearly unchanged, while the other undergoes disordering) encounter substantial contradictions. Indeed, the FPs and their interactions are fundamentally isotropic. Meanwhile experiments show that the defects responsible for the SI phase transition have a spatial orientation. It is found, in particular, that the temperature of the phase transition depends strongly on the external electric field, and in a number of SI crystals there is not only a phase transition to a SI state but also a phase transition to a ferroelectric state. SI domains have been detected (see Refs. 45–49). Unlike the Frenkel pairs, the UPs are invariably anisotropic, and in ionic crystals this is expressed in the formation of short-lived dipoles. The observed domains are short-lived, with a lifetime of 10^{-11} s, which agrees with the estimate of the lifetime of UPs in ionic crystals which we made at the beginning of this paper.

Anisotropy of the excitations is observed, in particular, in the study of NMR and neutron scattering: ions very rarely go far from their regular positions in the lattice; the majority of them execute very large-amplitude oscillations but around ''their own'' site. In Refs. 50 and 51 the microwave absorption of a number of SI crystals was studied, and it was shown that ''the ions jump out and immediately jump back,'' and the lifetime of these lattice excitations is of the order of 5×10^{-11} s, a value which also agrees exactly with the lifetime of UPs estimated in paragraph 2.1 [Eq. (3)].

Skipping a little ahead, let us point out that the theory of the SI state presented below, which is based on the UP model, successfully describes not only the lifetime but also the features of the absorption spectra of SI crystals in the far infrared and microwave regions.[52] We should mention an interesting paper[53] in which the dielectric features of SI crystals were described successfully, but a number of other effects could not be described without taking the IZs into account.

Here is the basic idea of the theory of SI crystals based on the UP model.[52] Unstable pairs in an ionic crystal are short-lived dipoles. These dipoles are born independently and are oriented randomly in the lattice. Fluctuations in which there arises a certain local predominance of a parallel orientation of short-lived dipoles are probable. In such a region an average electric field arises which stimulates the formation of new UPs with the same orientation of the dipoles. It is easy to see that it is sufficient to have a predominance of only the projections of the dipole moments of the UPs on some direction, so that a one-dimensional model is adequate. The mean field approximation gives the following expression for the energy of formation of an individual UP in the collective field of all the other UPs, which comprise dynamic (and not static) dipoles:

$$E=(x_1+x_2)E_{UP}-\varphi(x_1-x_2)^2. \tag{16}$$

It is clear that, depending on the value of the second term in (16), the formation energy of an unstable pair can be decreased substantially. In Eq. (16) φ is the total field that would arise if all the dipoles formed and were oriented in each cell of the lattice; x_1 and x_2 are the relative number of projections of the dynamic dipoles oriented in opposite directions; (x_1+x_2) is the total concentration of UPs; (x_1-x_2) characterizes the predominance of one of the two orientations, which is what causes a nonzero total field of all the existing UP dipoles and lowers the energy of formation of each UP in the traditional orientation—along the total field. The origin of the nonlinear term in (16) of a given UP is as follows: the value of the self-consistent field increases with increasing fraction of the the UPs which are oriented, but even the birth of a ''correctly'' oriented UP has been stimulated by this collectively determined field. In a collective interaction the traditional orientation, as expected, is thermodynamically more favorable, even if the pairs are unstable. $Z=(x_1-x_2)/(x_1+x_2)$ is a dimensionless orientational order parameter of the unstable dipoles, and it characterizes the predominance of the parallel orientation. Minimizing the free energy with respect to the total concentration of UPs and also

with respect to Z gives equations for determining the equilibrium values of the UP concentration and Z. The main parameter of the joint solution of these equations, $\gamma = 2\varphi/E_{UP}$, gives a relation between the energy of the UP dipoles in the self-consistent field and the energy of their formation in the absence of this field. In the region $0<\gamma<2$ the theory predicts two possible phase transitions, one of which must invariably be second-order. The higher-temperature transition may not actually be realized if the crystal melts before reaching it. The general regularities of the phase transitions in SI crystals demonstrate just such behavior (see Ref. 45). One rather unusual result:[52] at low temperatures the order parameter $Z=0$ (reflecting the absence of the objects of the ordering, since their concentration is thermally activated), and as the temperature is raised and the concentration of interacting particles increases, their ordering occurs due to the predominance of the potential energy of interaction over the kinetic energy ($Z>0$), but at still higher temperature, when the average energy of the lattice vibrations becomes larger than the average interaction energy, the ordering is suppressed and again $Z=0$. A result with a similar physical meaning was obtained by Freiman *et al.*[54] in a study of the orientational degrees of freedom in molecular cryocrystals. The theory of Ref. 52 also permits interpretation of the superionic–ferroelectric phase transition: such a transition occurs when the interaction of the UPs in their self-consistent field is sufficiently strong in comparison with the energy of formation of the UPs ($\gamma>2$). Then the UPs become stable ordered dipoles. In Ref. 52 the state diagram was constructed for systems in which both insulator–superionic-crystal transitions (one or two phase transitions are possible) and superionic-crystal–ferroelectric transitions occur. Thus the phase transition to the SI state is determined by the UPs and their interaction.

However, the high ionic conductivity, the most distinctive property of SI crystals, is governed by the transfer not only of charge but also of mass, and it cannot be due to UPs, since, as we have seen, the UPs die at the same point where they were born, and are unable to migrate during their short lifetimes.

The charge carriers in a SI crystal are free interstitials, i.e., components of FPs which, as we have seen, coexist at low concentrations but compete statistically with UPs. At large concentrations of UPs these short-lived dipoles in the field of isolated i and v turn out to be oriented, and they lower the energy of an isolated interstitial and vacancy. This is a sort of solvation, as, for example, for ions in water. Thus the growth of the concentration of UPs leads to a decrease of the activation energy for FP formation, i.e., to growth of the concentration of FPs, which is one of the main distinctive features of SI crystals.[45,52]

Let us discuss the mobility of interstitial ions in a SI crystal. The mean free path of i is determined by their annihilation on encountering v belonging to either FPs or UPs. In either case the cross section of the process is the same—the sizes of the RIZ (Eq. (1)). The classic Drude model with the use of the above considerations not only is capable of describing the temperature dependence of the conductivity of SI crystals but can also be used to calculate the absolute value of the highest conductivity observed in SI crystals experimentally, which is actually close to the theoretical limit (of the order of $1\Omega^{-1}\,\mathrm{cm}^{-1}$). The model can also be refined by taking into account the interaction of the interstitials with each other, with a scattering cross section equal to the size of the SIZ.

Thus the UP model can give a consistent and quantitative interpretation of many collective phenomena in the physics of cyrstals.

8. UNSTABLE DEFECTS AND MATERIALS FOR TECHNOLOGY

8.1. In paragraph 6.1 it was shown that UP concepts permit one to propose a criterion for choosing metallic alloys which would have exceptionally high radiation stability—these are alloys with inherent structural vacancies. Of course it must be kept in mind that their plastic parameters are much inferior; they are more brittle than the construction materials used in today's nuclear reactors. However, their advantage is that their operating characteristics should be less affected by particle fluxes than those of contemporary structural alloys. It appears that the use of the method developed by Bakai[44] for constructing state diagrams of multicomponent systems under ionizing irradiation can give a realistic prognosis for the use of such alloys with allowance for the sharp decrease in the generation of stable FPs. It is quite probable that these alloys with structural vacancies will be the construction materials for nuclear reactors of the future. It can be hoped that taking the IZs associated with dislocations into account will provide the prerequisites for a microscopic theory of point defect sinks.

8.2. In paragraphs 6.2–6.4 we stated a criterion for choosing semiconductors and insulators with a high radiation stability. These are loose-packed crystal structures with rather large RIZs and with suppressed focusing of atomic collisions. The crystallographic criterion (15) now enables one without any special calculations to make a selection of crystalline materials having a high radiation stability. For insulators everything is clear (Y_2O_3, In_2O_3, etc.), with the restrictions mentioned in paragraph 7.1, of course.

It has been shown that semiconductors of the In_2Te_3 type, whose crystal structure, as we have seen, satisfies criterion (15) and whose exceptionally high radiation stability has been subjected to comprehensive experimental verification, can be used as detectors of extremely high intensities and fluences of high-energy particle radiation,[3] where the use of classic semiconductors is completely ruled out. Can one create a radiation-stable electronics based on In_2Te_3 and structurally related semiconductor compounds? It turns out that it is not a simple task. The problem is that semiconductors of the In_2Te_3 type have one more unusual property: their electronic parameters, unlike those of other semiconductors, are practically independent of impurity concentration. This is also a consequence of the presence of structural vacancies. It has been found that the impurities are localized at structural vacancies, which they remain in an un-ionized, atomic state.[3] Therefore it is almost impossible to influence the electronic properties of such semiconductors by doping: they remain intrinsic at any doping level. How can one make active elements of electronics (diodes and transistors) with a high radiation resistance? In Ref. 55 it was shown theoretically that

heterostructures based on two intrinsic semiconductors have a pronounced nonlinearity of the current–voltage characteristic, and with the aid of some physical and constructional contrivances one can even create a transistor. Estimates shown[55] that both the rectifying coefficient and the signal-amplifying capabilities in heterostructures based on intrinsic semiconductors of the In_2Te_3 type are inferior to those of all such devices based on classic semiconductors. They have only one advantage: devices made from them can operate stably even in a nuclear reactor, in storage units for radioactive wastes, and on long missions in outer space. The radiation-stable electronics will be cruder but ultimately more reliable.

8.3. In the previous paragraphs of this Section we have discussed the technical capabilities of unconventional crystalline materials selected solely on the basis of their exceptionally high radiation resistance. At the same time, there is another technical problem: to look for radiation-resistant crystals among those which have already proven their practical value. Their radiation resistance might not have record values, but it would be high enough for specific applications. Some very efficient scintillators based on ZnSe isovalently doped with tellurium, which substitutes for Se in the anion sublattice, were described in Ref. 56. It was shown that the centers responsible for the luminescence are complexes: Te in a substitutional position with a zinc vacancy in the nearest coordination sphere (a doublet) and a doublet with an interstitial Zn ion attached to it (a triplet). The excitonic luminescence in pure form was immeasurably weaker than the emission on the impurity complexes, in complete agreement with what Broude, Eremenko, and Rashba showed back in the 1950s.[57] Of course, today it is possible to determine in detail what defects and defect complexes are responsible for the luminescence,[56] how to increase the equilibrium concentration of triplets, which are the most advantageous in respect to the scintillation parameters,[56,58] and to establish which II–VI compounds are better than others at maintaining their parameters under ionizing irradiation in accordance with the general concepts of the UP model.[11] In one way or another, the ideas of the 1950s are still relevant today.

The author is happy to be able to emphasize this point in connection with the jubilee of Prof. V. V. Eremenko.

9. SUMMARY

—Unstable pairs consisting of a vacancy and interstitial atom are present in crystals, representing a third type of equilibrium defect in solids along with Schottky defects and Frenkel pairs. The unstable pairs are responsible for features of the heat capacity and diffusion and for anomalies in relation to the concentrations of defects in equilibrium and upon quenching, especially at pre-melting temperatures. In equilibrium the UPs are manifested mainly at temperatures close to the melting point.

—The equilibrium concentration of UPs is determined by instability zones of interacting defects. The instability zones exist in all solids, without exception, from cryocrystals to refractor metals, and are important not only in the interaction of point defects but of any other interacting lattice defects.

—The instability zones govern the behavior of crystals under high-energy irradiation: the larger the instability zones, the higher the radiation stability of the material. We have formulated a crystallographic criterion of radiation stability and stated the limits of its applicability.

—We have indicated some possible uses for the consequences of the instability zone and unstable pair models in physics and engineering.

This study was carried out thanks to grants from INTAS and the Ministry of Education and Science of Ukraine.

The author expresses his sincere gratitude to both of those organizations and to Dr. I. V. Sinel'nik for assistance in preparing the manuscript.

*E-mail: koshkin@kpi.kharkov.ua

[1] J. B. Gibson, A. M. Goland, M. Milgram, and G. H. Vineyard, Phys. Rev. **120**, 1229 (1960).
[2] Ya. I. Frenkel', Selected Works, Vol. 2 [in Russian], Izd. AN SSSR, Moscow–Leningrad (1958).
[3] V. M. Koshkin and Yu. N. Dmitriev, in *Chemistry and Physics of Compounds with Loose Crystal Structure*, Ser. Chemistry Reviews, edited by M. E. Vol'pin, 19/2, Harwood Acad. Publ., Switzerland (1994).
[4] V. M. Koshkin, Mol. Phys. Rep. **23**, 24 (1999).
[5] V. F. Zelenskiĭ, I. M. Neklyudov, and T. P. Chernyaeva, *Radiation Defects and Swelling of Metals* [in Russian], Naukova Dumka, Kiev (1988).
[6] V. M. Koshkin and Yu. R. Zabrodskiĭ, Fiz. Tverd. Tela (Leningrad) **16**, 3480 (1974) [Sov. Phys. Solid State **16**, 2256 (1974)].
[7] A. M. Kosevich, *Principles of Crystal Lattice Mechanics* [in Russian], Nauka, Moscow (1972).
[8] V. M. Koshkin, B. I. Minkov, L. P. Gal'chinetskiĭ, and V. N. Kulik, Fiz. Tverd. Tela (Leningrad) **15**, 128 (1973) [Sov. Phys. Solid State **15**, 87 (1973)].
[9] B. L. Oksengendler, in *Physical Properties of Irradiated Silicon* [in Russian], Izd. FAN, Tashkent (1987), p. 6.
[10] V. M. Koshkin, A. L. Zazunov, V. D. Ryzhikov, L. P. Galchinezkii, and N. G. Starzhiskii, Functional Mater. **8**, 240 (2001).
[11] V. M. Koshkin, I. V. Sinelnik, V. D. Ryzhikov, L. P. Galchinezkii, and N. G. Starzhinskii, Functional Mater. **8**, 552 (2001).
[12] V. M. Koshkin, Yu. R. Zabrodskiĭ, and N. M. Podorozhanskaya, Vopr. At. Nauki Tekh. (Kharkov), No. 3(11), 21 (1979).
[13] V. M. Koshkin and Yu. R. Zabrodskiĭ, Dokl. Akad. Nauk SSSR **227**, 1323 (1976) [Sov. Phys. Dokl. **21**, 203 (1976)].
[14] K. Nordlund and R. S. Averbak, Phys. Rev. Lett. **80**, 4201 (1998).
[15] Yu. N. Dmitriev, L. P. Gal'chinetskiĭ, V. N. Kulik, and V. M. Koshkin, Fiz. Tverd. Tela (Leningrad) **17**, 3685 (1975) [Sov. Phys. Solid State **17**, 2396 (1975)].
[16] Ya. Kraftmakher, Phys. Rep. **299**, 79 (1998).
[17] V. M. Koshkin, J. Phys. Oceanogr. **59**, 841 (1998).
[18] V. M. Koshkin, Mater. Res. Innov. **3**, 92 (1999).
[19] Ya. Kraftmakher, Philos. Mag. A **74**, 811 (1996).
[20] V. M. Koshkin and V. M. Ekkerman, Fiz. Tverd. Tela (Leningrad) **16**, 3728 (1974) [Sov. Phys. Solid State **16**, 2426 (1974)].
[21] V. M. Ékkerman, L. P. Gal'chinetskiĭ, and V. M. Koshkin, Fiz. Tverd. Tela (Leningrad) **16**, 1558 (1974) [*sic*].
[22] N. V. Doan and Y. Adda, Philos. Mag. A **56**, 269 (1986).
[23] M. J. Gillan, J. Phys. C **19**, 3517 (1986).
[24] M. W. Thompson, *Defects and Radiation Damage in Metals*, Cambridge Univ. Press (1969), Mir, Moscow (1971).
[25] M. A. Élango, *Elementary Inelastic Radiation Processes* [in Russian], Nauka, Moscow (1988); E. V. Savchenko, A. N. Ogurtsov, and O. N. Grigorashchenko, Chem. Phys. **189**, 415 (1994); Fiz. Tverd. Tela **40**, 903 (1998) [Phys. Solid State **40**, 831 (1998)].
[26] V. M. Koshkin and Yu. R. Zabrodskiĭ, in *Computer Modeling of Defects in Metals* [in Russian], edited by Yu. A. Osip'yan, Nauka, Leningrad (1990).
[27] Yu. I. Gofman and O. G. Oleĭnik, Metally **3**, 137 (1997).
[28] A. N. Orlov and Yu. V. Trushin, *Energies of Point Defects in Metals* [in Russian], Energiya, Moscow (1983).
[29] V. M. Koshkin and Yu. N. Dmitriev, Mater Res. Innov. **1**, 97 (1997).
[30] V. L. Indenbom, Pis'ma v Zh. Tekh. Fiz. **5**, 489 (1979) [Sov. Tech. Phys. Lett. **5**, 200 (1979)].

[31] L. P. Gal'chinetskiĭ, V. M. Koshkin, V. M. Kulakov, V. N. Kulik, M. I. Rudenko, P. I. Ryabka, U. A. Ulmanis, V. I. Shakhovtsov, and V. L. Shindich, Fiz. Tverd. Tela (Leningrad) **14**, 646 (1972) [Sov. Phys. Solid State **14**, 554 (1972)].
[32] V. M. Koshkin, B. I. Minkov, L. P. Galchinezkii, V. N. Kulik, and U. A. Ulmanis, Solid State Commun. **13**, 1 (1973).
[33] V. M. Koshkin, L. P. Galchinezkii, V. N. Kulik, and U. A. Ulmanis, Radiat. Eff. **29**, 1 (1976).
[34] P. Partyka, Y. Zhong, K. Nordlund, R. S. Averbak, I. Robinson, and P. Ehrhart, Phys. Rev. B **64**, 2352 (2001).
[35] I. C. Torrens and L. T. Chadderton, Phys. Rev. **159**, 671 (1967).
[36] V. M. Koshkin, Yu. N. Dmitriev, Yu. R. Zabrodskiĭ, R. A. Tarnopol'skaya, and U. A. Ulmanis, Fiz. Tekh. Poluprovodn. **18**, 1373 (1984) [Sov. Phys. Semicond. **18**, 860 (1984)].
[37] Yu. N. Dmitriev, V. M. Koshkin, and U. A. Ulmanis, Phys. Status Solidi A **106**, K7 (1988).
[38] D. V. Anan'ina, V. L. Bakumenko, G. G. Grushka, L. N. Kurbatov, and L. M. Shalyapina, Izv. AN SSSR Ser. Neorg. Mater. **12**, 2074 (1976).
[39] V. M. Koshkin and Yu. N. Dmitriev, Mater. Res. Soc. Symp. Proc. **327**, 381 (1994).
[40] Yu. R. Zabrodskiĭ and V. M. Koshkin, Fiz. Tverd. Tela (Leningrad) **18**, 2857 (1976) [Sov. Phys. Solid State **18**, 1669 (1976)].
[41] Ya. E. Geguzin, Yu. R. Zabrodskiĭ, and V. M. Koshkin, Fiz. Tverd. Tela (Leningrad) **21**, 1755 (1979) [Sov. Phys. Solid State **21**, 1005 (1979)].
[42] I. M. Lifshits, M. I. Kaganov, and L. V. Tanatarov, At. Énerg. **6**, 391 (1959).
[43] B. B. Gulyaev, N. V. Kamyshanchenko, I. M. Neklyudov, A. M. Parshin, and E. I. Pryakhin, *Structure and Properties of Alloys* [in Russian], Metallurgiya, Moscow (1993).
[44] A. S. Bakai, Mater. Sci. Forum **97–99**, 307 (1992).
[45] Yu. Ya. Gurevich and Yu. I. Kharkats, *Superionic Conduction in Solids* [in Russian], Ser. Itogi Nauki, Izd. VINITI AN SSSR, Moscow (1987).
[46] R. J. Cava, F. Reidinger, and B. J. Buensch, Solid State Commun. **24**, 411 (1977).
[47] S. Yu. Stefanovich, L. A. Ivanova, and A. V. Astaf'ev, *Ionic and Superionic Conduction in Ferroelectrics* [in Russian], Nauka, Moscow (1989).
[48] V. I. Valyukenas, A. S. Orlyukas, A. P. Sakalas, and V. A. Mikola, Fiz. Tverd. Tela (Leningrad) **21**, 2449 (1979) [Sov. Phys. Solid State **21**, 1409 (1979)].
[49] K. Funke, J. Klaus, and R. E. Lechner, Solid State Commun. **14**, 1021 (1974).
[50] K. Funke and H. J. Schneider, Solid State Ionics **13**, 335 (1984).
[51] A. A. Volkov, Yu. G. Goncharov, G. V. Kozlov, G. I. Mirzoyants, and A. M. Prokhorov, Dokl. Akad. Nauk SSSR **289**, 846 (1986) [Sov. Phys. Dokl. **31**, 632 (1986)].
[52] Yu. R. Zabrodskiĭ, Yu. B. Reshetnyak, and V. M. Koshkin, Ukr. Fiz. Zh. (Russ. Ed.) **35**, 611 (1990); Fiz. Tverd. Tela (Leningrad) **32**, 69 (1990) [Sov. Phys. Solid State **32**, 38 (1990)]; Izv. AN SSSR Ser. Fiz. **54**, 1207 (1990); Dokl. Akad. Nauk UkrSSR **7**, 57 (1990).
[53] V. E. Zil'bervarg and N. A. Trufanov, Fiz. Tverd. Tela (Leningrad) **27**, 1537 (1985) [Sov. Phys. Solid State **27**, 926 (1985)].
[54] Yu. A. Freiman, S. M. Tretyak, A. Jezowski, and R. J. Hemley, J. Low Temp. Phys. **113**, 723 (1998).
[55] Yu. G. Gurevich, I. N. Volovichev, and V. M. Koshkin, Microelectron. J. **29**, 535 (1998); Phys. Status Solidi A **174**, 221 (1999).
[56] V. D. Ryzhikov (Ed.), *Scintillating Crystals and Ionizing-Radiation Detectors Based on Them* [in Russian], Naukova Dumka, Kiev (1998).
[57] V. L. Broude, V. V. Eremenko, and É. I. Rashba, Dokl. Akad. Nauk **114**, 520 (1957).
[58] V. M. Koshkin, A. Ya. Dulfan, V. D. Ryzhikov, L. P. Galchinezkii, and N. G. Starzhinskii, Functional Mater. **8**, 709 (2001).

Translated by Steve Torstveit

Influence of structural inhomogeneity on the luminescence properties of silicon nanocrystallites

I. V. Blonskiĭ,* M. S. Brodyn, A. Yu. Vakhnin, A. Ya. Zhugayevych, V. M. Kadan, and A. K. Kadashchuk

Institute of Physics, National Academy of Sciences of Ukraine, pr. Nauki 46, 03650 Kiev, Ukraine
(Submitted January 10, 2002)
Fiz. Nizk. Temp. **28**, 978–987 (August–September 2002)

The features of the photoluminescence and the manifestation of thermally stimulated and tunneling luminescence due to the separation of nonequilibrium charge carriers between the photoexcited silicon core of a nanocrystallite and its peripheral layers of SiO_x and SiO_2 are investigated for different forms of nanostructured silicon. A model is proposed wherein a ''two-stroke charge piston'' acts in turn on the electron and hole components by means of an Auger process which occurs under restricted volume conditions and brings about a spatial separation of the charge carriers. © *2002 American Institute of Physics.*
[DOI: 10.1063/1.1511717]

1. INTRODUCTION

An unsolved mystery of porous silicon (por-Si) is the nature of its bright luminescence in the visible region of the spectrum, which is observed at room temperature and under various means of excitation. In the many papers devoted to this phenomenon a number of different factors, each of which (or in combination with others) can explain only individual properties of this luminescence. Among the main factors considered responsible for the formation of luminescence channels are the quantum size effect in the nanometer-sized silicon wires and the luminescence of the etching products on their surface. The advantages and disadvantages of these two approaches are discussed in detail not only in original papers but also in monographs (e.g., in Refs. 1 and 2). A unified explanation of the entire complex of observed properties of the emission from por-Si and of the different forms of nanostructured silicon obtained by different methods (enhanced oxidation of por-Si, the implantation of SiO_2 layers with Si^+ ions, followed by high-temperature annealing, the thermally stimulated phase separation of films of nonstoichiometric SiO_x into silicon nanoparticles and SiO_2) has not yet been achieved. Our approach to the solution of this problem is to take into account the influence of the structural inhomogeneities of the silicon nanoparticles on the formation of the luminescence properties of porous silicon.

For the majority of nanostructured silicon samples one can distinguish three levels of their structural inhomogeneity. The first level has to do with the inhomogeneity over the thickness. As is seen in Fig. 1a, even in the simplest case the samples of this material must be treated as a two-layer medium. It is obvious that the fundamental properties of the substrate material and the layer deposited on it are substantially different. A typical example of this type of object is a layer of por-Si in natural contact with monolithic silicon. In Ref. 3, in particular, it was shown that the thermal properties of por-Si layers depend on their porosity ρ; for example, at $\rho \cong 70\%$ the thermal diffusivity of por-Si layers decreases to a value equal to that of SiO_2. This means that the thermal conditions under which the por-Si layers emit depend on ρ. The difference in the degree of heating of the por-Si layers can affect, for example, the degree of thermal activation of the trap states responsible for the properties of the recombination radiation.

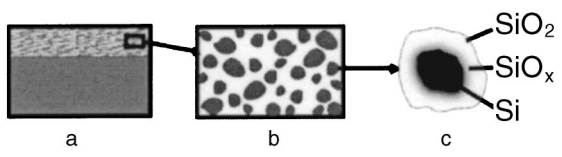

FIG. 1. Illustration of the different levels of structural inhomogeneity of porous silicon: inhomogeneity over thickness (a); variance of sizes (b); multilayer structure of individual nanocrystallites (c).

The second level of structural inhomogeneity has to do with the variance of the sizes of the silicon nanoparticles (Fig. 1b), which depends on the technological conditions. Because the band gap ΔE_g of a nanoparticle depends on its average dimension L ($\Delta E_g \propto L^{-2}$), for an ensemble of nanoparticles there is typically an inhomogeneous broadening of the electronic states, and the amount of broadening, which is thus dependent on the conditions under which the samples were prepared, is reflected in the spectral composition of the radiation, its polarization, and damping kinetics.[1,2,4–6]

Finally, the third level of the structural inhomogeneity has to do with the inhomogeneity of an individual silicon nanoparticle. As is seen in Fig. 1c, each nanocrystallite should be treated as a three-layer structure with a silicon core, a transition layer of SiO_x ($x<2$) with a gradient in terms of x, and an outer layer of SiO_2. The parameters of each of these three layers can vary over wide limits and also depend on the technology used to prepare the samples. The ensemble-averaged energy diagram of a silicon nanocrystallite with allowance for the quantum size effect, the variance of the size of the nanoparticles, the variable-gap nature of the SiO_x layer, and the numerous defect states in the SiO_x and SiO_2 layers is shown schematically in Fig. 2. The problem of determining those structural components of a multicomponent medium which are responsible for the absorption of

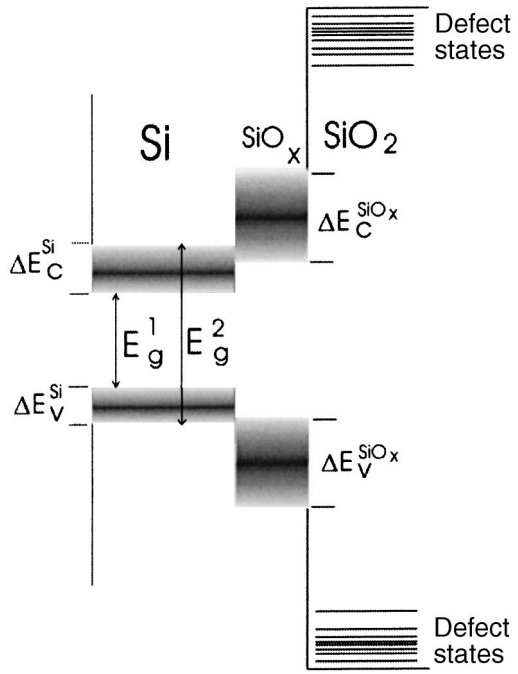

FIG. 2. Schematic diagram of the energy states of a silicon nanocrystal.

light and luminescence has to do with the third level of inhomogeneity. Very often the absorption of light occurs in one of the components and the emission in another. In that case there is also the problem of adequately describing the mechanism of transport of the charge carriers from the photoexcitation region to the secondary-emission region. Here it is important to search for signs of spatial separation of the charge carriers taking part in the radiative recombination in the multicomponent medium. In this paper we solve that problem on the basis of a comparison of the properties of the photo-, thermo-, and tunneling components of the luminescence of nanostructured silicon. A model is proposed by which the whole set of data obtained can be explained from a unified point of view.

2. EXPERIMENTAL TECHNIQUE

The basic objects of study were samples of highly oxidized por-Si and nanoparticles of silicon in SiO_2, obtained by the ion implantation. The por-Si samples were prepared by the conventional technology of electrochemical etching[1] of p-type silicon wafers having a resistivity of about $10\ \Omega$/cm and a crystallographic orientation (111) at anodizing current densities of $5-80\ \mathrm{mA/cm^2}$ and etching times of 15 to 90 min. The samples of the second type were obtained by the implantation of SiO_2 layers of the order of 500 nm thick with Si^+ ions at an irradiation dose of $6\times10^{16}\ \mathrm{cm^{-2}}$, followed by annealing for 30 min in a nitrogen atmosphere at $T_{\mathrm{ann}}=1150\,^{\circ}\mathrm{C}$.[6]

The photoluminescence (PL) was excited by radiation from a mercury lamp or a pulsed nitrogen laser with a wavelength of 337 nm. The luminescence was detected with a diffraction spectrometer with a CCD-array detector. The temperature was controlled and stabilized to 1 K or better.

The thermally stimulated luminescence (TSL) and the tunneling luminescence (TL) were measured in the temperature range 4.2–300 K on an automated device for thermally activated spectroscopic research. The TL and TSL signals were registered by a cooled photomultiplier operating in the photon-counting mode. The sample was placed in a controlled-temperature optical helium cryostat, and after cooling was irradiated by a high-pressure mercury lamp for 10–60 s at a steady temperature, which was stabilized to 0.1 K in the range 5–250 K. The kinetics of the TL were measured directly after the excitation was turned off, with a delay of 1 to 1000 s, and the signal integration time was 1 s. The technique used to measure the TL was analogous to that described previously,[7] and the details may be found in Ref. 8. The TSL was measured starting 7–15 min after excitation, when the intensity of the TL had decreased to the dark (background) signal level. The TSL was measured in two different modes: a linear heating mode, with the sample heated at a constant rate of 0.15 K/s, and a fractional thermoluminescence (FTL) mode. The fractional heating mode is a superposition of a slow linear heating of the sample and relatively low-amplitude (up to 10 K) temperature oscillations. The FTL mode, which is a modification of the initial-segment method, makes it possible to determine the activation energy for detrapping of a charge carrier to a higher accuracy and thus has a higher resolving power than the linear heating mode. This is the main advantage of using the FTL mode, since the usual methods of processing the TSL curves are extremely imprecise or altogether inapplicable in the case of a continuous or quasi-continuous distribution of the traps over energy and also when there is a discrete set of traps with very close activation energies. The details of the FTL method and the data processing are described in Refs. 9 and 10. The main difference of our implementation of the FTL method[9] from that proposed earlier[10] is the extension of the temperature interval of the measurements from liquid-nitrogen temperature down to 4.2 K, making it possible to study shallow carrier traps.

The effective average activation energy E_a is determined in each cycle of temperature oscillation by the expression

$$E_a=-\frac{d\ln I_{TSL}(T)}{d(1/k_BT)}, \tag{1}$$

where I_{TSL} is the TSL intensity, T is the temperature, and k_B is Boltzmann's constant. In accordance with the technique developed in Ref. 10, the distribution function of the filled traps $h(E)$ can be calculated to within a normalizing factor as

$$h(E)\propto\frac{I_{TSL}(E)}{dE_a/dT}, \tag{2}$$

where $I_{TSL}(E)$ is the TSL intensity after conversion of the temperature scale to an energy scale with the use of the $E_a(T)$ dependence obtained experimentally.

The TSL and TL signals, as a rule, were rather weak, ruling out the use of a monochromator for studying their spectral composition. Therefore the spectral distribution of the radiation was estimated using a set of light filters placed between the window of the cryostat and the photomultiplier.

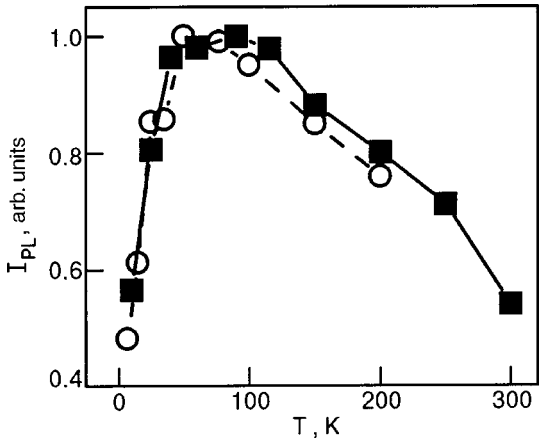

FIG. 3. Temperature dependence of the integrated PL intensity. The density of excitation is 1 kW/cm^2 (circles, dashed curve) and 20 kW/cm^2 (squares, solid curve).

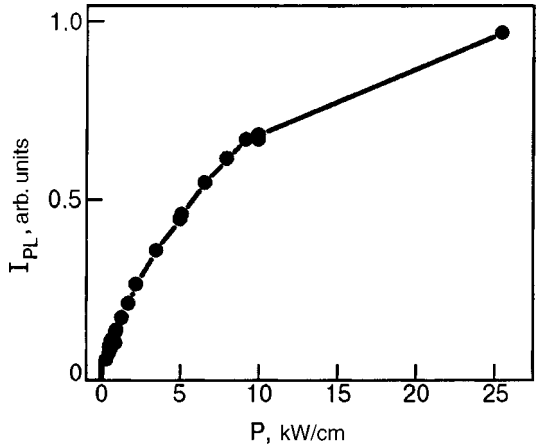

FIG. 4. Typical dependence of the integrated PL intensity of por-Si on the excitation density.

3. EXPERIMENTAL RESULTS

Photoluminescence

Let us consider those properties of the photo-, thermo-, and tunneling luminescence of nanostructured silicon that can be explained in the framework of radiation recombination of spatially separated charge carriers. Several results, in particular the temperature dependence and lux–intensity characteristic of the photoluminescence, were obtained previously in Ref. 11. Since the study of the PL of por-Si has been the subject of many papers and reviews (see, e.g. Ref. 1), we will mention only those properties of the PL which are common to samples of nanostructured silicon obtained by different technological processes. We are talking about the complex of properties of the red–orange emission band with a maximum of around 680 nm for oxidized por-Si and 740 nm for silicon nanoparticles obtained by ion implantation. We note three features of the PL of nanostructured silicon.

1. A nonmonotonic temperature dependence of the integrated photoluminescence intensity I_{PL} of the red–orange band and a dependence of the point of inversion of the sign of dI_{PL}/dT on the excitation density. As we see in Fig. 3, with increasing temperature one initially observes a growth of the integrated intensity, which gives way at high temperatures to the typical Arrhenius quenching. With increasing density of excitation the point of inversion of the sign of dI_{PL} is shifted to higher temperatures.

2. Nonlinearity of the lux–intensity characteristic of this same band, which is especially pronounced at excitation densities P above 2 kW/cm^2 (see Fig. 4).

3. Long-term degradation of the PL (the ''fatigue effect'') with an approach to a stationary value (Fig. 5). This effect displays temperature and spectral sensitivity and is most strongly expressed at the short-wavelength edge of the red–orange band at helium temperature. After the samples were heated to room temperature the emission spectrum was restored.

To explain the nonmonotonic behavior of $I_{PL}(T)$ and the dependence of the position of the point of inversion of the sign of dI_{PL}/dT on the excitation density and the technology used to prepare the samples, in Ref. 11 a model was proposed based on the assumption of a thermal detrapping of charge carriers and their subsequent localization in states from which recombination accompanied by radiation in the red–orange PL band occurs. To check this model we measured the TSL and TL of these same samples.

Thermally stimulated luminescence

TSL measurements can elucidate the role of the trap states (which are assumed to be associated structurally with the SiO_x and SiO_2 layers) in the luminescence properties of nanostructured silicon. For this it is important to study the spectral properties of the TSL. We investigated por-Si samples for which a nonmonotonic dependence of $I_{PL}(T)$ is observed. Here it should be noted that in some papers on por-Si (see the literature cited in Ref. 11) a monotonic $I_{PL}(T)$ dependence of the Arrhenius type was also observed. It was shown in Ref. 11 that the cause of that behavior is that the red–orange PL band contains a contribution from other oscillators, most likely involving residual etching products. This was confirmed by the fact that a gradual cleaning of the por-Si surface by laser ablation was accompanied by a transition from the simple Arrhenius behavior to a nonmonotonic $I_{PL}(T)$ characteristic.

Figure 6 shows typical TSL curves measured in different spectral ranges of the PL. It is known that the total PL spec-

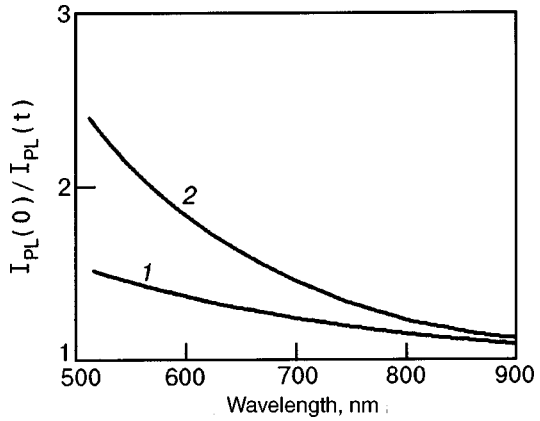

FIG. 5. Spectral dependence of the degree of degradation of the PL of por-Si at $T=6$ K, an excitation density of 30 kW/cm^2, and irradiation times t [min]: 15 (*1*) and 60 (*2*).

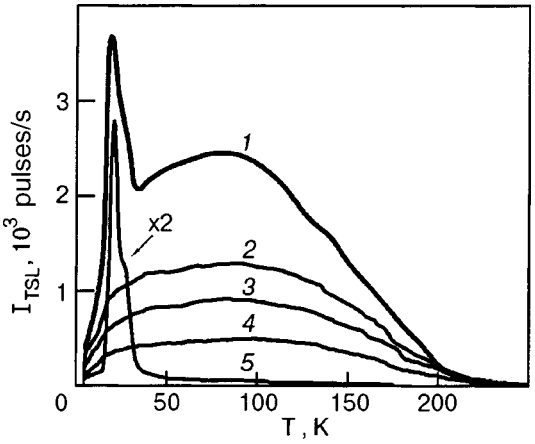

FIG. 6. Temperature dependence of the TSL signal for por-Si in different spectral ranges: total signal (detection region $\lambda > 800$ nm) (*1*), $\lambda > 640$ nm (*2*), $\lambda > 690$ nm (*3*), $\lambda > 730$ nm (*4*), $\lambda > 580$ nm (*5*).

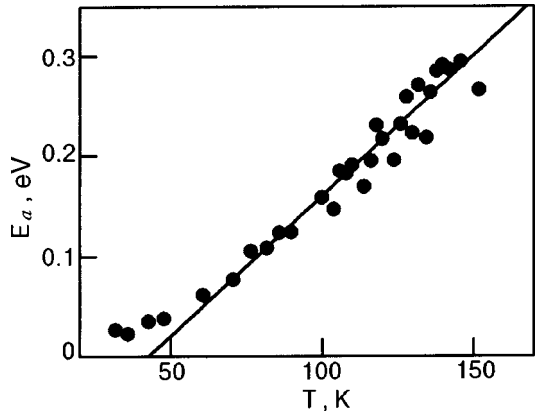

FIG. 7. Temperature dependence of the average activation energy E_a.

trum consists of a main red–orange band with a maximum at around 680 nm and a less intense blue band with a maximum at around 440 nm, the origin of which has been linked to the energy levels of defect states in the peripheral SiO_2 layer.[1] As we see in Fig. 6, the components of the emission spectrum of por-Si consist of two components of the TSL signal: a narrow low-temperature doublet near 25 K, and a wide, structureless band extending all the way to 200 K. One also notices the following features of the TSL in por-Si.

1. There is a clear correlation between the low-temperature doublet in the TSL and the blue PL band. In view of the nature of the blue PL band, the origin of the low-temperature doublet is also naturally associated with discrete trap states of a defect nature in the SiO_2 layer. This conclusion is supported by the data of Ref. 12, in which, in a study of the damping kinetics of the blue PL band in por-Si, it was observed that, in addition to the main nanosecond damping component, as the temperature is lowered from room to helium temperature, a millisecond damping component arises in a threshold manner at about 30 K, i.e., the temperature of its onset is practically equal to the position of the low-temperature component of the TSL. In Ref. 12 the appearance of the slow component of the PL kinetics is attributed to a manifestation of trap states in the emission from the peripheral SiO_2 layer. The narrowness of the low-temperature doublet in the TSL signal indicates the following features of the PL: a small variance of the energy interval between the emitting and trapping states (the blue PL band), and a narrow width of the trap level, which is more characteristic of defect states in SiO_2 than in the silicon core or the SiO_x layer, since the latter are typified by an inhomogeneous broadening of the electronic levels.

2. A comparison of the curves in Fig. 6 shows that the broad high-temperature component of the TSL signal corresponds to the red–orange PL band. Using light filters to cut out different parts of the main emission band, we found that there was no shifting or deforming of the contour of the TSL band, only a decrease in the total signal. This fact suggests that (for por-Si samples cleansed of residual etching products) the main emission band is structureless, i.e., it is not a superposition of bands of various natures.

3. The FTL technique was used to obtain the temperature dependence of the thermal activation energy E_a for the detrapping of carriers (the points in Fig. 7), which is described well by the empirical expression

$$E_a = 0.0028T - 0.12[\text{eV}]. \tag{3}$$

The energy spectrum of the trapped states responsible for the formation of the red–orange PL band can be calculated by starting from the TSL curve (curve *2* in Fig. 6) and expressions (2) and (3). It follows from the results obtained that the distribution of the traps over energy is continuous and quite wide (lying at a depth of up to 0.3 eV), its width being close to the half-width of the main PL band.

One reason why the TSL curve is so wide is the appreciable scatter of the trap states with respect to energy, apparently because of their localization in a layer of variable composition SiO_x. Another reason is the variance of the sizes of the silicon nanocrystallites, which leads to significant variation of the energy interval between the trap levels in SiO_x and the bottom of the conduction band of the silicon core (Fig. 2).

Tunneling luminescence

It is known that the detrapping of charge carriers usually occurs in a thermally activated process, but tunneling (subbarrier) transitions can also occur,[8] and they are particularly important at low temperature. The light emitted at these transitions is called tunneling luminescence. It is known that TL is an ordinary phenomenon in glasses, alkali–halide crystals, and heavily doped semiconductors,[13–15] and its damping kinetics, as a rule, obeys a Becquerel distribution law of the form $I \propto t^{-\beta}$, where t is the time and $\beta \cong 1$ is the Becquerel index. Thus the tunneling luminescence is the longest-lived emission component.

The curves of the damping kinetics of the integrated TL intensity measured in the temperature interval 5–250 K for a samples of oxidized por-Si are shown in Fig. 8. We see that the damping of the TL has a Becquerel character with an exponent $\beta \approx 1$, where β has an explicit nonmonotonic temperature dependence (Fig. 9). As far as we know, this is the first time that such a nonmonotonic $\beta(T)$ dependence has been observed in semiconductor materials.

To describe the damping kinetics of the tunneling component of the PL we consider a model based on the hopping transport of a charge carrier between localized states in the

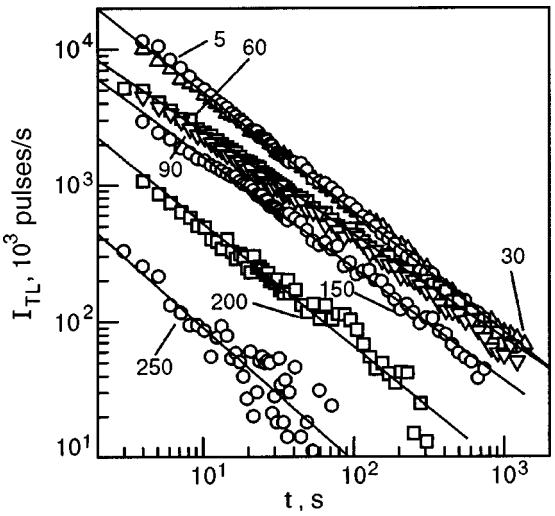

FIG. 8. Damping kinetics of the TL at different temperatures T [K], for each of which the Becquerel index β was calculated (excitation wavelength $\lambda_{exc}=405$ nm).

disordered SiO_x layer. The intensity, or the probability per unit time of a tunneling/thermally activated hop from one localized state (site) with energy ε_i to an adjacent state with energy ε_f, is described by the well-known expression[16]

$$\nu=\Gamma_{if}\exp\left(-\frac{E_{if}}{k_BT}\right), \tag{4}$$

$$\text{where}\quad E_{if}=\begin{cases}0, & \varepsilon_f\leqslant\varepsilon_i\\ \varepsilon_f-\varepsilon_i, & \varepsilon_f>\varepsilon_i\end{cases},$$

E_{if} is the activation energy of a hop, Γ_{if} is the activationless component of the hopping probability, which is determined mainly by the overlap of the wave functions of the states.

Because of the disorder in the SiO_x layer, the values of ε_i, ε_f, and Γ_{if} on going from one site to another vary in a random manner. The problem confronted by a theoretical description of the phenomenon under discussion is that the spatial distributions of these quantities and the dependence (density) of states over energy are unknown. Moreover, they can be different for different samples and even for different nanocrystallites,[1] and that also makes it difficult to do exact calculations on the basis of expression (4). Therefore, in this situation it is advisable to use the effective medium approximation (see, e.g., the review[17]). Thus we replace the spatially nonuniform quantities E_{if} and Γ_{if} in Eq. (4) by spatially uniform effective quantities E and Γ, which actually describe a process in which an electron and a hole are transported to the same site, where their recombination can occur in a single hop with a probability

$$\nu=\Gamma\exp\left(-\frac{E}{k_BT}\right), \tag{5}$$

where Γ and E are random variabes with a certain effective distribution. Such an approximation is justified in the case when the distance between the electron and hole is small (within a few hops). The admissibility of this approximation for the system under study is ensured by the small thickness of the SiO_x layer and the small size of the silicon nanocrystallite as a whole. In such an approach one can also take into account the possible transitions of the carriers from the SiO_x layer to the silicon core and back, by considering the core to be an individual trap with state energy $\varepsilon=E_g$.

Taking into account that the probability per unit time for the recombination of an electron–hole pair localized on the same site is much larger than the average hopping rate, the time dependence of the luminescence intensity I can be written as

$$I(t)=q\langle v e^{-\nu t}\rangle_{E,\Gamma}, \tag{6}$$

where the factor q takes into account the quantum yield of radiative recombination, and the angle brackets denote averaging over the effective distributions of Γ and E. Since we are interested in the temperature dependence of the Becquerel index, we shall replace the nearly temperature-independent quantity Γ by its average value. We then obtain the following expression for the damping kinetics of the TL:

$$I(t)=q\Gamma\int_0^\infty\exp\left[-\frac{E}{k_BT}-\Gamma t\exp\left(-\frac{E}{k_BT}\right)\right]f(E)dE. \tag{7}$$

Expression (7) can be converted to a form more convenient for analysis by taking the integral by the method of steepest descent. Such a simplification is justified for the case of the long-time asymptotic behavior that we are interested in, primarily because it is at long times that the damping has a Becquerel character. Here the saddle-point value E_0 is determined from the equation

$$k_BT\psi(E_0)=1-\Gamma t\exp\left(-\frac{E}{k_BT}\right), \tag{8}$$

$$\text{where}\quad \psi(E_0)\equiv\frac{d\ln f(E_0)}{dE_0}.$$

The physical interpretation of the method of steepest descent is rather transparent: in the course of a certain time interval from time t to $t+\Delta t$ the charge carriers that take part in emission are predominantly those which are held in traps with an activation energy close to $E_0(t,T)$. The longer the observation time t or the higher the temperature T, the larger the value of $E_0(t,T)$. For this reason, by studying the long-time asymptotics one can ''probe'' the distribution func-

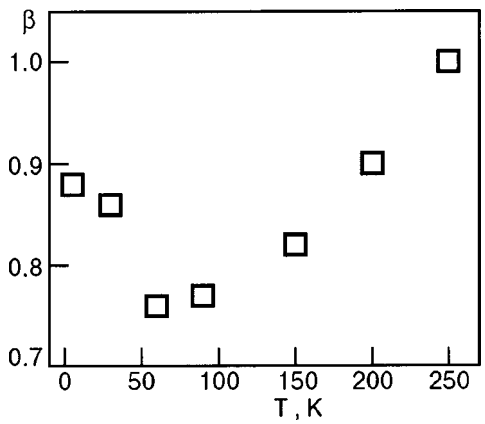

FIG. 9. Temperature dependence of the Becquerel index β.

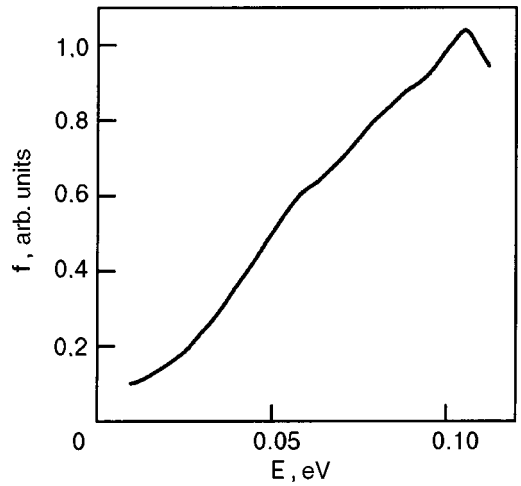

FIG. 10. Distribution function of the trapped-carrier activation energy, $f(E)$, recovered from the TL damping kinetics.

tion $f(E)$ of the effective activation energy, much as this is done by increasing T in TSL measurements. The damping exponent is given by the formula

$$\beta(t) = -\frac{d\ln I(t)}{d\ln t} = (1-k_BT\psi) \times\left[1-\frac{(k_BT)^2\psi'+(k_BT)^3\psi''}{2(1-k_BT\psi-(k_BT)^2\psi')^2}\right]. \quad (9)$$

Since the TL is measured mainly at low temperature, when the condition $k_BT \ll \Delta E$ holds, where ΔE is the effective width of the distribution $f(E)$ (in practice this condition means that $\beta \approx 1$, as is observed in experiment), this allows us to make a simplification in expression (9), whereupon the relation between the Becquerel index and the energy distribution of the traps takes the simple form

$$E_0 = k_BT\ln(\Gamma t), \quad (10)$$

$$\psi(E_0) = [1-\beta(t,T)]/k_BT. \quad (11)$$

Equation (10) establishes the relation between the energy scale, on the one hand, and the temperature and time (on a logarithmic scale) on the other. Equation (11) relates β and $\psi(E)$ [and, hence, $f(E)$, according to Eq. (8)].

From the experimental data on the TL damping kinetics (Fig. 8) we calculated the function $\psi(E)$ using expressions (10) and (11). The value $1/\Gamma \approx 0.2$ s was obtained from the condition of consistency of the kinetic curves measured at different temperatures. This value characterizes the mean time between successive activationless hops. Then, using Eq. (8), we recovered the function $f(E)$. The result of the calculation is presented in Fig. 10.

Thus the results of TSL and TL measurements are complementary and to a certain degree are in mutual agreement. The TSL gives an estimate for the width of the activation energy distribution: $\Delta E \geqslant 0.3$ eV. The TL measurements indicate a monotonic growth of the function $f(E)$ at low energies $E \leqslant 0.1$ eV. This sort of behavior can be explained by the fact that the charge carriers execute several hops prior to recombination.

4. DISCUSSION OF THE EXPERIMENTAL RESULTS

The results of the previous Section attest to the fact that a portion of the photogenerated charge carriers leave the silicon core, becoming localized in the peripheral layers of SiO_x and SiO_2. The experimental data can be explained from a unified point of view in an approach which we call the ''two-stroke charge piston'' model. It is assumed that the absorption of light with the generation of an electron–hole ($e-h$) pair occurs in the silicon core of the nanocrystallite (Fig. 11a). After this their radiative recombination can occur, with the production of a photon of secondary emission. However, the characteristic recombination time is rather long (up to several milliseconds), and therefore at the excitation densities usually used it is quite probable that prior to recombination the first $e-h$ pair will generate a second pair (Fig. 11b). As has been noted in a number of papers (see, e.g., Ref. 6), in the presence of more than two pairs of charge carriers in a nanosize silicon core a radiationless Auger recombination process becomes probable, in which the energy of recombination of one $e-h$ pair is expended on the ejection of one of the carriers of the other $e-h$ pair into the outer layer of the nanocrystallite. As a result, the nanoparticle undergoes a transition to a state in which, e.g., an electron is localized in the SiO_x layer and a hole remains in the silicon core (Fig. 11c), or vice versa. The rate of recombination of such a spatially separated $e-h$ pair is quite low because of the small probability of a tunneling transition. Therefore, when yet another $e-h$ pair is generated in a silicon core in such a state (Fig. 11d), the radiationless Auger process is again the most probable, and the result is that now a hole is ejected into the SiO_x layer (Fig. 11e). Thus the silicon core of the nanocrystallite is free of charges, which are now localized in the peripheral layers, and the core has returned to a potentially radiative state. This cyclic return of the sample to a radiative state can account for the experimentally observed ''luminescence fatigue'' effect, when the intensity of the PL does not go to zero but to a finite value of the saturation signal (Fig.

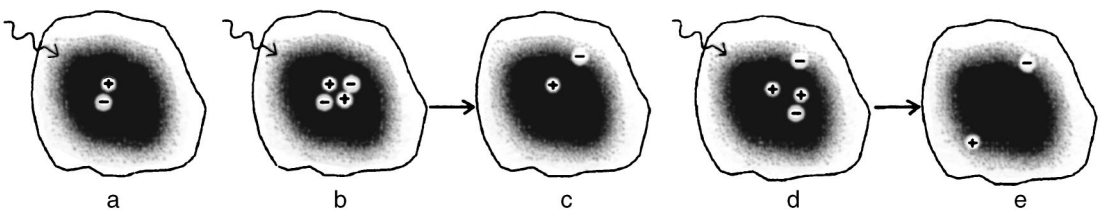

FIG. 11. Schematic illustration of the operation of the ''two-stroke charge piston'' in nanocrystalline silicon.

5). Here the efficiency of the expulsion of charge carriers in the two-cycle process described can in general be different for electrons and holes because of the difference of the energy distributions of their traps.

The model set forth above is based on the assumption of a high efficiency of the electronic Auger process, which is the motive force of the ''two-stroke charge piston,'' alternately ejecting electrons and holes from the silicon core of a nanocrystallite into its peripheral layers. This is in fact a justifiable assumption. It is known the the rate of the Auger process for free charge carriers is proportional to the square of their concentration. At a distance between interacting particles of the order of 10 nm (which corresponds to a volume density of around 10^{18} cm^{-13}) the cross section for Auger scattering is comparable to the cross section of the crystalline cell ($\sim 10^{-15}$ cm^2), i.e., it is even greater than cross section of the electron–phonon interaction.[6] Auger scattering is therefore the main dynamical process governing the lifetime of the $e-h$ pairs, the radiationless recombination time, and the other kinetic parameters of the system.

The high efficiency of the Auger process should result in efficient population of the trap states (including those of a defect nature) localized in the peripheral layers, and that circumstance is manifested in the aforementioned features of the PL spectra and of the TSL and TL signals and also their dependence on the technological conditions under which the nanostructured silicon samples were prepared. We note that the efficiency of the Auger process is higher for smaller sizes of the nanocrystallite. Therefore, the more intense TSL and TL signals are observed for samples with the smaller (on average) nanocrystallites.

Let us conclude by noting the differences between our model and that proposed in Ref. 6. The process considered in Ref. 6 ends with the transition of the nanocrystallite to a nonradiative state (corresponding to Fig. 11c), and the incomplete degradation of the PL is explained by the partly thermally activated detrapping of electrons in the peripheral layers. However, it follows from our TSL results that the majority of the trapped charge carriers are detrapped at $T > 50$ K. Therefore, to explain the quantitative degradation indices of the PL spectrum (especially near helium temperature) it is not enough to take into account only the thermal restoration of the trapped carriers: the maximum degree of degradation of the PL does not exceed a factor of three even at $T = 4.2$ K. We have therefore refined the model proposed in Ref. 6, extending the effect of the Auger process to the hole component of the electronic subsystem of the silicon core and proposing the possibility of multiple repetition of the process within a single nanocrystallite. As a result, bound charge carriers accumulate in the outer layer of the crystallite, and their recombination is manifested as features of the TSL and TL.

CONCLUSION

The luminescence properties of a system of silicon nanoparticles depends substantially on their average size and structural inhomogeneity. The influence of the size factor is manifested not only in a variation of the spectral composition of the emission due to the variation in the band gap of the nanocrystallite but also in the efficiency of the Auger process, the cross section of which is inversely proportional to the size of the crystallite. A ''two-stroke charge piston'' model is proposed, the motive force of which is the Auger process, which brings about the expulsion of charge carriers from the photoexcited silicon core of the crystallite to its peripheral oxide layers and the subsequent localization of the carriers in them. A feature of the model is the extension of the action of the Auger process successively to the electron and hole components of the silicon core. The proposed model can explain from a unified point of view a whole complex of experimental results: the nonmonotonic temperature dependence of the integrated PL intensity and the shift of the position of the extremum of this dependence on variation of the excitation density, saturation of the lux–intensity characteristic of the main PL band, the ''emission fatigue'' effect in the PL spectra, the features of the TSL signal, the presence of a tunneling component of the luminescence, and the higher intensity of TSL and TL for samples with smaller sizes of the nanocrystallites. The proposed model is of a general nature and can be invoked to explain the features of the luminescence in ensembles of nanoparticles of other semiconductors.

This study was done under the grant ''Electrical and Optical Physics of Nanostructures Based on Silicon and Germanium'' of the Russian–Ukrainian Intergovernment Program ''Nanophysics and Nanoelectronics.''

*E-mail: blon@iop.kiev.ua

[1] O. Bisi, S. Ossicini, and L. Pavesi, Surf. Sci. Rep. **38**, 1 (2000).
[2] P. Hess, *Progress in Photothermal and Photoacoustic Science and Technology*, Vol. IV Semiconductors and Electronic Materials Series, SPIE Press, Bellingham, Washington (2000).
[3] S. V. Bravina, I. V. Blonskyy, N. V. Morozovsky, and V. O. Salnikov, Ferroelectrics **254**, 65 (2001).
[4] M. S. Brodin, I. V. Blonskii, and V. A. Tkhorik, JETP Lett. **20**, 580 (1994).
[5] I. V. Blonskyy, M. S. Brodin, and V. A. Thoryk, Semicond. Sci. Technol. **12**, 11 (1997).
[6] D. Kovalev, B. Averboukh, M. Ben-Chorin, F. Koch, A. L. Efros, and M. Rosen, Phys. Rev. Lett. **77**, 2089 (1996).
[7] X. Guo and G. D. Mendenhall, Chem. Phys. Lett. **152**, 146 (1988).
[8] A. Kadashchuk, Yu. Skryshevskii, A. Vakhnin, N. Ostapenko, V. I. Arkhipov, E. V. Emelianova, and H. Bässler, Phys. Rev. B **63**, 115205 (2001).
[9] A. Kadashchuk, D. S. Weiss, P. M. Borsenberger, S. Nespurek, N. Ostapenko, and V. Zaika, Chem. Phys. **247**, 307 (1999).
[10] I. A. Tale, Phys. Status Solidi A **66**, 65 (1981).
[11] S. N. Bashchenko, I. V. Blonskiĭ, M. S. Brodyn, V. N. Kadan, and Yu. A. Skryshevskiĭ, Zh. Tekh. Fiz. **71**(1), 66 (2001) [Tech. Phys. **46**, 63 (2001)].
[12] A. Kux, D. Kovalev, and F. Koch, Appl. Phys. Lett. **66**, 49 (1995).
[13] D. E. Aboltin, V. J. Grabovskis, A. R. Kangro, Ch. Lushchik, A. A. O'Konnel-Bronin, I. K. Vitol, and V. E. Zizap, Phys. Status Solidi A **47**, 667 (1978).
[14] E. A. Kotomin and A. B. Doktorov, Phys. Status Solidi B **114**, 287 (1982).
[15] K. G. Zamaraev, R. F. Zaĭrutdinov, and V. P. Zhdanov, *Electron Tunneling in Chemistry: Chemical Reactions at Large Distances* [in Russian], Nauka, Novosibirsk (1985).
[16] A. Miller and E. Abrahams, Phys. Rev. **120**, 745 (1960).
[17] J. W. Haus and K. W. Kehr, Phys. Rep. **150**, 263 (1987).

Translated by Steve Torstveit